Thése de doctorat
presentée devant
L'Univérsité Claude Bernard Lyon - I
École Doctorale de Physique et d'Astrophysique

Spécialité

PHYSIQUE THÉORIQUE / PHYSIQUE DES PARTICULES

présentée par

Mlle. BOGNA KUBIK

en vue de l'obtention du grade de

DOCTEUR de L'UNIVERSITÉ CLAUDE BERNARD (Lyon 1)

Symétrie électrofaible à la lumière du LHC

Soutenue publiquement le 5 Octobre 2012 devant la commission d'examen formée de :

M.	J.	Gascon	*Président du jury*	-	IPN Lyon
Mme.	G.	Bélanger	*Rapporteuse*	-	LAPTH Annecy
M.	Ch.	Grojean	*Rapporteur*	-	CERN Genève
Mme.	N.	Mahmoudi	*Examinateur*	-	LPC Clermont-Ferrand
M.	A.	Arbey	*Examinateur*	-	CRAL Lyon
M.	G.	Cacciapaglia	*Directeur de thèse*	-	IPN Lyon
M.	A.	Deandrea	*Directeur de thèse*	-	IPN Lyon

PhD thesis delivered by Claude Bernard University of Lyon

Speciality:

THEORETICAL PHYSICS / PARTICLE PHYSICS

submitted by

Mrs. BOGNA KUBIK

for the degree of

DOCTOR OF PHILOSOPHY

Electroweak symmetry breaking in the light of LHC

---

defended October 5th, 2012 in front of the following Examining Committee:

Mr.	J.	Gascon	*President*	-	IPN Lyon
Mrs.	G.	Bélanger	*Reviewer*	-	LAPTH Annecy
Mr.	Ch.	Grojean	*Reviewer*	-	CERN Genève
Mrs.	N.	Mahmoudi	*Examiner*	-	LPC Clermont-Ferrand
Mr.	A.	Arbey	*Examiner*	-	CRAL Lyon
Mr.	G.	Cacciapaglia	*Supervisor*	-	IPN Lyon
Mr.	A.	Deandrea	*Supervisor*	-	IPN Lyon

Aknowledgments

This work was realized in the University of Lyon in the Laboratory of Nuclear Physics (IPNL) thanks to the research grant founded by the Ministry of Higher Education and Research. I would like to thanks the two successive directors of IPNL, Bernard Ille and Guy Chanfray for stay in the IPNL I could have.

I would like to thank especially to my PhD advisors, Aldo Deandrea and Giacomo Cacciapaglia, for supporting me during these past three years. You have been supportive and have given me the freedom to pursue various projects without objection. You have also provided insightful discussions about the research. I am also very grateful for the scientific advices and knowledge and many insightful discussions and suggestions. The research projects and discussions that we had together allowed me the insertion in the scientific word not only French but in the entire world. Thanks for your enthusiasm and joy during my PhD!

I also have to thank Jules Gascon for accepting to be the president of my PhD committee and for many useful remarks about my work. I also thank my two referees, Geneviève Bélanger and Christophe Grojean for the time they dedicated for reading my thesis and also for their very smart remarks, questions and opinions. Finally I have to thank the members of my PhD committee, Nazila and Alexandre for the time to go to Lyon and listening my presentation.

I also thank my collaborator, Alexandre A., for his help and ideas about the dark matter stuff. Thanks to Sacha D. for discussions and helping in first steps in Lyon. I would also like to thanks the Antares group in the IFIC in Valencia and especially Juanjo Hernandez-Rey for the possibility of spending some time in the experimental group and visiting Spain. Also, thanks to the program Multidark I could go the meeting in Madrid. Thanks to all my colleagues in Spain for the great time I had there.

Finally I have to thank to my colleagues from 334 - Jeremy L., Gregoire G. and Ahmad T. for the imagination, invention, joyfulness, political formation and musical sessions. Thanks to Nico C., Vincent J., Nico B. and Clem B. for introducing me in the real life of the IPNL students. Finally thanks Olivier B., Benoit M. and Antonio U. for the adventure with antiquarks! Thanks to Max and Julien for the "soirées" unforgettable. Thanks to Luca for the MadGraph help and to Antoine for being my "parrain".

Special thanks to the IPNL stuff for the help (especially for the answers on my "informatic" questions and problems).

Na koniec dziękuje moim rodzicom za wszystko.

Abstract

The extra-dimensional extensions of the Standard Model of particles are now in a very active epoch of development. The motivations of introducing extra dimensions are based on one hand on string theories that require the existence of new dimensions to be consistent. On the other hand such theories can potentially explain the hierarchy problem, number of fermion generations, proton stability and other enigmas of the Standard Model. The common feature of these models is that they provide a new neutral weakly interacting particle - perfect candidate to the Dark Matter. It's stability is preserved by the so-called KK parity which prohibits the decays of the LKP into SM particles. The geometry of the underlying space determines the particle spectrum of the model, thus the mass and the spin of the DM candidate, which in turn plays the key role in the phenomenological studies

We present a model with two universal extra dimensions compactified on a real projective plane. This particular geometry is chosen because chiral fermions can be defined on such orbifold and the stability of the neutral dark matter candidate arise naturally from the intrinsic geometrical properties of the space without adding any new symmetries *ad hoc*.

We present the particle spectrum at loop order up to the second level in Kaluza-Klein expansion. The particularity of the spectrum is that the mass splittings within each KK level are highly degenerated providing a very interesting potential signatures in the LHC. We study the dark matter phenomenology in our model and constrain the parameter space by comparing our results with WMAP data and direct detection experiments. Using the obtained bounds we focus on the collider phenomenology of our model.

Contents

List of Figures

List of Tables

Introduction

My adventure with particle physics begun rather early, when I was in college, with a famous book of Leon M. Lederman "The God Particle“. I red when ill lying in the bed. Since then the world of elementary particles, and especially the ”god particle“ motivated and guided all my scientific career. Now I am really pleased that I can contribute in the community of physicists and put a small brick into a great construction that is particle physics.

The history of particle physics is rather recent. It begins about 1890s when new discoveries have caused significant paradigm shifts that pushed scientists to review the basic concepts that were considered as a very solid background of all the scientific theories. The General Relativity of Einstein (1916) revealed some questions about the nature of space and time and the geometry of our Universe. Even more dangerous consequences had the discovery of quantum mechanics. This theory raised in the minds of physicists confronted to the problems such as the Black Body radiation explained by Planck in 1900 or photoelectric effect described by Einstein in 1905. These discoveries were only a prelude before the great epoch of particle physics when efforts of thousands of theorists and experimentalists from “both sides of the scale” were put together with the common goal - to explain the nature of the Universe. “Both sides of the scale” refers to the micro and macro physics because, that is remarkable, some explanations of the very microscopic world can come from the observations and theories at the cosmological scale.

Now our best understanding of how the basic constituents of the Universe behave, is encapsulated in the Standard Model of Particles. Formulated in the early 1970s it has successfully explained a host of experimental results and precisely predicted a wide variety of phenomena. Over time and through many experiments by many physicists, the Standard Model has become established as a well-tested physics theory. Its power has been confirmed once more with the observation a peek that can be interpreted as a Higgs boson - the key to the origin of particle mass. Although the discovery of Higgs does not write the final ending to the story. Even though the Standard Model is currently the best description we have of the subatomic world, it does not explain the complete picture. The theory incorporates only three out of the four fundamental forces, omitting gravity. There are also important questions it cannot answer, such as what is dark matter, what happened to the missing antimatter, and more.

In order to study the limits of this theory, new experiments in high energy physics and in observational cosmology have been developed in the last decade. The results from Large Hadron Collider (LHC), a proton-proton collider located at CERN, are now the most expected to reveal what is hidden above the Standard Model domain of predictability. For sure the experimental data using the high energies reached by the LHC can push knowledge forward, challenging those who seek confirmation of established knowledge, and those who dare to dream beyond the paradigm.

As high energies are required, the Universe itself can accelerate our investigation as it is home to numerous exotic and beautiful phenomena, some of which can generate almost inconceivable amounts of energy. Supermassive black holes, merging neutron stars, streams of hot gas moving close to the speed of light are only few examples of phenomena that generate gamma-ray radiation, the most energetic form of radiation. What is the origin of such high energies? Studying these energetic objects add to our understanding of the nature of the Universe and how it behaves. These are the goals of FERMI telescope. At the cosmological scale WMAP mission was proposed to NASA in 1995. It was launched in 2001 and is still collecting data from the cosmic microwave background radiation - the radiant heat left over from the Big Bang. The properties of the radiation contain a wealth of information about physical conditions in the early universe and a great deal of effort has gone into measuring those properties since its discovery.

The role of theorists in all this world of experiments is to guide them. To analyze data in the LHC one has to know where to search a weak signal hidden in a huge QCD background. Therefore a huge effort is made by theorists to make predictions as precise as possible and to suggest what could be the nature of new physics potentially visible at LHC. A part of this thesis will aim to give some new directions that could be explored in the collider. On the other hand we use the cosmological parameters derived from WMAP observations to put some bounds on our model.

I started the three-year period of doctorate with one principal goal - to understand the microscopic nature of the Universe, to investigate the problems that arise within the newest theories and the motivations that push thousands of physicists to not stop searching. I had an opportunity to familiarize myself with the supersymmetry formalism during my Master studies. I must say that the mathematical construction of superfields and superspace seems very attractive to me and particularly beautiful in its simplicity. Then I started studying extra-dimensional models that propose a completely different mathematical formulation of the new physics and thus the nature of new predicted constituents would be somehow distinct from those predicted by supersymmetry.

In the first year of my PhD I joined a group that was already working on a model based on a six-dimensional space-time with two flat extra dimensions compactified on a real projective plane. The main attractive feature of this model that motivates our work is that the geometrical properties of the underlying space provide a stable dark matter candidate in a natural way. The existence of extra dimensions will manifest itself in our four-dimensional space as a tower of Kaluza-Klein states propagating as “ordinary” particles. It is however not sufficient to stop here. The main goal of our team was to study the phenomenology of the model in both, the LHC collider environment and in the dark matter sector. To this aim we need to proceed through some steps that are summarized in this thesis.

The document divided in three parts:

- Part I describes the basic models of physics that are currently used and that are a framework of our study. In this part there are three chapters.
  - In the fist chapter we introduce some notions about the mathematical language used in physics and its motivations.
  - In Chapter 2 we present the Standard Models of Particles and of Cosmology that put

bounds on our models on one hand and on the other had have some problems that our model tries to solve.
  - In Chapter 3 is dedicated to Dark Matter phenomenology. Here we summarize the current experimental searches of Dark Matter particle and we present the relic abundance calculation method that we used in our study.

- Part II introduces tools for working with extra-dimensional models. We present the construction of the simplest orbifolds and quantum fields propagating in extra dimensions. We introduce the notion of Kaluza Klein states also. Then we present the methods used in loop calculation in extra dimensions. The main classes of extra-dimensional models known in the literature are presented at the end of this part.

- Part III presents the model and our results. This part is divided in three chapters.
  - Chapter 5 is completely dedicated to the description of the model. We present the construction of the orbifold first. Then we define the quantum fields and give the tree level spectrum of particles present in the scenario.
  - Chapter 6 presents the calculation of the radiative corrections to the (2,0)-(0,2) Kaluza-Klein states. Using the techniques presented in the Part II we have calculated the spectrum of the model at one loop level for two different geometries of the orbifold $R_4 \gg R_5$ and $R_4 = R_5$. The main feature of the spectrum of the model is underlined - a very small mass splittings within each KK level. This will have interesting consequences in the phenomenological signatures of our model. We introduce also the free parameter m_{loc} - a localized mass of Higgs bosons that will allow in the later study to change considerably the bounds of the compactification scale.
  - Chapter 7 focuses on the Dark Matter phenomenology. We study the bounds on the compactification scale coming from the relic abundance WMAP data. First we show in analytical manner the impact of co-annihilations on the relic abundance bounds. They are expected to be strong as the mass splittings negligible at least for KK leptons. In the next step we perform a full numerical study of the model using MicrOMEGAs. We include all the loop induced couplings and use loop-level spectrum of the model to predict the precise bounds on the compactification scale in both geometries $R_4 \gg R_5$ and $R_4 = R_5$. Then we try to vary parameters of the model to investigate their impact on the relic abundance. Finally we present the bounds coming from the direct detection experiments.
  - Chapter 8 is dedicated to the LHC phenomenology. We identify the main interesting channels that are studied in the LHC experiments and that could potentially give signatures of our model in collider searches. We infer bounds on the compactification scale from those processes in two considered geometries $R_4 \gg R_5$ and $R_4 = R_5$. To finish this chapter we summarize all the numerical bounds on the compactification scale we have obtained in our analysis.

- In the Appendices we give our notation conventions and summarize the analytical results of the annihilation cross sections used in the main chapters.

Part I

Elementary Particles and Interactions - Introduction

Chapter 1

Mathematics, Geometry, and Space-Time

1.1 Mathematics

By convention there is color,
By convention sweetness,
By convention bitterness,
But in reality there are atoms and space"
-Democritus (circa 400 BCE)

Mathematics is a natural science that describes the most general forms of processes in nature as assumes Galileo. Mathematics deals with reality, postulating axioms believed to be true and confirmed pragmatically by the empirical truth of the theorems derived from them. It distinguishes itself from other natural sciences only in that it obtains very few concepts and relations directly from experience, and infers from them the laws of more complex phenomena by purely deductive means. The idea of securing knowledge by logical deduction from unquestionable principles was explicitly proposed by Aristotle, and successfully applied by Euclid in his Elements and later on by Galileo, Newton and their successors. From its inception in ancient Greece, and again in modern times, science adopted a mathematical interpretation of nature. This problem of mathematical interpretation is much deeper than could be seen at first sight and many philosophers, mathematicians and physicists, now also neuropsychologists join the team that discuss whether the Universe has an intrinsic mathematical *nature* or it can only be accurately described by mathematical formulas used as a *language*.

Einstein wondered how it was possible that mathematics, a product of human thought, so admirably described reality. Mathematical science is "unreasonably effective" in describing physical reality and it predicts with an extreme accuracy the natural processes.

In his 1933 Oxford lecture, Einstein highlighted the physical, empirical nature of mathematics by inviting us to consider Euclidean geometry as the science of the possible mutual relations between practically rigid bodies in space – in other words, to treat geometry as a physical science, without abstracting from its original empirical content. Without considering geometry as a natural science he could have never formulated the theory of relativity. Supporting the view of mathematics as a natural science that describes the logic of nature, mathematics often pre-discovers physical reality. For example Dirac's equation predicted the positron. Moreover,

the fact that natural forms can be described by abstract mathematical concepts suggested to Pythagoras and Heraclitus, and later to Galileo and modern scientists, that mathematics describes the "logic" of the universe.

1.2 Geometry

"La géométrie euclidienne s'accorde assez bien
avec les propriétés des solides naturels,
ces corps dont se rapprochent nos membres et notre œil
et avec lesquels nous faisons nos instruments de mesure."
H.Poincaré "La valeur de la science"

I think that it was the discovery of non-Euclidean geometries in mathematics that has led to the theory that space is not Euclidean or Galilean. The Euclidean axiom of parallels, which was the basis of the axiom system of Euclid, was causing serious concern to mathematicians. This axiom states that for any plane on which there is a line L and a point P that does not lies on the line, there is in the same plane a unique line L' which passes through P and is parallel to L which means that two lines in a plain can have at most one common point. In the XIX-th century the mathematicians tried to derive this statement from other axioms of the Euclidean system. It turned out that the statement about two lines on a plane was independent from others axioms and as such it could not be derived as a theorem but must be admitted as another axiom. It was then straight forward to postulate another axioms and derive other geometrical systems. We can cite as examples:

1. Riemannian geometry: for any plane on which there is a line L and a point P that does not lie on the line there is no line L' parallel to L that passes through P.
2. Lobachevsky geometry: for any plane on which there is a line L and a point P that does not lie on the line there are more than one line L' parallel to L that pass through P (and then it can be demonstrated that if there is more than one L' parallel to L then there must be an infinite number of lines parallel to L passing through P.)

This was this purely axiomatic view of geometries (that even has a name of "pure geometry") that was objected by Einstein in his conference "Geometry and experience" where he postulated that we should abandon the difference between the "pure geometry" and "applied geometry" as the main reason for which we started to study geometry was the need or desire to describe the physical phenomena.

On cosmic scales, the only force expected to be relevant is gravity. The first theory of gravitatys, derived by Newton, was embedded later by Einstein into the General Relativity (GR). However, GR is relevant only for describing gravitational forces between bodies which have relative motions comparable to the speed of light. In most other cases, Newton's gravity gives a sufficiently accurate description. The speed of neighboring galaxies is always much smaller than the speed of light. So, a priori, Newtonian gravity should be able to explain the Hubble flow. One could even think that historically, Newton's law led to the prediction of the Universe expansion, or at least, to its first interpretation. Amazingly, and for reasons which are more mathematical than physical, it happened not to be the case: the first attempts to describe the global dynamics of the Universe came with GR, in the 1910's. Newton himself did the first step in the argumentation. He noticed that if the Universe was of finite size, and governed by the law of gravity, then all massive bodies would unavoidably concentrate into a

single point, just because of gravitational attraction. If instead it was infinite, and with an approximately homogeneous distribution at initial time, it could concentrate into several points, like planets and stars, because there would be no center to fall in. In that case, the motion of each massive body would be driven by the sum of an infinite number of gravitational forces. Since the mathematics of that time did not allow to deal with this situation, Newton did not proceed with his argument (97).

When Einstein tried to build a theory of gravitation compatible with the invariance of the speed of light, he found that the minimal price to pay was to abandon the idea of a gravitational potential, related to the distribution of matter, and whose gradient gives the gravitational field in any point, to assume that our four-dimensional space-time is curved by the presence of matter, to impose that free-falling objects describe geodesics in this space-time (97).

1.3 Space and Time

"L'experience nous a appris
qu'il est plus commode d'attribuer
trois dimensions à l'espace."
H.Poincaré "La valeur de la science"

The problem of the number of dimensions of our space-time is not new. We can cite some of the great philosophers and scientists in the history who tried to answer this question:

1. Johannes Kepler (1571 – 1630, German mathematician, astronomer and astrologer)
   In "Mysterium Cosmographicum" (1595): As he indicated in the title, Kepler thought he had revealed God's geometrical plan for the universe. Much of Kepler's enthusiasm for the Copernican system stemmed from his theological convictions about the connection between the physical and the spiritual; the universe itself was an image of God, with the Sun corresponding to the Father, the stellar sphere to the Son, and the intervening space between to the Holy Spirit. His first manuscript of Mysterium contained an extensive chapter reconciling heliocentrism with biblical passages that seemed to support geocentrism.
2. Gottfried Leibniz (1646 – 1716, German philosopher-mathematician)
   Rather than being an entity that independently exists over and above other matter, Leibniz held that space is no more than the collection of spatial relations between objects in the world: "space is that which results from places taken together". Unoccupied regions are those that could have objects in them, and thus spatial relations with other places. For Leibniz, then, space was an idealized abstraction from the relations between individual entities or their possible locations and therefore could not be continuous but must be discrete. Space could be thought of in a similar way to the relations between family members. Although people in the family are related to one another, the relations do not exist independently of the people
3. Sir Isaac Newton (1642 – 1727 English physicist, mathematician, astronomer, natural philosopher, alchemist, and theologian)
   For Newton space and time are absolute.
4. Immanuel Kant (1724 – 1804, German philosopher)
   In the eighteenth century the German philosopher Immanuel Kant developed a theory where he refuses to see the space and time as objective features of the world but as a framework that helps us to organize our experiences: *"Space and time are the framework*

within which the mind is constrained to construct its experience of reality." ("Critique of Pure Reason -chpt. Transcendental Aesthetic").

The idea that our space-time could have more than three dimensions dates back to the 1920s. Then Theodor Kaluza (1919) and Oscar Klein (1926) published their works on the unification of gravity and electromagnetism in five dimensions - the only two forces known at that time. The discovery of new forces and particles during the following years revealed the Kaluza-Klein theory not sufficient and the theory was forgotten for a while. The revival of extra-dimensional theories was due to the birth of (super)string theories in the 1970s and 1980s. However the extra dimensions introduced on the grounds of superstring theory are expected to be very small, they have a scale of about $M_P^{-1} \sim 10^{-35}\,\mathrm{m}$, and thus there was no hope for probing such small scales in existing and upcoming experiments.
The new ideas begun to emerge in the 1990s. In 1990 Antoniadis explains the supersymmetry breaking by introducing a large extra dimension at a scale of $\mathrm{TeV}^{-1}\,\mathrm{m}$. In the late 1990s the ADD scenario, the warped space model and some inventions in the string theory (D-branes) and M-theory propose the existence of new dimensions at the scales accessible in current searches at colliders.

In this thesis we will adopt the modest point of view and assume that mathematics is a powerful language which can describe the natural phenomena. We will present the mathematical construction of the fundamental models of the Universe that aim to embed in simple mathematical formulas the processes that we observe in micro and macro scale. Then, we will be less conservative, from the "classical physics" point of view, and we will assume the existence of two additional dimensions. The mathematical language will allow to describe this assumption in terms of physical observables - a Kaluza Klein states. We will then study what are the implications of such assumption.

Chapter 2

Standard Models in (micro and macro) Physics

2.1 The Standard Model of Particle Physics

The Standard Model of particle physics (SM) describes the interactions of quarks and leptons that are the constituents of all matter we know about. The strong interactions are described by quantum chromodynamics (QCD) while the electromagnetic and the weak interactions are described by the electroweak theory. This theory has proven to be very successful in describing a tremendous variety of experimental data ranging over many decades of energy. The discovery of neutral currents in the 1970s followed by the direct observation of the W and Z bosons at the CERN $Sp\bar{p}S$ collider in the early 1980s confirmed the ideas underlying the electroweak framework. Since then, precision measurements of the properties of the W and Z bosons at both e^+e^- and hadron colliders have allowed a test of electroweak theory at the 10^{-3} level. QCD has been tested in the perturbative regime in hard collision processes that result in the breakup of the colliding hadrons. The main and most mysterious feature of the SM is that particles are associated to the mathematical beings, a state vectors Ψ with given transformation properties under the Lorentz group. This tight relation between a physical particle as it is observed indirectly in the accelerator detectors and the intrinsic properties of a mathematical operator associated to the particle is very profound. The group structure of the SM is even more exciting, as for a long time physicists looked suspiciously on the particle ZOO that was discovered in the first accelerator searches.

2.1.1 Gauge Invariance Principle - Gauge Theories

The dynamic arises from a symmetry principle. If we require the lagrangian to be invariant under local gauge transformations we are forced to introduce a set of gauge fields with couplings to elementary scalar and fermion matter that are completely determined by symmetry properties (up to global symmetry transformations). Below we describe the construction of a general Young-Mills theory which is the basis of the construction of the Standard Model.

Consider the lagrangian density $\mathcal{L}[\phi, \partial_\mu \phi]$ which is invariant under a D-dimensional continuous group of transformations Γ:

$$\phi' = U(\theta^A)\phi \qquad \text{with } A = 1, 2, \ldots, D \tag{2.1}$$

For θ^A infinitesimal, $U(\theta^A) \simeq 1 + ig\sum_A \theta^A T^A$, where T^A are the generators of Γ in the representation of the fields ϕ. We restrict ourselves to the case of internal symmetries, so that the matrices T^A are independent of the space-time coordinates. The generators T^A are normalized in such a way that for the lowest dimensional non-trivial representation $\{t^A\}$ of Γ we have

$$tr[t^A t^B] = \frac{1}{2}\delta^{AB} \tag{2.2}$$

The generators satisfy the commutation relations:

$$\left[T^A, T^B\right] = iC_{ABC}T^C \tag{2.3}$$

where C_{ABC} are the structure constants. If the transformation parameters θ^A depend on the space-time coordinates, $\theta^A = \theta^A(x^\mu)$, then the lagrangian density $\mathcal{L}[\phi, \partial_\mu\phi]$ is, in general, no longer invariant under the gauge transformations $U\left[\theta^A(x_\mu)\right]$ and should be replaced by $\mathcal{L}[\phi, D_\mu\phi]$ where the ordinary derivative is replaced by a covariant derivative D_μ

$$D_\mu = \partial_\mu + igV_\mu \tag{2.4}$$

where we define $V_\mu = \sum_A T^A V_\mu^A$ for a set of D gauge fields $\{V_\mu^A\}$ (in a one-to-one correspondence with the group generators) with the transformation law

$$V'_\mu = UV_\mu U^{-1} + \left(\frac{i}{g}\right)(\partial_\mu U)U^{-1} \tag{2.5}$$

for constant θ^A, V reduces to a tensor of the adjoint representation of Γ

$$V'_\mu = UV_\mu U^{-1} \simeq V_\mu + ig[\theta, V_\mu] \tag{2.6}$$

which implies that

$$V_\mu^{A'} = V_\mu^A - gC_{ABC}\theta^B V_\mu^C \tag{2.7}$$

Equations 2.4 and 2.5 ensure that ϕ and $D_\mu\phi$ have the same transformation properties

$$(D_\mu\phi)' = U(D_\mu\phi) \tag{2.8}$$

The gauge-invariant kinetic term for the gauge fields V_μ is constructed in terms of the field strength

$$F^A_{\mu\nu} = \partial_\mu V^A_\nu - \partial_\nu V^A_\mu - g C_{ABC} V^B_\mu V^C_\nu \tag{2.9}$$

that transforms as a tensor of the adjoint representation

$$F'_{\mu\nu} = U F_{\mu\nu} U^{-1} \tag{2.10}$$

The complete Yang-Mills lagrangian invariant under gauge transformations can be written in the form:

$$\mathcal{L}_{YM} = \frac{1}{4} \sum_A F^A_{\mu\nu} F^{A\,\mu\nu} + \mathcal{L}[\phi, D_\mu \phi] \tag{2.11}$$

For an abelian theory the gauge transformation reduces to $U[\theta(x_\mu)] = \exp[ieQ\theta(x_\mu)]$, where Q is the charge generator. The associated gauge field, according to equation 2.5, transforms as

$$V'_\mu = V_\mu - \partial_\mu \theta(x) \tag{2.12}$$

In this case the field strength $F_{\mu\nu}$ is linear in V_μ, so that in the absence of matter the theory is free. On the other hand, in the non-abelian case, the $F^A_{\mu\nu}$ tensor contains both linear and quadratic terms in V^A_μ, so the theory is non-trivial even in the absence of matter.

2.1.2 SM lagrangian

The SM is a non-abelian gauge theory based on the gauge group $\mathrm{SU}(3)_C \times \mathrm{SU}(2)_L \times \mathrm{U}(1)_Y$. The $\mathrm{SU}(3)_C$ is the Quantum Chromodynamics (QCD) gauge group, which governs the strong interactions. $\mathrm{SU}(2)_L \times \mathrm{U}(1)_Y$ is the gauge group that unifies the weak and electromagnetic forces and is spontaneously broken to $\mathrm{U}(1)_{em}$ by the higgs mechanism. The $\mathrm{SU}(3)_C$ is assumed to be unbroken.

The matter fields of the Standard Model are the three generations of quarks $\{(u,d),(c,s),(t,b)\}$ and leptons $\{(e,\nu_e),(\mu,\nu_\mu),(\tau,\nu_\tau)\}$ as well as three kinds of gauge bosons $\{B_\mu, W^a_\mu, G^A_\mu\}$ that mediate the three interactions described by the Standard Model. There is also a scalar particle, the higgs boson Φ, that is responsible for the electroweak symmetry breaking. In order to allow for a chiral structure for the weak interactions, the left- and right-handed components of quark and lepton fields are assigned to different representations of the electroweak gauge group $\mathrm{SU}(2)_L \times \mathrm{U}(1)_Y$. Thus, the mass terms for fermions, of the form $\bar{\psi}_L \psi_R + h.c.$ are forbidden in the symmetric limit (here ψ_L and ψ_R refer to a doublet and singlet of $\mathrm{SU}(2)_L$ respectively, that belong to the same generation). The $\mathrm{SU}(3)_C$ gauge bosons are the gluons and the resulting gauge theory is the Quantum Chromodynamics (QCD). Quarks are assigned to the fundamental **3** representation. Thus antiquarks are assigned to the conjugate $\bar{\mathbf{3}}$ representation. All other particles are $\mathrm{SU}(3)_C$ singlets, and do not directly couple to gluons.

The $\mathrm{SU}(3)_C \times \mathrm{SU}(2)_L \times \mathrm{U}(1)_Y$ assignments for the matter fields of the first generation of quarks and leptons are shown in the table 2.1. Other generations are copies of this in that they have the same quantum numbers.

Field	$SU(3)_C$	$SU(2)_L$	$U(1)_Y$	$U(1)_{em}$
$L = \begin{pmatrix} \nu_L \\ e_L \end{pmatrix}$	**1**	**2**	-1	$\begin{pmatrix} 0 \\ -1 \end{pmatrix}$
e_R	**1**	**1**	-2	+1
$Q = \begin{pmatrix} u_L \\ d_L \end{pmatrix}$	**3**	**2**	$\frac{1}{3}$	$\begin{pmatrix} \frac{2}{3} \\ -\frac{1}{3} \end{pmatrix}$
u_R	**3**	**1**	$\frac{4}{3}$	$\frac{2}{3}$
d_R	**3**	**1**	$-\frac{2}{3}$	$-\frac{1}{3}$
Φ	**1**	**2**	1	0
B_μ	**1**	**1**	0	0
W^a_μ	**1**	**3**	0	0, ± 1
G^A_μ	**8**	**1**	0	0

Table 2.1: Dimensions of representations and charges of fermions of the first generation. Fermions of the second and the third generations have the same quantum numbers.

The lagrangian of the Standard Model is given by:

$$\mathcal{L}_{SM} = \mathcal{L}_{gauge} + \mathcal{L}_{matter} + \mathcal{L}_{higgs} + \mathcal{L}_{Yukawa} \tag{2.13}$$

Gauge sector

The kinetic terms of the gauge fields have the compact form

$$\mathcal{L}_{gauge} = -\frac{1}{4} B_{\mu\nu} B^{\mu\nu} - \frac{1}{4} \sum_{a=1}^{3} W^a_{\mu\nu} W^{a\,\mu\nu} - \frac{1}{4} \sum_{A=1}^{8} G^A_{\mu\nu} G^{A\,\mu\nu} \tag{2.14}$$

where $B_{\mu\nu}$ $W^a_{\mu\nu}$ and $G^A_{\mu\nu}$ are the field strengths associated to the U(1)$_Y$, SU(2)$_L$ and SU(3)$_C$ respectively

$$\begin{aligned} B_{\mu\nu} &= \partial_\mu B_\nu - \partial_\nu B_\mu \\ W^a_{\mu\nu} &= \partial_\mu W^a_\nu - \partial_\nu W^a_\mu - g_2 \epsilon^{abc} W^b_\mu W^c_\nu \\ G^A_{\mu\nu} &= \partial_\mu G^a_\nu - \partial_\nu G^a_\mu - g_s f^{ABC} G^B_\mu G^C_\nu \end{aligned} \tag{2.15}$$

The g_2 and g_3 are the coupling constants of SU(2)$_L$ and SU(3)$_C$ gauge groups respectively. The $SU(2)_L$ structure constants ϵ^{abc} form the totally antisymmetric Levi-Civita tensor with $\epsilon^{123} = +1$. The f^{abc} are the SU(3)$_C$ structure constants.

Matter sector

The matter lagrangian is given by

$$\mathcal{L}_{matter} = \sum_{generations} \left[iL^\dagger \bar{\sigma}_\mu D^\mu L + ie_R^\dagger \sigma_\mu D^\mu e_R + iQ^\dagger \bar{\sigma}_\mu D^\mu Q + iu_R^\dagger \sigma_\mu D^\mu u_R + id_R^\dagger \sigma_\mu D^\mu d_R \right] \tag{2.16}$$

where the covariant derivatives have the form

$$D_\mu = \partial_\mu - ig_1 \frac{y}{2} B_\mu - ig_2 \sum_{a=1}^{3} t^a_{L/R} W^a_\mu - ig_3 \theta_3 \sum_{A=1}^{8} \frac{\lambda_A}{2}{}^A G^A_\mu \tag{2.17}$$

where $Y_{L/R}/2$ and $t^A_{L/R}$ are the $SU(2)_L$ and $U(1)_Y$ generators, respectively, in the reducible representations $\psi_{L/R}$. λ_A are the generators of the $\mathrm{SU}(3)_C$ algebra, which in the fundamental representation correspond to the Gell-Mann matrices. $\theta_3 = +1, 0$ for triplets and singlets of $\mathrm{SU}(3)_C$ respectively.

Higgs sector and electroweak symmetry breaking

The electroweak symmetry breaking sector of the SM is particularly simple, and consists of a single complex $\mathrm{SU}(2)_L$ doublet Φ of spin zero fields with gauge quantum numbers shown in the table 2.1. Φ must be a doublet in order to write down the gauge invariant mass terms for fermions in the Yukawa sector. The field Φ acquires a VEV (Vacuum Expectation Value) signaling the spontaneous breakdown of the electroweak symmetry. This VEV is left invariant by one combination of $\mathrm{SU}(2)_L$ and $\mathrm{U}(1)_Y$ generators which generates a different U(1) group which is identified as $\mathrm{U}(1)_{em}$. The corresponding linear combination of gauge fields remains massless and is identified with the photon A_μ. The dynamics of the higgs field Φ is governed by the lagrangian

$$\mathcal{L}_{higgs} = |D_\mu \Phi|^2 - V(\Phi) \tag{2.18}$$

where the covariant derivative of the higgs field has the form

$$D_\mu = \partial_\mu - ig_1 \frac{y}{2} B_\mu - ig_2 \sum_{a=1}^{3} t^a_L W^a_\mu \tag{2.19}$$

The potential $V(\Phi)$ is the most general renormalizable, gauge invariant polynomial of degree 4 with two parameters $\mu^2, \lambda > 0$

$$V(\Phi) = -\mu^2 \Phi^\dagger \Phi + \lambda (\Phi^\dagger \Phi)^2 \tag{2.20}$$

The Φ fields receives the vacuum expectation value at the minimum of the potential $V(\Phi)$ at $|\Phi|^2 = \frac{\mu^2}{2\lambda} = v^2$. One then expands the higgs field around the minimal value

$$\Phi = \begin{pmatrix} \phi^+ \\ \frac{1}{\sqrt{2}}(v + h + i\phi^0) \end{pmatrix} \tag{2.21}$$

Introducing the above expansion of Φ into the lagrangian $\mathcal{L}_{SM}$ one finds the physical states, A_μ, a pair of charged massive spin 1 bosons $W^\pm$ and a massive spin 1 neutral boson Z^0. Their masses that can be written in terms of the initial gauge fields as

$$\begin{aligned} A_\mu &= \sin\theta_W W^3_\mu + \cos\theta_W B_\mu \\ Z_\mu &= -\cos\theta_W W^3_\mu + \sin\theta_W B_\mu \\ W^\pm_\mu &= \tfrac{1}{\sqrt{2}}\left(W^1_\mu \mp i W^2_\mu\right) \end{aligned} \tag{2.22}$$

with $\sin\theta_W = g_2/\sqrt{g_1^2+g_2^2}$ and $\cos\theta_W = g_1/\sqrt{g_1^2+g_2^2}$. The masses then are given by the formulas

$$m_A = 0 \qquad m_Z = \frac{1}{2}\sqrt{g_1^2+g_2^2}v \qquad m_W = \frac{1}{2}g_2 v \tag{2.23}$$

The neutral scalar higgs boson h, which is left over as the relic of spontaneously broken symmetry, receives a mass $m_h^2 = 2\lambda v^2$.

Yukawa sector and the CKM matrix

The fermion masses are generated in the Yukawa sector by interactions of fermionic fields with the higgs boson Φ.

$$\mathcal{L}_{Yukawa} = -\sum_{generations} Y^u Q^\dagger (i\sigma_2 \Phi*) u_R - \sum_{generations} Y^d Q^\dagger \Phi d_R - \sum_{generations} Y^e L^\dagger \Phi e_R + h.c \tag{2.24}$$

where $Y^{u,d,e}$ are the three 3×3 complex Yukawa matrices. In order to find the mass eigenstates, as for the gauge fields, one introduces the higgs field expansion defined in the equation 2.21 into the above formula. Then to diagonalize $\mathcal{L}_{Yukawa}$ it is necessary to introduce unitary matrices related to the Yukawa matrices by a unitary transformation

$$Y^u_{diag} = V^u_L Y^u V^{u\dagger}_R \qquad Y^d_{diag} = V^d_L Y^d V^{d\dagger}_R \qquad Y^e_{diag} = V^e_L Y^e V^{e\dagger}_R \tag{2.25}$$

The physical states are then given by

$$\begin{aligned} u'_L &= V^{u\dagger}_L u_L & d'_L &= V^{d\dagger}_L d_L \\ u'_R &= V^{u\dagger}_R u_R & d'_R &= V^{d\dagger}_R d_R \\ e'_L &= V^{e\dagger}_L e_L & \nu'_L &= V^{e\dagger}_L \nu_L \\ e'_R &= V^{e\dagger}_R e_R \end{aligned} \tag{2.26}$$

and their diagonal mass matrices are $M^{u,d,e} = \frac{v}{\sqrt{2}} Y^{u,d,e}_{diag}$.

What results from this diagonalization are the mixings between different generations of quarks. Looking at the quark part of $\mathcal{L}_{matter}$ one can easily see that the charged currents are now modified as

$$\mathcal{L}_{matter} \supset -\frac{g_2}{\sqrt{2}} u^\dagger_L \bar{\sigma}^\mu W^+_\mu d_L + h.c = -\frac{g_2}{\sqrt{2}} u'^\dagger_L V^u_L V^{d\dagger}_L \bar{\sigma}^\mu W^+_\mu d'_L + h.c \tag{2.27}$$

where the Cabibbo-Kobayashi-Maskawa matrix $V_{CKM} = V_L^u V_L^{d\dagger}$ is a unitary matrix that mixes the three quark generations. The CKM matrix definition contains only one physical phase which is the source of CP-violation in the quark sector of the Standard Model.

2.1.3 Precision tests of the Standard Model predictions and parameters

The success of the Standard Model lies in the extreme accuracy of its predictions of physical phenomena form the atomic scales down to scales of about 10^{-18} m. The predictions of the SM have been probed by Tevatron and LEP up the the scales of order of few hundred GeV. The impressive predictability of the SM is a consequence of the renormalizabitliy of its parameters.

There are 19 parameters within the SM that remain unexplained and that are chosen to fit the data. In the electroweak gauge sector they include the three gauge coupling constants g_1, g_2 and g_3 for the three gauge groups $U(1)_Y$, $SU(2)_L$ and $SU(3)_C$ respectively (equivalently three other parameters can be used: $\alpha_s = \frac{g_3^2}{4\pi}$, $\alpha_{ew} = \frac{e^2}{4\pi}$ with $e = g_2 \sin\theta_W$ and $\sin^2\theta_W = \frac{g_1^2}{g_1^2+g_2^2}$).

In the matter sector there are nine parameters associated with the masses of charged fermions and four mixing angles in the CKM matrix. Moreover there are two parameters associated with higgs boson: the higgs VEV v and the quartic coupling λ. The remaining one is the θ_{QCD} parameter. Moreover, we should also care about the parameters in the neutrino sector, as the data from neutrino oscillation experiments provide convincing evidence for neutrino masses. With 3 light Majorana neutrinos there are at least 9 additional parameters in the neutrino sector: 3 masses and 6 mixing angles and phases.

Those parameters have to be constrained with an outstanding precision by various experiments that probe the SM observables and the influence of new physics should be investigated in order to constrain the possible extensions of the SM as we shall see later. As the SM is a model that has been constructed in not so far past and its mathematical construction seems very efficient and relatively simple, many experiments have been dedicated to investigate the predictions of this exciting theory.

The main progress in the domain was made in LEP e^+e^- collider in the 1990's and has already given first bounds on the top and the higgs masses. The observations of the top quark was later confirmed by Tevatron data in 1995. Recently new results from ATLAS and CMS collaborations released new data providing an indication of a higgs boson with the mass of about 125 GeV as illustrated in the figure 2.1.

At LEP 1 and SLC, there were high-precision measurements of various Z pole observables (8), (55). These include the Z mass and total width Γ_Z and partial widths into fermions $\Gamma_{f\bar{f}}$. In the table 2.2 the referenced values are given also for the partial width into hadrons Γ_{had}, charged leptons $\Gamma_{l^+l^-}$ and the width for invisible decays Γ_{inv}. The latter can be used to determine the number of neutrino flavors much lighter than the $\frac{m_Z}{2}$ to be $N_\nu = \Gamma_{inv}/\Gamma^{th}(\nu\bar{\nu}) = 2.984 \pm 0.009$ for $(m_t, m_H) = (173.4, 117)$. The other observables refer to $\sigma_{had} \equiv 12\pi\Gamma_{e^+e^-}\Gamma_{had}/m_Z^2\Gamma_Z^2$ and the branching ratios $R_f \equiv \Gamma_{f\bar{f}}/\Gamma_{had}$ for hadrons and analogous expressions for R_l related to leptons. The R_l parameters are especially useful to constrain the α_s value.

The measurements of the left-right asymmetry

$$A_{LR} \equiv \frac{\sigma_L - \sigma_R}{\sigma_L + \sigma_R} \tag{2.28}$$

has been measures by SLD and SLC (55) collaborations and can heavily constrain the $\sin\theta_W$ parameter. The observables that were measured indirectly include the A_f parameters, where

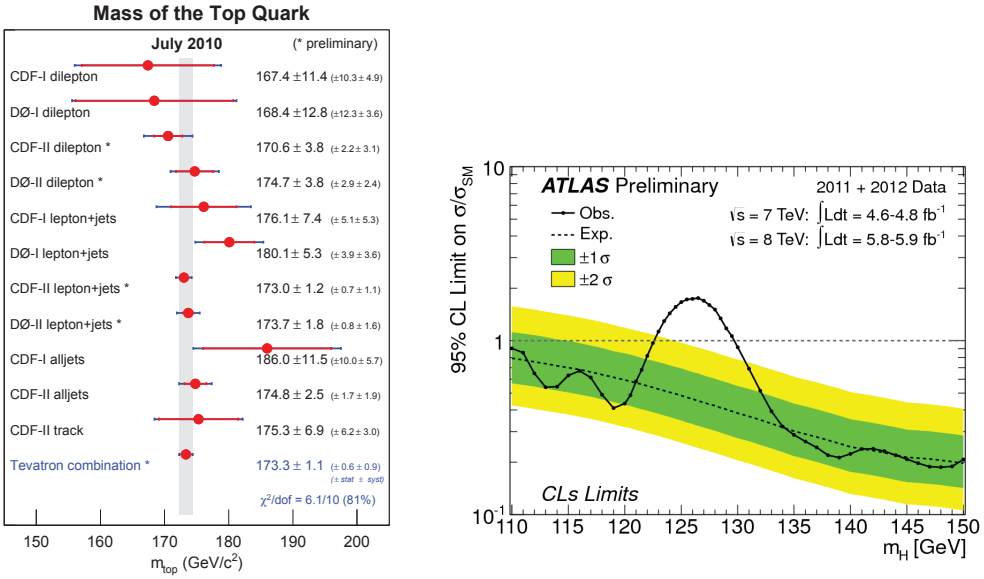

Figure 2.1: **Left panel**. Combined results D0 and CFD on the top quark mass. Extracted from (78). **Right panel:**The observed (full line) and expected (dashed line) 95% CL combined upper limits on the SM higgs boson production cross section divided by the Standard Model expectation as a function of m_h in the low mass range of this analysis. The dashed curves show the median expected limit in the absence of a signal and the green and yellow bands indicate the corresponding 68% and 95%. Extracted from (5).

$f = e, \mu, \tau, b, c, s$ defined as

$$A_f \equiv \frac{2\bar{g}_V^f \bar{g}_A^f}{\bar{g}_V^{f2} + \bar{g}_A^{f2}} \tag{2.29}$$

and the forward-backward asymmetries $A_{FB}^{(0,f)} = \frac{3}{4} A_e A_f$.

The $\bar{g}_V^f$ and $\bar{g}_A^f$ parameters in the above formulas refer to vector and axial-vector couplings in the SM lagrangian after the electroweak symmetry braking and are defined as

$$g_V^f \equiv t_{3L}^f - 2q_f \sin^2\theta_W \tag{2.30}$$

$$g_A^f \equiv t_{3L}^f \tag{2.31}$$

and here t_{3L}^f is the weak isospin of a given fermion and q_f is its charge in units of e. In the bar quantities $\bar{g}_V^f$ and $\bar{g}_A^f$ correspond to the effective values where the electroweak radiative has been taken into account.

Finally the $\bar{s}_l^2$ parameter were extracted from the measurements of forward-backward asymmetries A_{FB} for e^+e^- final states in $p\bar{p}$ collisions in $D0$ and CDF (80) experiments.

The global fit results to the experimental data are summarized in the table 2.2 for the main Z-pole observables.

The magnitude of the CKM matrix elements has been measured with an extreme precision in the experiments such as BELLE (study of meson mixings) (129) or BABAR (study of B-mesons) (96). Using the set of Wolfenstein parameters (λ, A, ρ, η) the CKM matrix can be written as

Quantity	Value	Standard Model	Pull	Dev.
M_Z [GeV]	91.1876 ± 0.0021	91.1874 ± 0.0021	0.1	0.0
Γ_Z [GeV]	2.4952 ± 0.0023	2.4961 ± 0.0010	−0.4	−0.2
Γ(had) [GeV]	1.7444 ± 0.0020	1.7426 ± 0.0010	—	—
Γ(inv) [MeV]	499.0 ± 1.5	501.69 ± 0.06	—	—
$\Gamma(\ell^+\ell^-)$ [MeV]	83.984 ± 0.086	84.005 ± 0.015	—	—
σ_{had}[nb]	41.541 ± 0.037	41.477 ± 0.009	1.7	1.7
R_e	20.804 ± 0.050	20.744 ± 0.011	1.2	1.3
R_μ	20.785 ± 0.033	20.744 ± 0.011	1.2	1.3
R_τ	20.764 ± 0.045	20.789 ± 0.011	−0.6	−0.5
R_b	0.21629 ± 0.00066	0.21576 ± 0.00004	0.8	0.8
R_c	0.1721 ± 0.0030	0.17227 ± 0.00004	−0.1	−0.1
$A_{FB}^{(0,e)}$	0.0145 ± 0.0025	0.01633 ± 0.00021	−0.7	−0.7
$A_{FB}^{(0,\mu)}$	0.0169 ± 0.0013		0.4	0.6
$A_{FB}^{(0,\tau)}$	0.0188 ± 0.0017		1.5	1.6
$A_{FB}^{(0,b)}$	0.0992 ± 0.0016	0.1034 ± 0.0007	−2.6	−2.3
$A_{FB}^{(0,c)}$	0.0707 ± 0.0035	0.0739 ± 0.0005	−0.9	−0.8
$A_{FB}^{(0,s)}$	0.0976 ± 0.0114	0.1035 ± 0.0007	−0.5	−0.5
$\bar{s}_\ell^2(A_{FB}^{(0,q)})$	0.2324 ± 0.0012	0.23146 ± 0.00012	0.8	0.7
	0.23200 ± 0.00076		0.7	0.6
	0.2287 ± 0.0032		−0.9	−0.9
A_e	0.15138 ± 0.00216	0.1475 ± 0.0010	1.8	2.1
	0.1544 ± 0.0060		1.1	1.3
	0.1498 ± 0.0049		0.5	0.6
A_μ	0.142 ± 0.015		−0.4	−0.3
A_τ	0.136 ± 0.015		−0.8	−0.7
	0.1439 ± 0.0043		−0.8	−0.7
A_b	0.923 ± 0.020	0.9348 ± 0.0001	−0.6	−0.6
A_c	0.670 ± 0.027	0.6680 ± 0.0004	0.1	0.1
A_s	0.895 ± 0.091	0.9357 ± 0.0001	−0.4	− 0.4

Figure 2.2: The principal Z-pole observables and their SM predictions.The column denoted Pull gives the standard deviations for the principal fit with m_H free, while the column denoted Dev. (Deviation) is for m_H = 124.5 GeV fixed. Extracted from (72)

$$V_{CKM} = \begin{pmatrix} 1-\lambda^2/2 & \lambda & A\lambda^3(\rho - i\eta) \\ -\lambda & 1-\lambda^2/2 & A\lambda^2 \\ A\lambda^3(1-\rho-i\eta) & -A\lambda^2 & 1 \end{pmatrix} \tag{2.32}$$

The $\lambda = \sin\theta_{Cabibbo}$ parameter is a critical ingredient in determinations of the other parameters and in tests of CKM unitarity. Current experiments of kaon and hyperon decays suggest a value $\lambda \approx 0.220$ and $\lambda \approx 0.225$ and this discrepancy is discussed in therm of violation of the unitarity condition

$$|V_{11}^2| + |V_{12}^2| + |V_{13}^2| = 1 \tag{2.33}$$

For a more complete review of experiments and constraints on the SM observables one can refer

to (72).

2.1.4 Standard Model is not a final story

The standard electroweak model is a mathematically-consistent renormalizable field theory which predicts many of the experimental facts. It successfully predicted the existence and form of the weak neutral current, the existence and masses of the W and Z bosons, and the charm quark, as necessitated by the GIM mechanism. The charged current weak interactions, as described by the generalized Fermi theory, were successfully incorporated, as was quantum electrodynamics. The consistency between theory and experiment indirectly tested the radiative corrections and ideas of renormalization and allowed the successful prediction of the top quark mass. When combined with quantum chromodynamics for the strong interactions, the Standard Model is almost certainly the approximately correct description of the elementary particles and their interactions down to at least 10^{-16} cm. When combined with general relativity for classical gravity the SM accounts for most of the observed features of nature. However, the theory has far too much arbitrariness to be the final theory.

The new physics models can be tested by the ρ_0 parameter

$$\rho_0 = \frac{m_W^2}{m_Z^2 \cos^2\theta_W \rho} \tag{2.34}$$

which describes the new sources of electroweak symmetry breaking that cannot arise within the SM. Here $\rho = m_Z^2/m_W^2 \cos\theta_W^2$ is the " default" parameter assuming validity of the SM. Another set of parameters, S, T and U can be used to constrain the many new physics models as well [1]. The T parameter is proportional to the difference between the W and Z self-energies at $q^2 = 0$ (measures the electroweak symmetry breaking), while S ($S+U$) is associated with the difference between the Z (W) self-energy at $q^2 = m_Z^2$. The data allow for a simultaneous determination of $sin\theta_W^2$ (from the Z pole asymmetries), S (from m_Z), U (from m_W), T (mainly from Γ_Z), α_s (from R_l, σ_{had}, and the τ lifetime τ_τ), and m_t (from the hadron colliders). Assuming 115.5 GeV $< m_h <$ 127 GeV the values are (72):

$$\begin{array}{lll} S = 0.00^{+0.11}_{-0.10} & \sin\theta_W^2 & = 0.23125 \pm 0.00016 \\ T = 0.02^{+0.11}_{-0.12} & \alpha_s(m_Z) & = 0.1197 \pm 0.0018 \\ U = 0.08 \pm 0.11 & m_t & = 173.4 \pm 1.0\text{GeV} \end{array} \tag{2.35}$$

These values depend only weakly on the m_h mass but can give quite stringent constraints on the exotic extensions of the SM. For example the S parameter can be used to constrain the number of fermion families, under the assumption that there are no new contributions to T or U and therefore that any new families are degenerate. Then an extra generation of SM fermions is excluded at the 5.7 σ level. This restriction can be relaxed by allowing T to vary as well, since $T > 0$ is expected from a non-degenerate extra family. Then, a fourth family is disfavored but not excluded by the current electroweak precision data. One important consequence of a heavy fourth family is to increase the higgs production cross section by gluon fusion by a factor ~ 9, which considerably strengthens the exclusion limits from direct searches at the Tevatron (41) and LHC (4). In contrast, heavy degenerate non-chiral fermions (also known as vector-like or

1. There is no simple parametrization to describe the effects of every type of new physics on every possible observable. The S, T, and U formalism describes many types of heavy physics which affect only the gauge self-energies, and it can be applied to all precision observables.

multiplets), which are predicted in many grand unified theories (72) and other extensions of the SM, do not contribute to S, T, and U (or to ρ_0), and do not require large coupling constants.

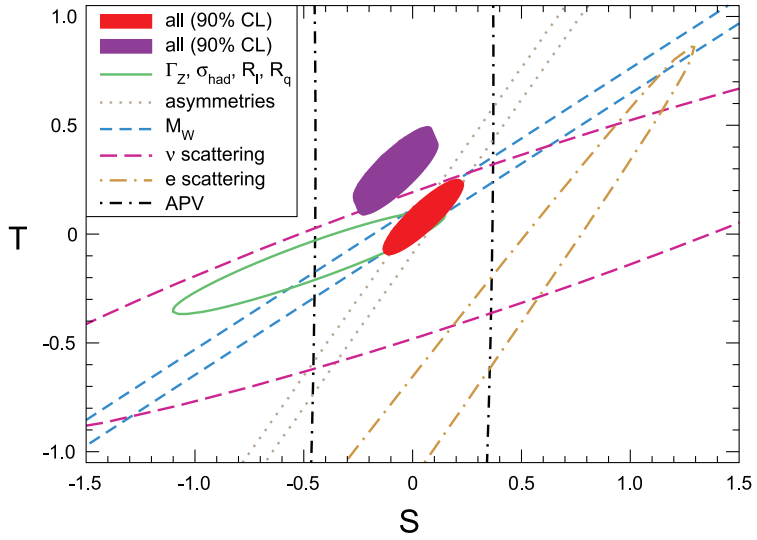

Figure 2.3: 1 σ constraints (39.35%) on S and T parameters from various inputs combined with m_Z. S and T represent the contributions of new physics only. The contours assume 115.5 GeV $< m_h <$ 127 GeV except for the larger (violet) one for all data which is for 600 GeV $< m_h <$ 1 TeV. Extracted from (72)

Here we briefly summarize the theoretical enigmas and possible explanations of the Standard Model of fundamental interactions and basic constituents of our world.

Gauge group: The Standard Model is a complicated direct product of three subgroups, $SU(3)_C \times SU(2)_L \times U(1)_Y$, with three independent gauge couplings. There is no explanation for why only the electroweak part is chiral (parity-violating). The charge quantization is left unexplained as well. The complicated gauge structure suggests the existence of some underlying unification of the interactions, such as one would expect in a superstring or GUT theories.

Fermions: We know from the every-day life that under ordinary terrestrial conditions all matter can be constructed out of fermions of the first family (u, d, e, ν_e). Yet, three families of fermions exist with no obvious role in nature. The number of families nor the huge extent between the masses of fermions, which varies over 5 orders of magnitude between the top quark and the electron, can not be explained within the Standard Model. Even more mysterious are the neutrinos, which are many orders of magnitude lighter. A related difficulty is that while the CP violation observed in the laboratory is well accounted for by the phase in the CKM matrix, there is no SM source of CP breaking adequate to explain the baryon asymmetry of the universe.

Naturalness: Another unexplained mass hierarchy exists in the higgs sector. Quantum corrections to the higgs mass give quadratically divergent contributions

$$\delta m_h^2 \sim \frac{1}{32\pi^2}\left[\left(\frac{1}{4}(3g_2^2 + g_1^2) + 6\lambda - 6y_t^2\right)\Lambda^2 + \mathcal{O}(\log\Lambda)\right] \tag{2.36}$$

Therefore if the Standard Model were valid up to the Planck scale $M_P = 1.22 \times 10^{19}$ GeV the "bare" mass in the higgs lagrangian should be fine tuned with a precision of 10^{-32} to cancel the radiative corrections and get the higgs mass of order of 100 GeV.

The strong CP problem: Another fine-tuning is known as the strong CP problem. On can add the CP breaking term in the QCD lagrangian, a term proportional to $\theta_{QCD}\epsilon^{\mu\nu\rho\sigma}G^A_{\mu\nu}G^A_{\rho\sigma}$ which is consistent with gauge symmetries. This term, if present, would induce an electric dipole moment for the neutron. The rather stringent limits on the dipole moment lead to the upper bound $\theta_{QCD} < 10^{-11}$. The question is therefore why θ_{QCD} is so small? It is not sufficient to set θ_{QCD} to zero because of the CP violation in the electroweak sector.

Gravity: Gravity is not fundamentally unified with other interactions in the Standard Model. General relativity, which describes the gravity, is not a quantum theory and there is no obvious way to formulate its quantum version. Possible solutions include Kaluza-Klein and supergravity theories which connect gravity with other interactions in a more natural way but do not yield renormalizable theories of quantum gravity.

Dark ingredients: Some new ingredients motivated by experiments and observations have to be incorporated within the Standard Model. The cosmological observations involving the cosmic microwave background radiation (CMB), acceleration of the universe as determined by Type Ia supernova observations, large scale distribution of galaxies and clusters, and big bang nucleosynthesis has allowed precise determinations of the cosmological parameters putting in evidence that universe is close to flat, with some form of dark energy making up about 74% of the energy density. Dark matter constitutes 21%, while ordinary matter represents only about 4-5%. The mysterious dark energy which is the most important contribution to the energy density and leads to the acceleration of the expansion of the universe is not accounted for in the SM. Similarly, the Standard Model has no explanation for the observed dark matter, which contributes much more to the matter in the universe than the ingredients we are made of.

2.1.5 Possible extensions

Many possible scenarios of beyond the Standard Model physics has been proposed in the literature. In general they predict new heavy degrees of freedom at high energies (typically at about 1 TeV) and one hopes to see their effects in the on-going experiments (like the Large Hadron Collider (LHC) in CERN). Moreover all the influences of the high-energy physics on the low-energy phenomena, that are experimentally constrained with a great precision, should be negligible.

The most known and widely studied theory extending the SM is the supersymmetry (SUSY). In 1967, Coleman and Mandula provided a rigorous argument which proves that, given certain assumptions, the Poincaré symmetry, internal global symmetries related to conserved quantum numbers as well as discrete symmetries C, P and T are the only possible symmetries of the S-matrix (62). In particular, the theorem assumes that the symmetry algebra of the S-matrix involves only commutators. Weakening this assumption to allow anticommuting generators as well as commuting generators leads to the possibility of supersymmetry. In 1975, Haag, Lopuszanski, and Sohnius proved that supersymmetry is the only additional symmetry of the S-matrix allowed by this weaker set of assumptions making of SUSY the only possible extension of the known space-time symmetries of particle physics (79). There are many theoretical motivations of the supersymmetric models such that the gauge coupling unification within a percent level of accuracy (much more than in the SM alone), the higgs boson mass in the MSSM is lower than 135 GeV and the quadratic divergences are not present (notice that this was initially one of the

main motivations to study the SUSY theories). They provide also a cold dark matter candidate, which usually is the neutralino. Other theories were proposed as well. The little higgs model, a theory proposed by Arkani-Hamed, Cohen and Georgi (31) protects the quadratic divergences to higgs mass by a spontaneously broken global symmetry. Strongly coupled theories such as technicolor (95) proposed in 1980's are based on the dynamical generation of the mass scales present in the SM. We will review more in details the extra-dimensional extensions of the SM in the next section.

2.2 Standard model of cosmology

2.2.1 Friedmann-Robertson-Walker model

Another standard model in physics is the standard model of cosmology. Cosmological models are based on the *observation* that the universe appears isotropic and the *assumption* that observers in any other galaxy also see the universe isotropic. Isotropy demands that on the surface of a sphere of a radius R, the local matter and radiation densities, the local expansion rate as well as the redshift of light and the ticking rate of clocks must be independent of direction. If we require that also all observers find the universe isotropic, this places strong restrictions on the metric. In particular it requires the universe to be homogeneous. Surveys, such as Sloan Digital Sky Survey and the 2dF Galaxy Redshift Survey have now shown that the universe is homogeneous (to within several percent in density) on scales larger than a hundred Mpc.

The Friedmann-Lemaître-Robertson-Walker (FLRW) model is defined as the most general solution of the laws of General Relativity, assuming that the universe is isotropic and homogeneous. The FLRW metric has the form

$$ds^2 = dt^2 - a(t)^2 \left[\frac{dr^2}{1 - kr^2} + r^2(d\theta + \sin^2\theta d\phi^2) \right] \tag{2.37}$$

where t is time, r is the co-moving distance, $a(t)$ is the scale factor and k is the spatial curvature. The k parameter can take three possible values. $k = -1$ corresponds to a generalization of a hyperbolic or saddle-point geometry. The universe is open and infinite. $k = 0$ gives a flat geometry, the one that makes the co-moving coordinates Euclidean in every point of space. For $k = +1$ the metric is a three dimensional surface of a sphere. The universe is closed and has finite volume. The scale factor $a(t)$ measures the size of the universe at a time t. The normalization convention for the scale factor is arbitrary and the most common choice is to normalize it to unity at the present time $a_0 = 1$. The physical distance dl between two objects will be the product of the scale factor and the co-moving distance dr, $dl = a(t)dr$. The rate of change of the proper distance is

$$dv = \frac{d(dl)}{dt} = \frac{\dot{a}}{a} dl = H(t)dl \tag{2.38}$$

where the Hubble "constant" H is the unique "constant" in physics that changes with time! H is one of the most important numbers in cosmology because it may be used to estimate the size and age of the universe. In 1929, Edwin Hubble announced that almost all galaxies appeared to be moving away from us. This phenomenon was observed as a redshift of a galaxy's spectrum. This redshift appeared to have a larger displacement for faint, presumably further, galaxies. Hence, the farther a galaxy, the faster it is receding from Earth. This was the first hint that the universe is non-static. The law of the cosmological expansion,that is the dependence of the scale factor a on time is determined by the Einstein equations

$$R_{\mu\nu} - \frac{1}{2} g_{\mu\nu} R = 8\pi G T_{\mu\nu} \tag{2.39}$$

where $R_{\mu\nu}$ and R are the Ricci tensor and scalar respectively.

The solution to Einstein's equation for the homogeneous and isotropic universe relates the rate of the cosmological expansion H to the total energy density ρ and to the spatial curvature. The energy density in the present universe is due to non-relativistic matter ρ_M (baryons, dark matter, eventually neutrino species whose mass is considerably larger than $\sim 10^{-3}$ eV), relativistic matter ρ_{rad} (photons and light neutrinos with mass less than 10^{-4} eV if such neutrinos

exist) and dark energy ρ_Λ. In general the universe can have a non-vanishing spatial curvature ρ_{curv}. All these contributions account for the Friedmann solution to Einstein's equations giving

$$H^2 = \frac{8\pi}{3} G \left(\rho_M + \rho_{rad} + \rho_\Lambda + \rho_{curv}\right) \tag{2.40}$$

The critical density $\rho_c = \frac{3H_0^2}{8\pi G}$ can be used to determine the geometry of the universe. Its numerical value can be found to be

$$\rho_c = 1.05\, h^2 \cdot 10^{-5} \frac{\text{GeV}}{\text{cm}^3} \approx 0.52 \cdot 10^{-5} \frac{\text{GeV}}{\text{cm}^3} \tag{2.41}$$

the value that corresponds approximately to only five proton masses per cubic meter! One defines parameters $\Omega_i \equiv \frac{\rho_i}{\rho_c}$ which are one of the most important sets of parameters in modern cosmology. For the flat universe we have $\sum_i \Omega_i = 1$. The experimental determination of the five parameters $\{\Omega_i, k, H_0\}$ is sufficient to fully describe the FLRW universe and that is the reason why precise measurement of those parameters were performed in observational cosmology for the last 30 years.

2.2.2 Short history of the universe

Curiously, after the discovery of the Hubble expansion and of the Friedmann law, there were no significant progress in cosmology for a few decades. Nevertheless, a few pioneers tried to think about the origin of the universe. A first simple model, called "Cold Big Bang" was proposed where the basic assumption was that the expansion of the universe was always dominated by a single component - a pressureless matter. However this scenario had to be abandoned as it turned out to be inconsistent with the early nucleosynthesis studies. Other possibility is the commonly approved model of a Hot Big Bang in which the radiation density dominated at early time. Between the 1960's and today, a lot of efforts have been made in order to study the various stages of the Hot Big Bang scenario with increasing precision. The exciting history of the universe can be traced by combining observations and theoretical predictions.

For the earliest stages, there are still many competing scenarios – depending, for instance, on assumptions concerning string theory. Following the most conventional picture, gravity became a classical theory (with well–defined time and space dimensions) at a time called the Planck time $t \sim 10^{-36}$ s. Then there was a stage of inflation possibly related to GUT (Grand Unified Theory) symmetry breaking at $t \sim 10^{-32}$ s. Then the reheating era came and the scalar field, responsible for inflation, decayed into a thermal bath of SM particles. At $t \sim 10^{-6}$ s the electroweak symmetry breaking occurred and at $t \sim 10^{-4}$ the quarks combined themselves into hadrons during the era called QCD phase transition (97). After these stages, the universe entered into a series of processes that are much better understood, and well constrained by observations.

Nucleosynthesis had place at $t \sim 1 - 100$ s. This was the epoch responsible for the formation of light nuclei like H, He and Li. By comparing the theoretical predictions with the observed abundance of light elements in the present universe, it is possible to give a very precise estimate of the total density of baryons in the universe: $\Omega_B h^2 = 0.021 \pm 0.005$. At $t \sim 10^4$ yr the transition between radiation dominated towards the matter dominated universe occurred. After that, at $t \sim 10^5$ yr the recombination of atoms caused the decoupling of photons. After that time, the universe became almost transparent: the photons free–streamed along geodesics. So, by looking at the CMB, we obtain a picture of the universe at decoupling. After recombination,

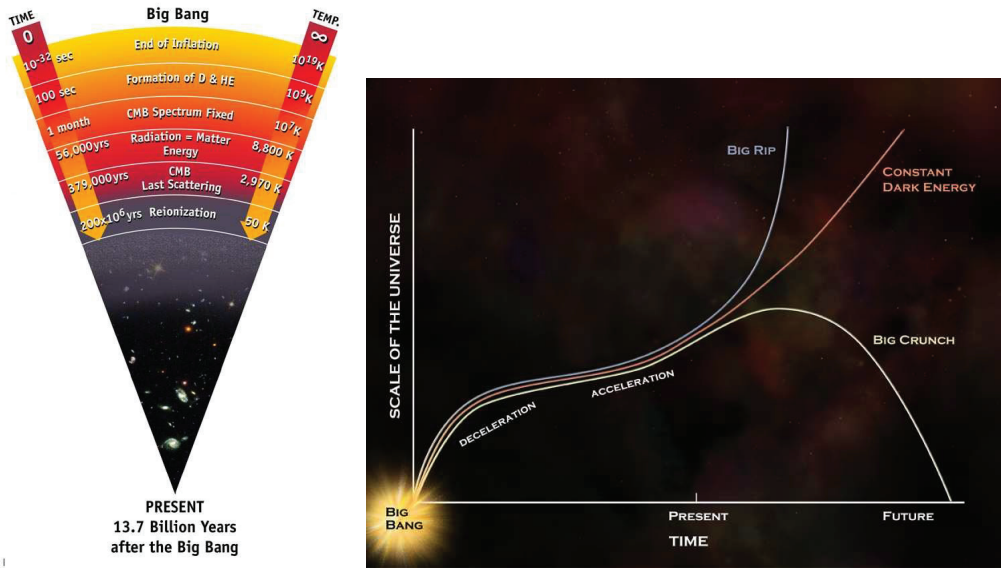

Figure 2.4: **On the left:** The past history of the universe on the left panel (extracted from *http://conferences.fnal.gov/lp2003/forthepublic/cosmology/index.html*) and the possible future scenarios on the right panel (image extracted from *http://chandra.harvard.edu/photo/2004/darkenergy/more.html*).

the small inhomogeneities of the smooth matter distribution are amplified what leads to the formation of stars and galaxies.

The future of the universe is mostly determined by its geometry and the properties of dark energy. If the spatial curvature is non-zero, it will sooner or later start to dominate over energy density of non-relativistic matter and hence at the late times the competition between the Dark energy and the curvature component will determine the fate of the universe. If the dark energy density is time dependent and will relax to zero sufficiently rapidly then the positive curvature would imply the expansion rate slowing down and finally the collapse of the universe to singularity. The space with negative curvature would expand forever though its expansion rate would slow down. All the systems that are not gravitationally bounded would disappear. The same holds for flat space but then the expansion will be even slower. If the dark energy density is time-independent or depends on time slowly then it will play a crucial role in the evolution of the universe. Positive dark energy density implies exponential expansion while negative density, a possibility that cannot be excluded, would slow down the expansion and the universe would re-collapse to singularity.

Chapter 3

Dark Matter - Where? What? Why?

3.1 Evidences for the dark Matter

One of the most astounding revelations of the twentieth century in terms of our understanding of the universe is that ordinary baryonic matter, that is, matter made up of protons and neutrons, is not the dominant form of material in the universe. Rather, some strange new form of matter, dubbed dark matter, fills our universe, and it is roughly five times more abundant than ordinary matter. The evidence that the dark matter is required to be present in our universe has be building for some time. First predictions of dark matter were made almost simultaneously in the early 1930s by Jan Hendrick Oort and Fritz Zwicky.

Oort found that the motion of stars in the Milky Way hinted at the presence of far more galactic mass than anyone had previously predicted. By studying the Doppler shifts of stars moving near the galactic plane, Oort was able to calculate the velocities of stars in the Milky Way, and thus made the startling discovery that they should be moving quickly enough to escape the gravitational pull of the luminous mass in the galaxy. Oort postulated that there must be more mass present within the Milky Way to hold these stars in their observed orbits. However, he noted that another possible explanation was that 85% of the light from the galactic center was obscured by dust and intervening matter or that the velocity measurements for the stars in question were simply in error (105). Around the same time, Swiss astronomer Franz Zwicky found similar indications of missing mass but at larger scale. Zwicky, studying the observed Doppler shifts in galactic spectra, found that the velocity dispersion of galaxies in the Coma cluster, situated about 99 Mpc from Earth, was far too large to be supported by the luminous matter.

A little bit later, in the 1970s the rotation curves of individual galaxies were measured by Vera Rubin and collaborators confirming Zwicky's result (49). Since then many other phenomena were observed putting in evidence the dark matter component.

A complete understanding of dark matter requires utilizing several branches of physics and astronomy. The creation of dark matter during the hot expansion of the universe is understood through statistical mechanics and thermodynamics. Particle physics is necessary to propose candidates for dark matter and explore its possible interactions with ordinary matter. General relativity, astrophysics, and cosmology dictate how dark matter acts on large scales and how the universe may be viewed as a laboratory to study dark matter. Here we briefly explain the hints that dark matter exists.

3.1.1 Galactic scale

The most convincing and direct evidence for dark matter on galactic scales comes from the observations of the rotation curves of galaxies. The typical graph, such as shown in the figure 3.1 from (35), represents circular velocities $v(r)$ of stars and gas as a function of their distance from the galactic center r.

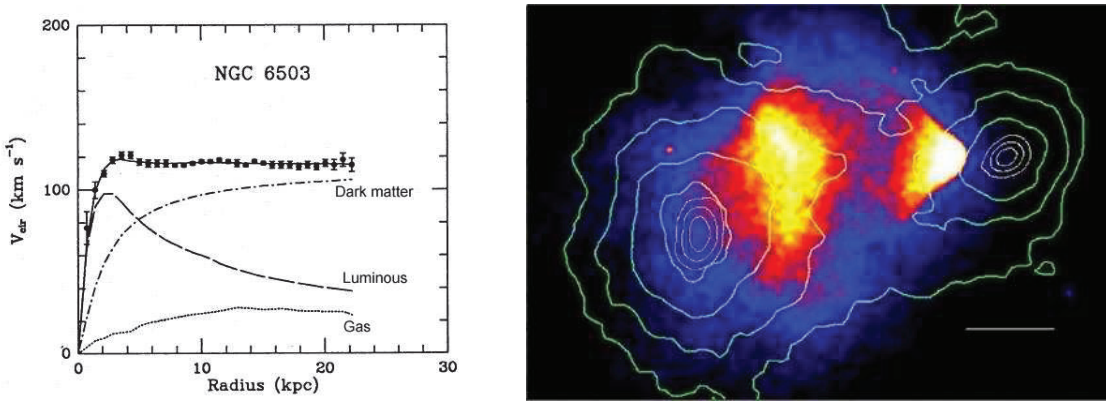

Figure 3.1: **On the left:** Rotation curve of NGC 6503. The dotted, dashed and dash-dotted lines are the contributions of gas, disk and dark matter, respectively.
On the right: Bullet Cluster (1E 0657-56) image from CHANDRA X-ray telescope. The visible matter (in red and yellow) contributes a little in the total mass of the cluster. The full mass density contours (in green) were obtained from the the gravitational lensing measurements by VLT and Hubble telescopes.

Rotation curves are usually obtained by combining observations of the 21 cm line with optical surface photometry. Observed rotation curves exhibit a characteristic flat behavior at large distances far beyond the edge of the visible disks. In classical Newtonian dynamics the circular velocity is expected to be

$$v(r) = \sqrt{\frac{GM(r)}{r}} \tag{3.1}$$

where $M(r) = 4\pi \int \rho(r) r^2 dr$ is the mass enclosed within a radius r and $\rho(r)$ is the mass density profile. If all the galaxy mass were contained in the optical disc of radius R_G then $v(r)$ should be falling as $\propto r^{-\frac{1}{2}}$ beyond the optical disc, i.e. for $r > R_G$. The fact that $v(r)$ is approximately constant implies the existence of an halo with $M(r) \propto r$ and $\rho \propto r^{-2}$.

Among the most interesting objects, from the point of view of the observation of rotation curves, are the so–called Low Surface Brightness (LSB) galaxies, which are probably everywhere dark matter-dominated, with the observed stellar populations making only a small contribution to rotation curves - an important feature to facilitate the disentanglement of the dark and visible contributions to the rotation curves.

A great variety of observational data provides other arguments for dark matter existence, both on sub-galactic and inter–galactic scales. Without being exhausting we can cite some of them:

1. Weak modulation of strong lensing around individual massive elliptical galaxies. This provides evidence for substructure on scales of $\sim 106 M\odot$ (101) (103).
2. The so–called Oort discrepancy in the disk of the Milky Way (84). The argument is based on the inconsistency between the amount of stars, or other tracers in the solar

neighborhood, and the gravitational potential implied by their distribution which allow to infer the existence of some unobserved matter.

3. Weak gravitational lensing of distant galaxies by foreground structure (82).
4. The velocity dispersions of dwarf spheroidal galaxies which imply mass–to–light ratios larger than those observed in our "local" neighborhood. While the profiles of individual dwarfs show scatter, there is no doubt about the overall dark matter content (102).
5. The velocity dispersions of spiral galaxy satellites which suggest the existence of dark halos around spiral galaxies, similar to our own, extending at the radii $\gtrapprox$ 200 kpc, that is well behind the optical disc. This applies in particular to the Milky Way, where both dwarf galaxy satellites and globular clusters probe the outer rotation curve (33).

3.1.2 Galaxy clusters scale

Today the most direct and spectacular evidence for dark matter comes form the Bullet cluster, the result of a sub cluster colliding with the larger galaxy cluster 1E 0657-56 (125). During the collision, the galaxies within the two clusters passed by each other without interacting (a typical distance between galaxies is approximately 1 Mpc). However, the majority of a cluster's baryonic mass exists in the extremely hot gas between galaxies, and the cluster collision (at roughly six million miles per hour) compressed and shock heated this gas; as a result, a huge amount of X-ray radiation was emitted which has been observed by NASA's Chandra X-ray Observatory. Combination of optical and X-ray images with the weak lensing map shows an interesting discrepancy; the areas of strong X-ray emission and the largest concentrations of mass seen through gravitational lensing are not the same. The majority of the mass in the clusters is non-baryonic and gravity points back to this missing mass. The right panel of the figure 3.1 shows the collision of the two clusters. The hot barionic matter (in red and yellow) is detected via the X-ray emissions while the total mass density contours (in green) are obtained from weak gravitational lensing. We clearly see that the total mass distribution seems to be quite isotropic and not much affected by the collision. This effect can be understood if we assume a presence of massive and weakly interacting component of matter. Another recent example of colliding clusters of galaxies was observed in MACS J0025.4-1222 system in mid-2008 (46).

In general the mass of a cluster can be determined via several methods, including application of the virial theorem to the observed distribution of radial velocities, by weak gravitational lensing, and by studying the profile of X–ray emission that traces the distribution of hot emitting gas in rich clusters.

Considering the hydrostatic equilibrium of a spherically symmetric system

$$\frac{1}{\rho}\frac{dP}{dr} = -a(r) \tag{3.2}$$

where P, ρ and a are respectively the pressure, density and gravitational acceleration of the gas at radius r, one can infer the relation of the temperature as a function of the radius r:

$$kT \approx (1.3 - 1.8)\text{keV}\left(\frac{M_r}{10^{14}M_\odot}\right)\left(\frac{1\text{Mpc}}{r}\right) \tag{3.3}$$

where M_r is the mass enclosed within the radius r. If we assume that the total mass M_r is the observed mass, the discrepancy between the temperature obtained using the above equation

and the observed temperature $T \approx 10$keV suggests the existence of a substantial amount of dark matter in clusters.

These conclusions can be checked against estimates from gravitational lensing data shown in the figure 3.2. Following Einstein's theory of general relativity, light propagates along geodesics which deviate from straight lines when passing near intense gravitational fields. The distortion of the images of background objects due to the gravitational mass of a cluster can be used to infer the shape of the potential well and thus the mass of the cluster (see (124) for a spectacular demonstration of gravitational lensing in clusters).

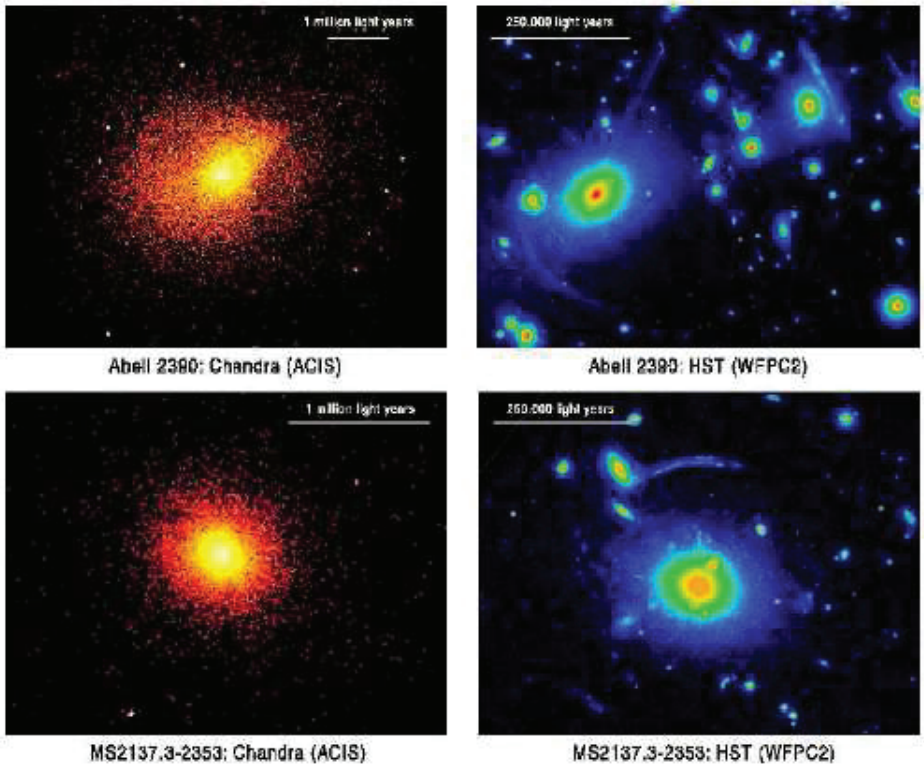

Figure 3.2: Chandra X-ray (left) and Hubble Space Telescope Wide Field Planetary Camera 2 optical (right) images of Abell 2390 (z = 0.230) and MS2137.3-2353 (z =0.313). Note the clear gravitational arcs in the Hubble images.

3.1.3 Cosmological scale

The astrophysical scale data allow us to infer the existence of the dark matter component of the universe and its distributions at various scales, from solar scale up to galaxy cluster scales. The overall amount of the dark matter in the universe can be extracted from the analysis of the Cosmic Microwave Background (CMB) discovered by Penzias and Wilson in 1964 (107). COBE (Cosmic Background Explorer) launched in 1989, verified two fundamental properties of the CMB: the CMB is remarkably uniform (2.73 K across the sky) and the CMB, and thus the early universe, is a nearly perfect blackbody. Next, COBE's Differential Microwave Radiometer

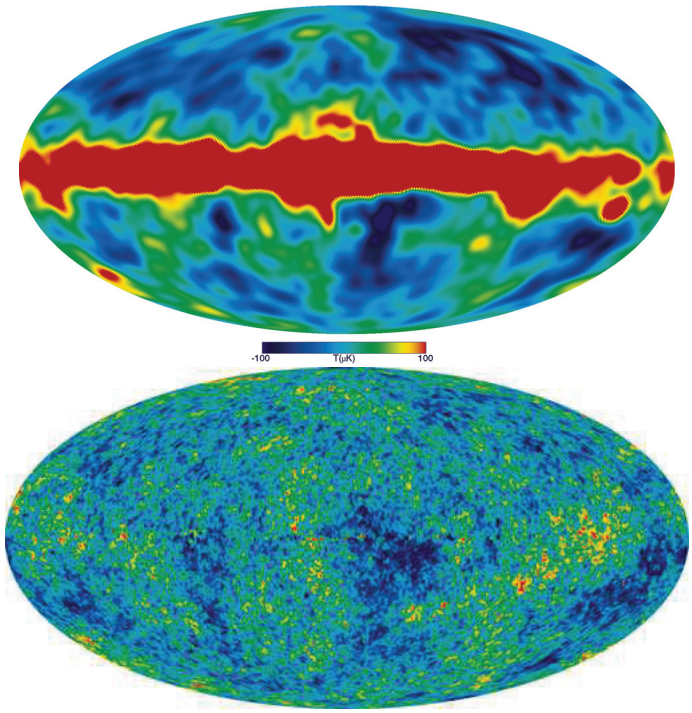

Figure 3.3: **On the top**: The all-sky image produced by the COBE Satellite. It is a low resolution image of the sky (7 degree resolution), but obvious cold and hot regions are apparent in the image. The large red band is the microwave emissions from our own galaxy. This image shows a temperature range of $\pm 100\mu$K.
On the bottom: The detailed, all-sky picture of the infant universe created from seven years of WMAP data. The image reveals 13.7 billion year old temperature fluctuations (shown as color differences) that correspond to the seeds that grew to become the galaxies. The signal from the our Galaxy was subtracted using the multi-frequency data. This image shows a temperature range of $\pm 200\mu$K. Extracted from *http://map.gsfc.nasa.gov/*

(DMR) discovered in its first year fundamental fluctuations within the CMB of an extremely small magnitude of 30 ± 5 μK as shown in the figure 3.3. These fluctuations were too small to have solely accounted for the seeds of structure formation, given the size of the CMB fluctuations, the structure of the universe we see today would not have had time to form. The COBE results showed a need for an electrically neutral form of matter that could jump start the structure formation process well before recombination (121).

WMAP (Wilkinson Microwave Anisotropy Probe) was launched in 2001 with the mission to more precisely measure the anisotropies in the CMB. Located at the Earth-Sun L2 point (about a million miles from Earth), the satellite has taken data continuously and is able to detect temperature variations as small as one millionth of a degree. Due to the increased angular resolution of WMAP we now know the total and baryonic matter densities (83)

$$\Omega_m h^2 = 0.1334^{+0.0056}_{-0.0055} \qquad \Omega_b h^2 = 0.02260 \pm 0.00053 \tag{3.4}$$

where $\Omega_m h^2$ is the total matter density, and $\Omega_b h^2$ is the baryonic matter density. This implies that the dark matter density $\Omega_{dm} h^2 = 0.1123 \pm 0.0035$ makes about 83% of the total mass density. Locally this corresponds to an average density of dark matter $\rho_{dm} \approx 0.3\text{GeV/cm}^3 \approx 5 \times 10^{-28}\text{kg/m}^3$ at the Sun's location.

The CMB data show that the temperature of the universe at the time of photon decoupling was isotropic and homogeneous up to perturbations smaller than 10^{-5}. The small scale

fluctuations shown in the figure 3.3 in the primordial plasma allow us to infer the cosmological parameters. The angular spectrum of the CMB is excellently fitted by the ΛCDM model, assuming a gaussian, adiabatic and nearly scale invariant power spectrum of primordial fluctuations. The structure of acoustic peaks requires the presence of a cold dark matter and the best fit of 7-years WMAP data gives $\Omega_b h^2 = 0.02267 \pm 0.00058$

The big bang nucleosynthesis provides another estimation of the matter content in the universe. In fact, BBN is the largest source of deuterium in the universe as any deuterium found or produced in stars is almost immediately destroyed by fusing it into He^4. Thus the present abundance of deuterium in the universe can be considered a lower limit on the amount of deuterium created by the big bang. It turns out that the deuterium to hydrogen ratio is heavily dependent on the overall density of baryons in the universe. R. H. Cyburt calculated two possible values for $\Omega_b h^2$ depending on what deuterium observation is taken (64):

$$\Omega_b h^2 = 0.0229 \pm 0.0013 \qquad \text{or} \qquad \Omega_b h^2 = 0.0216^{+0.0020}_{-0.0021} \tag{3.5}$$

Finally analyses of the large scale structure of the universe also yield evidence for dark matter and help break degeneracies present in the CMB data analysis. By calculating the distance to galaxies using their redshifts, cosmologists have been able to map out the approximate locations of more than 1.5 million galaxies. For example, the Sloan Digital Sky Survey (SDSS) has created 3-D maps of more than 900,000 galaxies, 120,000 quasars, and 400,000 stars during 7 its eight years of operation (11).

By measuring large scale structure one can experimentally determine the power spectrum $P(k)$ of density perturbations. By obtaining the matter power spectrum from galaxy surveys, the amount of total matter and baryonic matter can be found: the peak of P(k) is sensitive to the value of m, and the amount of baryons has effects on the shape of $P(k)$ through baryonic acoustic oscillations, i.e. excesses in galaxies separated at certain distances due to sound waves in the prerecombination plasma. Using these techniques, a final study based on data from SDSS yielded

$$\Omega_b h^2 = 0.02258^{+0.00057}_{-0.00056} \qquad \Omega_{dm} h^2 = 0.1109 \pm 0.0056 \tag{3.6}$$

Note that these results agree with both CMB and BBN predictions. In the figure 3.4 we show the combined results for the $\Omega_m - \Omega_\Lambda$ values from different observations where the privileged parameter region is showed.

The astrophysical and cosmological evidence for dark matter is both impressive and compelling. What is perhaps the most striking are the multiple lines of evidence which point to the need for dark matter. Elemental abundances from big bang nucleosynthesis and fundamental anisotropies in the cosmic microwave background radiation both predict very similar baryon abundances, yet each describes a completely separate era in the history of the universe in which very different physical processes are occurring. Dark matter is necessary to both describe galaxies and clusters of galaxies, and is a necessary ingredient in the formation of large scale structure. Dark matter seems to be a fundamental and necessary component of our universe pushing us to find possible particle candidates for dark matter, and therefore theories beyond the Standard Model are necessary to solve the puzzle. The new dark matter model must fit those relic density bounds. Moreover, the stability of the dark matter particle impose its lifetime to be at least the age of the universe. Taking into account the estimates of the Hubble Space Telescope Key Project (75) and in agreement with the result derived by WMAP, $H_0 = 72 \pm 3(\text{stat}) \pm 7(\text{sys}) \text{kms}^{-1}\text{Mpc}^{-1}$ we require the lifetime $\tau \gtrapprox 4.3 \times 10^{17}$s.

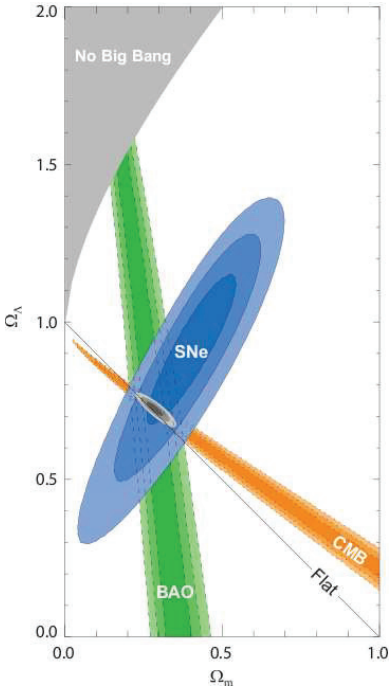

Figure 3.4: **On the left:** best fit 68.3%, 95.4% and 99.7% confidence level contours in the $\Omega_m - \Omega_\Lambda$ plane for the CMB, BAO and the union SN set as well as their combination (assuming $w = -1$ for the dark Energy). Extracted from (92).

3.2 Dark matter candidates

In the previous section we have reviewed the most relevant astrophysical and cosmological evidences for non-baryonic dark matter. We have also stressed that any model with particle dark matter whose abundance is roughly 6 times higher than that of the baryonic matter, has necessarily to invoke physics beyond the Standard Model of particle physics.

This connection between the dark matter problem and particle physics has prompted the proliferation of dark matter candidates that are currently being searched in the accelerators, direct and indirect detection experiments. Remarkably, some of them are predicted in theories originally proposed for different intents (e.g. supersymmetry or Peccei-Quinn model) and which could also have important implications in other cosmological contexts, strengthening therefore the link between particle physics and cosmology. As our understanding of particle physics improves, we accumulate information about the properties of dark matter which progressively reduces the allowed regions in the parameter space of those theories. In this section we present the main properties that a particle has to have in order to be considerate as a "good" dark matter candidate. We will therefore review the fundamental properties of the dark matter and review some of the best motivated candidates far from being exhausting as a proliferation of dark matter candidates in the literature still makes the overall summary quasi-impossible!

Supersymmetric candidates

Among the supersymmetric particles there are several dark matter candidates. By far the most widely studied are neutralinos whose stability is protected by the R-parity. Sneutrinos has

been also long considered as dark matter candidates. It has been shown that sneutrinos will have a cosmologically interesting relic density if their mass is in the range of 550 to 2300 GeV. However the expected scattering cross section of a sneutrino with nucleons is much larger than the limits found by direct detection experiments (74).

In some supersymmetric models, gravitinos, superpartners of gravitons, can be the lightest supersymmetric stable particles. With only gravitational interactions they are however very difficult to observe. Moreover it has been known for some time that long lived gravitinos can pose problems for cosmology. In particular their presence can destroy the abundances of primordial light elements. Gravitinos may also be overproduced in the early universe it the temperature of reheating is not sufficiently low.

Kaluza Klein candidates

Models with extra spatial dimensions can provide an alternative candidate for dark matter. In particular, in models in which all of the Standard Models fields are free to propagate in the bulk, called universal extra dimensions (UED), the lightest Kaluza-Klein particle (LKP) may be stable and a potentially viable dark matter candidate. Extra dimensions compacted on an orbifold often have some geometric symmetry which is a subgroup of the higher dimensional Poincaré group. As a result, momentum (which for compactified dimensions is quantized and takes the name of "KK-number") conservation in extra dimensions is broken down to some discrete symmetry KK-parity, which can play the role of the "dark matter symmetry" preventing the decay of the lightest KK particle. The lightest Kaluza-Klein excitation charged under the KK-parity can be the dark matter particle if it is electrically neutral. In the simplest (UED) scenario (where there is only one extra dimension compactified on an interval) the potential candidates are KK gauge boson, KK neutrino, KK scalar or KK graviton depending on the parameters (40). Additionally, a dark matter candidate has been proposed in the framework of "warped" universal extra-dimensions: an exotic particle with gauge quantum numbers of a right-handed neutrino, but carrying fractional baryon number (19).

Neutrinos

Standard Model neutrinos have been considered, until recently, excellent dark matter candidates. However their total relic density is predicted to be

$$\Omega_\nu h^2 = \sum_{i-1}^{3} \frac{m_i}{93\text{eV}} \tag{3.7}$$

A good laboratory constraint on neutrino masses comes from tritium β-decay experiments at Troitsk and Mainz (126), pointing to the upper limit on the neutrino mass to be $m_\nu < 2.05$ eV (95% C.L.) This implies an upper bound on the total neutrino relic density of $\Omega_\nu h^2 < 0.07$ which means that neutrinos are simply not abundant enough to be the dominant component of dark matter. Another argument against neutrinos as a viable dark matter candidate is that being relativistic collisionless particles, neutrinos erase fluctuations below a scale ~ 40 Mpc. This would imply a top-down formation history of structure in the universe, where big structures form first which is in contradiction with current cosmological observations (45).

Sterile neutrinos, hypothetical particles similar to Standard Model neutrinos, but without Standard Model weak interactions, were proposed as dark matter candidates in 1993 by Dodelson

and Widrow (67). Stringent cosmological and astrophysical constraints on sterile neutrinos come from the analysis of their cosmological abundance and the study of their decay products (10). The WMAP measurements of the reionization optical depth suggests that the the dark matter structures were in place to form massive stars prior to redshift $z > 20$, which is is simply not possible if the dark matter particle mass is smaller than ~ 10 keV (130).

Axions

Introduced in an attempt to solve the problem of CP violation in particle physics, axions have also often been discussed as a dark matter candidate. Laboratory searches, stellar cooling and the dynamics of supernova 1987A constrain axions to be very light (<0.01 eV). Furthermore, they are expected to be extremely weakly interacting with ordinary particles, which implies that they were not in thermal equilibrium in the early universe. Although the calculation of the axion relic density depends on the assumptions made regarding the production mechanism, it is possible to find an acceptable range where axions satisfy all present-day constraints and represent a possible dark matter candidate (114).

Superheavy candidates

Dark matter particles are usually assumed to be relatively ”light”, meaning lighter than a few hundred TeV. This upper ”limit” mas was derived by Griest and Kamionkowski under the assumption that the dark matter particle is a thermal relic of the early universe. The superheavy candidates, named commonly “wimpzillas” were thus proposed with masses $> 10^{10}$ GeV. They could not be in thermal equilibrium during freeze-out and therefore their relic abundance does not depend on their annihilation cross section, but rather is a function of the wimpzilla's production cross section. There are many ways to produce wimpzillas in the early universe. Among the most studied is gravitational production at the end of inflation, resulting from the expansion of the background spacetime (90). A common motivation for superheavy dark matter comes from the observation of cosmic rays at ultra-high energies. The universe is opaque to ultra-high energy protons over cosmological distances > 50 Mpc. Since no astrophysical sources of ultra-high energy protons are known within this range, more exotic scenarios have been developed to account for these observed events. Such scenarios include ultra-high energy cosmic-ray production via the decay or annihilation of superheavy dark matter particles (115), (131).

3.3 Detection Schemes

Finally here we summarize all the informations about the dark matter that we are able to infer from the experimental data

3.3.1 Direct searches

In this section all the theoretically calculated values as well as the experimental limits are given using the standard astrophysical assumptions of an isothermal WIMP halo with the mean velocity $v_0 = 220$ km/s, the local density of 0.3 GeV/c^2 and escape velocity 544 km/s (73) unless we mention different values.

The signature of DM elastic scattering off nuclei are nuclear recoils, characterized by an exponential recoil spectrum with typical energies $\mathcal{O}(10)$keV or less, for WIMP masses between 1 and 100 GeV (see (85) for more details).

Simple estimation of the recoil energy E_r

We can simply estimate an approximate value of the recoil energy expected in a direct detection experiment (76) considering an elastic scattering WIMP-nucleon where all the kinetic energy is transmitted to the nucleon. Assuming the standard astrophysical value for the mean velocity of the WIMP $v_0 = 220$ km/s and WIMP of mass $m_{WIMP} = 100$ GeV the WIMP kinetic energy is

$$T = \frac{1}{2} m_{WIMP}\, v_0^2 = \frac{1}{2}(1.783 \times 10^{-25}\,\mathrm{kg}) \cdot (220\,000\,\mathrm{m/s})^2 \approx 4.314 \times 10^{-15}\,\mathrm{J} \approx 26.9\,\mathrm{keV} \quad (3.8)$$

This is the upper limit for a 100 GeV WIMP traveling at 220 km/s could deposit in the detector, but the actual amount would certainly be smaller. Natural radioactivity generally emits MeV energies, making a keV increase in energy due to nuclear scattering nearly impossible to find. For this reason, direct detection devices must be radioactively clean.

As extremely low event rates are expected, the direct search detectors must have very large mass, long exposure times (and therefore good stability over time), low energy thresholds and very good background shielding. Such detectors are insensitive to very strongly interacting dark matter, which would be stopped in the atmosphere or earth and would be undetectable underground. However, such dark matter would be seen by rocket and other space-borne experiments or would settle to the core of the Earth, leading to other fascinating and weird implications.
In the case of inelastic scattering off nuclei or orbital electrons, the recoil is followed by a decay photon from the excited state (71), (122). However, the natural radioactivity background makes the detection of this signal very problematic.

Although heavy nuclei are used in current direct detection experiments, the results are often given in terms of scattering cross section off protons in order to allow easy comparison between different experimental settings, involving different target materials. Current experiments exploit a variety detection techniques focusing on signals such as scintillation, phonons, ionization or a combination of some of them. Also different targets are used (NaI, Ge, Si, Xe). Below we summarize the principal experiments of direct detection that are used to compare our theoretical limits.

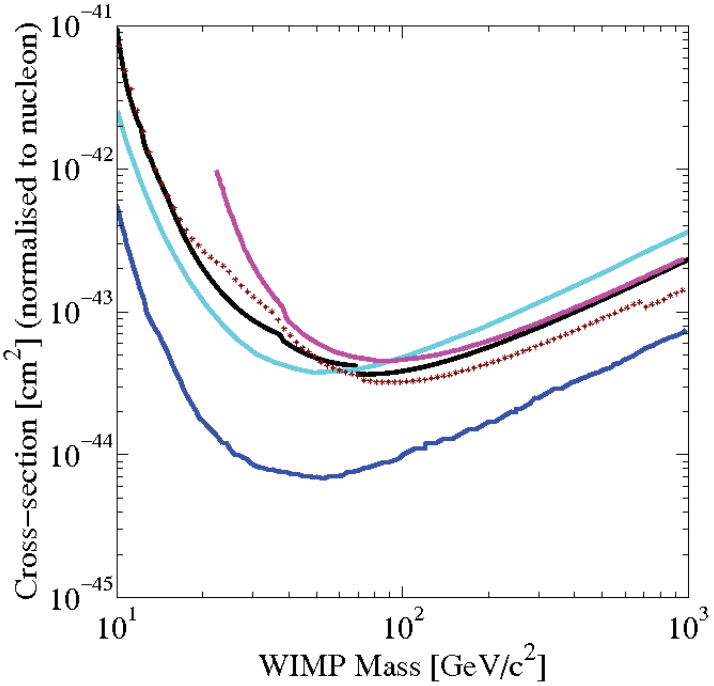

Figure 3.5: The upper limits for spin-independent WIMP-nucleon cross section. From top to bottom at 1000 GeV mass: ZEPELIN-III (cyan) , EDELWEISS-II (pink), CDMS-II (black) , CDMS+EDELWEISS combined results (red) XENON1000 (blue) . The plot is made in DM Tools *http://dmtools.brown.edu*

.

CDMS II Soudan The Cryogenic Dark Matter Search (CDMS II) (20) experiment, located at the Underground Laboratory, uses 19 Ge ($\sim$ 230 g) and 11 Si ($\sim$ 100 g) particle detectors operated at cryogenic temperatures ($<$ 50 mK). The data were taken during four periods of stable operation between July 2007 and September 2008. The result is a minimum cross section of 7.0×10^{-44} cm^2 (3.8×10^{-44} cm^2 when combined with the previous results) for a WIMP of mass 70 GeV/c^2.

EDELWEISS II

The EDELWEISS experiment (32) is located in the Laboratoire Souterrain de Modane (LSM). Like CDMS collaboration, the EDELWEISS experiment uses a heat-ionization germanium bolometer. The latest data were collected over a period of fourteen months from April 2009 to May 2010. The experiential derive the 90%CL upper limits on the WIMP-nucleon spin-independent cross section with the minimum cross-section of 4.4×10^{-8} pb for a WIMP mass of 85 GeV.

XENON10 and XENON100

The XENON10 experiment (25) at the Gran Sasso National Laboratory operates a 15 kg xenon dual phase (liquid and gas) time projection chamber (XeTPC) to search for dark matter WIMPs in liquid xenon (LXe). Liquid xenon is an attractive target for a sensitive WIMP search.

Its high density (~ 3 g/cm^3) and high atomic number (Z = 54, A = 131) allow for a compact detector geometry. The high mass of the Xe nucleus is favorable for WIMP scalar interactions provided a low recoil energy threshold.

Since natural xenon contains ^{129}Xe (26.4%) and ^{131}Xe (21.2%) isotopes, each of which has an unpaired neutron, the XENON10 results substantially constrain the spin dependent (SD) WIMP-nucleon cross section as well.

The data was taken with the XENON10 detector at Gran Sasso during the period between October 2006 and February 2007. The upper limits at 90% C.L. for the WIMP-nucleon spin independent (SI) cross-section exclude the region above 8.8×10^{-44} cm^2 (4.5×10^{-44} cm^2) for a WIMP of mass of 100 GeV/c^2 (30 GeV/c^2).

The next phase, XENON100 (30), operate a total of 170 kg of xenon ($\lessapprox$ 70 kg fiducial) in a dual phase TPC in an improved XENON10 shild at the Gran Sasso Laboratory. While the fiducial mass is increased by more than a factor of 10, the background is lowered by about a factor of 100 (through careful selection of ultra-low background materials, the placing of cryogenic devices and high voltage feed-troughs outside of the shield and by using 100 kg of active LXe shield). Featuring a large target mass and an extremely low background, XENON100 is the most sensitive dark matter direct detection experiment in operation today. The ultimate design goal of XENON100 is to achieve a spin-independent WIMP-nucleon scattering cross section sensitivity of $\sigma = 2 \times 10^{-45}$ cm^2 for a 100 GeV/c^2 WIMP. A first dark matter analysis has been carried out, using 11.17 live days of background data, taken from October to November 2009. The initial results based on only 11.17 live days of data give the 90% confidence upper limit, with a minimum at a cross section of 3.4×10^{-44}cm^2 for a WIMP mass of 55 GeV/c^2.

ZEPLIN III

The ZEPLIN-III experiment (23) operated at the Boulby laboratory (UK) under a rock overburden of 2 850 m water equivalent. This two-phase xenon emission detector measures both scintillation and ionization responses from particle interactions in its 12-kg LXe target. In the second science run (SSR), WIMP-search data were acquired over 319 days between Jun 2010 and May 2011. The yielded data allow for exclusion of the scalar cross-section above 4.8×10^{-44} cm^2 near 50 GeV/c^2 WIMP mass with 90% confidence. When combined with data from the first run, this result improves to 3.9×10^{-44} cm^2. The results for the experiments mentioned above are shown in the figure 3.5 and summarized in the table 3.1.

Experiment	Ref.	Data Taking Period	Target	$10^{-8}\sigma^{SI}$[pb]	m_{WIMP} [GeV]
CDMS II	(20)	2009	Ge/Si	3.8	70
EDELWEISS II	(32)	2009 - 2010	Ge	4.4	85
CDMS+EDELWEISS	(21)	2009-2010	Ge/Si	3.3	90
XENON10	(25)	2006 - 2007	LXe	4.5	30
XENON100	(30)	2009	LXe	3.4	55
ZEPELIN III	(23)	2010 - 2011	LXe	4.8	50

Table 3.1: Direct Detection Experiments and the corresponding upper bounds on spin-dependent (SI) WIMP-nucleon cross section.

DAMA

In order to discriminate the DM signal against the natural background some experiments have been searching for an annual modulation of the measured event rate (69). In fact, the Earth rotation around the Sun is expected to produce a modulation of the relative velocity of DM particles given by

$$v_E = 220 \text{ km/s} \cdot \{1.05 + 0.07 \cos[2\pi(t - t_m)]/1 \text{ year}\} \tag{3.9}$$

where t_m is approximatively the begin of June. The variation of the WIMP flux is actually small $\approx 7\%$, so that a large number of events has to be collected and therefore a large detector is needed.

In 1998, the DAMA collaboration obtained evidence for a modulation of the event rate, that was later confirmed with the confidence level of 6.3σ (44).

If interpreted in terms of a SI scattering of a WIMP off NaI, and further assuming an isothermal spherical DM halo, with a characteristic velocity of the Maxwell-Boltzmann distribution of $v_0 = 270$ km/s, with a local DM density of $\rho = 0.3$ GeV cm^3, and with a slope $\rho \sim r^{-2}$, the DAMA result is compatible with the detection of a WIMP with a mass of around 50 GeV and a WIMP-nucleon scattering cross section of order of $10^{-41} \div 10^{-42}$ cm^2.

Other experiments, such as CDMS or EDELWEISS, have explored the region of parameter space allowed by the DAMA modulation signal, finding null results (42), (22). The comparison between the DAMA annual modulation and other experiments is however model-dependent. Taking into account astrophysical uncertainties, the DAMA allowed region is sensibly increased, with masses extending up to 250 GeV and SI cross section down to 10^{-43} cm^2.

3.3.2 Indirect searches

Another way to search for the dark matter is through the detection of its annihilation products. Because the annihilation rate of the dark matter particles is proportional to the square of its density, natural places to look for dark matter annihilations are those expected to have high DM densities, such as the sun, earth, and galactic center. Annihilation products include gamma-rays, neutrinos, and antimatter.

Gamma Rays: Gamma-rays from WIMP annihilation are believed to occur most frequently in the galactic center. One way this process can take place is through a WIMP annihilation yielding a quark and anti-quark, which then produce a particle jet from which a spectrum of gamma-rays is released. A second form of gamma-ray production is the decay of WIMPs directly to gamma-rays, $\chi\chi \rightarrow \gamma\gamma/\gamma Z$ which produces gamma-ray lines proportional to the mass of the WIMPs involved. Since typical WIMP masses can be on the order of 100s of GeV, these are extremely high energy gamma rays. Although the flux is small and quite difficult to detect, observing such a gamma-ray line would be an smoking gun indication for dark matter annihilation and the WIMP mass (66). The EGRET Collaboration reported an excess of gamma-rays in 1998, pointing toward already accepted characteristics of dark matter: a 50-70 GeV WIMP mass and a ring of concentrated dark matter at a radius of 14 kpc from the galactic center. This discovery is initially encouraging, but as Bergström et al. have shown, observed antiproton fluxes would have to be much larger if these excess gamma rays are being produced by neutralino or generic WIMP self annihilation (43). For this reason and others, EGRET's results remain controversial.

Neutrinos: Neutrinos can be another important products of WIMP annihilation. As WIMPs travel through the universe and through matter, they lose small amounts of energy due to scattering off of nuclei. Therefore, WIMPs can gather at the centers of large gravitating bodies, increasing their density until their annihilation rate equals half the capture rate. Because neutrinos are so weakly interacting, neutrino telescopes must be massive to detect a significant signal. AMANDA-II is a neutrino detector at 1500 to 2000 meters underground within the ice of the South Pole where Cherenkov radiation can travel and be seen easily by optical modules. This experiment has not detected statistically significant results from the direction of the sun, but has placed firm limits on the muon flux (14). The IceCube experiment integrates AMANDA into a much larger detection experiment, with 7200 optical modules and a detector volume of a cubic kilometer (88). Super-Kamiokande is another indirect detection experiment, located underground in the Kamioka-Mozumi mine in Japan. The detector consists of 50 000 tons of water and detects Cherenkov radiation from incoming muons as well. Super-K looks in the direction of the sun, earth, and galactic center, and, like AMANDA, has not detected any excess of muon rates above the expected background (128).

Antimatter: Antimatter can be a excellent signal of WIMP annihilation precisely because antimatter is relatively rare, and many of the astrophysical processes which create antimatter are well understood. For example, the annihilation of WIMPs can also produce antiprotons via $\chi\chi \to q\bar{q}$ through hadronization (where the dominate annihilation process yields b quarks and antiquarks), and positrons through secondary products of the annihilation such as WW^+W^- where $W \to \bar{e}\nu_e$. Unlike gamma-rays and neutrinos, these products are charged and thus affected by magnetic fields within space and also lose energy due to inverse Compton and synchrotron processes, so we cannot make any conclusions about where the annihilations occurred. In 1994, the HEAT Collaboration detected an excess of cosmic ray positrons of energies around 10 GeV possibly caused by neutralino self-annihilation, and confirmed this signal again in 2000 (34). A boost factor however, must be applied to the WIMP annihilation rate of a smooth halo in order to match the HEAT data; this is perhaps an indication that we exist within an extremely clumpy halo, or that there are other unknown sources of antimatter.

Quite recently, the results from the PAMELA (a Payload for Antimatter Matter Exploration and Light-nuclei Astrophysics) satellite-borne experiment's flight from July 2006-February 2008 were released. The collaboration found that the positron fraction increases sharply over much of the range of 1.5-100 GeV and thus concluded that a primary source, either an astrophysical object or dark matter annihilation, must be present to account for the abundance of cosmic-ray positrons (16). The data from PAMELA also require heavy WIMP candidates or large boost factors associated with non-uniform clumps in the dark matter distribution, thus constraining the nature of the possible dark matter. Further data is necessary to determine if excess gamma ray and antimatter fluxes are indeed signals of dark matter annihilation or signatures of local astrophysical objects and backgrounds.

3.4 Relic abundance of dark matter

In the early universe, very energetic and massive particles were created and existed in thermal equilibrium. As the universe expanded and cooled, however, two things occurred: lighter particles no longer had sufficient energy to produce heavier particles through interactions and the universe's expansion diluted the number of particles such that interactions did not occur as frequently or at all. At some point, the density of a particular particle species became too low to support frequent interactions and conditions for thermal equilibrium were violated and their comoving number density remains constant. The exact moment or temperature of freeze-out can be calculated by equating the reaction rate with the Hubble expansion rate.

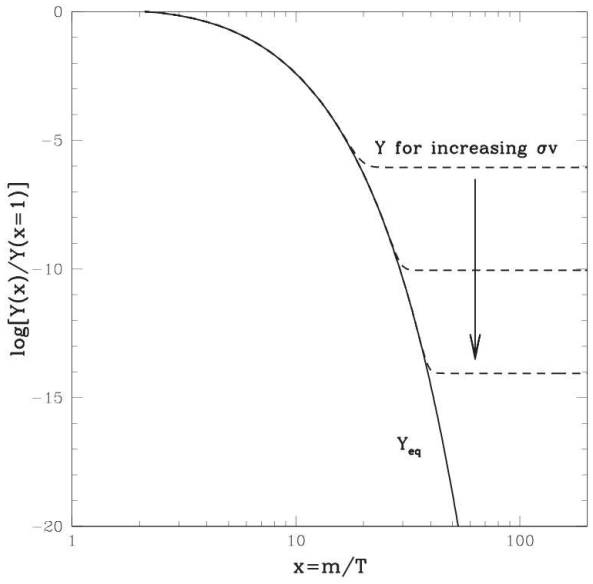

Figure 3.6: The numerical simulation for the evolution of the co-moving relic density extracted from (76). Here $Y \propto nT^{-3}$ includes the dilution effect coming from the expansion of the universe. The solid line represents the equilibrium density and the dashed lines the current density.

3.4.1 The standard case of relic abundance - only annihilations

We first summarize the standard calculation for the relic abundance of a particle species χ which was in thermal equilibrium in the early universe and decoupled when it became non relativistic. One usually has to assume that the particles χ in thermal equilibrium with cosmic

plasma at sufficiently high temperatures and that its interactions with the rest of the plasma are strong enough that it remains in equilibrium a temperatures somehow below m_χ. Moreover one has to assume that there is no asymmetry between the particles χ and their antiparticles $\bar{\chi}$. Another possibility, inherent in supersymmetric and extra-dimensional extensions of the Standard Model is that χ is its own antiparticle. In the treatment of relic abundance calculation presented here we follow the authors of (120). The relic abundance is found by solving the Boltzmann equation for the evolution of the χ number density

$$\frac{dn}{dt} = -3Hn - \langle \sigma v_{rel} \rangle \left(n^2 - n_{eq}^2 \right) \tag{3.10}$$

where H is the Hubble parameter, v_{rel} is the relative velocity between two χ's, $\langle \sigma v_{rel} \rangle$ is the thermally averaged total cross section times relative velocity, n_{eq} is the equilibrium thermal density.

$$\begin{aligned} n_{eq} &\sim T^3 && \text{for} && T \gg m_\chi \\ n_{eq} &= g \left(\frac{m_\chi T}{2\pi} \right)^{\frac{2}{3}} e^{-\frac{m_\chi}{T}} && \text{for} && T \ll m_\chi \end{aligned} \tag{3.11}$$

g is the number of internal degrees of freedom. At high temperature there are roughly as many χ particles as photons and particles are abundant and rapidly convert into lighter particles and vice versa. At low temperatures the n_{eq} is Boltzmann-suppressed. Shortly after the temperature drops below m_χ the number density n_{eq} decreases exponentially and the annihilation rate $\Gamma = \langle \sigma v_{rel} \rangle n$ drops below the expansion rate H. At this point, χs stop annihilating and escape out of the equilibrium and become thermal relics.

The thermally averaged total cross section can be approximated by the non-relativistic expansion

$$\langle \sigma v_{rel} \rangle = a + b \langle v_{rel}^2 \rangle + \mathcal{O}\left(\langle v_{rel}^2 \rangle \right) \approx a + \frac{6b}{x} + \mathcal{O}\left(\frac{1}{x^2} \right) \tag{3.12}$$

where $x = \frac{m_\chi}{T}$.

By solving Boltzmann equation analytically with appropriate approximations the abundance of χ's is given by

$$\Omega_\chi h^2 = \frac{1.04 \times 10^9}{M_P} \frac{x_F}{\sqrt{g_\star(x_F)}} \frac{1}{a + 3b/x_F} \tag{3.13}$$

where $M_P = 1.22 \times 10^{19}\,\text{GeV}$ and $g_\star$ is the number of effectively massless degrees of freedom

$$g_\star(T) = \sum_{i=bosons} g_i + \frac{7}{8} \sum_{i=fermions} g_i \tag{3.14}$$

The coefficient $\frac{7}{8}$ accounts for the difference in Fermi and Bose statistics. Notice that $g_\star$ is a function of T as the thermal bath quickly gets depleted of the heavy species (with masses $m < T$).
The freeze-out temperature is found iteratively from equation

$$x_F = \ln \left(c(c+2) \sqrt{\frac{45}{8}} \frac{g}{2\pi^3} \frac{m_\chi M_P (a + 6b/x_F)}{\sqrt{g_\star(x_F) x_F}} \right) \tag{3.15}$$

The c constant is found empirically by comparing to numerical solutions of the Boltzmann equation and usually is taken $c = \frac{1}{2}$.

3.4.2 Case with co-annihilations

When the particle χ is nearly degenerated with other particles, one has to take into account the co-annihilation cross-sections. The previous calculation can be generalized to this "coannihilations" case straight forward. We assume that the particles χ_i are labeled according to their masses, so that $m_i < m_j$ if $i < j$. The number densities of each specie i obey the Boltzmann equation. It can be shown that the relic density n of the lightest species χ_1 (after all the heavier particles have decayed into χ_1) obeys the following simple Boltzmann equation

$$\frac{dn}{dt} = -3Hn - \langle \sigma_{eff} v_{rel} \rangle \left(n^2 - n_{eq}^2 \right) \tag{3.16}$$

where

$$\sigma_{eff}(x) = \sum_{ij}^{N} \sigma_{ij} \frac{g_i g_j}{g_{eff}^2} (1+\Delta_i)^{\frac{3}{2}} (1+\Delta_j)^{\frac{3}{2}} e^{-x(\Delta_i+\Delta_j)} \tag{3.17}$$

$$g_{eff}(x) = \sum_{i=1}^{N} g_i (1+\Delta_i)^{\frac{3}{2}} e^{-x\Delta_i} \tag{3.18}$$

$$\Delta_i = \frac{m_i}{m_1} - 1 \tag{3.19}$$

where $\sigma_{ij} \equiv \sigma(\chi_i \chi_j \to SM)$, g_i is the number of internal degrees of freedom of particle χ_i and $n = \sum_{i=1}^{N} n_i$ is the density of χ_1 we want to calculate. This Boltzmann equation can be solved in a similar way as in no-coannihilation case, resulting in

$$\Omega_\chi h^2 = \frac{1.04 \times 10^9}{M_P} \frac{x_F}{\sqrt{g_\star(x_F)}} \frac{1}{I_a + 3I_b/x_F} \tag{3.20}$$

with

$$I_a = x_F \int_{x_F}^{\infty} a_{eff}(x) x^{-2} dx \tag{3.21}$$

$$I_b = 2x_F^2 \int_{x_F}^{\infty} b_{eff}(x) x^{-3} dx \tag{3.22}$$

The corresponding formula for x_F becomes

$$x_F = \ln \left(c(c+2) \sqrt{\frac{45}{8}} \frac{g_{eff}(x_F)}{2\pi^3} \frac{m_\chi M_P (a_{eff}(x_F) + 6b_{eff}(x_F)/x_F)}{\sqrt{g_\star(x_F) x_F}} \right) \tag{3.23}$$

The a_{eff} and b_{eff} are the first two terms in the velocity expansion of σ_{eff}

$$\sigma_{eff} v_{rel} = a_{eff} + b_{eff} v_{rel}^2 + \mathcal{O}\left(v_{rel}^4\right) \tag{3.24}$$

Comparing the equations 3.17 and 3.24 one gets

$$a_{eff}(x) = \sum_{ij}^{N} a_{ij} \frac{g_i g_j}{g_{eff}^2} (1+\Delta_i)^{\frac{3}{2}} (1+\Delta_j)^{\frac{3}{2}} e^{-x(\Delta_i+\Delta_j)} \tag{3.25}$$

$$b_{eff}(x) = \sum_{ij}^{N} b_{ij} \frac{g_i g_j}{g_{eff}^2} (1+\Delta_i)^{\frac{3}{2}} (1+\Delta_j)^{\frac{3}{2}} e^{-x(\Delta_i+\Delta_j)} \tag{3.26}$$

The last detail one has to take into account are the relativistic corrections to the above treatment which result with an additional subleading term which can be accounted for by a simple substitution

$$b \to b - \frac{a}{4} \tag{3.27}$$

in the above formulas (127), (94).

There is compelling evidence for the existence of dark matter. Although our understanding of its nature and distribution is still incomplete, many independent observations suggest that about 30% of the total energy density of the universe is made of some sort of non-baryonic dark matter. We will then present in the next sections how another natural dark matter candidate can be introduced to the literature in the context of extra-dimensional extensions of the Standard Model. First, we need to introduce the basic theoretical tools commonly used in the extra-dimensional community.

Part II

Extra Dimensions - models and techniques

Chapter 4

Compactified space general description of the extra dimensional models

4.1 Orbifolds

Most of the fundamental theories such as supergravity or superstrings require spacetime to have more dimensions than four we know about today. Such extra dimensions must be microscopic or curled up in some non-trivial way. These ideas are so interesting that they have inspired much experimental work during last few years (15).

It seems that the first reference to dimensional reduction appears in the work of Gunnar Nordström who in 1914 formulated a vector-scalar theory in four dimensions, unifying electromagnetism and a scalar theory of gravitation, starting from Maxwell theory in a five-dimensional flat spacetime (112). Even if this theoretical proposal did not turn out to be physically correct and was, after a couple of years, replaced by Einstein's tensor theory, it was a milestone in the investigation of gravitational phenomena. It provided for the first time the idea that we could aim at explain the unknown physics in our known spacetime by known physics in a spacetime with extra, compactified dimensions.

Much more known is the work of Theodor Kaluza, published in 1921, who showed that gravity in five dimensions could yield a theory unifying the Einstein's gravity and the Maxwell's equations. It was Oscar Klein who came with the idea of compactifying the fifth dimension on a circle. The Fourier expansion in modes, today known as the Kaluza-Klein tower, allowed him to compute the radius of compactification by identifying the charge of the first massive mode with the electric charge. With a single stroke, the quantization of electric charge was given an explanation, and the size of the compact dimension, which turned to be of the order of the Plank length, explained why we only see effectively four dimensions. The other side of the story is the very wrong result for a mass of such a mode, which was of the order of the Plank mass (70).

The compactification on a 2-sphere from six dimensions was considered by Wolfgang Pauli in 1953, where the Yang-Mills field strength made its appearance as a consequence of a non-Abelian reduction (106). Since this epoch many physicists investigated the consistency of dimensional reduction in context of General Relativity (81), (93), (119),(24).

The idea of extra dimensions is closely related to the string theory. A nonsupersymmetric string theory, to be consistent, has to be defined in 26 dimensions. The number of dimensions required by the superstring theories is ten. In 1975 Joel Scherk and John H. Schwarz proposed

to consider superstrings in a product space $\mathcal{M}^4 \times \mathrm{M}$, where M is a compact manifold whose size is about M_{Pl}^{-1} (118). In 1985 it was realized that to obtain $N = 1$ supersymmetry as a low energy limit of a superstring theory, the six small extra dimensions need to be compactified on a Calabi-Yau manifold. As the typical sizes of compact dimensions on Calabi-Yau manifolds are of the order of $M_{Pl}^{-1} \approx 10^{33}$ cm, there is no way to observe them in human-designed experiments.

The celebrated paper of Candelas et al.(53), which opened the first string revolution of 1985, demonstrates that if the extra six compact dimensions form a Calabi-Yau manifold, then in the low energy theory limit one recovers the $E(8) \times E(8)$ gauge theory which includes SM with tree generations of fermions as observed in nature.

In the late 1990s it was realized that extra spatial dimensions are not necessarily linked to the Planck scale and could potentially be relevant for TeV scale physics (26), (100), (28). Since then, extra dimensional models have enjoyed great popularity among physicists. A general feature of these models is that the extra dimensions are compactified on the so-called orbifolds.

Let us point out the two different philosophies that underlie the issue of dimensional reduction. On one side there is the *compactification approach*, whose paramount example today is string theory, where one expects that dimensional reduction from ten dimensions, or eleven in M-theory, will eventually deliver a four dimensional space-time together with an internal compact manifold, or a more general structure like an orbifold, that carries physical information within. In this approach the fundamental theory is the higher dimensional one, and the compactification procedure should eventually be understood as a physical process driven by some physical principles. The physical consequences that have their origin in the compactified structure and the process of compactification itself, are an essential part of the whole physical picture. Perhaps some of these effects, take for instance the presence of massive Kaluza-Klein modes, may become irrelevant when the theory is examined in the low energy regime, due to the small size of the compactified structure, but the effects are there anyway. This was in fact Klein's elaboration (expanding in Fourier modes) on the original Kaluza's idea, which corresponds to the second approach which we address now.

On the other side one can conceive the dimensional reduction as a mathematical means to formulate a theory in a given space-time dimension having started with a higher dimensional theory as an auxiliary artifact, the extra dimensions never physically existing. In this case we speak of a *consistent truncation* from the higher dimensional theory to the lower one. One can start with a higher dimensional theory whose formulation is perhaps simpler and eventually end up with a more complicated theory at a lower dimension with the remarkable advantage of keeping full control of its symmetries (including supersymmetry when appropriate) or even with the right internal symmetries one was willing to implement. In Klein's interpretation of Kaluza's work, this means that a truncation is made on the tower of Fourier modes to keep only the singlet ones. In this sense, this second approach can be understood as a method of model building, having used the higher dimensional theory as an intermediate device that helps to formulate a fundamental theory at a lower dimension. This has proven to be a useful method in supergravity: in this way, different dimensional reductions of the eleven dimensional supergravity theory have yielded a fairly good recollection of supergravity theories with extended supersymmetry at lower dimensions (108).

4.1.1 Basic definitions

In this section we follow the definitions of (104) and (117). An orbifold, a generalization of the concept of manifold, is a topological space with some additional structure. Recall that a manifold is a space locally modeled in $\mathbb{R}$.

Definition 1 *We define an orbifold*[1] *as a quotient space* $\mathbb{R}^n/\Gamma$ *of a n-dimensional space* $\mathbb{R}^n$ *modulo a discrete symmetry group* Γ*.*

In mathematics one generally makes a difference between an orbifold and a manifold in the following way:

– If Γ has no fixed points then $\mathbb{R}^n/\Gamma$ is called a manifold.
– If Γ has fixed points then $\mathbb{R}^n/\Gamma$ is called an orbifold.

We will however use the name "orbifold" for all the spaces of the form $\mathbb{R}^n/\Gamma$. In our case we are not free to choose any arbitrary discrete group, but are restricted to so-called space groups.

Definition 2 *An n-dimensional (nD) space group is defined as a co-compact*[2] *discrete group of isometries of* $\mathbb{R}^n$ (123)*. One can define a space group as a discrete symmetry group of a n-dimensional space.*

Discrete symmetry groups come in three types:

1. Finite point groups, which include only rotations, reflections, inversion and rotoinversion. They are in fact just the finite subgroups of O(n).
2. Infinite lattice groups which include only translations.
3. Infinite space groups, which combines elements of both previous types, and may also include extra transformations like screw axis and glide reflection.

There are also continuous symmetry groups, which contain rotations of arbitrarily small angles or translations of arbitrarily small distances. The group of all symmetries of a sphere O(3) is an example of this and in general such continuous symmetry groups are studied as Lie groups. With a categorization of subgroups of the Euclidean group corresponds a categorization of symmetry groups. In 3-dimensions there are 219 unique types (or 230 if chiral copies are considered unique) of space groups, also known as crystallographic groups. In 2-dimensions the 17 space groups are called also wallpaper groups. The general classification of discrete space groups is known for dimensions $n \leq 6$.

4.1.2 One dimensional orbifolds and manifolds

There are only two discrete isometries of a 1-dimensional space: reflections r and translations t. The structure of a group is uniquely defined by the set of generators of the group and relations among them. Therefore we can define the space groups in a purely algebraic way:

1. A formal definition of an orbifold in terms of topological spaces can be found in the paper of Thurston (123). The terminology orbifold was first used in one of his lecture courses in 1976. The concept itself occurs first in 1956 as V-manifold in (1) and (116)

2. In mathematics, an action of a group G on a topological space X is co-compact if the quotient space X/G is a compact space.

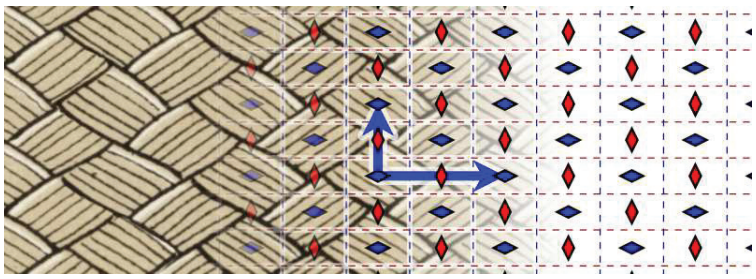

Figure 4.1: Example of diagram for **pgg** group. The pattern comes from a bronze vessel in Nimroud, Assyria. The diamonds corresponds to the centers of rotation over π. The arrows to fundamental translations.

$$\begin{array}{lcl} \mathbb{Z} & = & \langle\, t \,\rangle \\ \mathbb{Z}_2 & = & \langle\, r \,|\, r^2 = \mathbb{I} \,\rangle \\ \mathbb{D}_\infty & = & \langle\, t, r \,|\, r^2 = \mathbb{I},\ (tr)^2 = \mathbb{I} \,\rangle \end{array} \tag{4.1}$$

It is important to notice that the choice of generator is not unique. For example, the space group $\mathbb{D}_\infty$ can be equivalently defined in terms of two π-rotations [3]:

$$\mathbb{D}_\infty \simeq \mathbb{Z}_2 * \mathbb{Z}_2 = \langle\, r_1 \,|\, r_1^2 = \mathbb{I} \,\rangle * \langle\, r_2 \,|\, r_2^2 = \mathbb{I} \,\rangle \quad \text{with} \quad r_2 \equiv t r_1 \tag{4.2}$$

This representation-independent notation has many advantages for discussing the possible parities of the fields on the orbifolds. More intuitive way of defining the groups is by identifying the isometries of $\mathbb{R}^n$ that act as generators of the group.

One dimensional orbifolds are the quotient spaces $\mathbb{R}/\Gamma$ where Γ is one of the one-dimensional space groups $\mathbb{Z}$ or $\mathbb{D}_\infty$. The result of the action of these groups on the infinite line $\mathbb{R}$ is a circle for $\mathbb{Z}$ or an interval in the case of $\mathbb{D}_\infty$.

Γ	$\mathbb{R}/\Gamma$	notation	geometry
$\mathbb{Z}$	$\mathbb{R}/\mathbb{Z}$	S^1	circle
$\mathbb{D}_\infty$	$\mathbb{R}/\mathbb{D}_\infty$	$S^1/\mathbb{Z}_2$	interval

Table 4.1: Classification of 1-dimensional orbifolds.

4.1.3 Two dimensional orbifolds and manifolds

The possible discrete isometries of a plane $\mathbb{R}^2$ are translations t, reflections r, $2\pi/n$-rotations [4] f with $n = 2, 3, 4, 6$ and so-called glide-reflections g, which are translations with a simultaneous mirror reflection. There is 17 distinct space-groups Γ and hence 17 possible orbifolds $\mathbb{R}^2/\Gamma$. In the table 4.2 and equations (4.3) we give the definitions of four two-dimensional orbifolds which are mentioned later in the text.

3. The two rotations r_1 and r_2 do not commute, $[r_1, r_2] \neq 0$. Hence the *free product* $*$ and not the *cross product* $\times$ is used.

4. The restriction to only 2,3,4, and 6-folded rotations is often named the crystallographic restriction theorem.

Γ	$\mathbb{R}^2/\Gamma$	notation	geometry	free parameters
$p1$	$\mathbb{R}^2/\mathbb{Z}^2$	T^2	Torus	r, θ
pg	$\mathbb{R}^2/pg$	-	Klein bottle	r
pgg	$\mathbb{R}^2/pgg$	$\mathbb{R}P^2$	Real projective plane	r
$p4$	$\mathbb{R}^p 4$	$T^2/\mathbb{Z}_4$	Chiral square	-

Table 4.2: Classification of some 2-dimensional orbifolds.

$$\begin{aligned} \text{p1} &= \langle\, t_1 \,\rangle \times \langle\, t_2 \,\rangle \\ \text{pg} &= \langle\, t, g \,|\, [g^2, t] = 0,\ t_2 g t g^{-1} = \mathbb{I} \rangle \supseteq \mathbb{Z}^2 \\ \text{pgg} &= \langle\, r, g \,|\, r^2 = (g^2 r)^2 = \mathbb{I} \rangle \supseteq \mathbb{Z}^2, \mathbb{Z}_2 \\ \text{p4} &= \langle\, t_1, t_2, \,|\, r^4 = (t_1 r^3)^4 = \mathbb{I},\ r t_1 = t_2 r,\ [t_1, t_2] = 0 \rangle \supseteq \mathbb{Z}^2, \mathbb{Z}_4, \mathbb{Z}_2 \end{aligned} \tag{4.3}$$

The fundamental domains of those orbifolds with the symmetry generators and fixed points are shown in the figures 4.1 and 4.2 - 4.3

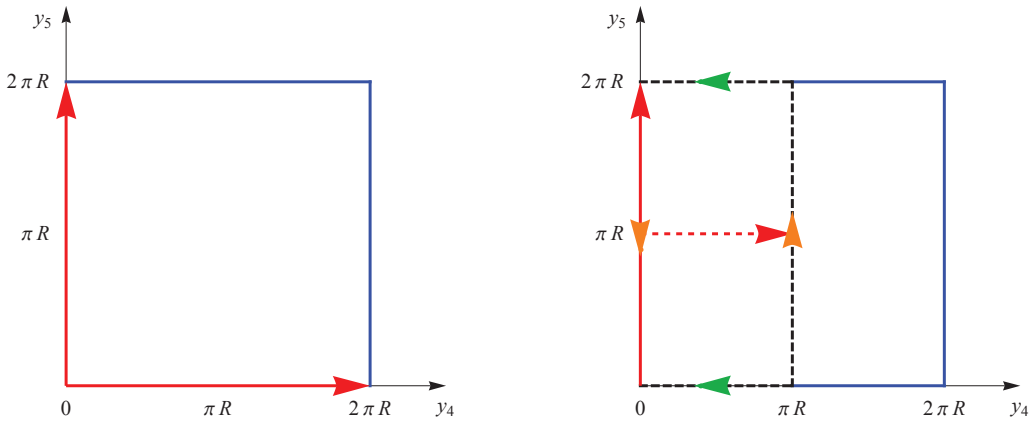

Figure 4.2:
On the left: Fundamental domain of torus T^2. Red arrows correspond to the translation generators t_1 and t_2.
On the right: Fundamental domain of the Klein bottle $\mathbb{R}^2/pg$ (within black dashed lines). In blue - torus fundamental domain. Red arrow - translation generator t. Red dashed arrow - glide generator g. The green and orange arrows indicate the identification of the edges.

Now we are ready to consider the quantum fields propagation on the spaces constructed from the Minkowsky space and the orbifolds.

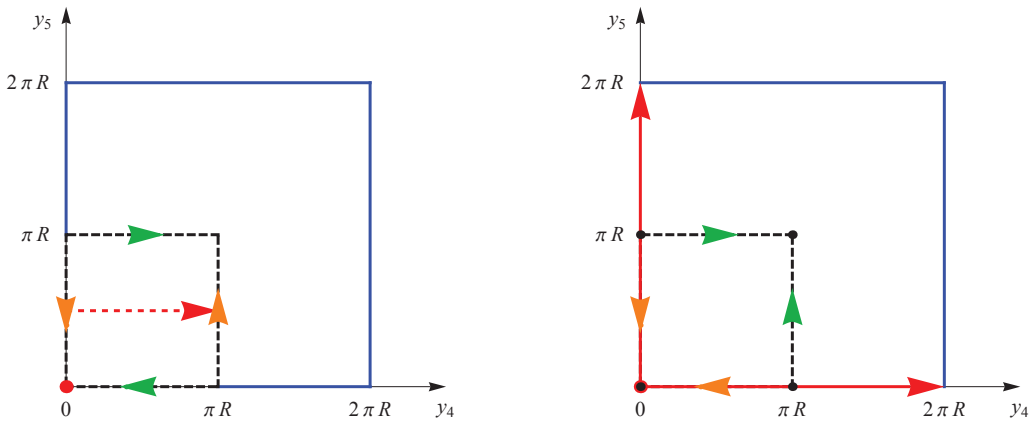

Figure 4.3:
On the left: Fundamental domain of the real projective plane $\mathbb{R}^2/pgg$ (within black dashed lines). Red dot - π-rotation generator. Red dashed arrow - glide generator g. The green and orange arrows indicate the identification of the edges.
On the right: Fundamental domain of the chiral square $\mathbb{R}^2/p4$ (within black dashed lines). Red arrows correspond to the translation generators t_1 and t_2. Red dot - $\pi/2$-rotation generator. Fixed points are marked as black dots. The green and orange arrows indicate the identification of the edges.

4.2 Quantum fields in the extra dimensions

4.2.1 Basics of Kaluza Klein decomposition

Here we will consider the Kaluza Klein decomposition of a scalar, spinor and gauge fields propagating in a five dimensional space $\mathcal{M}_4 \times S^1$. This is the simplest case of compactification of extra dimensions but not free of problems. As we will see, the chiral fermions cannot be defined on such space. We will therefore use this simple space only to emphasize the most important properties of the KK decomposition. Then we will present the KK decomposition of quantum fields on a six dimensional space $\mathcal{M} \times \mathbb{R}P^2$ which is much more involved mathematically due to the presence of two extra dimensions and more complicated defining symmetries of the orbifold.

Scalar field on $\mathcal{M}_4 \times S^1$

Consider the following 5D action for a real scalar field of the mass M:

$$S = \int d^x \int dy \left[\partial^M \Phi \partial_M \Phi - M^2 \Phi\Phi\right] \tag{4.4}$$

As we already have told in the section 4.1, the extra dimension must be compactified. Here we compactify the extra space on a circle S^1 of a radius R. That means that the y variable domain is $-\infty < y < \infty$ but we impose the identifications

$$y \sim y + 2\pi R \qquad \text{with} \qquad -\infty < y < \infty \tag{4.5}$$

Equally one can restrict the domain to $0 < y < 2\pi R$ but with a condition that $(y = 0) \equiv (y = 2\pi R)$. Now we require that the higher dimensional lagrangian $\mathcal{L}_{5D}$, rather than individual fields Φ, has to be invariant under transformations 4.5. In the majority of cases, the lagrangian will

include bilinear terms, such as kinetic terms or mass terms. Therefore in the case of the real scalar the invariance of $\mathcal{L}_{5D}$ requires that

$$\mathcal{L}_{5D}[\Phi(y)] \equiv \mathcal{L}_{5D}[\Phi(y + 2\pi R)] \tag{4.6}$$

what in terms of fields Φ reads as the periodicity conditions

$$\Phi(y) = \Phi(y + 2\pi R) \tag{4.7}$$

Then, as we have a compact space S^1 and a periodic function defined on it, we can expand the 5D scalar fields in the Fourier modes as follows:

$$\Phi(x^\mu, y) = \sum_{n=-\infty}^{\infty} \phi^{(n)}(x^\mu) f_n(y) \tag{4.8}$$

Substituting this expansion into S_{5D} we require that after integrating over extra dimensions we get:

$$S_{4D} = \int x^4 \sum_n \left[\partial_\mu \phi^{(n)} \partial^\mu \phi^{(n)} - \left(M^2 + \frac{n^2}{R^2} \right) \phi^{(n)} \phi^{(n)} \right] \tag{4.9}$$

so that we can interpret the $\phi^{(n)}$s as particle KK modes form the 4D point of view. This requirement gives us the following conditions:

1. Orthonormality condition
$$\int dy f_m^*(y) f_n(y) = 1 \tag{4.10}$$

2. Differential equations
$$\partial_y^2 f_n(y) - M^2 f_n^2(y) = -m_n^2 f_n^2(y) \tag{4.11}$$

Thus the KK decomposition reduces to an eigenvalue problem whose solutions will give us the KK masses m_n and the KK profiles $f_n(y)$. For the simple case of a 5D scalar with a bulk mass M, we get the following solutions to the differential equation

$$f_n = e^{\pm iny/R} \qquad \text{with} \qquad m_n^2 = M^2 + \frac{n^2}{R^2} \tag{4.12}$$

This implies that from the 4D point of view the 5D scalar field appears as an infinite tower of 4D fields which are called the Kaluza-Klein (KK) modes $\phi^{(n)}$ with masses squared, $m_n^2 = M^2 + \frac{n^2}{R^2}$ as is illustrated in the figure 4.4. We can easily generalize to the case of $d-4$ extra dimensions, each of which is compactified on a circle of the radius R_α to obtain the tree level spectrum $m_n^2 = M^2 + \sum_{\alpha=4}^{d} \frac{n_\alpha^2}{R_\alpha^2}$. Thus, we see that the signature of an extra dimension from the 4D point of view is the appearance of infinite tower of KK modes: to repeat, the lightest (zero)-modes is identified with the SM particle and the heavier ones (KK modes) appear as new particles beyond the SM .

4.2.2 Orbifold or Interval?

Now I would like to emphasize the difference between the orbifold vision of the extra space and the "finite space" vision.

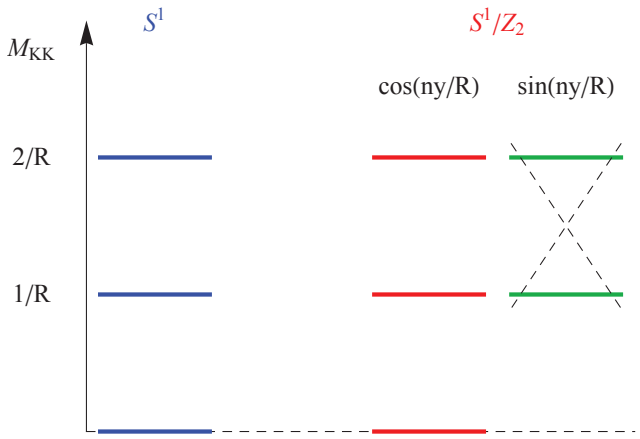

Figure 4.4: Spectrum of the scalar field on the circle and on the interval. On an interval the scalar field can have a parity $p = +1$ represented by red states $\sim \cos(ny/R)$ or a negative parity $p = -1$ corresponding to the green states $\sim \sin(ny/R)$.

Interval

We consider a real scalar field defined on an interval $[0, \pi R]$. The bulk action has the standard form

$$S = \int d^4x \int_0^{\pi R} \left(\frac{1}{2} \partial^M \Phi \partial_M \Phi - V(\Phi) \right) \tag{4.13}$$

in this action we do not have any boundary terms (operator localized on the branes = boundaries).

In order to find the solutions one needs to solve equations of motion obtained form the variational principle $\delta S = 0$. The fields Φ are assumed to vanish at infinity $x^\mu \to \infty$, but one cannot assume the same for the compact dimensions. Therefore we are left with the bulk equations of motion of the standard form and a set of boundary conditions (BC):

$$\delta S_{bulk} = \int d^4x \int_0^{\pi R} \left[-\partial^M \partial_M \Phi - \frac{\partial V}{\partial \Phi} \right] \delta\Phi - \left[\int d^4x \partial_y \Phi \delta\Phi \right]_0^{\pi R} = 0 \tag{4.14}$$

We have two possibilities of the boundary conditions

$$\partial_y \Phi|_{bound} = 0 \qquad \text{Neumann BC} \tag{4.15}$$

or

$$\delta\Phi|_{bound} = 0 \qquad \text{Dirichlet BC} \tag{4.16}$$

The latter case would follow form the condition $\Phi|_{bound} = 0$. One defines the boundary conditions as natural if they leave the boundary variation of the field $\delta\Phi|_{bound}$ arbitrary. However, we would only like to allow the natural boundary conditions in the theory since these are the ones that will not lead to explicit (hard) symmetry breaking once more complicated fields like gauge fields are allowed. Thus in order to still allow the Dirichlet BC one needs to reinterpret that as the natural BC for a theory with additional terms in the lagrangian added on the boundary. The simplest possibility is to add a mass term to modify the lagrangian as

$$S = S_{bulk} - \frac{1}{2}\int d^4x \int_0^{\pi R} dy \left(M_1^2\delta(y-0) + M_2^2\delta(y-\pi R)\right)\Phi^2 \tag{4.17}$$

Thus the natural BCs are given by

$$\begin{cases} \partial_5\Phi + M_2^2\Phi = 0 \quad \text{at} \quad y = \pi R \\ \partial_5\Phi - M_1^2\Phi = 0 \quad \text{at} \quad y = 0 \end{cases} \tag{4.18}$$

It is clear that for $M_i \to \infty$ we recover the Dirichlet BCs. This is the way we will always understand the Dirichlet BCs: we will interpret them as the case with infinitely large boundary induced mass terms for the fields.

Orbifold

One gets a completely equivalent image from the orbifold point of view. To show clearly how the things work in this approach let's focus on the simplest orbifolds - a circle S^1 and an interval $S^1/\mathbb{Z}_2$. Mathematically speaking, a circle is a smooth manifold since it has no special points. We can "mod out" this smooth manifold by a discrete symmetry to obtain an orbifold. Specifically, we impose the discrete $\mathbb{Z}_2$ identification: $y \sim -y$ in addition to $y \sim y + 2\pi R$. Thus, the physical or fundamental domain extends only from $y = 0$ to $y = \pi R$. The endpoints of the orbifold $y = 0$ and $y = \pi R$ do not transform under $\mathbb{Z}_2$ and hence are called fixed points of the orbifold. Note also that the end points of this extra dimension are not identified with each other either by the periodicity condition $y \sim y + 2\pi R$ (unlike the endpoints $y = 0$ and $y = 2\pi R$ on S^1) or by the $\mathbb{Z}_2$ symmetry. Let us consider how the KK decomposition is modified in going from a circle to an orbifold. Starting from the bulk action of the form given by in the equation 4.14 and imposing the identifications $y \sim y + 2\pi R$ one in fact impose the periodic BC on the fields as well:

$$\Phi(0) \equiv \Phi(2\pi R) \tag{4.19}$$

up to global symmetries. The field can be then expanded in Fourier series

$$\Phi = \frac{1}{\sqrt{2\pi R}} + \frac{1}{\sqrt{\pi R}}\sum_{n=-\infty}^{\infty} \phi^{(n)}(x^\mu)e^{iny/R} \tag{4.20}$$

where the coefficient in front has been chosen for proper normalization. Then while going to the interval $S^1/\mathbb{Z}_2$ one can decompose the field into the functions odd and even under transformations $y \to -y$, namely:

$$\Phi = \frac{1}{\sqrt{2\pi R}}\phi^{(0)} + \sum_{n=1}^{\infty}\left(\phi_+^{(n)}\cos\left(\frac{ny}{R}\right) + \phi_-^{(n)}\sin\left(\frac{ny}{R}\right)\right) \tag{4.21}$$

with $\phi_+^{(n)} = \frac{1}{\sqrt{2}}(\phi^{(n)} + \phi^{(-n)})$ and $\phi_-^{(n)} = \frac{i}{\sqrt{2}}(\phi^{(n)} - \phi^{(-n)})$. The physics must be invariant under the symmetry transformations $y \to -y$ thus we must assign the parity of the fields

$$\Phi(x^\mu, -y) = p\Phi(x^\mu, y) \tag{4.22}$$

The assignment $p = +1$ sets $\phi_-^{(n)} \equiv 0$, while $p = -1$ sets $\phi_+^{(n)} \equiv 0$ and $\phi^0 \equiv 0$. Thus one can see that the fact of orbifolding the space reduce the number of modes by the factor of two, and it removes the zero mode in the case of parity assignment $p = -1$ to the field Φ as illustrated on the figure Fig.4.4.

Moreover by imposing the parities one recovers exactly the functions one would found by imposing Neumann (for $p = -1$) and Dirichlet (for $p = +1$) BCs.

The main difference between orbifold and interval point of view is that while considering the orbifold notation one starts form an infinite domain. Thus the field initially is defined on the infinite space $-\infty < y < \infty$. Then during the compactification one requires the physics invariant under symmetry transformations and not the fields themselves. It means that on the fundamental domain of an orbifold a field can be multiply defined.

4.2.3 Fermions on the circle and on the interval - chirality problem

The smallest irreducible representation for 5-dimensional fermions is a 4-(complex) component spinor. The simplest 5D action for such a spinor is

$$S_{5D} = \bar{\Psi}(i\partial_M \Gamma^M - M)\Psi \tag{4.23}$$

As for the scalar field we decompose the six-dimensional field into the KK modes:

$$\Psi_\sigma = \sum_n \psi_\sigma^{(n)} e^{(iny/R)} \tag{4.24}$$

and the effective 4 dimensional effective action is

$$S_{4D} = \sum_n \bar{\psi}^{(n)} \left(i\partial_\mu \Gamma^\mu - M - \frac{in}{R} \right) \psi^{(n)} \tag{4.25}$$

thus, as in the scalar case we find the tower of Dirac spinors with masses $m_n^2 = M^2 + \frac{n^2}{R^2}$. The problem now is that if the 5D fermions transforms under some 5D gauge symmetry, then the massless chirality states L and R (zero modes for $M = 0$) transform identically under this gauge symmetry. Hence, such a scenario cannot correspond to the Standard Model, where the left handed and right handed states transform as doublets and singlets respectively under the SU(2) gauge symmetry. We can obtain the chiral fermions by compactifying the 5D theory on an interval instead of a circle. As the 5D action contains the terms of the form $\bar{\Psi}\Gamma^5\partial_5\Psi \ni \Psi_L^\dagger \partial \Psi_R$, which must be even under Z_2 symmetry, then if Ψ_L is even under Z_2 then Ψ_R must be odd. The corresponding decomposition will give

$$\Psi_L \sim \sum_n \Psi_L^{(n)} \cos\frac{ny}{R} \qquad\qquad \Psi_R \sim \sum_n \Psi_R^{(n)} \sin\frac{ny}{R} \tag{4.26}$$

Therefore we get a massless zero mode only for Ψ_L. Of course we would have chosen Ψ_R to be even instead to obtain a right handed zero mode as is schematically shown in the figure 4.5.

4.2.4 Gauge fields on S^1 and S^1/Z_2

Finally we consider a five dimensional gauge field. The 5-dimensional action for the 5D gauge field $A_M = (A_\mu, A_4)$ has the form

$$S_{5D} = \int d^4x dy \frac{1}{4} F_{MN} F^{MN} = \int d^4x dy \frac{1}{4} \left(F_{\mu\nu} F^{\mu\nu} + F_{\mu 4} F^{\mu 4} \right) \tag{4.27}$$

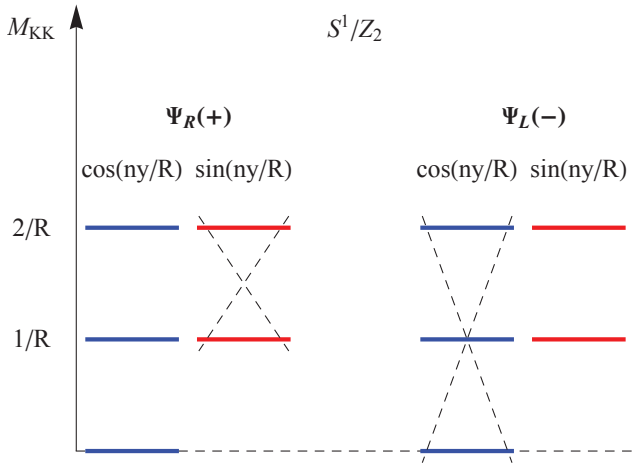

Figure 4.5: Spectrum of the right- and left handed fermion on the interval.

As usual, the KK decomposition is given by

$$A_{\mu,4} = \sum_n A^{(n)}_{\mu,4} f_{\mu,4\ n}(y) \tag{4.28}$$

On the circle both, A_μ and A_4 components have zero-modes. The former is a vector, whereas the latter is a scalar. On the interval it is possible to get rid of the A_4 zero mode using the parities. Note that for the term $F_{\mu 4}$ to have a well defined parity we have two choices:

1. A_μ is even - it has a zero mode identified with the SM gauge boson, and A_4 is therefore odd and does not have zero mode.
2. A_μ is odd so that A_4 is even and has a zero mode.

Hence we obtain the following KK decomposition for the gauge field with even A_μ component on the $S^1/\mathcal{Z}_2$

$$\begin{aligned} f_{\mu\ 0} &= \frac{1}{2\pi R} \qquad \text{flat profile} \\ f_{\mu\ n}(y) &= \frac{1}{\sqrt{\pi R}} \cos\frac{ny}{R} \\ f_{4\ n}(y) &= \frac{1}{\sqrt{\pi R}} \sin\frac{ny}{R} \end{aligned} \tag{4.29}$$

$$\tag{4.30}$$

Where the modes are normalized over $-\pi R \leq y \leq +\pi R$, even though the physical domain is $0 \leq y \leq \pi R$. It can be shown (17) that $A^{(n\neq 0)}_\mu$ "eats" $A^{(n)}_4$ to form a massive spin-1 gauge boson from the following mass terms:

$$F^2_{\mu 4} \ni \partial_\mu A_4 \partial_4 A^\mu \sim \sum_n A^{(n)}_\mu \partial_4 A^{(n)}_4 \partial_y f_{\mu\ n}(y) \tag{4.31}$$

4.2.5 Couplings of gauge modes

In this paragraph we show the very important property of the gauge couplings. Namely that the 4D effective couplings of gauge zero modes to all the KK modes of matter fields are of the same strength and given by $g_4 = \frac{g_5}{\sqrt{2\pi R}}$. This universality of the zero-mode gauge couplings is in fact guaranteed by 4D gauge invariance. We can show therefore explicitly that taking the interaction lagrangian for the gauge bosons with fermions we get

$$\begin{aligned} \int d^4x dy \bar{\Psi}\Gamma^M(\partial_M + g_5 A_M)\Psi \quad &\ni \quad \sum_n \bar{\psi}_L^{(n)}\gamma\psi_L^{(n)} \times \int dy f_{L\ n}^2(y)\left(\partial_\mu + A_\mu^{(0)}\frac{g_5}{\sqrt{2\pi R}}\right) \\ &= \quad \sum_n \bar{\Psi}_L^{(n)}\gamma^\mu\psi_L^{(n)}\left(\partial_\mu + A_\mu^{(0)}\right) \end{aligned} \tag{4.32}$$

with

$$g_4 = \frac{g_5}{\sqrt{2\pi R}} \tag{4.33}$$

The point is that the profile of the gauge zero-mode is flat so that the overlap integrals appearing in the kinetic term for fermion mode and in the coupling to gauge zero-mode are identical. However, the couplings of zero-mode fermions to gauge KK modes (coming from the overlap of profiles) are non-universal, i.e., these couplings depend on the 5D fermion mass (17).

4.3 Radiative corrections in extra dimensions

Radiative corrections are known to play an important role for precision measurements, but are generally not expected to radically change the nature of high energy processes like production and decays of new particles to be discovered. Note however that this is not true in the extra-dimensional models as the radiative corrections are crucial for determining the decays of KK excitations. This is because at tree level the KK masses are quantized and all momentum preserving decays are exactly at threshold. Radiative corrections become therefore the dominant effect in determining open decay channels.

In the previous section we have seen that the spectrum of the KK modes is degenerated, as at each level (n) the mass of the heavy mode is set by the relation $m_n^2 = \frac{n^2}{R^2}$. This mass degeneracy will be lifted by the radiative corrections.

4.3.1 Methods for loop calculation

In the literature three main methods of calculating loop corrections in extra dimensions are known: by the summation over winding modes making use of the Poisson summation formula (65), by the summation over Kaluza Klein towers in the expansion of the 6D propagator (60) and by using the mixed propagator method where the coordinates of the four infinite dimensions are Fourier-transformed to momentum space while those of the compactified space are kept in the configuration space (110). In this section we summarize briefly those main methods of calculating radiative corrections to the masses in extra dimensions. All those techniques give equivalent results but differ by small technical subtleties due to the choice of the regularization scheme.

Summation over winding modes

The expansion of 5D and 6D propagators in the winding modes for all the types of fields, scalar, vector and spinor were considered in (65). Following the author we show the main features of this technique.

The 5D scalar propagator in euclidean infinite space is the solution of the equation

$$(p^2 - \partial^j \partial_j)\tilde{G}(p, y_1 - y_2) = \delta(y_1 - y_2) \tag{4.34}$$

where one uses mixed representation, the coordinates of the Minkowski space are in momentum representation while the coordinate of the extra space are in the spatial representation. The solution to this equation is of the form

$$\tilde{G} = \frac{e^{-p|y_1 - y_2|}}{2p} \tag{4.35}$$

Due to the translation invariance of the infinite line $\mathbb{R}$ the propagator $\tilde{G}$ depends only on $|y_1 - y_2|$. If one considers compactification on a circle by identifying points $|y_1 - y_2| \sim |y_1 - y_2 + 2n\pi R|$ then the solution can be written as a sum of propagators restricted to the fundamental domain of the orbifold $y_1, y_2 \in [0, 2\pi R)$

$$\tilde{G}^{circle}(p, y_1, y_2) = \sum_{n-\infty}^{\infty} \tilde{G}(p, y_1 - y_2 + 2n\pi R) \tag{4.36}$$

It is instructive to study the separate contributions of each mode. For $n \neq 0$ the solution is exponentially damped, therefore the integrals of momenta running in loop will be finite. For $n = 0$ and $y_1 = y_2$ the function goes as p^{-1}. Therefore one easily sees that the divergent contributions are associated to the zero winding mode, i.e to short distances. The contributions of other modes are finite. Therefore it is easy to separate the divergent contributions using the formalism of winding modes.

Considering the winding mode expansion on an interval S^1/Z_2, due to identifications $y \sim -y$ one can write the propagator as

$$\tilde{G}^{int}_{\pm} = \sum_{n=-\infty}^{\infty} \left(\frac{e^{-p|y_1-y_2+2n\pi R|}}{2p} \pm \frac{e^{-p|y_1+y_2+2n\pi R|}}{2p} \right) \tag{4.37}$$

where $y_i \in [0, \pi R)$ and $\pm$ depends on the field parity in the loop. This propagator depends on $|y_1 + y_2|$ due to the breaking of translation invariance. In the above equation we can see that the propagator goes as p^{-1} for the following limits of the coordinates and windings: $(y_i \to 0, n = 0)$ and $(y_i \to \pi R, n = -1)$. Then we expect divergences localized on the fixed points of the orbifold. We can expect these terms because they do not break any symmetry of the theory.

For the six dimensional case the analysis is a little bit more involved but in what follows we sketch the main steps. The solution to the equation

$$(p^2 - \partial^j \partial_j)\tilde{G}(p, \vec{y}_1 - \vec{y}_2) = \delta^{(2)}(\vec{y}_1 - \vec{y}_2) \tag{4.38}$$

where $p^2 = p_\mu p^\mu$ is the 4D momentum and $j = 1, 2$ labels the extra dimensions, has the form

$$\tilde{G}(p, \vec{y}_1 - \vec{y}_2) = \frac{1}{2\pi} K_0(p|\vec{y}_1 - \vec{y}_2|) \tag{4.39}$$

where K_0 is the K Bessel function of zeroth order. Then the propagator in the compact space, in analogy to the 5D compactification, has the form

$$\tilde{G}^t(p, \vec{y}_1, \vec{y}_2) = \sum_{\vec{w}} \frac{K_0(p|\vec{y}_1 - \vec{y}_2 + \vec{w}|)}{2\pi} \tag{4.40}$$

with $|\vec{y}|$ the modulus of the vector measured with the flat metric of a torus and $\vec{w}$ stands for the defining identifications of points to obtain the compactified space.

6D Kaluza Klein expansion method

The Kaluza Klein expansion is the most widely used technique. It consists on decomposing the 6D field into the 4D KK modes and summation over all the KK tower. The loops are calculated using the usual 4D propagators for all the modes. The problem is that one needs to know the effective 4D couplings of the KK excitations that run in the loop which will be an important limitation to use this technique. The form of loop contributions on the real projective plane will be exactly the same as for the winding modes expansion.

Mixed propagator method

The third method consists in using mixed propagators, where the coordinates of the four infinite dimensions are Fourier-transformed to momentum space while those of the compactified dimensions are kept in configuration space. This method is broadly used in finite temperature

field theory calculations. One of its advantages is that one can easily separate the ultraviolet divergent terms of the uncompactified theory from the nonlocal finite corrections arising from windings around the compact dimensions (110). We show in details the form of the propagators used in this method as well as the regularization procedure because all the radiative corrections to the $(2,0)$ modes masses were calculated using this method.

5 dimensional propagators and regularization It was shown in (110) that the scalar $G_\Phi^{S^1}$, gauge $G_{\alpha\beta}^{S^1}$ and fermion $G_\Psi^{S^1}$ propagators on a S^1 manifold for a field of mass m and in the unitary gauge $\xi = 1$ can be written in a simple way:

$$\begin{aligned} G_\Phi^{S^1}(\chi_l, |y_1 - y_2|) &= \tfrac{i\cos\chi_l(\pi R - |y_1-y_2|)}{2\chi_l \sin(\chi_l \pi R)} \\ G_{\alpha\beta}^{S^1}(\chi_l, |y_1 - y_2|) &= (-g_{\alpha\beta}) G_\Phi^{S^1}(\chi_l, |y_1 - y_2|) \\ G_\Psi^{S^1}(\chi_l, |y_1 - y_2|) &= \left(p_\mu \gamma^\mu + i\gamma^5 \partial_5 + m\right) G_\Phi^{S^1}(\chi_l, |y_1 - y_2|) \end{aligned} \tag{4.41}$$

where $\chi_l = \sqrt{k^2 - m^2}$ and k is the 4-D momentum $k^2 = k^\mu k_\mu$.

It was also noticed in (110) that writing the $G_\Phi^{S^1}$ propagator as

$$G_\Phi^{analy}(\chi_l, |y_1 - y_2|) = G_\Phi(\chi_l, |y_1 - y_2|) + G_\Phi^{analy}(\chi_l, |y_1 - y_2|) \tag{4.42}$$

where G_Φ is the propagator on the uncompactified dimension and G_Φ^{analy} is an analytical function given by

$$G_\Phi^{S^1}(\chi_l, |y_1 - y_2|) = \frac{e^{i\chi_l|y_1-y_2|} + e^{-i\chi_l|y_1-y_2|}}{2\chi_l(e^{-2\pi i\chi_l} - 1)} \tag{4.43}$$

for large Euclidean momenta $\chi_l^E = i\sqrt{k_E^2 + l^2} \gg R^{-1}$ the G_Φ^{analy} is exponentially damped:

$$\frac{e^{-\chi_l^E|y_1-y_2|} + e^{\chi_l^E|y_1-y_2|}}{2\chi_l^E(e^{2\pi\chi_l^E} - 1)} \xrightarrow{\chi_E \gg R^{-1}} \frac{1}{2\chi_l^E e^{\chi_l^E(2\pi - |y_1-y_2|)}} \tag{4.44}$$

and thus the loop-integrals containing G_Φ^{analy} are finite. The UV divergence occur only form the G_Φ. Moreover,

$$G_\Phi^{analy} \to 0 \qquad \text{for} \qquad R \to \infty \tag{4.45}$$

what is one would expect as in this limit as the heavy modes can not contribute. This is in complete analogy to the $(0,0)$ mode contribution in the winding modes expansion method. The contributions that are due to the compactification contain exponential cutoff factors that render the corresponding integrals finite. The scale of this exponential cutoff is determined by the compactification scale R. From the physical point of view, this is easy to understand as the physics at distances much smaller than the radius R should not be sensible to the fact whether the space is compactified or not.

Due to small real part of $\cot(\chi R\pi)$ we can write the non-compactified limit $R \to \infty$ as

$$\cot(\chi_l \pi R) = -i\left(1 + \frac{2}{e^{-2i\pi R\chi_l} - 1}\right) \qquad \text{and} \qquad \lim_{R\to\infty} \cot(\chi_l \pi R) = -i \tag{4.46}$$

The infinite part in the integrals will then come only from the 0-mode propagation. To regularize the divergences that appear we will replace

$$\cot(\chi_l \pi R) \to \frac{-2i}{e^{-2i\pi R\chi} - 1} = \cot(\chi_l \pi R) + i \tag{4.47}$$

4.4 Extra dimensional models

To finish this chapter we present the two extra-dimensional scenarios which are not in the class of the UED models but which were the first models that incorporated the extra-dimensions to high-energy physics in order to explain the gauge hierarchy problem.

4.4.1 Large extra dimensions

The large extra dimensions scenario of Arkani-Hamed, Dimopoulos and Dvali (ADD) (27) was proposed as a potential solution to the hierarchy problem, i.e., the question of why the (reduced) Planck scale, $M_{Pl} \simeq 1.22 \cdot 10^{19}$ is so much larger than the weak scale ~ 1 TeV.

The ADD scenario assumes a $D = 4 + n$ dimensional spacetime, with n compactified spatial dimensions. The weakness of gravity arises since it propagates in the higher-dimensional space. The SM is assumed to be localized in a 4D subspace, a 3-brane, as can be found in certain string constructions. Gravity is described by the Einstein-Hilbert action in $D = 4+n$ spacetime dimensions.

$$S_D = -\frac{M_D^{2+n}}{2} \int d^4x d^n y \sqrt{-g} R + \int d^4x \sqrt{-g_{ind}} \mathcal{L}_{SM} \tag{4.48}$$

where x labels the ordinary four coordinates, y the n extra coordinates, g refers to the determinant of the D-dimensional metric whose Ricci scalar is defined by R, and M_D is the Planck scale of the D-dimensional theory. The extra dimensions are assumed to be flat and compactified in a volume V_n ADD propose that we (and all other SM particles!) live on an assumed to be rigid 4D hypersurface (sometimes called a wall or brane). On the other hand gravity is allowed to propagate in a $(4 + n)$ dimensional bulk which is,eg. an n-torus, T^n . Gauss law then tells us that the Planck scale we measure in 4D, M_{Pl} , is related to the (4+n)-dimensional fundamental scale M that appears in the higher dimensional general relativistic action, via the relation

$$M_{Pl}^2 = V_n M_*^{n+2} \tag{4.49}$$

where V_n is the volume of the n-dimensional compactified space. M can be thought of as the true Planck scale since it appears in the higher dimensional action which is assumed to describe ordinary general relativity but extended to (4+n)-dimensions. The gravity law will be modified by the extra-space. We can assume that the extra-space is a torus T^n all of whose radii are equal to R with a volume $V_n = (2\pi R)^n$. Then for $r \gg R$ the extra dimensions are essentially invisible and to all appearances the space looks to be 4D. Then we know that $F_{grav} \sim \frac{1}{r^2}$ thanks to Newton.

In the opposite limit $r \ll R$ the effects of being in a full $(4 + n)$-dimensional space will become obvious; at such small distances we do not even realize that the extra dimensions are compactified. One finds that now $F_{grav} \sim \frac{1}{r^{2+n}}$ which implies clearly significant deviations from conventional Newtonian gravity once $r \sim R$. Therefore R cannot be very large. For $n = 1$ one one obtains $R \sim 108$ m, a scale of order the Earth-Moon distance over which we know Newton's law holds very well; thus $n = 1$ is excluded. $n = 2$ implies $R \sim 100$ μm which is close to the limit of current experimental searches for deviations from Newton's law of gravity. If n is further increased R becomes much too small to probe for direct deviations from the $\frac{1}{r^2}$ Newton's law.

Consistency of the model requires a stabilization mechanism for the radii of the extra dimensions. The fact that we need $R \gg \frac{1}{M_D}$ leads to a new hierarchy problem, the solution of which might require imposing supersymmetry in the extra-dimensional bulk.

The searches of ADD type models have been performed in a number of experimental searches. The visible effects are expected from the KK gravitons emissions as gravitons produced in the final state would escape detection, giving rise to missing transverse energy. Notice that although each KK graviton has a purely gravitational coupling, suppressed by M_P^{-1}, one usually sums over almost continuous spectrum of available gravitons in the inclusive processes which have much larger cross sections. LEP results set limits M_D >0.66 - 1.60 TeV (13), while hadron colliders, where experimentally sensitive channels include the jet + MET (missing transverse energy) and γ + MET final states, give the bounds $M_D > 0.94$ - 1.94 TeV (CDF Tevatron) (72). The limits from LHC (CMS) with 1 fb^{-1} of data give $M_D > 1.03$ - 1.21 TeV (3).

Another limits can also be set by looking at the virtual graviton effects that can be formulated in terms of dimension-8 operator proportional to a coefficient noted usually as M_{TT} that is related to M_D in a model-dependent way. The bounds thus will be not generic. We can note that the last update from ATLAS with 2 fb^{-1} of data set the highest lower limit $M_{TT} > 2.7$ TeV (2) ($M_{TT} > 2.8$ from CMS 1 fb^{-1} dataset (56)).

4.4.2 Warped extra dimensions

Randall and Sundrum proposed another class of models, with only one extra dimension compactified on an interval S^1/Z_2 with $0 \leq y \leq L$ (111). The main motivation for this model was the possible solution of the hierarchy problem which was regarded as better as that provided by the ADD scenario. The point $y = 0$ is referred as UV (Planck)-brane. The end-point $y = L$ in called IR (TeV)-brane and is the point where all the SM fields are localized in the original model. The gravity lives in all the space. Solving the 5D Einstein's equations (in presence of negative vacuum energy in the bulk and fine-tuned vacuum energies on the branes) provides the metric of the space to be

$$ds^2 = e^{-2ky} g_{\mu\nu} dx^\mu dx^\nu - dy^2 \tag{4.50}$$

where k is the curvature of the space. This metric corresponds to a 5D AdS space. The factor e^{-ky} is called the "warp" factor and determines how 4D scales change as a function of the position in the extra dimension. In particular, this implies that energy scales for 4D fields localized at the boundary at $y = L$ are red-shifted by a factor e^{-kL} with respect to those localized at $y = 0$. A basic assumption of this model is that there are no large mass hierarchies present so that very roughly we expect that $k \sim M_\star$, the 5D fundamental or Planck scale. The low energy effective Planck scale M_P will be related to the fundamental gravity scale $M_\star$ by the relation

$$M_P = \frac{M_\star^3}{k}(1 - 2e^{-2\pi kL}) \tag{4.51}$$

The warp factor $e^{-\pi kL}$ is assumed to be a very small quantity which implies that M_P, $M_\star$ and k have essentially comparable magnitudes following from the assumption that no hierarchies exist. All dimensionfull parameters in the 5-dimensional action will have their mass scale set by $M_\star \sim M_P \sim k$ so that there is no fine-tuning. The warp factor however rescales them as one moves about in the y direction so that, in particular, all masses will appear to be of order the TeV scale on the SM brane. Note that if $kL \sim 11$ (a small hierarchy) this exponential suppression reduces a mass of order 10^{18} GeV to only 1 TeV. Thus the ratio of the weak scale

m_{ew} to M_P is explained through an exponential factor and no large ratios appear anywhere else in the model.

As the gravity can propagate in the bulk, then the graviton will be decomposed in KK modes. The zero-mode is localized on the UV-brane and its coupling to the SM particles is suppressed by $\frac{1}{M_P^2}$. The couplings of heavy KK gravitons with the IR-brane are however stronger and they could be produced in collider experiments in Drell-Yann processes. LHC experiments already constrain the mass of those modes to be at about TeV scale (57).

The simple RS model scenario has been extended in many ways to help with various model building efforts. A few possibilities that have been considered are for example the extensions to 3 or more branes (89) or extensions to 6 or more dimensions (54).

Models in which the SM gauge bosons propagate in TeV^{-1} sized extra dimensions give generically large corrections to electroweak observables. The warped models, where the 5D gauge coupling is large, the bounds give $m_{KK} >\sim 10$ TeV (77) or $m_{KK} >\sim 3$ TeV if a custodial symmetry is imposed (18).

The constraints on the RS type models are based on the searches of the decays of the lightest RS graviton into SM states. In the original RS model, where only graviton propagates in the bulk the current preliminary limits form LHC (2 fb^{-1} update of ATLAS) set the lower bound on the graviton mass $m_{grav} >1.95$ TeV (2). For much more exhaustive list of collider bounds on the extra-dimensional models we invite the reader to look at the PDG notes (72).

Part III

Study of the 6D Model on the Real Projective Plane

Chapter 5

General presentation of the model

5.1 Real projective plane - orbifold construction

In this section we first present the construction of the two-dimensional orbifold $\mathbb{R}P^2$ and then we summarize the Kaluza-Klein decomposition of quantum fields defined on the six-dimensional background $\mathcal{M}^4 \times RP^2$. We follow the work (51) where the model was introduced for the first time.

We will consider a quantum field theory defined on the d dimensional flat manifold which is chosen to be the direct product of the standard 4-dimensional Minkowski spacetime $\mathcal{M}^4$ and the $(d-4)$ -dimensional orbifold. Our aim is to consider orbifolds without fixed points. The fixed points are not dangerous by themselves, however, as in general they break the d-dimensional Lorentz invariance down to the 4-dimensional one, the predictivity of the theory defined on an orbifold with fixed points will be limited. This limitation arises from the fact that the divergences appearing when calculating loop corrections require counter-terms localized on these points. Furthermore, any symmetry associated with the geometry of the space, including the eventual KK-parity, will be broken by generic localized terms unless one imposes some *ad hoc* symmetry conditions relating the singularities. As the extra dimensional theories are appealing mainly because they provide a stable dark matter candidate we want the symmetry preserving the stability of the dark matter particle to be an inherent property of the space.

The other face of the coin is that the requirement of spaces having an exact KK parity is a very effective selection rule on the number of viable compact spaces. As it was pointed out in (51) there is a unique 2-dimensional orbifold, among the 17 non-equivalent orbifolds that can be defined on a 2-dimensional euclidean plane, that has no fixed points and such that massless chiral fermionic fields can be defined on it: the real projective plane.

5.1.1 Basic definitions

The real projective plane is a compact, non-orientable orbifold of Euler characteristic 1 without boundaries. Among all possible descriptions of the real projective plane that are topologically equivalent spaces, we choose the case of the flat metric. The spherical projective plane has been considered in (68), and it leads to a completely different phenomenology.

In our case the projective plane is described as a quotient space of a plane $\mathbb{R}^2$ modulo a discrete symmetry group Γ [1]

1. Recall that the structure of the group is entirely defined by the relations among the generators. The

$$\Gamma = \langle r, g | r^2 = (g^2 * r)^2 = \mathbb{I} \rangle \tag{5.1}$$

where r is the rotation of π around the origin of the coordinate system, and g is a glide-reflection.

$$r : \begin{cases} y_4 & \sim & r[y_4] = -y_4 \\ y_5 & \sim & r[y_5] = -y_5 \end{cases} \qquad g : \begin{cases} y_4 & \sim & g[y_4] = & y_4 + \pi R_4 \\ y_5 & \sim & g[y_5] = & -y_5 + \pi R_5 \end{cases} \tag{5.2}$$

One can imagine the fundamental domain of the real projective plane, obtained by applying the above identifications of points of $\mathbb{R}^2$, as a rectangle with sides of the length πR_4 and πR_5 and opposite boundaries identified in opposite directions as it was shown in the figure 4.3.

The corners of the rectangle are special points corresponding to conical singularities of the space where localized counter-terms emerge: in the fundamental space there are only two such points as facing corners are identified by the glide and therefore are identical points as shown in figure 5.1.

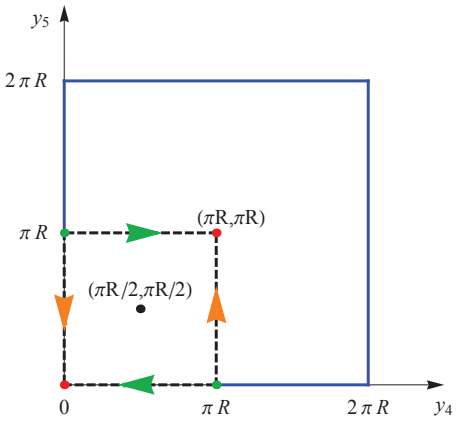

Figure 5.1: Fundamental domain of the real projective plane $\mathbb{R}^2/pgg$ (within black dashed lines). The identified pairs of singular points are marked by red and green dots. The center of the square (black dot) is the p_{KK} parity center.

Other symmetries of the plane that are combinations of g and r include two translations denoted as t_4, t_5 and another glide $g' = gr$ which is a product of a π-rotation r and the first glide g

$$g' = g * r : \begin{cases} y_4 & \sim & gr[y_4] = & -y_4 + \pi R_4 \\ y_5 & \sim & gr[y_5] = & y_5 + \pi R_5 \end{cases} \tag{5.3}$$

The translation symmetries that arise as combinations of g and r as:

$$t_4 = g^2 : \begin{cases} y_4 & \sim & t_4[y_4] = y_4 + 2\pi R_4 \\ y_5 & \sim & t_4[y_5] = y_5 \end{cases} \qquad t_5 = (g * r)^2 : \begin{cases} y_4 & \sim & t_5[y_4] = y_4 \\ y_5 & \sim & t_5[y_5] = y_5 + 2\pi R_5 \end{cases} \tag{5.4}$$

It is easy to see that this orbifold has no fixed points nor fixed lines. The opposite corners of the rectangle are identified by the glide: $(0,0) \sim (\pi R_4, \pi R_5)$ and $(0, \pi R_5) \sim (\pi R_4, 0)$.

particular representation of the generators, in terms of isometries acting on the plane is not necessary but helps in visualization.

$$(0,0) \xrightarrow{r} (0,0) \xrightarrow{g} (\pi R_4, \pi R_5) \tag{5.5}$$

$$(0,\pi R_5) \xrightarrow{[r,t_4]} (0,\pi R_5) \xrightarrow{[g,-t_4]} (\pi R_4, 0) \tag{5.6}$$

The fundamental space is invariant under a π rotation around the center of the fundamental domain $(\frac{\pi R_4}{2}, \frac{\pi R_5}{2})$, this symmetry maps the rectangle onto itself, including singular points and boundaries. In terms of the coordinates it can be written as

$$r' : \begin{cases} y_4 \to r'(y_4) = -y_4 + \pi R_4 \\ y_5 \to r'(y_5) = -y_5 + \pi R_5 \end{cases} . \tag{5.7}$$

As this symmetry changes sign to both coordinates, the components of 6-dimensional fermions with opposite chiralities will necessarily pick up opposite parity, therefore, this symmetry cannot be used as a parity defined on the KK fields. However, one can define an equivalent symmetry by combining it with the rotation in the orbifold symmetry group:

$$p_{KK} = r' * r : \begin{cases} y_4 & \sim & y_4 + \pi R_4 \\ y_5 & \sim & y_5 + \pi R_5 \end{cases} \tag{5.8}$$

It can be easily seen that all KK modes in the tier (k,l) will pick up the same phase $(-1)^{k+l}$ under the symmetry p_{KK}. Thus this is a perfect example of KK parity: states with $k+l$ odd will not be able to decay into SM states and the lightest one, belonging to the $(1,0)$ tier will be exactly stable.

If we assume that the lagrangians localized on the two singular points are identical then the fundamental domain also invariant under a mirror symmetry with respect to the axis $y_4 = \frac{\pi R_4}{2}$ which transforms the coordinates as

$$m_4 : \begin{cases} y_4 \to m_4(y_4) = -y_4 + \pi R_4 \\ y_5 \to m_4(y_5) = y_5 \end{cases} . \tag{5.9}$$

We can then define another KK parity by combining m_4 with the glide-rotation g':

$$p'_{KK} = m_4 * g' : \begin{cases} y_4 & \sim & y_4 + \pi R_4 \\ y_5 & \sim & y_5 \end{cases} \tag{5.10}$$

This is a good parity because all states in the tier (k,l) will pick up the same phase $(-1)^l$. If this parity were conserved, then transitions like $(0,1) \to (1,0)$ or $(1,1) \to (0,0)$ would be forbidden. p'_{KK} is also a relic of the Lorentz invariance in 6D as it is the case for p_{KK}. This means that processes that violates p'_{KK} can not be mediated by bulk loops, and only by the localized lagrangians.The main difference between the two KK parities is that the p'_{KK} can be broken by the UV completion on the boundaries. Thus we will not consider this parity as a fundamental symmetry of the orbifolds and we will assume it to be broken (51).

5.1.2 Localized terms on the $\mathbb{R}P^2$ and the KK parity

As we have seen, on the $\mathbb{R}P^2$ orbifold there are two pairs of identified points that form two conical singularities with the deficit angle π but where the metric is still finite. In general the

localized counterterm can be added on those singular points. Nevertheless, the KK parity is still preserved without any further assumptions. As the problem of localized operators is related to the fact that the fixed points of an orbifold are unrelated, on the $\mathbb{R}P^2$ the localized terms are identified by pairs as

$$\begin{array}{rcl} \mathcal{O}[0,0] & \equiv & \mathcal{O}[\pi R_4, \pi R_5] \\ \mathcal{O}[\pi R_4, 0] & \equiv & \mathcal{O}[0, \pi R_5] \end{array} \tag{5.11}$$

What is important to notice is that this symmetry is an intrinsic property of the orbifold and is not a consequence of an *ad-hoc* symmetry of the UV completion of the theory as it happens in other orbifolds, like a chiral square (47).

The KK states (k, l) of the quantum fields when transformed by the KK symmetry p_{KK} pick a phase $(-1)^{k+l}$. Therefore the $(1, 0)$ and $(0, 1)$ states will be the lightest tiers of odd particles and thus will provide a stable dark matter candidate. The next heavier tiers $(1, 1)$ and $(2, 0)$ will decay into Standard Model particles via localized interactions. This fact is well known in supersymmetry for example, where an analogue of KK parity is the R parity, and implies that the interactions between the KK states must be invariant under p_{KK}.

Although, if p'_{KK} is not broken there are several important consequences. The two states $(1, 0)$ and $(0, 1)$ would have different parities and there would be two independent dark matter candidates. The $(1, 1)$ state would be odd and stable under this symmetry as well.

5.2 Quantum Fields on the real projective plane

So we construct the space-time $\mathcal{M}^4 \times \mathbb{R}P^2$ with the flat metric $g^{MN} = diag(1,-1,-1,-1,-1,-1)$ with no fixed points. KK parity preserving the stability of the dark matter particle will be automatically preserved as it was shown in (51). In what follows we denote x^μ the coordinates of $\mathcal{M}^4$ with $\mu \in \{0,1,2,3\}$ and y^α the coordinates on the orbifold $\alpha \in \{4,5\}$. When needed we note a vector $\vec{y} = (y_4, y_5)$. The capital letters of the alphabet run over all the coordinates of the six-dimensional space, $M, N \in \{0,1,2,3,4,5\}$.

To simplify the notation we set $R_4 = R_5 = 1$. We introduce the fields defined in six dimensions: a scalar field $\Phi(x^\mu, y^\alpha)$, a gauge field $A_M(x^\mu, y^\alpha)$ and a spinor $\Psi(x^\mu, y^\alpha)$. For every transformation of the space, namely the rotation r and the glide g in our case, corresponds a transformation in the quantum field space.

$$X(r(y^\alpha)) = p_r \mathcal{R} X(y^\alpha) \qquad \text{and} \quad X(g(y^\alpha)) \to p_g \mathcal{G} X(y^\alpha)\,, \tag{5.12}$$

where $\mathcal{R}$ and $\mathcal{G}$ are the transformation operators in the adequate spin representation and X stands for any quantum field $X \in \{\Phi, \Psi, A\}$. We require the six-dimensional action to be invariant under these transformations. As it can easily be shown (see (104) for the scalar case, and (51) for fermions and gauge bosons), the possible parities of the fields under the rotation and glide-reflection are $(p_r, p_g) = (\pm, \pm)$ respectively. Thus every field will be characterized by a pair (p_r, p_g). The general important point is that the real projective plane has no boundaries. Therefore the variation of the action that leads to equations of motion for any quantum field defined on this orbifold will contain only the volume integral (assuming that the variation of fields for $x^\mu \to \infty$ is zero) and we do not have any boundary conditions to impose on the fields, which simplifies a lot following the calculations of loop corrections. We can thus decompose each field in KK modes as on the torus, where the wave functions are combinations of sine and cosine functions of the extra coordinates, and then impose the orbifold projection on each field.

5.2.1 Scalar field

The 6D action of the a complex scalar field $\Phi(x^\mu, y^\alpha)$ of mass M_Φ coupled to a SU(N) gauge boson A_M in representation r is written as

$$S_\Phi^{6D} = \int d^4x^\mu \int_0^{2\pi} dy^4 dy^5 \left[D_M \Phi^\dagger D^M \Phi - M_\Phi^2 \Phi^\dagger \Phi \right] \tag{5.13}$$

with $D_M = \partial_M - igA_M^a t_r^a$ the covariant derivative. The field is decomposed into Kaluza-Klein states labeled by a pair of non-negative numbers [2] (k,l), $k,l \geq 0$

$$\Phi(x^\mu, y^\alpha) = \sum_{k,l \geq 0} \phi^{(k,l)}(x^\mu) f_{k,l}(y^\alpha) \tag{5.14}$$

Solving the equation of motion obtained by requirement $\delta S = 0$ one finds the mass spectrum of the Kaluza-Klein tower associated to the complex scalar field $\Phi(x^\mu, y^\alpha)$ at tree level :

2. In general the sum over KK states should run over the full range $-\infty < k,l < +\infty$. One can refer to (104) to see that the transformation properties of the functions $f_{k,l}(y^\alpha) \sim exp\,(2\pi i(ky_4 + ly_5))$ allows us to restrict the labels k,l to non-negative numbers only.

$$\left(-\partial_4^2 - \partial_5^2 + M_\Phi^2\right) f_{k,l}(y^\alpha) = M_{k,l}^2 f_{k,l}(y^\alpha) = \left(m_{k,l}^2 + M_\Phi^2\right) f_{k,l}(y^\alpha) \tag{5.15}$$

with

$$m_{k,l}^2 = k^2 + l^2 \tag{5.16}$$

The basis functions $f_{kl}(y^\alpha)$ are labeled by a pair of non-negative numbers (k,l), $k,l \geq 0$. As the functions $f_{k,l}$ are found by solving the above equation and then imposing the parities (p_r, p_g), thus there are four possible solutions with different parities (51):

$$\begin{aligned}\Phi^{(++)}(x^\mu, y^\alpha) &= \tfrac{1}{2\pi}\phi^{(0,0)}(x^\mu) + \tfrac{1}{\sqrt{2}\pi}\textstyle\sum_{k=1}^{\infty}\left[\cos(2ky_4)\ \phi^{(2k,0)}(x^\mu) + \cos(2ky_5)\ \phi^{(0,2k)}(x^\mu)\right] \\ &+ \tfrac{1}{\pi}\textstyle\sum_{k,l>0}\left[\cos(ky_4)\ \cos(ly_5)\ \phi^{(k,l)}_{k+l=2m}(x^\mu) + \sin(ky_4)\ \sin(ly_5)\ \phi^{(k,l)}_{k+l=2m+1}(x^\mu)\right]\end{aligned} \tag{5.17}$$

$$\begin{aligned}\Phi_\mu^{(+,-)}(x^\mu, y^\alpha) &= \tfrac{1}{\sqrt{2}\pi}\textstyle\sum_{k=1}^{\infty}\left[\cos((2k-1)y_4)\phi_\mu^{(2k-1,0)} + \cos((2k-1)y_5)\phi_\mu^{(0,2k-1)}\right] \\ &+ \tfrac{1}{\pi}\textstyle\sum_{k,l=1}^{\infty}\left[\sin(ky_4)\sin(ly_5)\phi^{(k,l)}_{\mu\ (k+l=2m)} + \cos(ky_4)\cos(ly_5)\phi^{(k,l)}_{\mu\ (k+l=2m+1)}\right]\end{aligned} \tag{5.18}$$

$$\begin{aligned}\Phi_\mu^{(-,+)}(x^\mu, y^\alpha) &= \tfrac{1}{\sqrt{2}\pi}\textstyle\sum_{k=1}^{\infty}\left[\sin(2ky_4)\phi_\mu^{(2k,0)} + \sin((2k-1)y_5)\phi_\mu^{(0,2k-1)}\right] \\ &+ \tfrac{1}{\pi}\textstyle\sum_{k,l=1}^{\infty}\left[\sin(ky_4)\cos(ly_5)\phi^{(k,l)}_{\mu\ (k+l=2m)} + \cos(ky_4)\sin(ly_5)\phi^{(k,l)}_{\mu\ (k+l=2m+1)}\right]\end{aligned} \tag{5.19}$$

$$\begin{aligned}\Phi_\mu^{(-,-)}(x^\mu, y^\alpha) &= \tfrac{1}{\sqrt{2}\pi}\textstyle\sum_{k=1}^{\infty}\left[\sin((2k-1)y_4)\phi_\mu^{(2k-1,0)} + \sin(2ky_5)\phi_\mu^{(0,2k)}\right] \\ &+ \tfrac{1}{\pi}\textstyle\sum_{k,l=1}^{\infty}\left[\cos(ky_4)\sin(ly_5)\phi^{(k,l)}_{\mu\ (k+l=2m)} + \sin(ky_4)\cos(ly_5)\phi^{(k,l)}_{\mu\ (k+l=2m+1)}\right]\end{aligned} \tag{5.20}$$

At tree level the masses of the modes $\phi^{(k,l)}$ are given by the usual relation

$$m_{kl}^2 = M_\Phi^2 + k^2 + l^2 \tag{5.21}$$

where M_Φ is identified with the Standard Model mass of the particle. The only case with a zero mode is $(+,+)$, therefore a model with bulk higgs must have such a parity in order to include a higgs boson in the zero mode spectrum.

5.2.2 Gauge field

We introduce a gauge field $A_M(x^\mu, y^\alpha) = \{A_\mu(x^\mu, y^\alpha), A_\alpha(x^\mu, y^\alpha)\}$ corresponding to a non-Abelian gauge group SU(N). The 6D action for this fields reads

$$S^{6D}_{gauge} = \int d^4x^\mu \int_0^{2\pi} dy^4 dy^5 \left[-\frac{1}{4} F^a_{MN} F^{a\,MN} - \frac{1}{2\xi} \left(\partial_\mu A^{a\,\mu} - \xi(\partial_4 A^a_4 + \partial_5 A^a_5) \right)^2 \right] \tag{5.22}$$

where $F^a_{MN} = \partial_M A^a_N - \partial_N A^a_M + g f^{abc} A^b_M A^b_N$ is a field strength and the second term under the integral, the gauge fixing term, is introduced in order to remove the mixings between the components A_μ and $A_{4,5}$.

The equations of motion lead to the solutions for $A_\mu(x^\mu, y^\alpha)$ of the same form as for the scalar case if we decompose the $A_\mu(x^\mu, y^\alpha)$ field as

$$A_\mu(x^\mu, y^\alpha) = \sum_{k,l \geq 0} \tilde{A}^{(k,l)}_\mu(x^\mu) f_{k,l}(y^\alpha) \tag{5.23}$$

Then, the equation of motion for the vector component $A_\mu(x^\nu, y_4, y_5)$ will take the following form:

$$-\partial^\mu F_{\mu\nu} - \frac{1}{\xi} \partial_\nu \partial^\mu A_\mu + (\partial_4^2 + \partial_5^2) A_\nu = 0 \tag{5.24}$$

The general solution of the above equation is a linear combination of double products sines and cosines as for the scalar case. At this point we have to impose the parities (p_g, p_r) on the field $A_\mu(x^\nu, y_4, y_5)$. For the four possible choices of parities of the 4D-vector component A_μ: $(p_g, p_r) = (+,+),\ (+,-),\ (-,+),\ (-,-)$, the solutions will have exactly the same form as for the scalar field Φ given in equations 5.17-5.20.

Scalar components A_4 and A_5 Now we turn to the scalar components A_4 and A_5. As it was in the 5D case, the massive vector modes will get the longitudinal polarization by eating the tower of states constructed as a linear combination of A_4 and A_5. The second linear combination will correspond to a physical scalar states (52).

The parities of the scalar components A_4 and A_5 are determined by the fact that they are parts of a 6D vector field A_M which has to transform under the defining parities of the real projective plane as

$$A_M(x^\mu, g[(y_4, y_5)]) = \begin{cases} p_g A_\mu(x^\mu, y_4, y_5) \\ p_g A_4(x^\mu, y_4, y_5) \\ -p_g A_5(x^\mu, y_4, y_5) \end{cases} \qquad A_M(x^\mu, r[(y_4, y_5)]) = \begin{cases} p_r A_\mu(x^\mu, y_4, y_5) \\ -p_r A_4(x^\mu, y_4, y_5) \\ -p_r A_5(x^\mu, y_4, y_5) \end{cases} \tag{5.25}$$

Thus, for a gauge fields A_M once we assigns parities for the vector component A_μ as (p_g, p_r) the parities of A_4 and A_5 are determined to be $(p_g, -p_r)$ and $(-p_g, -p_r)$ respectively.

The equations of motion for A_4 and A_5 fields are non-diagonal:

$$\begin{cases} -\partial_\mu^2 A_4 + \xi \partial_4(\partial_4 A_4 + \partial_5 A_5) + \partial_5(\partial_5 A_4 - \partial_4 A_5) &= 0 \\ -\partial_\mu^2 A_5 + \xi \partial_5(\partial_4 A_4 + \partial_5 A_5) - \partial_4(\partial_5 A_4 - \partial_4 A_5) &= 0 \end{cases} \tag{5.26}$$

We can consider several gauge choices.

Feynman-'t Hooft gauge $\xi = 1$: In the Feynman-'t Hooft gauge, with $\xi = 1$, the equations of motion for A_4 and A_5 decouple giving

$$(\partial_4^2 + \partial_5^2 - \partial_\mu^2)A_{4/5} = 0 \tag{5.27}$$

Thus, the two scalar components are independent and we can proceed as in the scalar case. The wave-functions $f_n(y_4, y_5)$ and masses m_n will be the same as for the real scalar field given by equations 5.17-5.20 and 5.16.

Unitary gauge $\xi \to \infty$: In the unitary gauge $\xi \to \infty$ we must have

$$\partial_4 A_4 + \partial_5 A_5 = 0 \tag{5.28}$$

The two fields are not independent and we can expand them on the same basis of 4D fields $A_0^{(k,l)}$

$$A_{4/5}(x_\mu, y_\alpha) = \sum_{k,l=0}^{\infty} f_{k,l}^{4/5}(y_\alpha) A_0^{(k,l)}(x^\mu) \qquad \text{with} \qquad \partial_4 f_{k,l}^4 + \partial_5 f_{k,l}^5 = 0 \tag{5.29}$$

Plugging the above relation into the equation of motion 5.26 one finds that the two functions f_4 and f_5 respect the equation of motion of the scalar field

$$(\partial_\mu^2 - \partial_4^2 - \partial_5^2) f_{k,l}^{4/5} = 0 \tag{5.30}$$

Therefore the spectra of $f_{k,l}^{4/5}$ are again the same as for a scalar field but with the additional condition eq. 5.29. In the following tables 5.1 - 5.4 we summarize the normalized wave-functions in the unitary gauge for the components of a 6D gauge field A_M (51).

(k,l)	$A_\mu^{(+,+)}$	$A_4^{(-,+)}$	$A_5^{(-,-)}$
$(0,0)$	$\frac{1}{2\pi}$		
$(0,2l)$	$\frac{1}{\sqrt{2\pi^2}} \cos 2ly_5$		
$(0,2l-1)$		$\frac{1}{\sqrt{2\pi^2}} \sin(2l-1)y_5$	
$(2k,0)$	$\frac{1}{\sqrt{2\pi^2}} \cos 2ky_4$		
$(2k-1,0)$			$\frac{1}{\sqrt{2\pi^2}} \sin(2k-1)y_4$
$(k,l)_{k+l\ even}$	$\frac{1}{\pi} \cos ky_4 \cos ly_5$	$\frac{l}{\pi\sqrt{k^2+l^2}} \sin ky_4 \cos ly_5$	$-\frac{k}{\pi\sqrt{k^2+l^2}} \cos ky_4 \sin ly_5$
$(k,l)_{k+l\ odd}$	$\frac{1}{\pi} \sin ky_4 \sin ly_5$	$\frac{l}{\pi\sqrt{k^2+l^2}} \cos ky_4 \sin ly_5$	$-\frac{k}{\pi\sqrt{k^2+l^2}} \sin ky_4 \cos ly_5$

Table 5.1: Normalized wave functions for a $(+,+)$ gauge boson in unitary gauge

(k,l)	$A_\mu^{(+,-)}$	$A_4^{(-,-)}$	$A_5^{(-,+)}$
$(0,0)$			
$(0,2l)$		$\frac{1}{\sqrt{2\pi^2}}\sin 2ly_5$	
$(0,2l-1)$	$\frac{1}{\sqrt{2\pi^2}}\cos(2l-1)y_5$		
$(2k,0)$			$\frac{1}{\sqrt{2\pi^2}}\sin 2ky_4$
$(2k-1,0)$			$\frac{1}{\sqrt{2\pi^2}}\cos(2k-1)y_4$
$(k,l)_{k+l\ even}$	$\frac{1}{\pi}\sin ky_4\sin ly_5$	$\frac{l}{\pi\sqrt{k^2+l^2}}\cos ky_4\sin ly_5$	$-\frac{k}{\pi\sqrt{k^2+l^2}}\sin ky_4\cos ly_5$
$(k,l)_{k+l\ odd}$	$\frac{1}{\pi}\cos ky_4\cos ly_5$	$\frac{l}{\pi\sqrt{k^2+l^2}}\sin ky_4\cos ly_5$	$-\frac{k}{\pi\sqrt{k^2+l^2}}\cos ky_4\sin ly_5$

Table 5.2: Normalized wave functions for a $(+,-)$ gauge boson in unitary gauge

(k,l)	$A_\mu^{(-,+)}$	$A_4^{(+,+)}$	$A_5^{(+,-)}$
$(0,0)$		$\frac{1}{2\pi}$	
$(0,2l)$		$\frac{1}{\sqrt{2\pi^2}}\cos 2ly_5$	
$(0,2l-1)$	$\frac{1}{\sqrt{2\pi^2}}\sin(2l-1)y_5$		
$(2k,0)$	$\frac{1}{\sqrt{2\pi^2}}\sin 2ky_4$		
$(2k-1,0)$			$\frac{1}{\sqrt{2\pi^2}}\cos(2k-1)y_4$
$(k,l)_{k+l\ even}$	$\frac{1}{\pi}\sin ky_4\cos ly_5$	$\frac{l}{\pi\sqrt{k^2+l^2}}\cos ky_4\cos ly_5$	$-\frac{k}{\pi\sqrt{k^2+l^2}}\sin ky_4\sin ly_5$
$(k,l)_{k+l\ odd}$	$\frac{1}{\pi}\cos ky_4\sin ly_5$	$\frac{l}{\pi\sqrt{k^2+l^2}}\sin ky_4\sin ly_5$	$-\frac{k}{\pi\sqrt{k^2+l^2}}\cos ky_4\cos ly_5$

Table 5.3: Normalized wave functions for a $(-,+)$ gauge boson in unitary gauge

Generic ξ gauge: It was also shown in (52) that in order to compute the radiative corrections to the three-point functions one needs to consider a generic ξ gauge. In this case the $A_4(x^M)$ and $A_5(x^M)$ are not the eigenstates of the bilinear term

$$\mathcal{L}_{A_4,A_5} = \int dx^4 dx^5 \frac{1}{2}(A_4, A_5) \begin{pmatrix} -\partial_\mu^2 + \xi\partial_4^2 + \partial_5^2 & (\xi-1)\partial_4\partial_5 \\ (\xi-1)\partial_4\partial_5 & -\partial_\mu^2 + \partial_4^2 + \xi\partial_5^2 \end{pmatrix} \cdot \begin{pmatrix} A_4 \\ A_5 \end{pmatrix} \tag{5.31}$$

One has first expand the $A_4(x^M)$ and $A_5(x^M)$ fields into KK modes and then diagonalize the kinetic part of lagrangian term by term. The eigenstates one finds in this case, $A_\pi^{(k,l)}$ and $A_\phi^{(k,l)}$, are related to the $A_{4/5}$ fields by the following relations

$$A_4^{(k,l)} = \frac{l}{m_{kl}} A_\phi^{(k,l)} + \frac{k}{m_{kl}} A_\pi^{(k,l)} \tag{5.32}$$

(k,l)	$A_\mu^{(-,-)}$	$A_4^{(+,-)}$	$A_5^{(+,+)}$
$(0,0)$			$\frac{1}{2\pi}$
$(0,2l)$	$\frac{1}{\sqrt{2\pi^2}}\sin 2ly_5$		
$(0,2l-1)$		$\frac{1}{\sqrt{2\pi^2}}\cos(2l-1)y_5$	
$(2k,0)$			$\frac{1}{\sqrt{2\pi^2}}\cos 2ky_4$
$(2k-1,0)$	$\frac{1}{\sqrt{2\pi^2}}\sin(2k-1)y_4$		
$(k,l)_{k+l\ even}$	$\frac{1}{\pi}\cos ky_4 \sin ly_5$	$\frac{l}{\pi\sqrt{k^2+l^2}}\sin ky_4 \sin ly_5$	$-\frac{k}{\pi\sqrt{k^2+l^2}}\cos ky_4 \cos ly_5$
$(k,l)_{k+l\ odd}$	$\frac{1}{\pi}\sin ky_4 \cos ly_5$	$\frac{l}{\pi\sqrt{k^2+l^2}}\cos ky_4 \cos ly_5$	$-\frac{k}{\pi\sqrt{k^2+l^2}}\sin ky_4 \sin ly_5$

Table 5.4: Normalized wave functions for a $(-,-)$ gauge boson in unitary gauge

$$A_5^{(k,l)} = \frac{k}{m_{kl}} A_\phi^{(k,l)} + \frac{l}{m_{kl}} A_\pi^{(k,l)} \tag{5.33}$$

The $A_\pi^{(k,l)}$ field correspond to the Goldstone boson with the ξ-dependent mass $m_\pi^{k,l}2 = \xi m_{k,l}^2$ which will be eaten in the unitary gauge by the massive gauge boson. The $A_\phi^{(k,l)}$ field in turn is the new physical degree of freedom. If we consider a $(+,+)$ gauge boson A_M then, for $(k,0)$ and $(0,k)$ modes, the physical scalar is present only for k odd and no vector state is allowed. For k even the Goldstone and the vector fields are present. For the $(0,0)$ mode, only the massless vector part is allowed.

5.2.3 Spinorial field

Clifford Algebra in 6 dimensions

In six dimensions the simplest representation of the Clifford algebra $\{\gamma^M, \gamma^N\} = 2\eta^{MN}$ with $\eta^{MN} = diag(1,-1,\ldots,-1)$ are 8×8 gamma matrices Γ^M. In the Weyl representation they can be written as

$$\Gamma^\mu = \gamma^\mu \otimes \sigma^0, \qquad \Gamma_4 = i\gamma^5 \otimes \sigma^1, \qquad \Gamma_5 = i\gamma^5 \otimes \sigma^2 \tag{5.34}$$

with γ^μ, γ^5 the standard 4×4 Dirac matrices that we chose in Weyl basis, and σ^μ the Pauli 2×2 matrices. We also define the 6D chirality operators $P_\pm$ as

$$P_\pm = \frac{1}{2}(1+\Gamma^6) \qquad \text{with} \qquad \Gamma^6 = -\gamma^5 \otimes \sigma^3 \tag{5.35}$$

and the 4D chirality operators are given by

$$P_{R/L} = \frac{1}{2}(1\pm\gamma^5)\otimes\sigma^0 \tag{5.36}$$

A spinorial field is then written as $\Psi^{6D}(x^\mu, y^\alpha) = (\chi_+, \bar{\eta}_-, \chi_-, \bar{\eta}_+)$ where $\chi_\pm, \bar{\eta}_\pm$ are two-component Weyl spinors, left-handed and right-handed respectively. The $\pm$ indices label the eigenstates of chirality operators in six dimensions $P_\pm$:

$$P_+\Psi^{6D} = \begin{pmatrix} \chi_+ \\ 0 \\ 0 \\ \bar{\eta}_+ \end{pmatrix} \qquad P_-\Psi^{6D} = \begin{pmatrix} 0 \\ \bar{\eta}_- \\ \chi_- \\ 0 \end{pmatrix} \tag{5.37}$$

$$P_R\Psi^{6D} = \begin{pmatrix} 0 \\ \bar{\eta}_- \\ 0 \\ \bar{\eta}_+ \end{pmatrix} \qquad P_L\Psi^{6D} = \begin{pmatrix} \chi_+ \\ 0 \\ \chi_- \\ 0 \end{pmatrix} \tag{5.38}$$

6D action for fermion Ψ^{6D} and KK decomposition

As we have seen in 4.2, the 4D chirality of the fundamental mode is not an evident problem on the orbifolds. On the real projective plane the left- and right- handedness is ensured by the rotation parity (51). Starting from the standard action for a free fermionic field Ψ^{6D} as follows:

$$\begin{aligned} S &= \int d^4x dy_4 dy_5 \; i\bar{\Psi}^{6D}\Gamma^\alpha \partial_\alpha \Psi^{6D} \\ &= \int d^4x dy_4 dy_5 i\bar{\chi}_\pm \bar{\sigma}^\mu \partial_\mu \chi_\pm + i\eta_\pm \sigma^\mu \partial_\mu \bar{\eta}_\pm + \bar{\chi}_\pm(\partial_4 \mp i\partial_5)\bar{\eta}_\pm - \eta_\pm(\partial_4 \pm i\partial_5)\chi_\pm \end{aligned} \tag{5.39}$$

we find the equations of motion for the Weyl components

$$\begin{aligned} i\bar{\sigma}^\mu \partial_\mu \chi_\pm + (\partial_4 \mp \partial_5)\bar{\eta}_\pm = 0 \\ i\sigma^\mu \partial_\mu \bar{\eta}_\pm - (\partial_4 \pm \partial_5)\chi_\pm = 0 \end{aligned} \tag{5.40}$$

As usual we decompose the fields into the KK towers

$$\Psi^{6D}(x^M) = \begin{pmatrix} \chi_+ \\ \bar{\eta}_- \\ \chi_- \\ \bar{\eta}_+ \end{pmatrix} = \begin{pmatrix} \chi_+ = \sum_{k,l} f^1_{k,l}(y_4, y_5)\chi^{(k,l)}(x^\mu) \\ \bar{\eta}_- = \sum_{k,l} f^2_{k,l}(y_4, y_5)\bar{\eta}^{(k,l)}(x^\mu) \\ \chi_- = \sum_{k,l} f^3_{k,l}(y_4, y_5)\chi^{(k,l)}(x^\mu) \\ \bar{\eta}_+ = \sum_{k,l} f^4_{k,l}(y_4, y_5)\bar{\eta}^{(k,l)}(x^\mu) \end{pmatrix} \tag{5.41}$$

The 4D Dirac fermion at each KK level will be formed by the two components of the 6D fermion as:

$$\Psi^{4D}_{(k,l)} \sim \begin{pmatrix} \chi^{(k,l)} \\ \bar{\eta}^{(k,l)} \end{pmatrix} \tag{5.42}$$

Inserting this decomposition into the equation 5.40 we get

$$\begin{cases} i\,\bar{\sigma}^\mu \partial_\mu \chi - m_{kl}\bar{\eta} &= 0 \\ i\,\sigma^\mu \partial_\mu \bar{\eta} - m_{kl}\chi &= 0 \end{cases} \qquad \begin{cases} (\partial_4 \mp i\partial_5) f^{1/2}_{k,l} &= -m_{kl} f^{4/3}_{k,l} \\ (\partial_4 \pm i\partial_5) f^{4/3}_{k,l} &= m_{kl} f^{1/2}_{k,l} \end{cases} \tag{5.43}$$

In order to define chiral zero modes we need to have a possibility of imposing such a parities (p_g, p_r) to achieve

$$\Psi_L^{4D\ (0,0)} \sim \begin{pmatrix} \chi^{(0,0)} \\ 0 \end{pmatrix} \qquad \Psi_R^{4D\ (0,0)} \sim \begin{pmatrix} 0 \\ \bar{\eta}^{(0,0)} \end{pmatrix} \tag{5.44}$$

Chiralities of zero modes

At this stage we have to impose the parities under the glide and rotation to the fields χ and η. We can easily see that the requirement of the invariance of the 6D lagrangian 5.39 under the glide and rotation gives the conditions on the transformations of χ and η. The glide changes the sign of y_5, therefore looking at the terms with ∂_5 we deduce that the spinor Ψ^{6D} should transform as follows:

$$\begin{gathered} \mathcal{L}^{6D}[\Psi^{6D}(g[x^M])] \equiv \mathcal{L}^{6D}[\Psi^{6D}(x^M)] \\ \Downarrow \\ \Psi^{6D}(g[x^M]) = \Gamma_g \Psi^{6D}(x^M) \end{gathered} \tag{5.45}$$

where the transformation matrix Γ_g is given by

$$\Gamma_g = p_g \Gamma^5 \Gamma^6 = p_g \begin{pmatrix} 0 & 1 \\ 1 & 0 \end{pmatrix} \tag{5.46}$$

The Γ_g simply exchanges the $\pm$ components:

$$\Gamma_g \Psi^{6D} = p_g \begin{pmatrix} \chi_- \\ \bar{\eta}_+ \\ \chi_+ \\ \bar{\eta}_- \end{pmatrix} \tag{5.47}$$

As the right- and left-handed components of the $6D$ fermion transform equivalently under the glide transformation we can not define chiral zero modes by modding out one of the component. The rotation transformation changes the sign of both components $x_{4/5}$, therefore the invariance of the lagrangian will require that

$$\begin{gathered} \mathcal{L}^{6D}[\Psi^{6D}(r[x^M])] \equiv \mathcal{L}^{6D}[\Psi^{6D}(x^M)] \\ \Downarrow \\ \Psi^{6D}(r[x^M]) = p_r \Gamma_r \Psi^{6D}(x^M) \end{gathered} \tag{5.48}$$

where the transformation matrix Γ_r is given by

$$\Gamma_r = i\Gamma^4\Gamma^5\Gamma^6 = \begin{pmatrix} -\gamma^5 & 0 \\ 0 & -\gamma^5 \end{pmatrix} \tag{5.49}$$

which in terms of Weyl component means that $\bar{\eta}$ and χ have opposite sign under the rotation transformation:

$$\Gamma_r \Psi^{6D} = \begin{pmatrix} \chi_+ \\ -\bar{\eta}_- \\ \chi_- \\ -\bar{\eta}_+ \end{pmatrix} \tag{5.50}$$

This property allows us to define chiral modes. If we chose $p_r = +1$ the corresponding zero mode will be left-handed. $p_r = -1$ corresponds to the right-handed zero mode. This intrinsic

geometrical property makes of the real projective plane a unique 2-dimensional non-orientable orbifold without fixed points which the chiral zero KK modes can be defined on.

Solutions of the equations of motion

The solutions of the equations of motion eq. 5.40 $f^{1,2,3,4}$ are found by imposing the parities (p_g, p_r). The exact form of solutions were found in (51). The general form of the solution has the usual form of products of sines and cosines

$$\begin{aligned} f^{(k,l)}_{R/L\pm} &\sim A_1 \sin(ky_4)\sin(ly_5) + A_2 \sin(ky_4)\cos(ly_5) \\ &+ A_3 \cos(ky_4)\sin(ly_5) + A_4 \cos(ky_4)\cos(ly_5) \end{aligned} \tag{5.51}$$

After imposing the parities (p_g, p_r) one finds the exact form of $\Psi^{(k,l)}_{(+p_g)}$ with the parity $p_r = +1$, corresponding to the left-handed zero mode and of $\Psi^{(k,l)}_{(-p_g)}$ with the parity $p_r = -1$ corresponding to the right-handed zero mode. Following (51) the solutions normalized in such a way that $m_{(k,l)} = \sqrt{k^2 + l^2} \in \mathbb{R}$ are

$$\Psi^{(0,0)}_{(+p_g)} = \begin{pmatrix} \frac{1}{\sqrt{2\pi}}\chi^{(0,0)}_4 \\ 0 \\ \frac{1}{\sqrt{2\pi}}\chi^{(0,0)}_4 \\ 0 \end{pmatrix} \qquad \Psi^{(0,0)}_{(-p_g)} = \begin{pmatrix} 0 \\ \frac{1}{\sqrt{2\pi}}\bar{\eta}^{(0,0)}_4 \\ 0 \\ \frac{1}{\sqrt{2\pi}}\bar{\eta}^{(0,0)}_4 \end{pmatrix}$$

$$\Psi^{(0,l)}_{(+p_g)} = \begin{pmatrix} \frac{1}{2\pi}\cos(ly_5)\,\chi^{(0,l)}_4 \\ p_g\frac{i(-1)^l}{2\pi}\sin(ly_5)\,\bar{\eta}^{(0,l)}_4 \\ p_g\frac{(-1)^l}{2\pi}\cos(ly_5)\,\chi^{(0,l)}_4 \\ \frac{-i}{2\pi}\sin(ly_5)\,\bar{\eta}^{(0,l)}_4 \end{pmatrix} \qquad \Psi^{(0,l)}_{(-p_g)} = \begin{pmatrix} \frac{-i}{2\pi}\sin(ly_5)\,\chi^{(0,l)}_4 \\ p_g\frac{(-1)^l}{2\pi}\cos(ly_5)\,\bar{\eta}^{(0,l)}_4 \\ p_g\frac{i(-1)^l}{2\pi}\sin(ly_5)\,\chi^{(0,l)}_4 \\ \frac{1}{2\pi}\cos(ly_5)\,\bar{\eta}^{(0,l)}_4 \end{pmatrix}$$

$$\Psi^{(k,0)}_{(+p_g)} = \begin{pmatrix} \frac{1}{2\pi}\cos(ky_4)\,\chi^{(k,0)}_4 \\ -p_g\frac{i(-1)^k}{2\pi}\sin(ky_4)\,\bar{\eta}^{(k,0)}_4 \\ p_g\frac{(-1)^k}{2\pi}\cos(ky_4)\,\chi^{(k,0)}_4 \\ \frac{-1}{2\pi}\sin(ky_4)\,\bar{\eta}^{(k,0)}_4 \end{pmatrix} \qquad \Psi^{(k,0)}_{(-p_g)} = \begin{pmatrix} \frac{-i}{2\pi}\sin(ly_4)\,\chi^{(0,l)}_4 \\ p_g\frac{(-1)^l}{2\pi}\cos(ly_4)\,\bar{\eta}^{(0,l)}_4 \\ p_g\frac{i(-1)^l}{2\pi}\sin(ly_4)\,\chi^{(0,l)}_4 \\ \frac{1}{2\pi}\cos(ly_4)\,\bar{\eta}^{(0,l)}_4 \end{pmatrix} \tag{5.52}$$

$$\Psi^{(k,l)}_{(+p_g)} = \begin{pmatrix} (a_+\cos(ky_4)\cos(ly_5) + b_+\sin(ky_4)\sin(ly_5))\,\chi^{(k,l)}_4 \\ p_g(-1)^{k+l}\,(c_+\sin(ky_4)\cos(ly_5) - d_+\cos(ky_4)\sin(ly_5))\,\bar{\eta}^{(k,l)}_4 \\ p_g(-1)^{k+l}\,(a_+\cos(ky_4)\cos(ly_5) - b_+\sin(ky_4)\sin(ly_5))\,\chi^{(k,l)}_4 \\ (c_+\sin(ky_4)\cos(ly_5) + d_+\cos(ky_4)\sin(ly_5))\,\bar{\eta}^{(k,0)}_4 \end{pmatrix} \tag{5.53}$$

$$\Psi^{(k,l)}_{(-p_g)} = \begin{pmatrix} (a_- \ \sin(ky_4) \ \cos(ly_5) & + & b_- \ \cos(ky_4) \ \sin(ly_5)) \ \chi_4^{(k,l)} \\ p_g(-1)^{k+l} \ (c_- \ \cos(ky_4) \ \cos(ly_5) & - & d_- \ \sin(ky_4) \ \sin(ly_5)) \ \bar{\eta}_4^{(k,l)} \\ p_g(-1)^{k+l} \ (a_- \ \sin(ky_4) \ \cos(ly_5) & - & b_- \ \cos(ky_4) \ \sin(ly_5)) \ \chi_4^{(k,l)} \\ (c_- \ \cos(ky_4) \ \cos(ly_5) & + & d_- \ \sin(ky_4) \ \sin(ly_5)) \ \bar{\eta}_4^{(k,l)} \end{pmatrix} \tag{5.54}$$

where the normalization constants are defined as:

$$a_+ = \tfrac{\cos\,\alpha}{\sqrt{2}\pi} \qquad c_+ = -\frac{k\cos\,\alpha - il\ \sin\,\alpha}{\sqrt{2}\pi\,\sqrt{(k^2+l^2)}} \tag{5.55}$$

$$b_+ = \tfrac{\sin\,\alpha}{\sqrt{2}\pi} \qquad d_+ = \frac{k\sin\,\alpha - il\ \cos\,\alpha}{\sqrt{2}\pi\,\sqrt{(k^2+l^2)}} \tag{5.56}$$

$$a_- = \tfrac{k\ \cos\,\alpha + il\ \sin\,\alpha}{\sqrt{2}\pi\,\sqrt{(k^2+l^2)}} \qquad c_- = \frac{\cos\,\alpha}{\sqrt{2}\pi} \tag{5.57}$$

$$b_- = -\tfrac{k\ \sin(\alpha + il\ \cos\,\alpha}{\sqrt{2}\pi\,\sqrt{(k^2+l^2)}} \qquad d_- = \frac{\sin\,\alpha}{\sqrt{2}\pi} \tag{5.58}$$

For a state with both $k, l \neq 0$ there are two degenerate solutions at each level (k, l) corresponding to the angles $\alpha = \theta$ et $\alpha = \theta + \pi/2$ where θ is a mixing angle between the two modes. Any physical result should be independent on θ so one can keep it as free parameter. The explicit form for the fields with $(p_r, p_g) = (+, p_g)$ while we set $\theta = 0$

$$\Psi^{(k,l)}_{a(+p_g)} = \frac{1}{\sqrt{2}\pi} \begin{pmatrix} (\cos ky_4 \ \cos ly_5) \ \chi_4^{(k,l)} \\ p_g(-)^{k+l} \ \left(-\frac{k}{\sqrt{k^2+l^2}} \ \sin ky_4 \ \cos ly_5 + \frac{il}{\sqrt{k^2+l^2}} \cos ky_4 \ \sin ly_5\right) \ \bar{\eta}_4^{(k,l)} \\ p_g(-1)^{k+l} \ (\cos ky_4 \ \cos ly_5) \ \chi_4^{(k,l)} \\ \left(-\frac{k}{k^2+l^2} \ \sin ky_4 \cos ly_5 - \frac{il}{\sqrt{k^2+l^2}} \ \cos ky_4 \ \sin ly_5\right) \ \bar{\eta}_4^{(k,l)} \end{pmatrix} \tag{5.59}$$

$$\Psi^{(k,l)}_{b(+p_g)} = \frac{1}{\sqrt{2}\pi} \begin{pmatrix} (\sin ky_4 \ \sin ly_5) \ \chi_4^{(k,l)} \\ p_g(-)^{k+l} \ \left(\frac{il}{\sqrt{k^2+l^2}} \ \sin ky_4 \ \cos ly_5 - \frac{k}{\sqrt{k^2+l^2}} \cos ky_4 \ \sin ly_5\right) \ \bar{\eta}_4^{(k,l)} \\ p_g(-1)^{k+l+1} \ (\sin ky_4 \ \sin ly_5) \ \chi_4^{(k,l)} \\ \left(\frac{il}{k^2+l^2} \ \sin ky_4 \cos ly_5 + \frac{k}{\sqrt{k^2+l^2}} \ \cos ky_4 \ \sin ly_5\right) \ \bar{\eta}_4^{(k,l)} \end{pmatrix} \tag{5.60}$$

Summarizing, for each fermion in the SM we need to introduce two six-dimensional spinors $\Psi^{6D}_{(+p_g)}$ and $\Psi^{6D}_{(-p_g)}$ whose zero KK modes will corresponds to the left and right components of the well known 4D-spinors. The corresponding KK towers $\Psi^{(k,l)}_{(\pm p_g)}$ will contain both 4D chiralities, therefore the number of Dirac fermions on higher KK level will be doubled.

5.2.4 Higgs boson

In the same way as in the Standard Model we introduce also the higgs doublet Φ with parities $(p_g, p_r) = (+,+)$ with the standard bulk potential

$$\mathcal{H} = (D_\mu \Phi)^\dagger D^\mu \Phi - m_\phi^2 \Phi^\dagger \Phi + \frac{\lambda_6}{2}(\Phi^\dagger \Phi)^2 \tag{5.61}$$

where m_h is the higgs bulk mass and λ is the higgs quartic coupling [3]. For the zero mode the effective potential at tree level reads

$$V[\phi^{0,0}] = m_\phi^2 \phi^{(0,0)\dagger}\phi^{(0,0)} + \frac{\lambda_4}{2}(\phi^{(0,0)\dagger}\phi^{(0,0)})^2 \tag{5.62}$$

where $\lambda_4 = \frac{\lambda_6}{4\pi^2}$ is the effective quartic coupling in 4 dimensions. The physical mass of the higgs zero mode $\phi^{(0,0)}$ at tree level will then be given by

$$m_h^2 = -2m_\phi^2 = \lambda_4 v^2 \tag{5.63}$$

where we have expanded the $\phi^{(0,0)}$ in the usual way

$$\phi^{(0,0)} = \frac{1}{\sqrt{2}} \begin{pmatrix} 0 \\ v + H(x^\mu) \end{pmatrix} \tag{5.64}$$

including higgs the gauge fixing term in equation 5.22 changes to

$$\mathcal{L}_{fix} = -\frac{1}{2\xi}\left[\partial_\mu A^\mu - \xi\left(\partial_4 A_4 + \partial_5 A_5 - g v \phi_0\right)\right] \tag{5.65}$$

For the heavy tiers the higgs VEV induces mixings as in the SM. The electroweak neutral bosons are mixed with a large mixing angle as their masses are degenerate at tree level. The mixing angle is different from the SM Weinberg angle $\sin\theta_W = 0.23$ because of the loop corrections to the KK boson masses. Fermions are less affected by the higgs VEV and only top quark KK excitations will receive considerable higgs contributions that will mix the two heavy Dirac fermions corresponding to left-and right handed components of the Standard Model top quark. The equations of motion for the scalar components $A_{4/5}$ are now coupled with those of ϕ_0. One will get the two linear combinations of states, one of which will correspond to the physical scalars described in the previous sections, the second one, consisting mainly of the higgs component will correspond to the new physical scalar in the model (51).

For the heavy modes we decompose the higgs field as

$$\phi_{(n,0)} = \begin{pmatrix} \pi^+_{(n,0)} \\ \frac{H_{(n,0)} + i\pi^0_{(n,0)}}{\sqrt{2}} \end{pmatrix} \tag{5.66}$$

with tree level masses

$$m^2_{\pi_{(n,0)}} = n^2 m^2_{KK}\,, \qquad m^2_{H_{(n,0)}} = m^2_{\pi_{(n,0)}} - 2m_\phi^2\,. \tag{5.67}$$

3. The scalar has dimension $[\Phi] = 2$, therefore the dimension of the quartic coupling is $[\lambda] = -2$. This may be problematic as if we want to have higgs heavy enough we need a higher order operator with an un-naturally large coupling. We leave this issue aside and we consider the higgs sector in our scenario only as a toy model. However in the optic of recent LHC confirmation of a signal at 125 GeV attributed to the higgs boson we would need to study the properties of this sector in our model more in details if we want our study to be complete.

The fields $\phi^{\pm,0}$ are the would-be goldstone bosons that would provide the longitudinal polarization to the massive gauge bosons if the higgs VEV were the only source of mass. However, for the $(n,0)$ modes, the main contributions to the mass comes from the extra dimension, and the role of the goldstone bosons is played by the extra polarizations of the vectors. The higgs VEV will in general mix the $\pi^{\pm,0}$ with the gauge scalars: one effect of such mixing is to introduce a new correction to the mass of the physical states $s^{\pm,0}_{(n,0)}$. The tree level mass eigenstates are therefore given by:

$$m^2_{s^{\pm}_{(n,0)}} = m^2_{\pi_{(n,0)}} + m^2_W\,, \qquad m^2_{s^0_{(n,0)}} = m^2_{\pi_{(n,0)}} + m^2_Z\,. \tag{5.68}$$

Introducing loop corrections for the higgses we should worry about the additional mixing between different KK tiers. As we shell see later the higgs VEV will affect not only the zero modes of the fields but also the heavier excitations. This could be dangerous as the mixings between zero modes and higher states would affect the electroweak precision observables at tree level. This effect should be investigated in details in the further work.

5.2.5 Yukawa couplings for fermions

The Yukawa couplings are only relevant for top quarks. In term of the six dimensional spinors $\Psi_{Q/u}$ associated to the left and right handed SM top components the Yukawa lagrangian can be written as

$$\begin{aligned} \mathcal{L}_{Yukawa} &= Y_6 \bar{\Psi}_Q \Phi \Psi_u + h.c. \\ &= Y_6 \left[\eta^Q_+ \Phi \chi^u_- + \eta^Q_- \Phi \chi^u_+ + \bar{\chi}^Q_+ \Phi \bar{\eta}^u_+ + \bar{\chi}^Q_- \Phi \bar{\eta}^u_- \right] + h.c. \end{aligned} \tag{5.69}$$

This term can only be written if $p_r(\Psi_Q) = -p_r(\Psi_u)$. The corrections to the masses for the top quark zero modes can then be written as

$$\mathcal{L}_{Yukawa} \supset \frac{p_q(\Psi_Q) + p_g(\Psi_u)}{2} \frac{Y_6 v_6}{\sqrt{2}} \bar{q}^{(0,0)}_L u^{(0,0)}_R + h.c. \tag{5.70}$$

which implies that $p_q(\Psi_Q) = p_g(\Psi_u)$ and the SM top mass is

$$m_{top} = p_g \frac{Y_6 v_6}{\sqrt{2}} \tag{5.71}$$

For the $(0,l)$ and $(l,0)$ modes the Yukawa terms are

$$\mathcal{L}_{Yukawa} \supset -(-1)^l m_{top} (\bar{q}_L u_R - \bar{q}_R u_L) + h.c. \tag{5.72}$$

The mass eigenstates will be obtained by diagonalization of the system

$$\mathcal{L}_{mass} = -\left(\bar{q}_L \;\; \bar{u}_L\right) \cdot \begin{pmatrix} 1+\delta m_Q & -m_{top} \\ m_{top} & 1+\delta m_u \end{pmatrix} \cdot \begin{pmatrix} q_R \\ u_R \end{pmatrix} + h.c. \tag{5.73}$$

The mass eigenvalues are then

$$m^2_{t1,2} = 1 + m^2_{top} + \delta m_Q \left(1 + \frac{\delta m_Q}{2} \pm B\right) + \delta m_u \left(1 + \frac{\delta m_u}{2} \mp B\right) \tag{5.74}$$

with

$$B = \sqrt{\left(1 + \frac{\delta m_Q + \delta m_u}{2}\right)^2 + m_{top}^2} \tag{5.75}$$

And the eigenstates are then given by

$$\begin{pmatrix} t_{1l,r} \\ t_{2l,r} \end{pmatrix} = \begin{pmatrix} \cos\alpha_t & \pm\sin\alpha_t \\ \mp\sin\alpha_t & \cos\alpha_t \end{pmatrix} \begin{pmatrix} q_{l,r} \\ u_{l,r} \end{pmatrix} \tag{5.76}$$

with

$$\tan\alpha_t = \frac{1}{m_{top}} \left[B - \left(1 + \frac{\delta m_Q + \delta m_u}{2}\right) \right] \tag{5.77}$$

5.2.6 Standard Model on the real projective plane

As we have described the field theory on the real projective plane for each kind of quantum field, we now let propagate all the particles of the Standard Model on the space $\mathcal{M}^4 \times \mathbb{R}P^2$. We will study the SM gauge group $\mathrm{SU}(3)_C \times \mathrm{SU}(2)_W \times \mathrm{U}(1)_Y$ with a single higgs scalar doublet and a 6-dimensional fermion for each chiral Standard Model fermion. Therefore for each $\mathrm{SU}(2)_W$ doublet particle $Q = \{u_D, c_D, t_D, d_D, s_D, b_D\}$ for quarks and $L = \{e_D, \mu_D, \tau_D, nu_e, \nu_\mu, \nu_\tau\}$ for leptons we associate a 6-dimensional spinors $\Psi_D^{(+,+)}$. As well as for $\mathrm{SU}(2)_W$ singlets $u_R = \{u_R, c_R, t_R\}$, $d_R = \{d_R, s_R, b_R\}$, $e = \{e_R, \mu_R, \tau_R\}$ we associate a 6-dimensional spinor $\Psi_S^{(+.-)}$. Of course the gauge bosons will now become a 6-dimensional vectors B_α for $\mathrm{U}(1)_Y$, W_α^i with $i = 1 \ldots 3$ for $\mathrm{SU}(2)_W$ and G_α^a with $a = 1 \ldots 8$ for $\mathrm{SU}(3)_C$. To each SM field it corresponds a tower of Kaluza-Klein excitations, labeled by two non-negative integers (k, l) which correspond to the quantized momenta along the extra dimensions. The field content at each level (k, l) depends crucially on the parities assigned to the fields. The parities are assigned in such a way to reproduce at zero level the Standard Model content. At leading order, releasing the assumption $R - 4 = R_5 = 1$, the masses of the (k, l) states are given by the relation

$$m_{k,l}^2 = m_{SM}^2 + \frac{k^2}{R_4^2} + \frac{l^2}{R_5^2} \tag{5.78}$$

We summarise the field content on the generic (k, l) level in the table 5.5. The vector gauge bosons A_μ are absent on the levels of the form $(0, 2k-1)$ and $(2k-1, 0)$ while their scalar partners $A_{4/5}$ are present on those odd tiers but absent on $(0, 2k)$ and $(2k, 0)$ tiers. The scalar higgs is present on all the levels except $(0, 2k-1) - (2k-1, 0)$ like the gauge vectors. Fermions are present at all the levels. On the $(0, 0)$ we have chiral modes for each Standard Model fermion. On the higher level (k, l) the spinors are no more chiral in the 4-dimensional sense. On the generic (k, l) states we have two degenerate modes corresponding to (k, l) and (l, k) tiers.

Note that this is the simplest possible extension of the Standard Model on the real projective plane. Some more complicated extensions could be considered, like the non-flat metric or gauge-higgs unification. At tree level the masses of all the particles in a tier are degenerated. This degeneracy is lifted by loop corrections. Therefore, in order to study in details the phenomenology of the model we need to calculate the radiative corrections to the masses of the KK excitations. The corrections to the states $(0, 1) - (1, 0)$ were calculated in (51). In this work we concentrate on the influences of the $(2, 0) - (0, 2)$ modes on the phenomenological features of

(k,l)	p_{KK}	mass $[m_{KK}]$	$A_\mu^{(+,+)}$	$A_4^{(+,-)}$	$A_5^{(-,-)}$	$\Psi_D^{(+,+)}$	$\Psi_S^{(+,-}$	$\Phi^{(+,+)}$
(0,0)	+	0	$\surd$	-	-	$\surd^c$	$\surd^c$	$\surd$
(1,0)-(0,1)	-	1	-	$\surd^{(0,1)}$	$\surd^{(1,0)}$	$\surd$	$\surd$	-
(1,1)	+	$\sqrt{2}$	$\surd$	$\surd$	$\surd$	$2\surd$	$2\surd$	$\surd$
(2,0)-(0,2)	+	2	$\surd$	-	-	$\surd$	$\surd$	$\surd$
(k,l)	$(-1)^{k+l}$	$\sqrt{k^2+l^2}$	$\surd$	$\surd$	$\surd$	$2\surd$	$2\surd$	$\surd$

Table 5.5: Standard Model content on the (k,l) levels on the real Projective Plane. We indicate the KK parity p_{KK}, the tree level mass in $m_{KK} = R^{-1}$ units and the presence of each kind of fields. Superscript $\surd^c$ denotes that the fermion is chiral. The $2\surd$ means that there are two states degenerate in mass corresponding to (k,l) and (l,k) levels.

the model. Therefore we first calculate the loop corrections to those states and then investigate the consequences of those modes in the LHC and dark matter processes.

Chapter 6

Mass spectrum of the (2,0) - (0,2) modes at loop level

In this thesis we concentrate on the effects of $(2,0)$ modes on the phenomenology of the model on the real projective plane. The $(2,0)$ and $(0,2)$ tiers are even under the KK parity and thus the particles in these levels can decay directly into a pair of SM particles without missing energy. Potentially this could lead to very clean signatures with resonances.

Note that the $(2,0)$ is not the lightest even level. The $(1,1)$ level particles are lighter, however they cannot decay into SM particles via loops but via interactions localized on the singular points which violate maximally the symmetries of the bulk. Therefore the decays of the $(1,1)$ tier particles cannot be predicted and depend crucially on the UV completion of the theory. The operators responsible for the decays into SM particles are higher order operators, suppressed by the cut off scale. One may assume that they are small compared to the one-loop effects. Under this assumption all the states in the tier will decay into the lightest particle plus soft SM particles. The fate of the lightest $(1,1)$ particle is UV dependent. It may be stable, if protected by a symmetry in the UV theory, or long lived and seen as a missing energy in the experiments or it may decay into a pair of SM particles. The decay of the lightest $(1,1)$ state into two tops was studied in (50). It leads to a very clean signature with 4 tops in the final state. The cross section is very large as all the particles from the $(1,1)$ tier contribute in the process. Thus the bounds on mass and branching ratios into top pair would be quite severe.

The spectrum of the $(2,0)$ tier is quite similar to the $(1,0)$. The loop corrections however are quite large compared to the higgs VEV contribution as the former are proportional the mass of the tier while the latter to the electroweak scale.

We will discuss also the effect of the two different radii allowed by the compactification and the structure of the symmetries of the space and present in details the spectrum as a function of the two radii. This discussion is crucial in the understanding of the LHC and DM phenomenology of the model.

6.1 Divergences due to compactification - general remarks

Higher dimensional field theories should be regarded as effective theories with a cutoff Λ, above which a more fundamental UV completion is required. Therefore, when writing the lagrangian, one has to consider all the operators consistent with the "low-energy" theory and regard their coefficients as free parameters to be determined, if possible, by experiment. This means in particular, that one has to include all the operators localized on the fixed points of the

orbifold in question, which does not break the 4D Lorentz invariance. However, as the translation symmetry in the extra space is violated by the fixed points, the KK-parity, which is a remnant of the broken Lorentz invariance in the extra dimensions, is in general broken by the operators localized at the fixed points. It was noticed in many papers (65), (109), (52) that the fixed points of the compactified space are the source of divergent loop corrections in the effective 4D field theory. Therefore, the KK-parity is no more a consequence of the compactification, but it is imposed by hand on the general structure of the models and on its ultra-violet completion which is the ultimate origin of the localized counter-terms. It was shown also that the counterterms required to absorb divergences in the quantized theory are localized precisely at the fixed points of the underlying orbifold (109), (52). In the model presented in this thesis the compactified space has no fixed points. The conical singularities situated at the points $(0,0)$, $(0,\pi)$, $(\pi,0)$ and (π,π) are related by the geometry of the orbifold which is invariant under the π rotation about the center of the fundamental square. Localized counter-terms are not avoided, however the geometry of the space ensures that they do respect the KK-parity. The general form of the localized counterterms $\mathcal{L}_{ct}$ is therefore explicitly invariant under KK parity and can be written using two localization operators (51)

$$\delta\mathcal{L} = \frac{\delta_0 + \delta_\pi}{\Lambda^2}\mathcal{L}_{ct} \tag{6.1}$$

where

$$\delta_0 = \frac{1}{2}\left[\delta(x_4)\delta(x_5) + \delta(x_4 - \pi R)\delta(x_5 - \pi R)\right] \tag{6.2}$$

$$\delta_\pi = \frac{1}{2}\left[\delta(x_4)\delta(x_5 - \pi R) + \delta(x_4 - \pi R)\delta(x_5)\right] \tag{6.3}$$

The full set of counterterms in the model was considered in the recent work (52). They allow one to deduce the mass corrections and effective couplings relevant for the phenomenology. We will compare our results to those obtained in this work as the divergent contributions should be the same.

We will see in the explicit calculation of loop corrections to the $(2n,0)$ and $(0,2n)$ KK states masses that the $\tilde{\Pi}_T$ contribution corresponds to the fields propagation on the torus. The integral is UV divergent and the divergence comes from the $(0,0)$ mode propagation. As it was noticed in the section 4.3 this divergence is the same as for a field propagating in the non-compactified space and can be absorbed in the wave function renormalization of the 6D field (109), (52). After removing the $(0,0)$ mode part $\tilde{\Pi}_T$ gives a finite contribution $\Delta' = 1.22$. Glide symmetry do not have any fixed points. It is therefore natural that the $\tilde{\Pi}_G$ contribution is finite. Contribution due to the rotation projection of the orbifold will give a divergent part.

6.2 Winding modes on the real projective plane

First we illustrate how the winding modes method works in the 6-dimensional case. We emphasize the main properties of loop decomposition and the partial contributions coming from different symmetry projections of the orbifold. This method was used by G. Cacciapaglia and J. Llodra-Perez in (51) to verify the results of the $(1,0)$ radiative corrections to the masses.

Following the proposition of (110), on the two dimensional real projective plane the general form of the scalar propagator will have the form

$$\begin{aligned} G_S^{6D}(p,\vec{y}_1,\vec{y}_2) &= \tfrac{1}{4}\Big[G_S^{6D}(p,\vec{y}_1-\vec{y}_2+\vec{w})+p_g G_S^{6D}(p,\vec{y}_1-g(\vec{y}_2)+\vec{w}) \\ &+ p_r G_S^{6D}(p,\vec{y}_1-r(\vec{y}_2)+\vec{w})+p_r p_g G_S^{6D}(p,\vec{y}_1-r*g(\vec{y}_2)+\vec{w})\Big] \end{aligned} \tag{6.4}$$

where p_g and p_r are the glide and rotation parities of the field running in the loop respectively. The loop correction to the two point function of a scalar field will have the following form:

$$i\Pi = iN(2\pi)^2 \int d^4K \int d\vec{y} G_S^{6D}(k,\vec{y}_1,\vec{y}_2) f^{(n,0)}(q,\vec{y}) f^{(n,0)}(q\vec{y}) \tag{6.5}$$

where $f^{(n,0)}(q,\vec{y}) = \frac{1}{2\pi}\sin nx_5$ is the wave function of the external field, $g_{66} = -1$ is the metric factor and $g_6^2 = (2\pi)^2 g^2$ is the 6D gauge coupling. The normalization factor N is defined as $N = \frac{2g^2 C(r_2) g_{66}}{16\pi^2}$. Putting the above form of propagator eq. 6.4 into eq. 6.5 one can split the full loop contribution into four parts proportional to the parities of the field running in the loop, namely

$$\Pi = \Pi_T + p_g \Pi_G + p_r \Pi_R + p_g p_r \Pi_{GR} \tag{6.6}$$

The Π_T contribution comes from the torus and is finite after the kinetic term renormalization. The explicit form of the torus contribution after Wick rotation the euclidean space is as follows:

$$\Pi_T = \frac{N}{4} 4\pi^2 \int k^4 \sum_{\vec{w}} \frac{1}{4} H_0^{(1)}(k|\vec{w}|) \tag{6.7}$$

$$= \frac{N}{4} 4\pi^3 \int_0^\infty dk_E \sum_{(n_1,n_2)\in Z^2} k_E^3 K_0(2\pi k_E \sqrt{n_1^2+n_2^2}) \tag{6.8}$$

where K_0 is the K Bessel function of zeroth order. As in the 5D case, the propagator for a non-zero winding mode is exponentially damped at high energies $p|\vec{w}| \gg 1$

$$K_0(p|\vec{w}|) \to e^{-p|\vec{w}|}\sqrt{\frac{\pi}{2p|\vec{w}|}} \tag{6.9}$$

showing that winding contributions on a torus will always be finite. The zero winding mode contribution $(n_1,n_2) = (0,0)$ is UV divergent. This divergence is the same as one would get from an uncompactified space. Therefore this bulk divergence can be absorbed by the wavefunction renormalization of the $6D$ filed. We remove the $(0,0)$ mode from the sum in eq. 6.7 and integrating over k_E we get

$$\int_0^\infty dk_E k_E^3 K_0(k_e a) = \frac{4}{a^4} \tag{6.10}$$

and

$$\Pi_T = \frac{N}{4\pi} \sum_{(n_1,n_2)\neq(0,0)} \frac{1}{(n_1^2+n_2^2)^2} = \frac{N}{4} T_6 \tag{6.11}$$

with $T_6 \approx 1.92$. For arbitrarily small argument $K_0(x) \to -\log x$ and the propagator diverges at small distances in the extra dimensions. Therefore to compute Feynman integrals with $\vec{y} \to 0$

we have to regulate the propagator when $\vec{w} = 0$. The second contribution in eq. 6.6 is of the form

$$\Pi_G = \frac{N}{4} 4\pi^2 \int d^4k \int d\vec{y} \sum_{\vec{w}} \frac{1}{4} H_0^{(1)}(k|\vec{y} - g(\vec{y} + \vec{w})|) \frac{\sin^2 nx_5}{2\pi^2} \tag{6.12}$$

As the glide does not change the sign x_5 component, the Hankel function $H_0^{(1)}$ does not depend on x_5 and the integral along x_5 direction is simply given by the normalization of the wave function. Then after Wick rotation one gets the integral

$$\Pi_G = \frac{N}{4\pi^2} \sum_{(n_1,n_2)\in Z^2} \int_0^{2\pi} dx_6 \frac{1}{\left((n_1 - \frac{1}{2})^2 + (\frac{x_6}{\pi} + n_2^2 - \frac{1}{2})^2\right)^2} = \frac{N}{4} 7\zeta(3) \tag{6.13}$$

In an analogous way one can show that the Π_{GR} contribution will give a finite result

$$\Pi_{GR} = \frac{N}{4\pi^2} \sum_{(n_1,n_2)\in Z^2} \int_0^{2\pi} dx_5 \frac{1 - \cos 2nx_5}{\left((\frac{x_5}{\pi} + n_1 - \frac{1}{2})^2 + (n_2 - \frac{1}{2})^2\right)^2} = \frac{N}{4} \left(7\zeta(3) + B_1(n)\right) \tag{6.14}$$

The rotation contribution after Wick rotation can be written in the form

$$\Pi_R = \frac{N}{4} 2\pi \int_0^{\infty} dk_E \int_0^{2\pi} d\vec{y} \sum_{\vec{w}} k_E^3 K_0(k|2\vec{y} + \vec{w}|) \sin^2 nx_5 \tag{6.15}$$

It can be seen in the form of the integrand that the divergences appear for $|2\vec{y} + \vec{w}| = 0$. Those points correspond to the fixed points of the rotation transformation. Note that the divergent result depends on the KK number n of the considered mode. Therefore it cannot be reabsorbed into the renormalization of the bulk wave functions of the 6D fields. Those logarithmic divergences should be renormalized by counter-terms localized at the singular points. To extract the divergent part one can cut the 4D momentum k_E at a scale Λ and then integrate numerically. Then the result is

$$\Pi_R = \frac{N}{4} n^2\pi^2 \log \frac{\Lambda^2 + n^2}{n^2} \tag{6.16}$$

As we just have seen on the example of the winding modes expansion method, the main properties of the radiative corrections on the real projective plane are the following

1. Torus contribution is always finite. The UV divergence corresponding to the $(0, 0)$ mode propagation can be reabsorbed in the wavefunction renormalization of the $6D$ field.
2. Glide and glide-rotation contributions are finite as those symmetries do not heavy any fixed points.
3. Rotation contribution will give logarithmic divergences that should be removed by the counterterms localized on the fixed points of the rotation symmetry,

This method is useful to calculate the scalar tadpole loops but for the case two propagators in the loop the mathematical complexity will be much higher, as on should integrate the products of Bessel functions. In what follows we use the mixed propagator method to evaluate the loop corrections to the $(2, 0)$ and $(0, 2)$ tiers. We will show the results of the calculation performed for the gauge bosons and fermions on the $\mathbb{R}P^2$ and show the main features of the spectrum in contrast to other models.

6.3 One loop level spectrum of the $(2,0)-(0,2)$ tiers using the mixed propagator method

In the case of two extra dimensions we use propagators defined in the section 4.3 in eq. 4.41 but we have to take into account also the second dimension. We will Fourier-transform the non-compact coordinates $\{x^\mu\}$ into momentum space $\{p^\mu\}$, which contains the physical momentum and energy measured by 4-dimensional observers, and leave the other two coordinates in position space. It is then convenient to write the propagator in the mixed form - we keep the form eq. 4.41 in one direction while for the second direction we expand the propagator into the sum of KK modes. For a scalar field propagating on the torus we write

$$G_\Phi^{6D}(k,\vec{y}_1-\vec{y}_2)=\sum_{l=-\infty}^{\infty} G_\Phi^{S^1}\left(\chi_l,|y_1-y_2|\right) f_l^*(z_1)f_l(z_2) \tag{6.17}$$

where we note the two coordinates as $\vec{y}=(y,z)$. Now the functions χ_l are defined as $\chi_l=\sqrt{k^2-l^2-m^2}$ and in what follows we neglect the SM mass $m^2\ll l^2$. The functions f_l are the normalized wave functions on S^1

$$f_l(z)=\frac{1}{\sqrt{2\pi}}e^{ilz} \tag{6.18}$$

The G_Φ^{6D} propagator has to verify symmetries of the underlying manifold eq. 5.2. Therefore, following the proposition of (65) we write the propagator as the sum of terms proportional to the parities of the field running in the loop;

$$\begin{aligned} G_\Phi^{RPP}(k,\vec{y}_1-\vec{y}_2) &= \frac{1}{4}\Big[G_\Phi^{6D}(k,\vec{y}_1-\vec{y}_2)+p_g G_\Phi^{6D}(k,\vec{y}_1-g[\vec{y}_2]) \\ &+ p_g p_r G_\Phi^{6D}(k,\vec{y}_1-r*g[\vec{y}_2])+p_r G_\Phi^{6D}(k,\vec{y}_1-r[\vec{y}_2])\Big] \end{aligned} \tag{6.19}$$

Writing propagators in this way will simplify a lot the calculation of the mass corrections to the $(n,0)$ and $(0,n)$ KK modes as they do not carry momentum along one of extra dimensions z and y respectively. Therefore we can replace the integral along one of those directions by a sum using the orthonormality of the wave functions.

Using the above form of propagator eq. 6.19, a generic loop correction to any field can be decomposed as

$$i\Pi(m_{KK})=\frac{i}{4}\left[\Pi_T(m_{KK})+p_g\,\Pi_G(m_{KK}i)+p_g p_r\,\Pi_{GR}(m_{KK})+p_r\,\Pi_R(m_{KK})\right] \tag{6.20}$$

where the parities refer to any field propagating in the loop. The first term in eq. 6.20, Π_T, corresponds to the loop corrections of a theory defined on a torus: this contribution is generically divergent, however, it gives a finite contribution after renormalization of the bulk kinetic terms. Here we will follow the prescription of (110) where we remove the contribution of zero winding modes, i.e. modes that do not wrap around the torus. The terms Π_G and Π_{GR} correspond to glide symmetries and are finite. The reason behind the finiteness is that the points $\vec{y}$ and its image $g(\vec{y})$ (or $g'(\vec{y})$) never coincide, i.e. the glide(s) do not admit any fixed points. The last term, Π_R, in equation 6.20 corresponds to rotation transformation, and it is divergent because the rotation admits fixed points: from the tadpole loop it is clear that the divergences only arise in the points where $\vec{y_*}=r(\vec{y_*})$, i.e. on the corners of the rectangle. Thus, such divergences can be renormalized by adding counter-terms on the two singular points whose structure has been studied in (52). The bulk loops simply require equal terms on the singular points, as loop interaction cannot distinguish between the two.

6.3.1 Loop corrections to the $(2,0)-(0,2)$ gauge bosons

In this section we compute the quantum corrections to the two-point functions (sometimes we will refer to these as self-energies, even though they also include mixing among KK states) for gauge fields. We calculate the mass correction δ_m^2 given by

$$\delta_m^2 = m^2 - m_{tree}^2 \tag{6.21}$$

where m is the one-loop level mass and $m_{tree}^2 = m_{SM}^2 + \frac{k^2+l^2}{R^2}$ is the tree level mass of a (k,l) excitation mode.

We first consider one-loop corrections arising to the masses of the $(n,0)$ KK excitations of a SU(N) gauge boson. The contributing diagrams are shown in the figure 6.22. The calculation presented here is completely general for all the bosonic states on levels $(n,0)$ with n even.

$$i\Pi^{\mu\nu}(q) = i(g^{\mu\nu}q^2 - q^\mu q^\nu) = \tag{6.22}$$

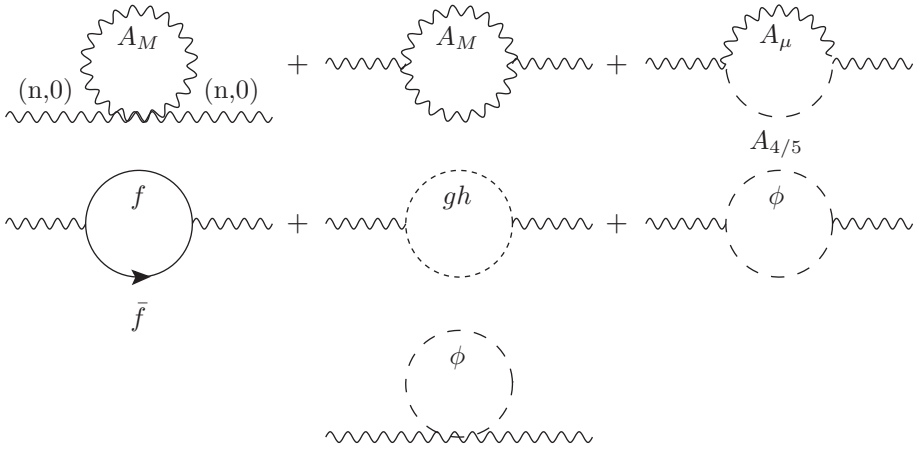

The couplings are deduced from FeynRules implementation of the model lagrangian given by the equations 5.22, 5.39, 5.65 and 5.69. The 4D Lorentz invariance requires $\Pi_{\mu\nu}$ to be of the form

$$\Pi_{\mu\nu} = g_{\mu\nu}\Pi_1 + q_\mu q_\nu \Pi_2 \tag{6.23}$$

and the mass corrections are proportional to the Π_1 part only:

$$\Pi_1 = \frac{1}{3}\left(\Pi_\mu^\mu - \frac{q^\mu q^\nu}{q^2}\Pi_{\mu\nu}\right) \tag{6.24}$$

The structure of loops with two gauge/scalar propagators is more complicated and although the calculation is much more involved the general scheme remain similar to the tadpole case. Therefore here we give only the form of the integrals with some remarks. In general the two vertices are situated on the points $\vec{y}_1 = (y_1, z_1)$ and $\vec{y}_2 = (y_2, z_2)$ in the extra space and for the tadpole loops Π_{1tp} those two points coincide and are noted as $\vec{y} = (y, z)$. The tadpole contribution takes the form

$$i\Pi_{1tp} = \int d^4k d\vec{y} \frac{P_X}{(2\pi)^4} G_A^{RPP}(k, \vec{y}-\vec{y}) A^{(n,0)}(\vec{y}) A^{(n,0)}(\vec{y}) \tag{6.25}$$

where G_X^{6D} is the 6D propagator of the particle $X \in \{A_{4/5}, A_\mu, \phi\}$ running in the loop and $A^{(n,0)}(\vec{y})$ is the wave function of the external particle. The P_X coefficient is simply the function coming from the vertex after taking the trace eq. 6.24. In an analogous way we write the loops with two propagators of the same type

$$i\Pi_{1loop} = \int d^4k d^2\vec{y}_1 d^2\vec{y}_2 \frac{P_X}{(2\pi)^4} G_\Phi^{RPP}(k+p, \vec{y}_1-\vec{y}_2) G_\Phi^{6D}(k+p, \vec{y}_1-\vec{y}_2) A^{(n,0)}(\vec{y}_1) A^{(n,0)}(\vec{y}_2) \tag{6.26}$$

The mixed loops $A_\mu - A_{4/5}$ have more involved form as the derivatives coming from the vertices appear:

$$\begin{aligned} i\Pi_{1\mu 5} &= -(2\pi)^2 \frac{N}{2} g_{55} \int d^4k d^2\vec{y}_1 d^2\vec{y}_2 G_\Phi^{RPP}(k+p, \vec{y}_1-\vec{y}_2) \\ &\quad \left[\partial_{z_1}^e \partial_{z_2}^e - \partial_{z_1}^e \partial_{z_2}^p - \partial_{z_1}^p \partial_{z_2}^e + \partial_{z_1}^p \partial_{z_2}^p\right] G_\Phi^{6D}(k+p, \vec{y}_1-\vec{y}_2) A^{(n,0)}(\vec{y}_1) A^{(n,0)}(\vec{y}_2) \end{aligned} \tag{6.27}$$

$$\begin{aligned} i\Pi_{1\mu 4} &= -(2\pi)^2 \frac{N}{2} g_{44} \int d^4k d^2\vec{y}_1 d^2\vec{y}_2 G_\Phi^{RPP}(k+p, \vec{y}_1-\vec{y}_2) \\ &\quad \left[\partial_{y_1}^e \partial_{y_2}^e - \partial_{y_1}^e \partial_{y_2}^p - \partial_{y_1}^p \partial_{y_2}^e + \partial_{y_1}^p \partial_{y_2}^p\right] G_\Phi^{6D}(k+p, \vec{y}_1-\vec{y}_2) A^{(n,0)}(\vec{y}_1) A^{(n,0)}(\vec{y}_2) \end{aligned} \tag{6.28}$$

where $\partial_{y_i}^{e/p}$ means the partial derivative with respect to y_i, $i \in \{1,2\}$ of the external leg wave function (e) or of the propagator (p). Fermion contribution finally is of the form

$$\begin{aligned} &i\Pi_f = N \int d^4k d^2\vec{y}_1 d^2\vec{y}_2 A^{(n,0)}(\vec{y}_1) A^{(n,0)}(\vec{y}_2) (k+p)_\beta \\ &Tr\left[\Gamma^\mu k_\alpha \Gamma^\alpha G_\Phi^{6D}(k, \vec{y}_1-\vec{y}_2) \Gamma^\nu (k+p)_\beta \Gamma^\beta G_\Phi^{RPP}(k+p, \vec{y}_1-\vec{y}_2)\right] \end{aligned} \tag{6.29}$$

To give an example of our calculation we consider in details the tadpoles $i\Pi_{1tp}$ contributions to the gauge self energy which can be easily generalized to other loops.

Expanding the 6D propagator as given in eq. 6.19 we can divide the loop correction into four parts which will be calculated separately. For the four contributions b),e) and i) we get

$$\begin{aligned} i\Pi_1 &= 2iN \left\{ \begin{array}{c} \frac{1}{2} \\ -1 \\ \frac{3}{2} \end{array} \right\} \int d^4k d\vec{y} G_\Phi^{RPP}(k, \vec{y} - \theta[\vec{y}]) \cos^2(ny) \\ &= \frac{iN}{2} \left\{ \begin{array}{c} \frac{1}{2} \\ -1 \\ \frac{3}{2} \end{array} \right\} \left(\tilde{\Pi}_T + p_g \tilde{\Pi}_G + p_g p_r \tilde{\Pi}_{GR} + p_r \tilde{\Pi}_R\right) \end{aligned} \tag{6.30}$$

with $N = \frac{2g^2 C_s(G)}{(2\pi)^4}$. For $A^{(n,0)}(\vec{y})$ we have used the $(n,0)$ wave functions derived in the section 5.2: $A^{(n,0)}(\vec{y}) = \frac{1}{\sqrt{2\pi^2}} \cos(ny)$. The $\theta[\vec{y}]$ stands for the orbifold projections $\mathbb{I}, g, g'$ and r.

Torus contribution

$$\begin{aligned}\tilde{\Pi}_T &= \int d^4k dy dz G_A^{6D}(k,0)\cos^2(nz) = \int d^4k dy dz \sum_{l=-\infty}^{\infty} G_A^{5D}(k,0) f_l^*(z) f_l(z)\cos^2(nz) \\ &= \int d^4k \sum_{l=-\infty}^{\infty} i\pi \frac{\cot(\chi_l \pi)}{2\chi_l} \end{aligned} \tag{6.31}$$

then we remove the UV divergence and Wick-rotate and we obtain

$$\begin{aligned}\tilde{\Pi}_T &= \int d^4k \sum_{l=-\infty}^{\infty} i\pi \frac{\cot(\chi_l \pi)+i}{2\chi_l} \\ &= 2\pi^3 \int_0^{\infty} dk_E k_E^3 \left[\frac{\coth(k_E\pi)-1}{k_E} + 2\sum_{l=1}^{\infty}\int_0^{\infty} dk_E k_E^3 \frac{\coth(\chi_{lE}\pi)-1}{\chi_{lE}}\right] \\ &= \zeta(3) + 4\pi^3 \sum_{l=1}^{\infty}\int_0^{\infty} dk_E k_E^3 \frac{\coth(\chi_{lE}\pi)-1}{\chi_{lE}} = \Delta' \end{aligned} \tag{6.32}$$

The above function can be calculated numerically and gives $\Delta' = 1.22$. The numerical value is different from the one obtained in eq. 6.2 as the regularization scheme is different, note thus the structure is still the same and gives the finite result.

Glide contribution

Glide symmetry is defined as

$$g : \begin{cases} y & \sim & y+\pi \\ z & \sim & -z+\pi \end{cases} \tag{6.33}$$

thus the wave functions will transform as

$$f_l(g[z]) = f_l(-z+\pi) = (-)^l f_{-l}(z) \tag{6.34}$$

Glide contribution to the gauge boson self energy will then take the form

$$\begin{aligned}\tilde{\Pi}_G &= \int d^4k dy dz G_A^{6D}(k, \vec{y} - g((\vec{y}))\cos^2(nz) \\ &= \int d^4k dy dz \sum_{l=-\infty}^{\infty} \frac{i}{2\chi_l \sin(\chi_l\pi)} \frac{(-)^l}{2\pi} e^{-2izl}\cos^2(nz) \\ &= \int d^4k \sum_{l=-\infty}^{\infty} \frac{i(-)^l}{2\chi_l \sin(\chi_l\pi)} \left[\frac{\pi}{2}\delta_{l,n} + \frac{\pi}{2}\delta_{l,-n} + \pi\delta_{l,0}\right] \\ &= \frac{i\pi}{2}\int d^4k \left(\frac{1}{\sqrt{k^2-n^2}\sin\left(\sqrt{k^2-n^2}\pi\right)} + \frac{1}{k^2\sin\left(\sqrt{k^2}\pi\right)}\right) \end{aligned} \tag{6.35}$$

After Wick rotation we obtain:

$$\begin{aligned}\tilde{\Pi}_G &= \pi^3 \int_0^\infty dk_E k_E^3 \left(\frac{1}{\sqrt{k_E^2+n^2}\sinh\left(\sqrt{k_E^2+n^2}\pi\right)} + \frac{1}{k_E^2 \sinh\left(k_E\pi\right)} \right) \\ &= \frac{1}{2}\left(7\zeta(3) + \Phi_1(n)\right)\end{aligned} \tag{6.36}$$

Glide-Rotation contribution

Glide-rotation transforms the coordinates as:

$$r*g : \left\{ \begin{array}{lcl} y & \sim & -y+\pi \\ z & \sim & z+\pi \end{array} \right. \tag{6.37}$$

The wave functions will transform as follows

$$f_l(r*g[z]) = f_l(z+\pi) = (-)^l f_l(z) \tag{6.38}$$

and the integral will take a simple form

$$\begin{aligned}\tilde{\Pi}_{GR} &= \int d^4k dy dz G_A^{6D}(k, \vec{y} - r*g[(\vec{y})] \cos^2(nz) \\ &= \int d^4k dy dz \sum_{l=-\infty}^{\infty} \frac{i\cos\left(\chi_l(\pi - |y - r*g[y]|\right)}{2\chi_l \sin(\chi_l \pi)} \frac{(-)^l}{2\pi} \cos^2(nz)\end{aligned} \tag{6.39}$$

For the integration on dy we have to remember that the variable has to be always within the fundamental domain $g*r[y] \in (0, 2\pi)$ so the integral will split in two parts

$$\begin{aligned}&\int_0^{2\pi} dy \cos\left(\chi_l(\pi - |y - r*g[y]|\right) = \\ &= \int_0^{\pi} \cos\left(\chi_l(\pi - |y - (-y+\pi)|\right) + \int_\pi^{2\pi} \cos\left(\chi_l(\pi - |y - (-y+3\pi)|\right) = \\ &= 2\frac{\sin(\chi_l\pi)}{\chi_l}\end{aligned} \tag{6.40}$$

then the $\tilde{\Pi}_{GR}$ simplifies to

$$\tilde{\Pi}_{GR} = \frac{i}{2}\int d^4k \sum_{l=-\infty}^{\infty} \frac{(-)^l}{k^2 - l^2} \xrightarrow{Wick} \pi^3 \int_0^\infty dk_E k_E^3 \frac{1}{k_E \sinh k_E \pi} = \frac{1}{2} 7\zeta(3) \tag{6.41}$$

Rotation contribution

Exactly analogous calculus give the rotation contribution:

$$r : \begin{cases} y & \sim & -y \\ z & \sim & -z \end{cases} \tag{6.42}$$

$$f_l(r[z]) = f_l(-z) = f_l^*(z) \tag{6.43}$$

$$\begin{aligned} \tilde{\Pi}_R &= \int d^4k dy dz G_\Phi^{6D}(k, \vec{y} - r[(\vec{y})] \cos^2(nz) \\ &= \int d^4k dy dz \sum_{l=-\infty}^{\infty} \frac{i \cos\left(\chi_l(\pi - |y - r[y]|)\right)}{2\chi_l \sin(\chi_l \pi)} \frac{1}{2\pi} e^{-2ilz} cos^2(nz) \\ &= \frac{i\pi}{4} \int d^4k \sum_{l=-\infty}^{\infty} \frac{1}{\chi_l^2} (\delta_{l,n} + \delta_{l,-n} + 2\delta_{l,0}) \\ &= \frac{i\pi}{2} \int d^4k \left(\frac{1}{\chi_n^2} + \frac{1}{\chi_0^2} \right) \\ &\xrightarrow{Wick} \pi^2 \int_0^\infty dk_E k_E^3 \left(\frac{1}{k_E^2 + n^2} + \frac{1}{k_E^2} \right) \end{aligned} \tag{6.44, 6.45}$$

To regularize the infinities coming from the rotation contribution we introduce the cutoff Λ and we obtain

$$\tilde{\Pi}_R = \pi^2 \left(\Lambda^2 - \frac{n^2}{2} \log \frac{\Lambda^2 - n^2}{n^2} \right) \tag{6.46}$$

The quadratic divergences appearing after the integration will cancel after adding all the contributions.

Gauge boson self energy - total contribution

In the same manner as detailed above we calculate all the loop corrections shown in eq. 6.22. Contributions we find for each loop are listed in the table 6.1 where we have introduced the functions Φ_i that appear systematically in the loop calculations:

$$\Phi_1(n) = 2\pi^3 \int_0^\infty dk \frac{k^3}{\sqrt{k^2 + n^2} \sinh\left(\pi \sqrt{k^2 + n^2}\right)} \tag{6.47}$$

$$\Phi_2(n) = 2\pi^3 \int_0^\infty dk \frac{kn\left(\sqrt{k^2 + n^2} - n\right)}{\sqrt{k^2 + n^2} \sinh\left(\pi \sqrt{k^2 + n^2}\right)} \tag{6.48}$$

$$\Phi_3(n) = 2\pi^3 \int_0^\infty dk \frac{k^3\left(\sqrt{k^2 + n^2} - n\right)}{n\sqrt{k^2 + n^2} \sinh\left(\pi \sqrt{k^2 + n^2}\right)} \tag{6.49}$$

$$\Phi_4(n) = 2\pi^3 \int_0^\infty dk \frac{kn^2}{\sqrt{k^2 + n^2} \sinh\left(\pi \sqrt{k^2 + n^2}\right)} \tag{6.50}$$

$$L = 2\pi^2 \log(\Lambda R) \tag{6.51}$$

$$V_g(n) = \frac{1}{3}\Phi_1(n) - \frac{14}{3}\Phi_2(n) + \frac{8}{3}\Phi_3(n) \tag{6.52}$$

$$V_s(n) = \frac{1}{2}\Phi_1(n) + \Phi_2(n) + \Phi_3(n) \tag{6.53}$$

the numerical values we find for $\Phi_i(n)$ are given in the table 6.2.

$\delta m^2_{(n,0)}$	Π_T	Π_G	Π_{GR}	Π_R
gauge loops	$4T_6$	$2\cdot 7\zeta(3)$	$2\cdot 7\zeta(3)+V_g(n)$	$\frac{7}{3}L$
fermion loops	$-8T_6$	0	0	0
scalar loops	T_6	$7\zeta(3)$	$7\zeta(3)+V_s(n)$	L

Table 6.1: Radiative corrections to the gauge $(n,0)$, n even, boson self energy

	$n=1$	$n=2$	$n=3$
$\Phi_1(n)$	1.43	0.109	0.0067
$\Phi_2(n)$	0.54	0.047	0.0030
$\Phi_3(n)$	1.02	0.037	0.0015
$\Phi_4(n)$	1.71	0.294	0.0286

Table 6.2: Numerical values for the loop functions $\Phi_i(n)$.

From the above results for the $(n,0)$ mode it is straight forward to obtain corrections to $(0,n)$ gauge boson. Torus contribution $\tilde{\Pi}_T$, as it is independent on n, will give exactly the same contribution. The same argument holds for $\tilde{\Pi}_R$. Contributions coming from glides $\tilde{\Pi}_G$ and $\tilde{\Pi}_{GR}$ will be simply exchanged. This simple exchange is easy to understand as we are free to expand the propagator G^{6D} in KK modes in z direction, as we have done it above, or in y direction leaving the part dependent on z in a compact form $\sim \cot(\chi_l \pi)$. Thus it is straight forward to write the corrections to $(0,n)$ modes listed in the table 6.3.

$\delta m^2_{(0,n)}$	Π_T	Π_G	Π_{GR}	Π_R
gauge loops	$4T_6$	$2\cdot 7\zeta(3)+V_g(n)$	$2\cdot\zeta(3)$	$\frac{7}{3}L$
fermion loops	$-8T_6$	0	0	0
scalar loops	T_6	$7\zeta(3)+V_s(n)$	$7\zeta(3)$	L

Table 6.3: Radiative corrections to the gauge $(0,n)$, n even, boson self energy

Once we have all the diagonal radiative corrections for the simple case SU(N) we can write the general loop correction for a gauge boson coupled to the fermionic matter and scalars we can sum the contributions to the loop corrections from all the particles in the model. The general formula for the mass correction has a compact form

$$\delta m^2_{(n,0)} = \frac{g^2}{64\pi^4 R^2}\left(C(G)\left(4T_6 + 2*14\zeta(3) + V_g(n) + 8n^2\pi^2 L\right) - \sum_f C(r_f)8T_6 + \sum_s C(r_s)\left(T_6 + 14\zeta(3) + V_s(n) - \frac{1}{3}n^2\pi^2 L\right)\right) \quad (6.54)$$

Adding all the contributions we obtain the corrections to the B, W and G gauge bosons

$$\delta^2_{B^2} = \frac{g_1^2}{64\pi^2}\left(-79T_6 + 14\zeta(3) + \frac{5}{3}\Phi_1(2) - \frac{4}{3}\Phi_2(2) - \frac{1}{3}L\right) \quad (6.55)$$

$$\delta^2_{W^2} = \frac{g_2^2}{64\pi^2}\left(-39T_6 + 70\zeta(3) + \frac{13}{3}\Phi_1(2) - \frac{35}{3}\Phi_2(2) + 2\Phi_3(2) + \frac{47}{3}L\right) \quad (6.56)$$

$$\delta^2_{G^2} = \frac{g_s^2}{64\pi^2}\left(-36T_64 + 84\zeta(3) + \Phi_1(2) - \frac{31}{2}\Phi_2(2) + 6\Phi_3(2) + 24L\right) \quad (6.57)$$

Gauge boson self energy - mixing between tiers

Unlike for the $(1,0)-(0,1)$ tiers, the mixing between the levels $(2,0)$ and $(0,2)$ is possible. We have calculated the cross-level contributions to the $(2,0)-(0,2)$ gauge boson masses that mix the tiers $(2,0)$ and $(0,2)$. In this case the only non-zero result comes from rotation and is logarithmically divergent. The loops we need to calculate now are shown in the figure 6.1.

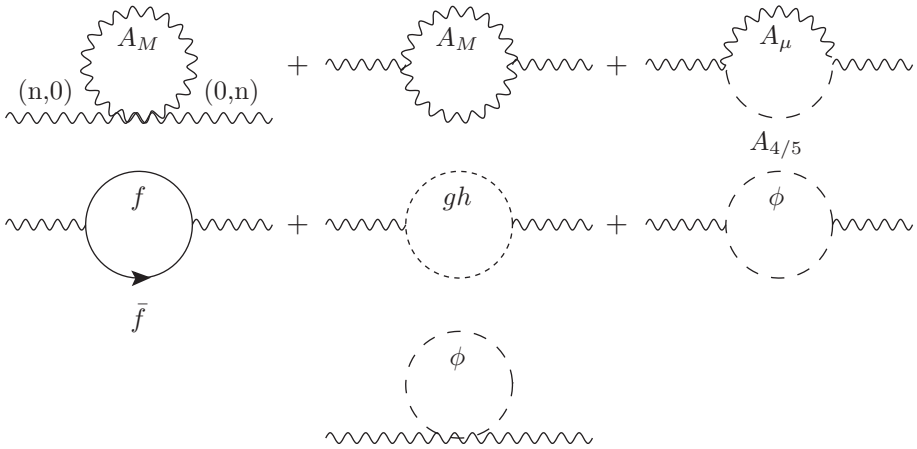

Figure 6.1: Cross-level loops for the gauge bosons.

The general structure of the loops is simple and can be written as

$$i\Pi_{1tp} = i(2\pi)^2\frac{N}{2}\int d^4k d\vec{y} G^{RPP}_\Phi(k, \vec{y} - \vec{y})\cos(ny)\cos(nz) \quad (6.58)$$

for the tadpole loops

$$i\Pi_{1loop} = i(2\pi)^2\frac{N}{2}\int d^4k d\vec{y}_1 d\vec{y}_2 P_X G^{RPP}_\Phi(k, \vec{y}_1 - \vec{y}_2) G^{6D}_\Phi(k, \vec{y}_1 - \vec{y}_2)\cos(ny)\cos(nz) \quad (6.59)$$

for the pure scalar and pure gauge loops, where again P_X is a function of the momenta of particles involved in the loop. The general structure of the mixed gauge-scalar loop $(A_\mu - A_4)$ is

$$\begin{aligned} i\Pi &= -(2\pi)^2 \frac{N}{2} g_{44} \int d^4k \int_0^{2\pi} d\vec{y}_1 d\vec{y}_2 G_\Phi^{RPP}\left(k+p, \vec{y}_1 - \vec{y}_2\right) \\ &\quad \left[\partial^l_{y_1}\partial^l_{y_2} - \partial^l_{y_1}\partial^e_{y_2}\right] G_\Phi^{6D}\left(k, \vec{y}_1 - \vec{y}_2\right) \frac{1}{2\pi} \cos nz_1 \cos my_2 \end{aligned} \tag{6.60}$$

and an analogous expression holds for the $(A_\mu - A_5)$ case

$$\begin{aligned} i\Pi &= -(2\pi)^2 \frac{N}{2} g_{55} \int d^4k \int_0^{2\pi} d\vec{y}_1 d\vec{y}_2 G_\Phi^{RPP}\left(k+p, \vec{y}_1 - \vec{y}_2\right) \\ &\quad \left[\partial^l_{z_1}\partial^l_{z_2} - \partial^e_{z_1}\partial^l_{z_2}\right] G_\Phi^{6D}\left(k, \vec{y}_1 - \vec{y}_2\right) \frac{1}{2\pi} \cos nz_1 \cos my_2 \end{aligned} \tag{6.61}$$

The only non-zero result comes from the rotation and as for the diagonal case is logarithmically divergent with Λ. The corrections will be given by the general formula

$$\delta_c m^2 = \frac{g^2}{64\pi^2}\left(8C(G) - \frac{1}{3}\sum_s C(r_s)\right) L \tag{6.62}$$

The explicit corrections are then

$$\delta^2_{cB^2} = -\frac{1}{3}\frac{g_1^2}{64\pi^2} L \tag{6.63}$$

$$\delta^2_{cW^2} = \frac{47}{3}\frac{g_1^2}{64\pi^2} L \tag{6.64}$$

$$\delta^2_{cG^2} = 24\frac{g_1^2}{64\pi^2} L \tag{6.65}$$

$$\tag{6.66}$$

The mass eigenvalues will then be modified by those off-diagonal mixings. We note the diagonal corrections to a gauge boson as δ^2 and the off-diagonal entries as δ^2_c. The mass matrix will have the form

$$\begin{pmatrix} 1+\delta^2 & \delta^2_c \\ \delta^2_c & 1+\delta^2 \end{pmatrix} \tag{6.67}$$

and can be easily diagonalized with new mass eigenvalues

$$m^2 = \frac{n^2}{R^2}\left(1 + \delta^2 \pm \delta^2_c\right) = \frac{n^2}{R^2}\left(1 + \delta^2_{n\pm}\right) \tag{6.68}$$

The new eigenstates will then have the form

$$B^{n\pm} = \frac{1}{\sqrt{2}}\left(B^{(n,0)} \pm B^{(0,n)}\right) \tag{6.69}$$

Note that if we impose the assumption $R_4 \gg R_5$ then there is no mixing between the two tiers as one of those is decoupled from the theory. As the divergent part in δ and δ_c have the same

coefficient, it turns out that the fields B_μ^{n-} are insensitive to divergences. This can also be explained by the fact that their wave function vanishes on the singular points. For the odd modes, no mixing takes place, therefore, at loop level, we have two exactly degenerate tiers of odd states, and in particular two degenerate dark matter candidates.

Electroweak symmetry breaking

The last thing we need to add to have all the relevant contributions for the $(2,0)-(0,2)$ gauge bosons at one loop order is the electroweak symmetry breaking effect from the higgs expectation value. Note that higgs corrections are diagonal, due to the flatness of the higgs VEV in the extra dimensions and thus do not introduce mixing between the two tiers. We can then still use the field expansion presented in the section 5.2 but with the mass eigenvalues modified by the higgs VEV contribution. The higgs VEV will mix the $B^{(k,l)}$ and $W_3^{(k,l)}$ gauge bosons in each tier separately. The mixing angle θ_{kl} will be different in each tier (k,l) because of different loop corrections.

The mass terms for the electroweak gauge sector after introducing the diagonal loop corrections and the higgs VEV will be written as

$$\left(W_3^{n\pm} B^{n\pm}\right) \cdot \begin{pmatrix} m_{W^{n\pm}}^2 + m_W^2 & -\tan\theta_W m_W^2 \\ -\tan\theta_W m_W^2 & m_{B^{n\pm}}^2 + \tan^2\theta_W m_W^2 \end{pmatrix} \cdot \begin{pmatrix} W_3^{n\pm} \\ B^{n\pm} \end{pmatrix} \tag{6.70}$$

We then diagonalize the system as in the simple Standard Model case

$$\begin{pmatrix} Z^{n\pm} \\ A^{n\pm} \end{pmatrix} = \begin{pmatrix} \cos\theta_{n\pm} & \sin\theta_{n\pm} \\ -\sin\theta_{n\pm} & \cos\theta_{n\pm} \end{pmatrix} \cdot \begin{pmatrix} W_3^{n\pm} \\ B^{n\pm} \end{pmatrix} \tag{6.71}$$

The mass eigenvalues at each level (k,l) will be then given by

$$m_{A^{n\pm}}^2 = \frac{n^2}{R^2} + \frac{1}{2}\left(m_Z^2 + \delta_{B^{n\pm}}^2 + \delta_{W^{n\pm}}^2 - \sqrt{(m_Z^2 + \delta_{B^{n\pm}}^2 - \delta_{W^{n\pm}}^2)^2 - 4m_W^2(\delta_{B^{n\pm}}^2 - \delta_{W^{n\pm}}^2)}\right) \tag{6.72}$$

$$m_{Z^{n\pm}}^2 = \frac{n^2}{R^2} + \frac{1}{2}\left(m_Z^2 + \delta_{B^{n\pm}}^2 + \delta_{W^{n\pm}}^2 + \sqrt{(m_Z^2 + \delta_{B^{n\pm}}^2 - \delta_{W^{n\pm}}^2)^2 - 4m_W^2(\delta_{B^{n\pm}}^2 - \delta_{W^{n\pm}}^2)}\right) \tag{6.73}$$

and the mixing angle is

$$\tan\theta_{n\pm} = \frac{m_{Z^{n\pm}}^2 - m_{A^{n\pm}}^2 + m_Z^2 - 2m_W^2 + \delta_{B^{n\pm}}^2 - \delta_{W^{n\pm}}^2}{2m_W m_Z \sin\theta_W} \tag{6.74}$$

The mixing angle for each tier depends on the compactification scale and for large masses m_{KK} becomes negligibly small. This is a general feature of extra-dimensional models. That is also why often one can neglect the mixing between gauge bosons when the experimentally privileged mass scale m_{KK} is sufficiently large.

Note that loop corrections are proportional to the characteristic mass scale of the given tier, m_{kl} and the correction $\delta_{B^2}^2$ is negative for both tiers. That is the reason why the mixing angle is smaller for heavier states.

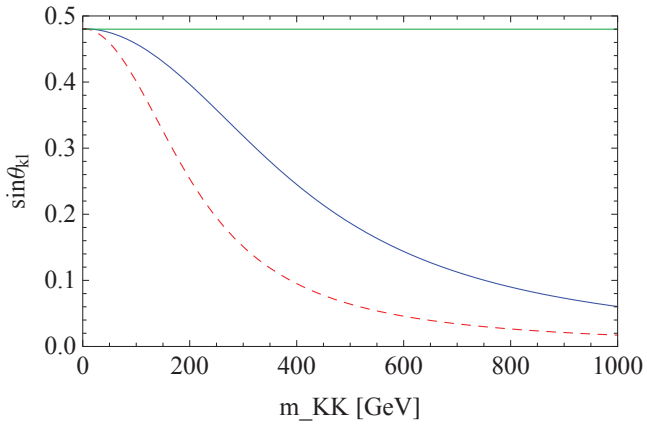

Figure 6.2: Mixing angle θ_{kl} for the first two tiers: $(1,0)$ in blue and for $(2,0)$ in red dashed. The green line corresponds to the Weinberg mixing angle $\sin\theta_W = 0.48$. Here we assume the degenerate radii $R_4 \gg R_5$.

Physical mass eigenstates After including the electroweak symmetry breaking, and all the diagonal and non-diagonal radiative corrections the mass eigenvalues for the physical states A^2_μ, Z^2_μ, W^2_μ and G^2_μ, assuming non degenerate radii, are given by

$$\begin{aligned} m^2_{A^2} &= 4m^2_{KK} - \delta + (\delta_{B^2} + \delta_{W^2})m^2_{KK} + m^2_W + s^2_w m^2_Z && (6.75)\\ m^2_{Z^2} &= 4m^2_{KK} + \delta + (\delta_{B^2} + \delta_{W^2})m^2_{KK} + m^2_W + s^2_w m^2_Z && (6.76)\\ m^2_{W^2} &= m^2_{KK}(4 + \delta_{W^2} + m^2_W) && (6.77)\\ m^2_{G^2} &= m^2_{KK}(4 + \delta_{G^2}) && (6.78) \end{aligned}$$

with

$$\delta^2 = -4\left(\delta_{B^2}\delta_{W^2}m^4_{KK} + (m^2_W\delta_{B^2} + s^2_W m^2_Z\delta_{W^2})m^2_{KK}\right) + \left((\delta_{B^2} + \delta_{W^2})m^2_{KK} + m^2_W + s^2_W m^2_Z\right)^2 \quad (6.79)$$

In the figure 6.3 we show mass splittings $\Delta m = m - 2m_{KK}$ for the gauge boson sector. $A^{(2,0)}$ receives the smallest corrections and is the lightest particle in the tier. Electroweak gauge bosons $Z^{(2,0)}$ and $W^{(2,0)}$ are heavier due to the $\mathrm{SU(2)_W}$ couplings and the heaviest particle is the gluon $G^{(2,0)}$ which receives the largest corrections from $\mathrm{SU(3)_C}$ interactions. Note also that as the mass corrections are proportional to the tree level mass of the tier, the $(2,0)$ level mass splittings are larger than their $(1,0)$ partners.

Those masses are calculated under the assumption that the radii are not-degenerated, that is $R_4 \gg R_5$. In that simplifying case only one tier, the $(2,0)$-one, will contribute to the physical states of the theory while the $(0,2)$ states will be decoupled being too heavy to participate in any phenomenologically detectable process. In the symmetric case $R_4 = R_5$, as it was mentioned, the mass corrections to the $(0,2)$ physical states will be the same as for $(2,0)$ tier. On each level we will have two degenerate in mass states that will mix with each other as there are non-diagonal contributions to the kinetic terms in the lagrangian coming from the rotation contribution. We are investigating the more general case, where we include the dependence on the ratio $\xi = R_4/R_5$, the phenomenology of this model is left to the future work.

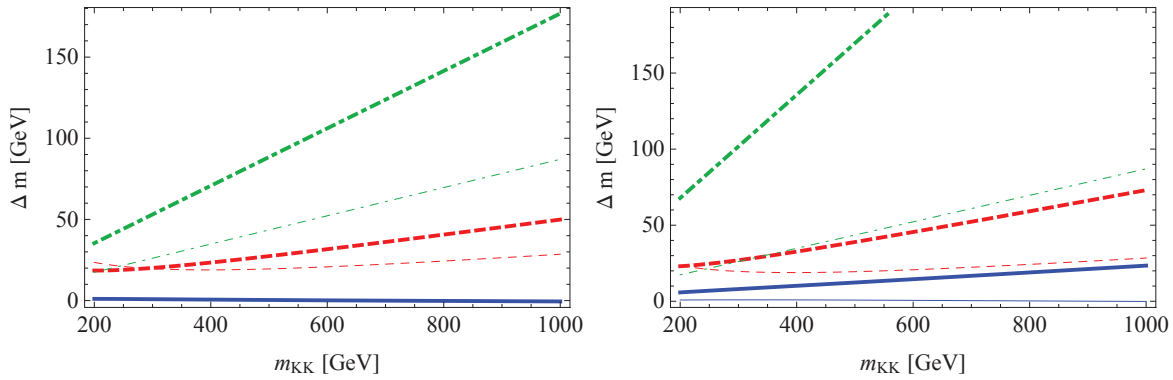

Figure 6.3: Mass splittings $\Delta m = m - m_{tree}$in the gauge sector. Thicks lines: blue - A^2, red dashed - W/Z^2, green dot-dashed G^2. For comparison, in the same colors and thin lines, we show also the $(1,0)$ gauge boson mass splittings. **On the left** non-symmetric case $R_4 \gg R_5$. **On the right** symmetric case $R_4 = R_5$

6.3.2 Loop corrections to the $(2,0) - (0,2)$ fermions

Diagonal corrections

The radiative corrections to a KK fermion excitation can be written as

$$\delta\mathcal{L} = a_L\bar{\Psi}\gamma^\mu p_\mu P_L\Psi + a_R\bar{\Psi}\gamma^\mu p_\mu P_R\Psi - b\bar{\Psi}\Psi \tag{6.80}$$

and the general form of the mass correction is

$$\delta m_F = b - \frac{m_n}{2}(a_L + a_R) \tag{6.81}$$

Radiative corrections arise from the loops shown in the figure 6.4 where we recall that the M index labels all the six components of a 6D gauge boson field.

Figure 6.4: Radiative corrections to fermion masses

The calculation of loops is analogous to the gauge boson self energy case. The general loop structure can be written in the following way:

$$i\Pi = N\int d^4k d^2\vec{y}_1 d^2\vec{y}_2 \Psi(\vec{y}_2)\Gamma^\alpha G_\Psi^{RPP}(k, \vec{y}_2 - \vec{y}_1)\Gamma_\alpha\Psi(\vec{y}_1)G_\Phi^{RPP}(k, \vec{y}_1 - \vec{y}_2) \tag{6.82}$$

where $N = \frac{g^2 C_2(r)}{16\pi^4}$ and $C_2(r) = \frac{N^2-1}{2N}$ for the fundamental representation of SU(N) and $C_2(r) = q^2$ for the $U(1)$ for the gauge boson running in the loop. For the scalar contribution $N = \frac{y_F^2}{16\pi^4}$ where y_F is the effective Yukawa coupling.

As in the previous section loop correction can be split into four parts and the contributions we find for a $(n,0)$ fermion with $p_r = +1$ are listed in the table 6.4.

$\delta m^2_{(n,0)}$	Π_T	Π_G	Π_{GR}	Π_R
$n^2 a_{Lg}$	0	0	$-\frac{1}{2}\Phi_2(n)$	0
$n^2 a_{Rg}$	0	0	$-\frac{1}{2}(\zeta(3)-\Phi_1(n)+\Phi_2(n)$	0
$n^2 b_g$	0	0	$-\frac{1}{2}3n\Phi_2(n)$	$4L$
$n^2 a_{Ls}$	0	0	$-\frac{1}{2}\Phi_2(n)$	0
$n^2 a_{Rs}$	0	0	$-\frac{1}{2}(\zeta(3)-\Phi_1(n)+\Phi_2(n)$	0
${}^2 b_s$	0	0	$-\frac{1}{2}3n\Phi_2(n)$	$2L$

Table 6.4: Radiative corrections to the fermion $(n,0)$ with n even, self energy.

In general the contributions for the 6D left and right fermions, i.e. with $p_r = \pm 1$ are different due to their different wave functions. The $\tilde{\Pi}_T$ gives always zero as the integral is linear in k. The glide contribution $\tilde{\Pi}_G$ for a fermion with $p_r = +1$ gives zero result as well, while for $p_r = -1$ we find in general the overall contribution proportional to $((-)^n - 1)\cdot\zeta(3)$. Therefore for the $n = 1$ modes the contribution will be automatically set to zero while for $n = 2$ states we get a part $\zeta(3)$. The situation is inversed for the $\tilde{\Pi}_{GR}$ contributions. Here the $p_r = -1$ states receive a zero contribution for every $n \in \mathbb{N}$ while the $p_r = +1$ states gain a contribution $\sim ((-)^n - 1)\cdot\zeta(3)$. The part coming from the rotation $\tilde{\Pi}_R$ gives the same divergent result for all the fermions $(2n,0)$ and $(0,2n)$ with $p_r = \pm 1$ which is equal to $\pi^2 n^3 L$. Contributions from scalar, a_s and b_s, are analogous to those of gauge bosons but give different coefficients as can be seen in the table 6.4. Besides this changes in $\tilde{\Pi}_{GR}$ and $\tilde{\Pi}_G$ for $p_r = \pm 1$ $(n,0)$ fermions the overall contribution to the loop , that is $\tilde{\Pi} = \tilde{\Pi}_T + \tilde{\Pi}_G + \tilde{\Pi}_{GR} + \tilde{\Pi}_R$ will be the same.

The general mass correction for a fermion in the fundamental representation of $\mathrm{SU(2)_W}$ and $\mathrm{SU(3)_C}$ with the hypercharge y_f can be written as

$$m\delta m = \frac{n^2}{64\pi^4 R62} \left[\left(y_f^2 g_1^2 + \frac{3}{4}g_2^2 + \frac{4}{3}g_3^2\right)\left(7\zeta(3) - \Phi_1(n) - 4\Phi_2(n) + 4n^2 L\right)\right. \quad (6.83)$$

$$\left. + \quad y_f\left(\frac{1}{2}7\zeta(3) - \frac{1}{2}\Phi_1(n) + \frac{1}{2}n^2 L\right)\right] \quad (6.84)$$

The first part in this equation comes from the gauge boson contribution in the loop, the second one comes from scalar propagation and is included only for top quarks.

Mixings between tiers

As for the gauge bosons, there are also mixings between levels $(2,0)$ and $(0,2)$. The contributions come from the rotation projection of the orbifold and are in general different for fermions with right- handed and left-handed zero mode. The full analysis of the mixing terms was performed by G. Cacciapaglia. Here we give a short summary of the results. The overall off-diagonal contribution to the masses can be written as

$$\delta_{cf} = \frac{1}{64\pi^4}\left[4\left(y_F^2 g_1^2 + \frac{3}{4}g_2^2 + \frac{4}{3}g_3^2\right) + \frac{1}{2}y_F^2\right] n^2 L \quad (6.85)$$

where the term in curly brackets corresponds to the corrections to the mass term and the last term to the corrections to the kinetic terms. One needs to diagonalize the mass terms which have the form

$$\frac{n}{R}\begin{pmatrix} 1+\delta & \delta_{cf} \\ \delta_{cf} & (1+\delta) \end{pmatrix} \tag{6.86}$$

This can be done by diagonalize of the squared mass matrix

$$M^\dagger M = \frac{n^2}{R^2}\begin{pmatrix} (1+\delta^2)^2+\delta_{cf}^2 & 2\delta_{cf}(1+\delta) \\ 2\delta_{cf}(1+\delta) & (1+\delta^2)^2+\delta_{cf}^2 \end{pmatrix} \tag{6.87}$$

and using unitary matrix $U^\dagger U = \mathbb{I}$ which mixes the states

$$\begin{pmatrix} \Psi_{2+} \\ \Psi_{2-} \end{pmatrix} = \begin{pmatrix} \cos\phi & -\sin\phi \\ \sin\phi & \cos\phi \end{pmatrix} \cdot \begin{pmatrix} \Psi^{(2,0)} \\ \Psi^{(0,2)} \end{pmatrix} \tag{6.88}$$

The mixing angle is the $\phi = \frac{\pi}{4}$ and the mass eigenstates are simply given by

$$m_\pm^2 = \frac{n^2}{R^2}(1+\delta^2 \pm \delta_{cf}^2) \tag{6.89}$$

In general analysis with an explicit dependence of the non-degenerate radii $R_4 \neq R_5$ but not $R_4 \gg R_5$, which is now in progress in our group, one can see that in general the corrections to fermions with the right- and left-handed zero mode differ. Then the calculation presented above has to be repeated twice for each type of fermion, the mixing angles ϕ_L and ϕ_R will then be different as well as the mass eigenstates. Once the assumption $R_4 \gg R_5$ is imposed the results simplify to the case presented here.

As it was mentioned in the section 5.2, we include Yukawa interactions for top quarks only. For the top quarks in the second tier we use the expressions 5.74 - 5.77 to calculate the mixing angle and the mass eigenstates and eigenvalues. In the figure 6.5 we show the mixing angles for the two tiers $(1,0)$ and $(2,0)$.

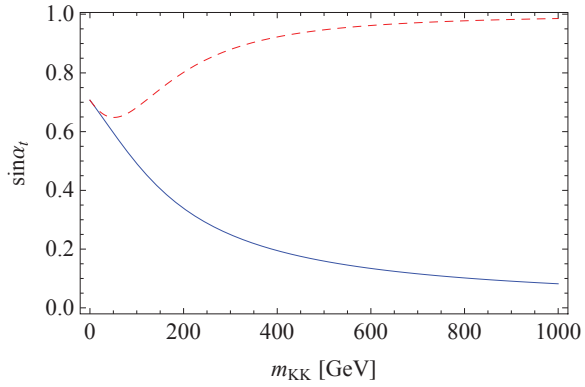

Figure 6.5: Mixing angle in the top sector. For the $(1,0)$ tier in blue, for the $(2,0)$ tier in red dashed.

Finally we give all the spectrum of fermions in our model. The smallest radiative corrections are those of singlet leptons. The $SU(2)_W$ doublet leptons receive stronger corrections due to electroweak interactions. KK quarks excitations, due to $SU(3)_C$, interactions suffer the higher mass splittings.

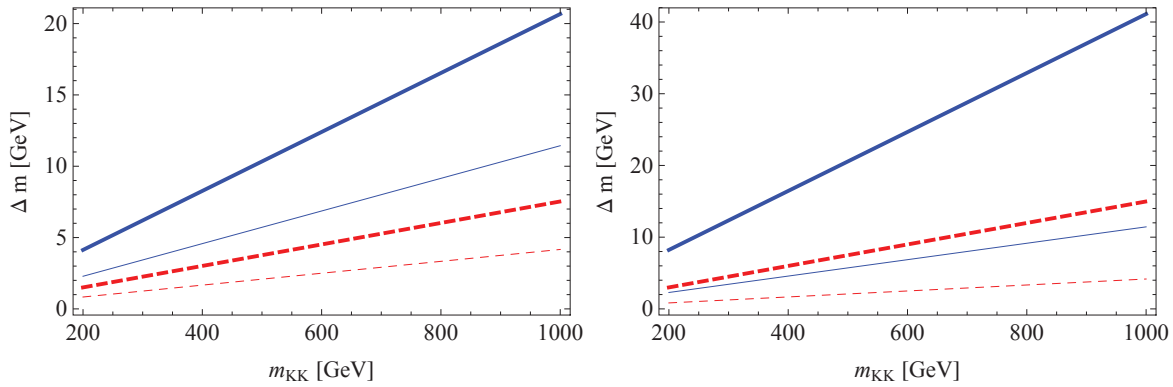

Figure 6.6: Mass splittings $\Delta m = m - m_{tree}$ in the leptonic sector. In both figures thick lines corresponds to the level $(2,0)$ and thin lines to the level $(1,0)$. Mass splittings for leptons L in blue and e_R in red. **On the left** non-symmetric case $R_4 \gg R_5$. **On the right** symmetric case $R_4 = R_5$

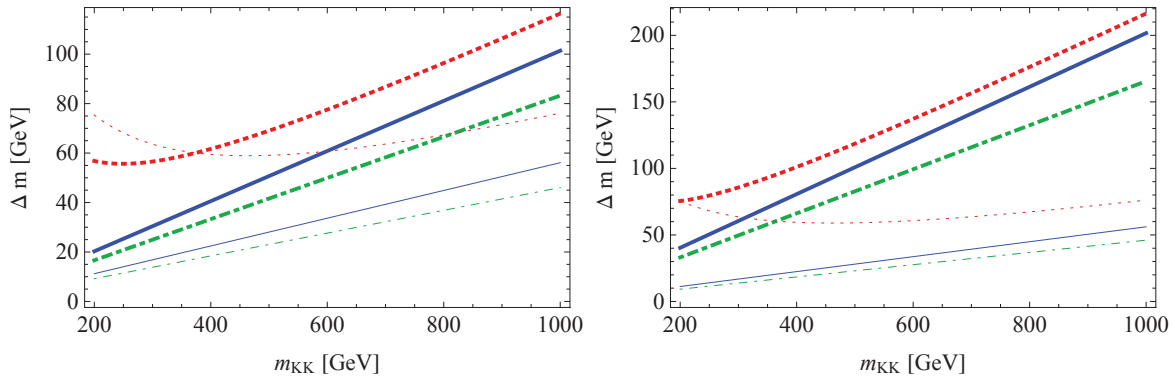

Figure 6.7: Mass splittings $\Delta m = m - m_{tree}$ in the quark sector. In both figures thick lines corresponds to the level $(2,0)$ and thin lines to the level $(1,0)$. Q_D in blue, q_S in green dot-dashed, *top* in red dotted. **On the left** non-symmetric case $R_4 \gg R_5$. **On the right** symmetric case $R_4 = R_5$

6.3.3 Heavy higgs bosons

On the second level the higgs boson excitations are also present while they were absent on the $(1,0)$ level due to vanishing $\Phi^{(+,+)}$ wave-functions. On the second level, there are four states arising from the higgs doublet as it was decomposed in eq. 5.66 which we name H^2 and S^{02} neutral, and charged partners $S^{2\pm}$. Loop corrections to the masses of those scalar particles were calculated by G. Cacciapaglia. Their structure is similar to the gauge bosons: there are finite contributions from the torus and glides which are almost mode-independent, while the logarithmically divergent terms are proportional to the mass of the mode. Loops also contain quadratically divergent contributions which correspond to a localized mass. At loop level the masses of the physical states H^2 and S^0 and $S^{2\pm}$ are given by

$$\begin{aligned} m^2_{H_{(2,0)}} &= m_h^2 + (4+\delta_{h^2})m_{KK} + m^2_{loc} \\ m^2_{s_{(2,0)}} &= (4+\delta_{h^2})m_{KK} + m^2_{loc} \end{aligned} \tag{6.90}$$

with the mass correction given by

$$\delta_{h^2} = -\frac{17}{64\pi^4}(g_1^2 + 3g_2^2)L \tag{6.91}$$

In the $R_4 = R_5$ case the mixing between $(n, 0)$ and $(0, n)$ levels must be taken into account as we have done for fermions and gauge bosons. As the quartic coupling is in the bulk, the off-diagonal terms will be the same for the four higgs states:

$$\delta_{ch} = -n^2 m_{KK}^2 \delta_{h^2} + 2m_{loc}\,. \tag{6.92}$$

In the degenerate radii case, new divergent corrections from rotation fixed points will arise with the same value as the diagonal correction given above. The new mass eigenvalues are given by:

$$m^2_{\pi(2+)} = m^2_{\pi,(2,0)} + \delta_{ch} = n^2 m_{KK}^2(1 - 2\delta_{h^2}) + 3m_{loc}^2\,, \tag{6.93}$$

$$m^2_{\pi,(2-)} = m^2_{\pi,(2,0)} - \delta_{ch} = n^2 m_{KK}^2 - m_{loc}^2\,. \tag{6.94}$$

Therefore in the symmetric case the value in eq. 6.91 must be multiplied by a factor of two. Note that the mass correction δ_{h^2} is negative and we find it to be equal to $\delta_{h^2} = -0.174$ for non-degenerate radii and $\delta_{h^2} = -0.348$ for the degenerate case. It will therefore become the lightest particle in the second tier and together with $A^{(2)}$ will play an important role in the relic abundance calculation.

The m_{loc} parameter corresponds to the localized mass parameter to the higgs particle on the fixed points of the orbifold. In the phenomenological analysis of the model we use the null value $m_{loc} = 0$ except for the dark matter relic abundance analysis where the resonances of the heavy higgs particles play a crucial role in the enhancement of the effective annihilation cross section. In the figure 6.8 we show the mass splittings of the heavy higgs particle for three different values of m_{loc} parameter. Note that for vanishing m_{loc} the higgs excitations will be the lightest particles in the second tier.

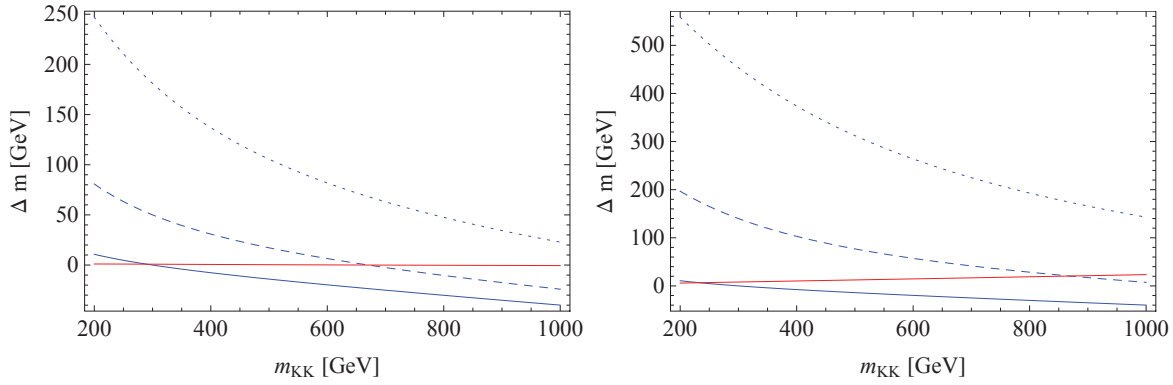

Figure 6.8: Mass splittings $\Delta m = m - m_{tree}$ in the higgs sector. In both figures thick lines corresponds to the level $(2, 0)$ and thin lines to the level $(1, 0)$. We show the splittings of $H^{(2)}$ for three values of m_{loc} parameter: $m_{loc} = 0$ GeV in blue, $m_{loc} = 250$ GeV in blue dashed and $m_{loc} = 500$ GeV in blue dotted. **On the left** non-symmetric case $R_4 \gg R_5$. **On the right** symmetric case $R_4 = R_5$. Red line corresponds to the $A^{(2)}$ splitting for comparison.

It is important to have a precise limit on m_{loc}. The simple estimate $m_{loc} < m_{KK}$ is a good starting point as we can assume that m_{loc} can be treated as a small parameter with respect to the heavy scales, allowing a perturbative approximation. In order to put more stringent limits note that this parameter will affect the electroweak precision test through mixing effects. This

can be understood as follows. An effect of m_{loc} is to generate mass mixing of the SM higgs with the heavy KK higgses in the form $m_{loc}^2 h^{(0,0)} H^{(n,m)}$. When the SM higgs mode acquires the VEV v, then the tadpole generated by this mixing term will generate the VEV for a heavy higgs modes:

$$\langle H^{(n,m)} \rangle \sim \frac{m_{loc}^2}{m_{KK}^2} \frac{v}{n^2+m^2} \tag{6.95}$$

Another effect of the higgs VEV is in the electroweak gage sector. The bulk kinetic term of the higgs contains terms $\sim H^{(0,0)} H^{(n,m)} W^{(0,0)} W^{(n,m)}$ which will be modified by the higgs VEV as

$$H^{(0,0)} H^{(n,m)} W^{(0,0)} W^{(n,m)} \to \frac{m_{loc}^2}{m_{KK}^2} \frac{v^2}{n^2+m^2} W^{(0,0)} W^{(n,m)} \tag{6.96}$$

The analogical expressions hold for Z bosons as well. By calculating the correction to the masses of SM W and Z gauge bosons we can extract the allowed bounds for m_{loc} by calculating the corrections to the ρ parameter. Our result is

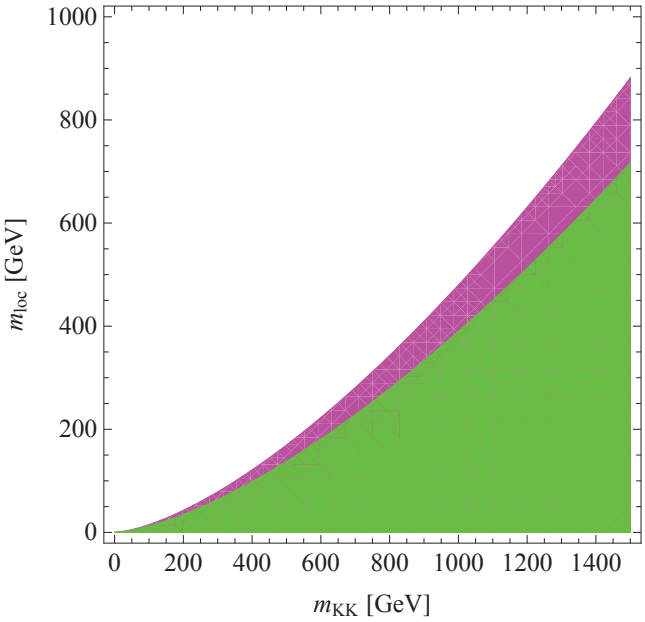

Figure 6.9: Bound on m_{loc} as a function of the m_{KK} mass, obtained imposing that the effect on the ρ parameter is not larger than the allowed measured value within 3 sigmas. In green we plot the excluded region in the symmetric scenario $R_4 = R_5$ and in magenta in the asymmetric case $R_4 \gg R_5$.

$$\delta\rho = -8 \frac{m_{loc}^4}{m_{KK}^4} \frac{m_Z^2 - m_W^2}{m_{KK}^2} f(\xi) \tag{6.97}$$

where $\xi = \frac{R_4}{R_5}$ and $f(\xi)$ is a number of order 1. We compare the $\delta\rho$ to the bounds given in PDG $\rho = 1.0004^{+0.0003}_{-0.0004}$ and obtain the bounds plotted in the figure 6.9 where in green we show the excluded region in the symmetric scenario $R_4 = R_5$ and in magenta for the asymmetric case $R_4 \gg R_5$.

6.3.4 Full mass spectrum at loop level - summary

In the tables 6.5 and 6.6 we give values of masses of all the particles present in the model for three benchmark points that will be important for the phenomenological analysis $m_{KK} =$ 300, 500, 800 GeV. The radiative corrections to the KK masses depend on whether we assume $R_4 = R_5$ or $R_4 \gg R_5$ only in the second tier $(2,0) - (0,2)$ as there are cross-level mixing terms. We give the mass spectrum in both cases.

m_{KK} [GeV]	300	500	800
$A^{(1,0)}$	300.9	500.5	800.2
$l_S^{(1,0)}$	301.3	501.5	803.0
$l_D^{(1,0)}$	303.4	504.5	808.4
$d_S^{(1,0)}$	313.8	519.2	836.6
$u_S^{(1,0)}$	314.2	519.7	837.6
$W^{(1,0)}$	317.8	515.0	822.1
$Z^{(1,0)}$	319.6	515.8	822.3
$q_D^{(1,0)}$	316.8	522.9	843.9
$t_S^{(1,0)}$	361.0	550.5	859.8
$t_D^{(1,0)}$	363.6	553.6	866.1
$G^{(1,0)}$	326.1	534.9	868.4

Table 6.5: Typical masses of the particles of the level (1,0) at $m_{KK} = 300$, 500 and 800 GeV. The mass splittings are independent on the symmetric or asymmetric case as there is no cross-level mixing.

In both tiers the lightest particle is the photon excitation $A^{(n)}$. The reason for that is the small mixing angle θ_n which makes of the $\mathrm{U(1)_Y}$ gauge boson $B^{(n)}$ the main component of the physical state $A^{(n)}$ and that the mass corrections to $B^{(n)}$ in both levels are negative.

In the first tier $A^{(1)}$ is neutral spin-0 particle and corresponds to the dark matter candidate in our model. For the $m_{KK} < 200$ GeV the lightest particle in the first tier is the singlet electron which excludes the model on this range of m_{KK} parameter as there would be no dark matter particle. Then the next lightest particles are singlet and doublet leptons and the $\mathrm{SU(2)_W}$ gauge bosons which will play an important role in the dark matter phenomenology in the coannihilation processes. $\mathrm{SU(3)_C}$ particles are heavy but still their role cannot be neglected in the dark matter prediction and in collider phenomenology as they have strong couplings which will enhance all the processes where quarks are involved.

In the second tier, the lightest particle is a vector gauge boson $A^{(2)}$ and higgs excitations if m_{loc} parameter is set to zero. Due to extremely small mass corrections of $A^{(2)}$ it will decay only into SM particles via localized interactions and thus will play an important role in the LHC phenomenology enhancing the resonant productions of SM particles. The weak gauge bosons $W^{(2)}$ and $Z^{(2)}$ will decay into other heavy particles but the resonant decays into SM fermions will not be negligible giving rise to an interesting phenomenology in the LHC. All the level (2) particles will also participate into resonant annihilations and coannihilations of the primordial

m_{KK} [GeV]	300	500 GeV	800
$S^{(2,0)}$	600.0	993.4	1568.3
$A^{(2,0)}$	600.9	1000.3	1599.8
$H^{(2,0)}$	600.0	1001.3	1573.3
$l_S^{(2,0)}$	602.3	1001.2	1605.4
$l_D^{(2,0)}$	606.2	1003.2	1615.0
$W^{(2,0)}$	619.6	1010.5	1636.8
$Z^{(2,0)}$	620.0	1010.8	1636.8
$d_S^{(2,0)}$	625.0	1014.7	1665.5
$u_S^{(2,0)}$	625.7	1015.0	1667.3
$q_D^{(2,0)}$	630.4	1017.5	1678.6
$t_S^{(2,0)}$	651.9	1031.3	1682.0
$G^{(2,0)}$	653.1	1031.8	1739.2
$t_D^{(2,0)}$	656.6	1033.7	1693.3

m_{KK} [GeV]	300	500 GeV	800
$S^{(2,0)}$	573.3	955.6	1528.9
$A^{(2,0)}$	601.0	1000.2	1599.5
$H^{(2,0)}$	586.8	963.7	1534.0
$l_S^{(2,0)}$	604.5	1007.5	1612.0
$l_D^{(2,0)}$	612.3	1020.6	1632.9
$W^{(2,0)}$	633.5	1050.5	1677.9
$Z^{(2,0)}$	633.8	1050.6	1677.9
$d_S^{(2,0)}$	659.9	1094.4	1744.0
$u_S^{(2,0)}$	661.4	1096.9	1748.0
$q_D^{(2,0)}$	670.7	1112.5	1772.9
$t_S^{(2,0)}$	688.4	1118.2	1768.7
$G^{(2,0)}$	721.1	1191.8	1893.5
$t_D^{(2,0)}$	697.7	1133.8	1793.6

Table 6.6: Typical masses of the particles of the level (2,0) at $m_{KK} = 300$, 500 and 800 GeV. **On the left** asymmetric case $R_4 \gg R_5$. **On the right** symmetric case $R_4 = R_5$.

cosmic plasma reducing significantly the relic abundance of the dark matter and thus changing strongly the bounds of the cosmologically allowed m_{KK} values. We will present in details those phenomenological aspects of the model in the following chapters.

Chapter 7

Relic Abundance of Dark Matter

Dark matter candidate

The full spectrum of our model at one loop order was presented in the chapter 6. The essential feature of the spectrum is that the viable dark matter candidates are the spinless photons $A^{(1,0)}$ and $A^{(0,1)}$. These particles, assuming degenerate radii $R_4 = R_5$, have the same mass and are the lightest particles in the first level for $m_{KK} \geq 200$ GeV. For $m_{KK} < 200$ GeV the lightest KK particle is the right handed electron $e_S^{(1,0)}$ and/or $e_S^{(0,1)}$. Note that there could be some contributions from the UV scale physics to the operators localized at the corners of the fundamental domain, that is on the points $\mathcal{O}_0$ and $\mathcal{O}_\pi$ which would modify the mass spectrum. In principle, these contributions, a priori dependent on some unknown parameters, could turn some other $(1,0)$ particle into the lightest KK odd state. Hence, the $(1,0)$ modes of neutrinos $\nu^{(1,0)}$ or the neutral electroweak gauge boson $Z^{(1,0)}$ could all be viable dark matter candidates. We leave the investigation of these possibilities for future work. Note that, in contrast to the chiral square and minimal UED (5-dimensional space with the extra dimension compactified on an interval denotes hereafter as mUED) models where the $(1,0)$ level higgs boson is also a viable dark matter candidate, the higgs $(1,0)$ mode vanishes $h^{(1,0)} \equiv 0$ on the $\mathbb{R}P^2$ so we won't have to consider this dark matter candidate.

General assumptions

In our computation we consider a most general particle spectrum without any simplifying assumptions. In particular we do not assume a completely degenerated particle spectrum but we keep the non-degenerated KK masses after one-loop corrections to the $(n,0)$ modes. We keep all the SM particle masses non zero, except the electron mass which will be neglected. Moreover we do not neglect the mixing between $B^{(1,0)}$ and $W_3^{(1,0)}$ that originates from the electroweak symmetry breaking and which is expected to be small for large m_{KK} but effectively is quite large for small values of m_{KK}.

In our analytical and numerical calculations we make some simplifying assumptions for the Yukawa couplings. We neglect all the Yukawa couplings, which are proportional to the corresponding fermion mass, for all the light SM particles except top quarks. This assumption is well justified as the annihilations into fermionic final states are suppressed by the corresponding fermion mass and thus their contribution is already negligible, adding the Yukawa couplings would not alter the final result in a significant way. The Yukawa coupling lead however to the resonant s - channel exchange of the SM higgs and its KK excitations. While the SM higgs effect

is negligible the resonances coming from the exchange of the $(2,0)$ level higgses are important and, as we will see, they enhance the effective cross section in a small region of m_{KK} near the resonant value. Aside those effects, we do not expect our results to be sensitive to the masses of light fermions.

In all the analytical calculations when examining the relic density as a function of the mass scale m_{KK} we neglect the weak, approximately logarithmic mass dependence of x_F. Typically, over the mass range m_{KK}=0.2 - 1 TeV, x_F varies by about 0.1 GeV/degree, or less than 15%. This variation has little effect on the relic density. This also shows that the dark matter is cold. In all cases considered here we obtain $22 \lessapprox x_F \lessapprox 30$ GeV, so that the particles are well approximated as non-relativistic. This translates to the freeze-out temperatures in the range 34-45 GeV depending on the scenario.

Note that in what follows we consider two simplifying assumptions. Namely we assume degenerate radii of extra-space $R_4 = R_5$ or a decoupling limit $R_4 \gg R_5$. As it was mentioned in chapter 6 the masses and couplings depend on the relative size of the two extra dimensions in our model. The study of this explicit dependence of the relic abundance bounds is left for further investigation. In the two simple cases considered here the mass spectrum of the first KK level does not depend on whether the radii are symmetric or not. The second KK level although is affected by the mixing terms in the symmetric scenario and the mass spectrum will be slightly shifted towards higher values. The important fact for the relic abundance calculation is that in both cases the KK vector photon $A^{(2)}$ and the KK scalar higgs excitation $H^{(2)}$ are the lightest particles in the second tier and will not decay into any KK excitations. This in turn will strongly reduce the relic abundance.

Decoupling limit $R_4 \gg R_5$

The mass corrections are proportional to R^{-2}. Thus when one of the radii is getting reduced the mass corrections will tend to infinity

$$R_5 \to 0 \quad \Rightarrow \quad \delta m_{(0,n)} \to \infty \tag{7.1}$$

This simply means that all the particles of the $(0,n)$ tier will decouple from the theory and will not interact with ordinary matter nor with the $(n,0)$ tier states. In this case the natural dark matter candidate will be of course the $A^{(1,0)}$ scalar photon which will interact with all the particles of the $(n,0)$ tiers and with the SM particles. The mass spectrum in this case is not affected by the cross level mixings, therefore the logarithmic contributions from rotation projection do not contribute making the masses of the $(2,0)$ level particles slightly lighter than in the symmetric case. For the typical masses of $(2,0)$ level particles in this case one has to refer to the right panel of the table 6.6. Notice that we can equivalently take the opposite limit $R_4 \ll R_5$ without changing any of the results.

Degenerate radii $R_4 = R_5$**.**

In the symmetric scenario $R_4 = R_5$ the masses of the two tiers $(0,n)$ and $(n,0)$ are degenerated and the mixing terms with logarithmic contributions make the spectrum slightly heavier. In this case we have still two dark matter particles: $A^{(1,0)}$ and $A^{(0,1)}$ with exactly the same masses and spins as the first KK level is insensitive to the orbifold geometry $R_4 \gg R_5$ or $R_4 = R_5$.

The important property is that $A^{(1,0)}$ and $A^{(0,1)}$ do not interact with each other due to the KK conserving interactions. Namely the tiers $(0,n)$ and $(m,0)$ are decoupled [1] In our scans we will consider therefore two independent dark matter particles not interacting with each other. Their contributions to the relic density will be therefore exactly the same and the total relic abundance will be twice larger than in the non-symmetric case.

To simplify the notation we denote all the particles in the given tier $(n,0)$ or $(0,n)$ with a single superscript (n), for example $A^{(1)}$ will stand for a first KK excitation of the photon in $(1,0)$ or $(0,1)$. For the second tier we will have to remember that the spectra change slightly but still we will note $A^{(2)}$ the two mass eigenstates.

7.1 Relic abundance - analytical results

We begin the study of the relic abundance by the analytical calculation of the annihilation and co-annihilation cross sections in our model. In the analytical approach we will restrict the study to the case with only Standard Model particles in the final states. Note that in the numerical implementations we keep all the KK masses at one-loop level. The analytical formulas will be however shown assuming the masses at each KK level degenerate: i.e. for any first level particle $X^{(1)}$ we assume $m_X = m_{KK}$ and for the second level particles $X^{(2)}$ the mass will be set to $m_X = 2m_{KK}$.

We will show here the calculation of annihilation cross section in details in order to fix the notation. The dark matter candidate can annihilate into all SM particles. As we will see the cross sections into SM gauge bosons give leading contributions. The fermionic final states will not contribute once we develop the cross section for small velocities.

7.1.1 Annihilations into gauge bosons

$\mathbf{A^{(1)}A^{(1)} \to ZZ}$

The annihilation $A^{(1)}$ into Z gauge bosons is mediated only by the Standard Model higgs exchange as shown in the figure 7.1. Interaction of the $A^{(1)}$ with the Standard Model higgs boson h is given by

$$\mathcal{L}_h^{4D} = -\frac{g_2^2}{2}\frac{(c_w s_{w1} - c_{w1} s_w)^2}{c_w^2} A^{(1)} A^{(1)} h(h+v) \tag{7.2}$$

1. Note that a possible coupling would be introduced via (n,n) tiers, then the $(1,1)$ tier cannot decay into two SM states at tree level. Therefore we do not take those contributions into account in our study. This simplification is legitimate here because we do not include loop induced coupling with $(2,0)$ states. Otherwise, the result to be completely consistent one should also care about the mixed interactions $(1,0)$ $(0,1)$ $(1,1)$. Note however that the resonance condition $(p_1+p_2)^2 \leq m_{res}^2$ is never satisfied for those modes and the decays into SM particles would mediated only by loop level couplings therefore the contributions of the (1,1) can be safely neglected.

where g_2 is the SU(2) gauge coupling constant, s_w and c_w are the sine and cosine of the Standard Model Weinberg mixing angle ($s_w^2 = 0.23$) and s_{w1}, c_{w1} are the electroweak mixing angles of the first KK tier and $v \approx 246$ GeV is the electroweak scale. The annihilation cross section into a pair of Z bosons reads

$$\sigma(A^{(1)}A^{(1)} \to ZZ) = Y_{A^1}^2 Y_Z^2 \frac{s^2 - 4sm_Z^2 + 12m_z^4}{128\pi s m_Z^4 (s - m_h^2)^2} \sqrt{\frac{s - 4m_Z^2}{s - 4m_{KK}^2}} \tag{7.3}$$

Where $Y_{A^1} = \frac{g_2^2 v(c_w s_{w1} - c_{w1} s_w)^2}{2c_w^2}$ is the higgs -$A^{(1)}$ coupling and $Y_Z = \frac{g_2^2 v}{2c_w^2}$ is the standard Model higgs-Z coupling constant.

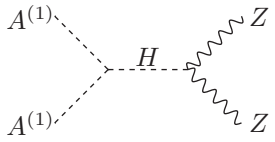

Figure 7.1: Annihilations of $A^{(1)}A^{(1)}$ into Standard Model Z gauge bosons.

Expanding the cross section in powers of the relative speed between the $A^{(1)}$ photons, v_{rel}, gives

$$v_{rel}\sigma(A^{(1)}A^{(1)} \to ZZ) \approx a_{ZZ} + b_{ZZ} v_{rel}^2 + \mathcal{O}(v_{rel}^4) \tag{7.4}$$

and the first two terms in this non-relativistic expansion are

$$a_{ZZ} = Y_{A^1}^2 Y_Z^2 \frac{4m_{KK}^4 - 4m_{KK}^2 m_Z^2 + 3m_Z^4 \sqrt{m_{KK}^2 - m_Z^2}}{64\pi m_{KK}^3 m_Z^4 (m_h^2 - 4m_{KK}^2)^2} \tag{7.5}$$

$$b_{ZZ} = -Y_{A^1}^2 Y_Z^2 \left[\frac{64m_{KK}^8 - 176m_{KK}^6 m_Z^2 + 4m_{KK}^4(3m_h^2 m_Z^2 + 52m_Z^4) -}{512\pi m_Z^4 (4m_{KK}^3 - m_{KK}m_h^2)^3 \sqrt{m_{KK}^2 - m_Z^2}} \right.$$
$$\left. + \frac{12m_{KK}^2(2m_h^2 m_Z^4 + 9m_Z^6) + 15m_h^2 m_Z^6}{512\pi m_Z^4 (4m_{KK}^3 - m_{KK}m_h^2)^3 \sqrt{m_{KK}^2 - m_Z^2}} \right] \tag{7.6}$$

$\mathbf{A^{(1)}A^{(1)} \to W^+W^-}$

The annihilation of $A^{(1)}$ into $W^\pm$ gauge bosons is mediated by the SM higgs exchange in the s-channel, by the $W^{(1)}$ scalar partners of W in t and u-channels and finally by a direct quartic coupling with two Standard Model $W^\pm$ gauge bosons as shown in the figure 7.2.

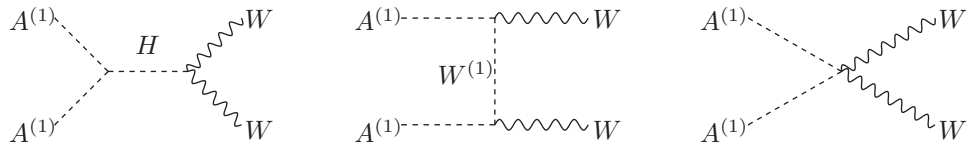

Figure 7.2: Annihilations of $A^{(1)}A^{(1)}$ into SM W gauge bosons.

For the annihilation cross section we obtain: (here to render the complicated formulas more readable we give the results for all the SM masses neglected)

$$\sigma(A^{(1)}A^{(1)} \to W^+W^-) = \frac{g_2 s_{w1}}{2\pi s(s-4m_{KK}^2)} \left[\frac{s^3-16sm_{KK}^4}{\sqrt{s(s-4m_{KK}^2)}} - 4m_{KK}^2(s-2m_{KK}^2)\ln\frac{s+\sqrt{s(s-4m_{KK}^2)}}{s-\sqrt{s(s-4m_{KK}^2)}}\right] \tag{7.7}$$

and the first two coefficients of the non-relativistic expansion are

$$a_{WW} = \frac{g_2^4 s_{w1}^4}{4\pi m_{KK}^2} \tag{7.8}$$

$$b_{WW} = -\frac{5}{6}a_{WW} \tag{7.9}$$

$\mathbf{A^{(1)}A^{(1)} \to hh}$

Finally for the higgs boson production (fig. 7.3), neglecting all the SM masses, we get

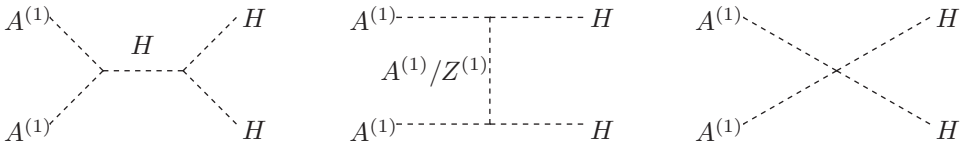

Figure 7.3: Annihilations of $A^{(1)}A^{(1)}$ into SM higgs bosons.

$$\sigma(A^1A^1 \to hh) = \frac{g_2^4(c_{w1}s_w - c_w s_{w1})^4}{128\pi c_w^4\sqrt{s(s-4m_{KK}^2)}} \tag{7.10}$$

and the non-relativistic coefficients read:

$$a_{HH} = \frac{g_2^4(c_{w1}s_w - c_w s_{w1})^4}{256\pi c_w^4 m_{KK}^2} \tag{7.11}$$

$$b_{HH} = = -\frac{1}{2}a_{hh} \tag{7.12}$$

7.1.2 Annihilations into fermions

The annihilation of $A^{(1)}$ into light fermionic degrees of freedom f (quarks u,d,s,c,b and all the charged leptons) is mediated through the exchange of level one singlet and doublet fermions $f^{(1)}_{D/S}$ into t and u channels. Moreover we include the Yukawa couplings of the top quark $t\bar{t}h$, thus the annihilation into two top quarks will have additional contribution form the SM higgs in s channel. The production of neutrinos is mediated only by the exchange of doublet neutrinos $\nu_D^{(1)}$ in t and u channel. In the figure 7.4 we show the diagrams contributing to the light fermions production.

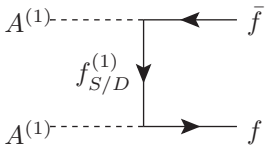

Figure 7.4: Annihilations of $A^{(1)}A^{(1)}$ into SM fermions

The coefficients a_{FF} and b_{FF} are both proportional to the SM fermion mass. In the first approximation they will give both a zero result, therefore we give their expressions without neglecting the SM masses but assuming degenerated KK spectrum for simplicity:

$$a_{FF} = (Y_D^2 + Y_S^2)^2 \frac{m_f^2 (m_{KK}^2 - m_f^2)^{3/2}}{8\pi m_{KK}^3 (m_f^2 - 2m_{KK}^2)^2} \tag{7.13}$$

$$b_{FF} = -a_{FF} \frac{(72m_{KK}^6 - 148m_{KK}^4 m_f^2 + 82m_{KK}^2 m_f^4 - 15m_f^6)}{24(m_{KK}^2 - m_f^2)^2} \tag{7.14}$$

where m_f is the outgoing fermion mas. $Y_{S/D}$ are the couplings between f, $f_{S/D}^{(1)}$ and $A^{(1)}$ defined in the table 7.1 in terms of $A = \frac{g_2 s_w c_{w1}}{c_w}$, $B = \frac{g_2 c_w s_{w1}}{c_w}$ and the fermion electric charge q_f. For the top quarks one has to include the Yukawa mixings between singlet and doublet states by multiplying the corresponding constants by the top mixing angle $\cos\alpha$ for $t_S^{(1)}$ and $\sin\alpha$ for $t_D^{(1)}$.

$f_S^{(1)}$	$q_f A$
$l_D^{(1)}$	$\frac{1}{2}(A+B)$
$\nu^{(1)}$	$\frac{1}{2}(A-B)$
$u_D^{(1)}$	$\frac{1}{6}A + \frac{1}{2}B$
$d_D^{(1)}$	$\frac{1}{6}A - \frac{1}{2}B$

Table 7.1: Couplings of $A^{(1)}$ with fermions. Here $f_S^{(1)}$ stands for any $\mathrm{SU(2)_W}$ singlet fermion, $l_D^{(1)}$ for the charged leptons, $\nu_D^{(1)}$ for neutrinos, $u_D^{(1)}$ and $d_D^{(1)}$ for up-type and down-type $\mathrm{SU(2)_W}$ doublet quarks respectively. Here we note $A = \frac{g_2 s_w c_{w1}}{c_w}$, $B = \frac{g_2 c_w s_{w1}}{c_w}$.

Neutrino production cross section expansion will then simply vanish. Top quarks production coefficients will have additional contributions from the s-channel higgs exchange

$$a_{TT} = a_{FF} + \frac{g_2^4 (c_w s_{w1} - c_{w1} s_w)^4}{4c_w^4} \frac{m_f^2 \sqrt{m_{KK}^2 - m_f^2}}{8\pi m_{KK}(m_h^2 - 4m_{KK}^2)^2} \tag{7.15}$$

$$b_{TT} = b_{FF} - \frac{g_2^4 (c_w s_{w1} - c_{w1} s_w)^4}{4c_w^4} \frac{m_f^2 (24m_{KK}^4 - 2m_{KK}^2(m_h^2 + 14m_f^2) + 3m_h^2 m_f^2)}{64\pi m_{KK}(m_h^2 - 4m_{KK}^2)^2 \sqrt{m_{KK}^2 - m_f^2}} \tag{7.16}$$

7.1.3 Relic abundance – annihilations

The goal in this section is to estimate the impact of releasing the assumption of the degenerate masses of the KK states $(1,0)$ and of the higgs boson contributions. The results are shown in the figure 7.5. We summarize also the values of m_{KK} compatible with the WMAP data in the table 7.2 where we give the bounds for the non-degenerate case $R_4 \ll R_5$ in the left and for the symmetric, degenerate case $R_4 = R_5$ in the right column.

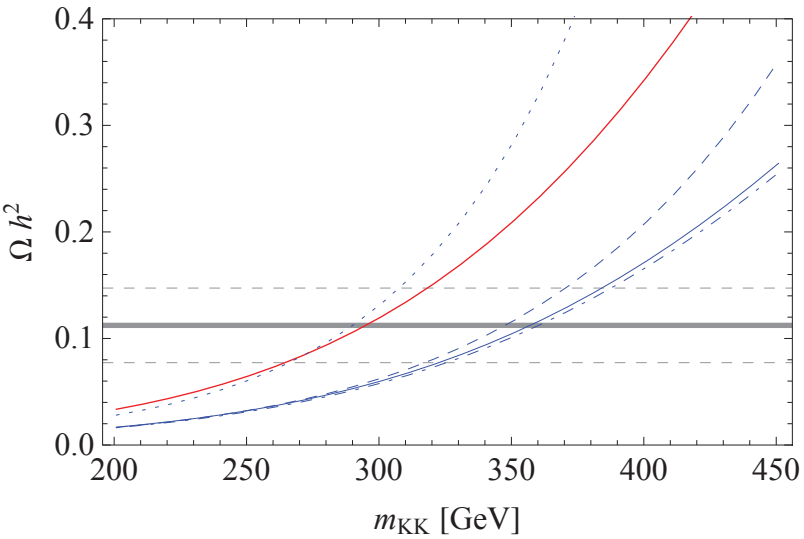

Figure 7.5: Analytical result of the relic abundance calculation on the Real Projective Plain. In this plot we show the impact of several factors on the relic abundance: we start with the simplest case (blue dotted line) where we assume fully degenerated spectrum of first KK level and no SM higgs exchange in s channel. Then progressively we add the contributions : the $(1,0)$ level degeneracy (blue dotted), higgs s-channel contribution (blue dot-dashed), relativistic correction (blue plain line). For comparison we present also the result assuming the symmetric radii $R_4 = R_5$ with all the above corrections included (red plain line).

corrections	$R_4 \ll R_5$	$R_4 = R_5$
deg m_{KK}	266 - 307	221 - 262
non-deg m_{KK}	317 - 370	263 - 313
s-channel higgs	325 - 388	267 - 321
relativistic corr.	322 - 384	264 - 318

Table 7.2: Bounds for m_{KK} in [GeV] from the analytical relic abundance calculation. Bounds for m_{KK} mass scale in the first approximation where we include only annihilations of LKP. In the first line we show the bounds obtained for the simplest case where all the SM masses are neglected and the KK spectrum is fully degenerated. Line 2: non-degenerated spectrum of the first KK level. Line 3: including s channel SM higgs exchange. Line 4: including relativistic correction to the b_{rel} coefficient. In the left column we present the results for the non-degenerated radii $R_4 \ll R_5$, in the right column - for the symmetric radii $R_4 = R_5$

The blue dotted line in the figure 7.5 presents the relic abundance assuming all the $(1,0)$ level KK states degenerated in mass and the higgs couplings are neglected as well. In this regime only annihilations into W gauge bosons contribute considerably. Annihilations into Z and higgs gauge bosons are turned off and the fermion production is negligible (see fig. 7.7). Then we release the assumption of the degeneracy of the KK states (blue dashed line). The relic abundance gets considerably reduced. If we take a representative point $m_{KK} = 350$ GeV, which lies in the range allowed by WMAP7yr data (for the most complete scenario with all the corrections included) we have $\Omega h^2 = 0.285$ for the simplest scenario, a value far above the experimental data, which is pushed down to $\Omega h^2 = 0.121$ for the degenerated spectrum - a value that satisfies the experimental bounds.

This enormous reduction of about 60% is due to the considerable changes in the annihilation cross section into W bosons. On the figure 7.6 we compare the first coefficient of the non-relativistic expansion a_{rel} for the tree cases studied here. First notice that effectively the contributions coming from annihilations into quarks and leptons are strongly suppressed by the m_f in the formula 7.13 while the annihilations into gauge bosons are two orders of magnitude larger.

Then when we release the degenerated spectrum approximation, as the masses of $W^{(1)}$ scalars exchanged in the t and u channels appear in the numerator and denominator it is difficult to guess what will be the overall impact of the mass degeneracy. From the plot we see that the mass degeneracy of the first KK level will reduce the value annihilation cross section $\sigma(A^{(1)}A^{(1)} \to W^+W^-)$. At the example point $m_{KK} = 350$ GeV we find the ratio $a_{WW}^{deg}/a_{WW}^{nondeg} = 0.376$.

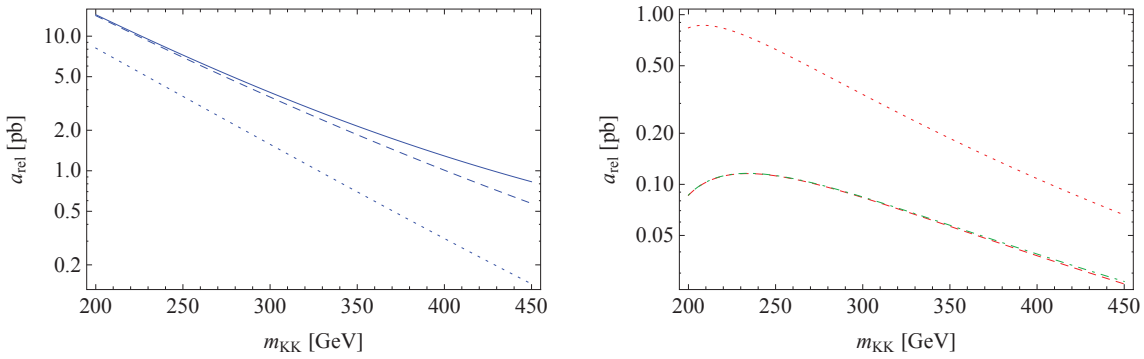

Figure 7.6: First coefficients of the non relativistic expansion $\langle \sigma v_{rel} \rangle \approx a_{rel} + v_{rel}^2 b_{rel}$. **On the left panel** the coefficients of the annihilations into gauge boson are showed, in blue dotted - for degenerate KK masses, in blue dashed - not degenerated KK masses, in blue dot dashed line - we add the higgs contribution. **On the right panel** - coefficients of the annihilations into all fermions summed. in red dotted - m_{KK} masses degenerated, in red dashed - m_{KK} masses not-degenerated and in green we add the higgs contribution.

The behavior of fermion production is completely different. The result is shown in the right panel of the figure 7.6. We sum annihilations into all the fermionic degrees of freedom and plot the first coefficient of the non-relativistic expansion for the degenerate spectrum of the first KK level in red dotted line and for the non-degenerated spectrum in the red dashed line. In this case, in contrast to the annihilations into gauge bosons, we see that the degeneracy of the spectrum will enhance the annihilation cross section $\sigma(A^{(1)}A^{(1)} \to f\bar{f})$. Analytically this is quite simple to explain as the masses of the first level fermions $f_{D/S}^{(1)}$ exchanged in t and u channels disappear in the numerators while taking trace of the S-matrix element. We are then left with the m_{f^1} in the denominators only. Schematically we can write that the annihilation cross section into

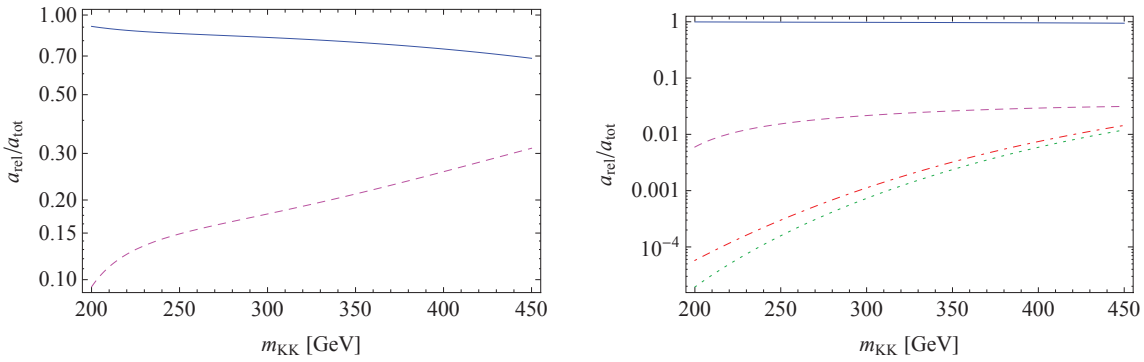

Figure 7.7: **On the left:** Relative contribution of WW annihilation (blue line) and all fermions annihilations (dashed magenta) for the degenerate spectrum. **On the right:** Relative contributions a_{XX}/a_{tot} for the degenerate spectrum and higgs channel added. In blue WW, in dotted green hh, in red dot-dashed ZZ, in magenta dashed - $f\bar{f}$ final states.

fermions is proportional to

$$\sigma \sim \frac{1}{(m_1^2 + m_{D/S}^2 - m_f^2)^2} \approx \frac{1}{(m_1^2 + m_{D/S}^2)^2} = \frac{1}{m_1^4(1+x^2)^2} \tag{7.17}$$

As KK quarks receive large loop corrections to the masses, for $m_{KK} = 350$ GeV we have $x = \frac{m_D}{m_1} = 1.17$ for the t_D^1 top quark then

$$\frac{\sigma_{nondeg}}{\sigma_{deg}} \approx \frac{4}{(1+x^2)^2} = 0.71 \tag{7.18}$$

Thus effectively the annihilation cross section into fermions is overestimated if one assumes degenerate KK spectrum. Contribution coming from quarks being considerably smaller than the gauge boson contribution, the enhancement of the bosonic cross section wins and we observe the effective decrease of the relic abundance.

Next we add the s-channel higgs exchange. The effect is small but visible. As we add new channels to the annihilation cross section the relic abundance is further reduced. Now the change is of about 13% compared to the previous case where we have considered the non-degenerate KK spectrum but without higgs contributions. Notice that now all the annihilation channels contribute, that is the cross sections $\sigma(A^{(1)}A^{(1)} \to ZZ,\ hh)$ and the Yukawa contributions in the top production are present. As can be seen from the figure 7.6 the cross sections for both, boson and fermion production grows (blue and green dot-dashed lines on the left and right panel respectively). The changes are more visible for the gauge bosons production as we open many new channels. For the fermions the higgs s-channel exchange in the top production gives only negligible contribution. The right panel in the figure 7.7 shows the relative contributions of different final states into the total annihilation cross section. Still the W^+W^- gauge boson production gives the leading contribution but we can observe growing contributions of ZZ and hh final states with increasing m_{KK}.

What is worth noticing is that while we do not neglect the Standard Model masses nor electroweak symmetry breaking we effectively get new contributions to the total annihilation cross section coming from fermionic, ZZ and hh final states which would be absent otherwise.

From this analysis we see that these processes cannot simply be neglected as their contribution changes of about 13% the relic abundance prediction.

7.1.4 Relic abundance – co-annihilation effects

Co-annihilations are expected to play a significant role when there are extra degrees of freedom with masses nearly degenerate with the dark matter particle. As it was pointed out in chapter 6, the radiative corrections to the KK spectrum in our model are quite small. Masses of the right/left handed leptons are shifted of about 0.1/0.8% respectively thus KK leptons can be considered as nearly degenerated with the LKP. Electroweak gauge bosons $W^{\pm(1)}$ and $Z^{(1)}$ receive corrections that push their masses of about 5% while the gluons are almost 10% heavier than $A^{(1)}$. The light quarks mass splittings are roughly of the same order that the weak gauge bosons mass splittings, i.e. about 5%. Top quarks $t^{(1)}_{D/S}$ receive the largest corrections pushing up their masses of about 15%. In the figure 7.8 we show mass splittings of the first level resonances as a function of m_{KK} in the non-degenerate scenario $R_4 \gg R_5$.

As the gauge bosons and quarks receive corrections larger than 5% in our analytical approach we will consider only co-annihilations with right- and left-handed leptons. It should be remembered however that due to stronger $SU(2)_{\rm W}$ and $SU(3)_{\rm C}$ couplings and a large number of degrees of freedom gauge bosons and quarks can bring important contributions into the total effective cross section. We postpone the analysis of the co-annihilations effect with those particles to the numerical part using MicrOMEGAs (36) in the section 7.2.

Co-annihilations of $A^{(1)}$ with one family of right-handed leptons $e^{(1)}_S$

First we include the co-annihilations with only one family of right-handed leptons $e^{(1)}_S$ and

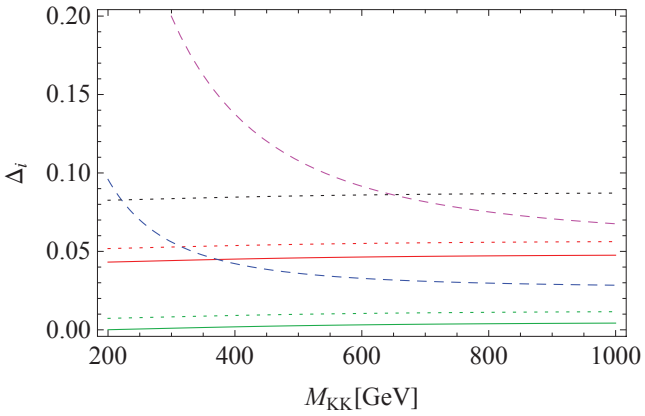

Figure 7.8: First KK level mass splittings as a function of m_{KK}. From bottom to the top at $m_{KK} = 1000$ GeV: right handed leptons (green), left handed leptons (green dotted), electro weak gauge bosons (blue dashed), singlet light quarks (red), doublet light quarks (red dotted), tops (magenta dashed), gluons (black dotted). Assumed geometry is $R_4 \gg R_5$

$\bar{e}_S^{(1)}$ with $g_e = 2$. We denote the mass splitting $\Delta = \frac{m_{e_S^1}}{m_{A^1}} - 1$. The formula for the effective number of degrees of freedom becomes

$$g_{eff} = 1 + 4(1+\Delta)^{\frac{3}{2}} e^{-x\Delta} \tag{7.19}$$

and the effective annihilation cross section reads

$$\begin{aligned} g_{eff}^2 \sigma_{eff} &= \sigma(A^{(1)}A^{(1)}) + 8\sigma(A^{(1)}e_S^{(1)})(1+\Delta)^{\frac{3}{2}} e^{-x\Delta} + \\ &+ 8\left(\sigma(e_S^{(1)}e_S^{(1)}) + \sigma(e_S^{(1)}\bar{e}_S^{(1)})\right)(1+\Delta)^3 e^{-2x\Delta} \end{aligned} \tag{7.20}$$

where we have assumed that the cross sections for annihilations of $A^{(1)}e_S^{(1)}$ and $A^{(1)}\bar{e}_S^{(1)}$ as well as $e_S^{(1)}e_S^{(1)}$ and $\bar{e}_S^{(1)}\bar{e}_S^{(1)}$ are equal. The cross section for annihilation $\sigma(A^{(1)}A^{(1)})$ is as derived before.

Annihilations of $A^{(1)}e_S^{(1)}$ proceed into Standard Model final states Ae, Ze, $W^-\nu_e$ and he. Pairs of $e_S^{(1)}e_S^{(1)}$ or $\bar{e}_S^{(1)}\bar{e}_S^{(1)}$ annihilate into a pair of electrons or positrons through a t and u channel exchange of $A^{(1)}$ and $Z^{(1)}$ gauge bosons. The annihilations of $e_S^{(1)}\bar{e}_S^{(1)}$ into all the leptonic final states $l\bar{l}$ are mediated by the s channel $A^{(1)}$ and $Z^{(1)}$ exchange as well as t and u channel exchange of $A^{(1)}$ and $Z^{(1)}$ if the same flavor in the in and out states are considered. Moreover there are diagrams transforming $e_S^{(1)}\bar{e}_S^{(1)}$ into a pairs of quark-antiquark and a pair of bosons AA, ZZ, AZ, Zh and W^+W^-. Note that in spite of the fact that $e_S^{(1)}$ does not couple directly to the $\mathrm{SU(2)_W}$ weak gauge bosons we have the $W^-\nu_e$ final state through the SM electron exchange in the s-channel. All the necessary annihilation cross section are summarized in the appendix B.

Our result when including one family of right-handed leptons $e_S^{(1)}$ almost degenerate with $A^{(1)}$ is a lower LKP relic density than in the case without $e_S^{(1)}$. Indeed, the self annihilation cross section of $e_S^{(1)}$ is much higher than the one for $A^{(1)}$ and the co-annihilation $e_S^{(1)}A^{(1)}$ cross section is of the same order of magnitude that $A^{(1)}A^{(1)}$ annihilations as it can be seen in the table 7.3. This effect translates into a m_{KK} mass window slightly above the window obtained for $A^{(1)}$ alone. The result is shown in the figure 7.9 and the numerical values found for the allowed m_{KK} scale are listed in 7.4.

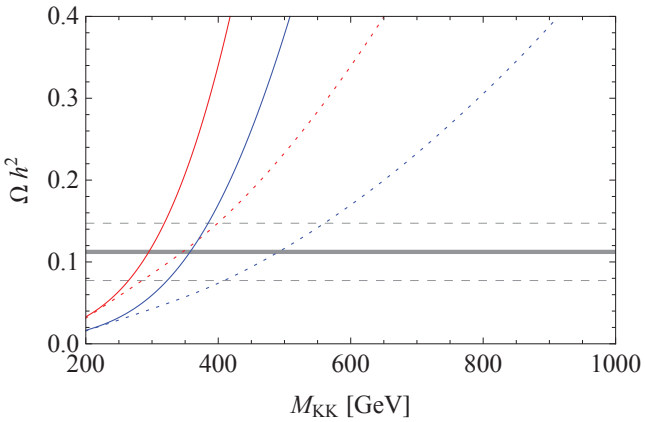

Figure 7.9: Relic abundance including the annihilations with one family of Kaluza Klein right-handed leptons in dotted lines. For comparison we show the annihilation only case in plain lines. In red we plot the relic abundance for the symmetric scenario $R_4 = R_5$, in blue for the asymmetric case $R_4 \gg R_5$.

co-annihilations	$\langle\sigma v\rangle$ [pb]
$A^{(1)}A^{(1)}$	0.48
$A^{(1)}e_S^{(1)}$	0.15
$\bar{e}_S^1 e_S^{(1)}$	5.84
$A^{(1)}e_D^{(1)}$	0.12
$\bar{e}_D^1 e_D^{(1)}$	9.02
$\bar{e}_D^1 e_S^{(1)}$	0.02

Table 7.3: Magnitudes of the averaged (co-)annihilations cross sections including the right-handed and left-handed leptons. The values are taken for $m_{KK} = 500$ GeV.

co-annihilations	m_{KK} [GeV] $R_4 \gg R_5$	m_{KK} [GeV] $R_4 = R_5$
$A^{(1)}$	320 - 384	265 - 320
$e_S^{(1)}$	410 - 560	285 - 400
$l_S^{(1)}$	420 - 575	300 - 415
$l_D^{(1)}$	470 - 635	325 - 465

Table 7.4: Bounds on the m_{KK} scale from the relic abundance including: only annihilations (line 1), one family of right-handed leptons $e_S^{(1)}$ (line 2), three families of left-handed leptons $l_S^{(1)}$ (line 3), three families of left-handed leptons $l_D^{(1)}$ (line 4)

Co-annihilations of $A^{(1)}$ with three flavors of right-handed leptons $l_S^{(1)}$

As the KK leptons are almost degenerate in mass we should include all the three leptonic flavors in our calculation and the cross flavor annihilation channels need to be added in the effective cross section. The formula for the number of effective degrees of freedom, neglecting the degeneracy from the SM masses, becomes

$$g_{eff} = 1 + 12(1+\Delta)^{\frac{3}{2}} e^{-x\Delta} \tag{7.21}$$

and the effective annihilation cross section reads

$$\begin{aligned} g_{eff}^2 \sigma_{eff} &= \sigma(A^{(1)}A^{(1)}) + 24\sigma(A^{(1)} l_{Sa}^{(1)})(1+\Delta)^{\frac{3}{2}} e^{-x\Delta} + \\ &+ 24\left(\sigma(l_{Sa}^{(1)} l_{Sa}^{(1)}) + \sigma(l_{Sa}^{(1)} \bar{l}_{Sa}^{(1)}) + 2\sigma(l_{Sa}^{(1)} \bar{l}_{Sb}^{(1)})\right)(1+\Delta)^3 e^{-2x\Delta} \end{aligned} \tag{7.22}$$

The result is shown in the figure 7.10 where on the left panel we display the relic abundance for the non degenerate scenario $R_4 \gg R_5$ and on the right panel the symmetric case $R_4 = R_5$. We can see that the influence of adding the co-annihilations of three families of right-handed leptons is to reduce further the relic abundance value. It is natural as we add many new co-annihilations channels with large cross sections while the effective number of degrees of freedom g_{eff} is not enhanced much. The m_{KK} bounds are shifted of about 3% towards heavier masses. The similar effect of corresponding enhancement of the relic abundance when adding three flavors was observed in the mUED scenario but in this model the influence of co-annihilations with right-handed leptons is to increase the relic abundance value (91), (120). We discuss the origin of this different behavior in the next section.

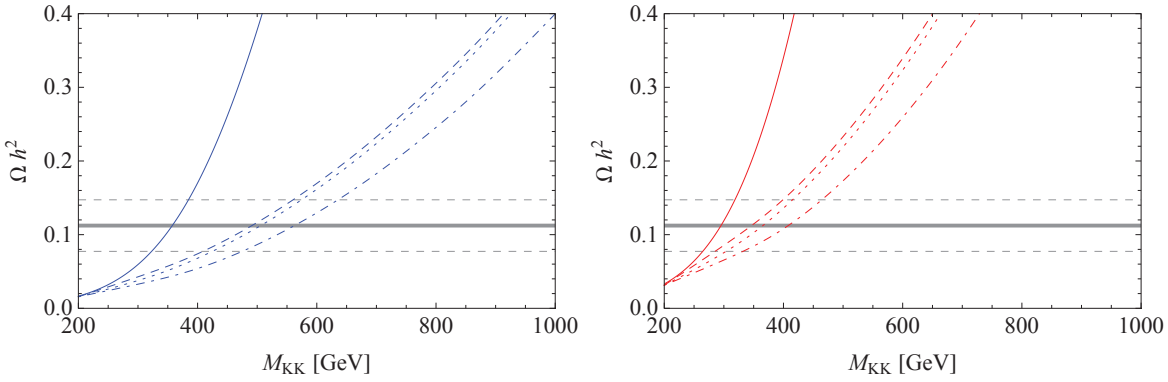

Figure 7.10: Relic abundance including the co-annihilations with KK leptons. **On the left panel:** the asymmetric scenario $R_4 \gg R_5$. **On the right panel:** the symmetric model $R_4 = R_5$. On both panel we apply the convention: plain line corresponds to the annihilations only, dashed line: co-annihilations with one family of right-handed leptons $e_S^{(1)}$, dotted line - co-annihilations with three flavors of right-handed leptons $l_S^{(1)}$, dot-dashed line: co-annihilations with three flavors of right-handed and left-handed leptons $l_{S/D}^{(1)}$.

Co-annihilations of $A^{(1)}$ with three families of right-handed leptons $l_S^{(1)}$ and left-handed leptons $l_D^{(1)}$

We are now in position to repeat the same analysis but adding new degrees of freedom - the left-handed KK lepton excitations. $g_i = 2$ for charged KK leptons and $g_i = 1$ for KK neutrinos. Note that the changes in g_{eff} are

$$g_{eff} = 1 + 12(1+\Delta_S)^{\frac{3}{2}} e^{-x\Delta_S} + 18(1+\Delta_D)^{\frac{3}{2}} e^{-x\Delta_D} \tag{7.23}$$

where we assume all the right-handed and left-handed leptons degenerated with mass splittings $\Delta_{S/D} = \left(\frac{m_{S/D}}{m_{KK}} - 1\right)$. The effective cross section will then have additional terms coming from co-annihilation channels of $l_{S/D}^{(1)}$, $\nu^{(1)}$ and $A^{(1)}$ between themselves. Notice that the main contribution will come from the annihilations of left-handed leptons as can be seen from the table 7.3 due to their weak interactions. The effective cross section will be once more increased and the corresponding value of the relic abundance will be reduced as can be seen in the figures 7.10 and in the table 7.4.

Notice that in the six-dimensional $\mathbb{R}P^2$ model the effect of co-annihilations is the same as in supersymmetric scenarios where the co-annihilations of sleptons tend to reduce the relic abundance value. The opposite effect is observed in the mUED model, where the net effect of co-annihilations with right-handed leptons is to increase the prediction for Ωh^2 while the co-annihilations with the left-handed leptons tend to decrease the Ωh^2 value (91). This difference between mUED and supersymmetric scenario have its origin in the fact that SUSY cross section for co-annihilations $\chi_1^0\chi_1^0 \to f\bar{f}$ is helicity suppressed while the co-annihilation processes are not. Adding co-annihilations therefore can only increase the effective cross-section and correspondingly decrease the relic abundance. The same situation happened in our model.

In mUED the annihilation channel of the LKP vector boson $B^{(1)}B^{(1)} \to f\bar{f}$ is already of normal strength. The effect of co-annihilations can be therefore guessed only if the new co-annihilation channels are either much weaker or much stronger. The co-annihilations with right-handed leptons in mUED are typically of the same order of magnitude that the $B^{(1)}$ annihilations and therefore the net effect will be difficult to guess. The left handed KK leptons, due to the stronger $\mathrm{SU(2)_W}$ interactions give more important contributions to the effective cross section while the effective number of degrees of freedom is not enhanced much. There are many studies in the literature investigating the influence of mass splittings between the KK excitations in mUED on the relic abundance. The observation is that the co-annihilations can either increase or decrease the relic abundance value depending on the cut-off of the theory which in turn controls the mass splittings. In general, if the KK mass splittings are neglected, the relic abundance will be increased by the co-annihilations but with growing splittings the co-annihilations will tend to reduce the relic abundance prediction in analogy to supersymmetric case (91), (48).

In our model the situation is different than in the mUED scenario because our dark matter candidate is a spin-0 particle and not a vector KK photon like in mUED. The magnitudes of (co)annihilation cross sections will therefore be different due to the different spin of the LKP. As we have seen, the annihilations of $A^{(1)}$ into fermions are suppressed like in SUSY case. Therefore the effect of decrease of the relic abundance while adding co-annihilations can be easily predicted and understood in analogy to the supersymmetric scenarios.

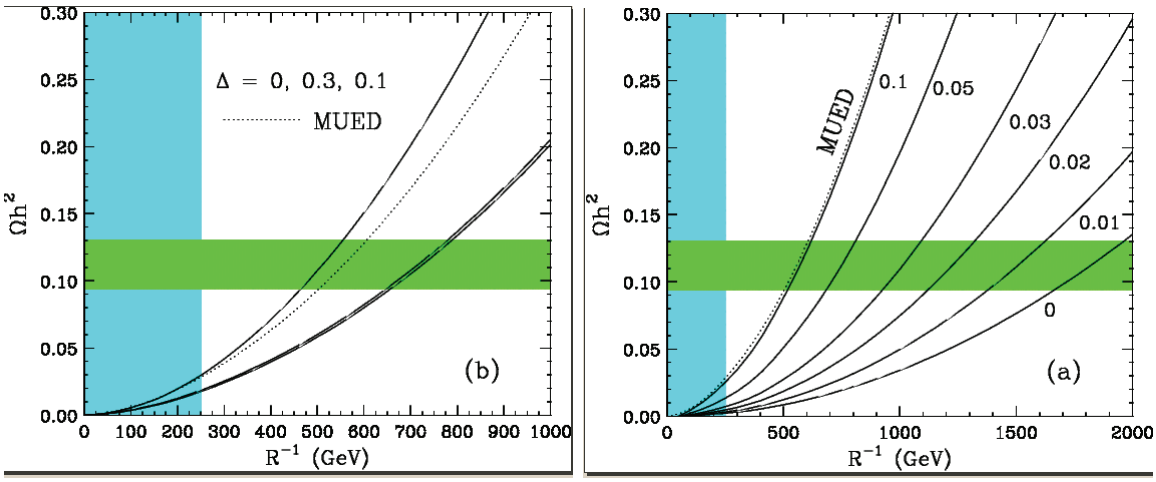

Figure 7.11: **On the left panel:** Relic abundance including the co-annihilations with KK singlet leptons in mUED. The lines from top to bottom correspond to the mass splittings $\Delta = 0, 0.3, 0.1$. **On the right panel:** Relic abundance including the co-annihilations with KK singlet quarks in mUED. The mass splittings are indicated below the corresponding lines. Extracted from (91).

It is important to notice that the heavier KK states, heavy quarks and gluons, although interact strongly, are expected to give negligible contributions to the relic abundance in models with large mass splitting like mUED. For example in (91) authors find that for the KK quarks with typical mass splitting of order of 10% the relic abundance is almost unaffected by the co-annihilations while when the mass splittings get smaller, of order of 5%, the observed enhancement of the relic abundance is even more important than in the case when one includes the co-annihilations with almost degenerated leptons. This is of course due to strong interactions increasing the value of the effective cross section. The effects of variable mass splittings in the leptonic and quark sectors can be seen in the figure 7.11 extracted from (91).

In our model all the masses are nearly degenerated, therefore all the particles are expected to play an important role in the relic abundance calculation. The analytical study we have performed is useful to understand the general behavior of the model with respect to the relic abundance calculations. We see that the co-annihilations effects play a very important role and thus a full numerical study including all effects has to be done. We have implemented the model into the MicrOMEGAs program (36) - a powerful program that allows one to study numerically the phenomenology of the dark matter candidate. The results we have obtained are shown in the next sections.

7.2 Relic abundance - numerical results

In the following we estimate the bounds on the compactification scale R of the extra dimensions using the relic abundance calculation performed numerically with MicrOMEGAs (37),(38). We have implement our model into MicrOMEGAs and validated the numerical implementation with the analytical results of the previous sections. The WMAP 7-year run bound on the relic density are $0.0773 < \Omega h^2 < 0.1473$. We calculate the relic abundance using the implementation of the model to MicrOMEGAs (version 2.4.1) and study two cases:

1. L1 where the relic abundance calculation includes only the SM final states i.e. we have the processes $(1,0)+(1,0) \to (0,0)+(0,0)$
2. L2 where we allow for the $(2,0)$ KK modes in the final state. We have thus the processes $(1,0)+(1,0) \to (0,0)+(0/2,0)$

In both cases the intermediate states are $(0,0)$ modes in s-channel or $(1,0)$ KK modes in t-channel with the couplings at tree level. Moreover in the L2 model the $(2,0)$ resonances can appear with tree level couplings as well. We will include also the loop level couplings in both scenarios to examine their influence on the relic abundance.

7.2.1 L1 scenario - relic abundance at tree level

Using MicrOMEGAs we calculate the relic abundance Ωh^2 as a function of the mass m_{KK}. Our results are presented on the plot 7.14 where we show four lines: the two dotted lines which are self-covering most of the time correspond to the case where we include only annihilations of $A^{(1)}$ with or without loop induced couplings. The dashed line shows the relic abundance with all the co-annihilations included and finally the plain line corresponds to the co-annihilations and the resonant processes turned on.

First we examine the influence of co-annihilations with all the $(1,0)$ level particles on the relic abundance. Schematically the processes that we take into account at tree level can be presented as in the figure 7.12.

When we include all the co-annihilations without loop induced couplings we observe a strong enhancement of the effective annihilation cross section σ_{eff} for $m_{KK} > 425$ GeV. Interestingly the co-annihilations tend to increase the value of Ωh^2 in the region $m_{KK} < 425$ GeV. This effect is unexpected as in general the co-annihilations should always decrease the value of Ωh^2. However the bounds we obtain from the analytical study of annihilations are identical to those obtained here from numerical scan with MicrOMEGAs. Therefore the effect should have another explanation. It can be due to the level crossing in masses. As can be seen from the figure 7.8 for low m_{KK} masses the (1,0) weak gauge bosons mass splittings (blue dashed line) are quite

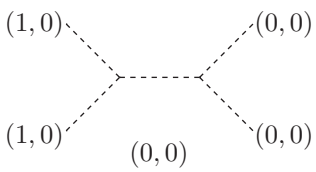

Figure 7.12: L1 scenario - tree level processes. Here we show inly schematically the contribution modes, t-channel diagrams also contribute.

high, of order of $\sim 10\%$ and only at $m_{KK} \approx 375$ GeV become smaller than the splittings of (1,0) quarks. Therefore in the low m_{KK} region the co-annihilations of electroweak gauge bosons will be strongly suppressed by large mass splittings Δ_i in the effective cross section formula 3.17:

$$\sigma_{eff}(x) = \sum_{ij}^{N} \sigma_{ij} \frac{g_i g_j}{g_{eff}^2} (1+\Delta_i)^{\frac{3}{2}} (1+\Delta_j)^{\frac{3}{2}} e^{-x(\Delta_i+\Delta_j)} \tag{7.24}$$

This would increase the value of Ωh^2. The "low" m_{KK} mass region should be quantified by more detailed study. As a starting point we can estimate that this region would correspond to the masses where mass splittings of (1,0) gauge bosons are larger than those of (1,0) quarks. This would give a limit $m_{KK} \lessapprox 375$ GeV. Notice that this is only a naive explanation. The problem should be investigated in further work. The main contribution comes of course from annihilations into W^+W^- then from about $m_{KK} \gtrapprox 431/448$ GeV the ZZ/HH processes become of some importance (1% up to 15% at 1000 GeV).

7.2.2 L1 scenario - relic abundance at loop level

In the second step we study in both models the influence of adding the loop induced couplings. This corresponds to the dotted and plain lines in the figure 7.14. Now we have additional contributions from (2,0) particles exchanged in the s-channel and decaying at loop level into SM final states as shown in the figure 7.13.

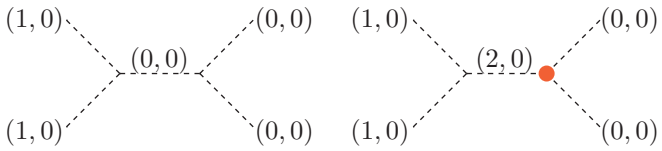

Figure 7.13: L1 scenario - loop level processes. Here we show only schematically the contribution modes, t-channel diagrams also contribute. In the left diagram all the couplings are at tree level. On the left diagram the loop level coupling is marked in red.

The formal calculation of effective couplings were performed in (52). The mass of the $(2,0)$ KK particles is almost twice mass of its first KK particle partners. Thus, the resonance processes in which the $(2,0)$ KK modes propagate in the s-channel are important for the calculation of the relic abundance. These effects in the mUED model are partially investigated in (87), (86) and (39). In the works (87), (86) the second KK particle resonances are studied for the LKP annihilation and co-annihilations relevant to the $\mathrm{SU(2)_W}$ singlet leptons $e^{(1)}$. However, it is found that the second KK resonance processes also play an important role in co-annihilation modes relevant to KK $\mathrm{SU(2)_W}$ doublet leptons and KK higgs particles. In our model the possible resonances can come from the following particles propagating into s channel: $t_{S/D}^{(2,0)}$, $W^{(2,0)}$, $Z^{(2,0)}$, $G^{(2,0)}$, $H^{(2,0)}$. Other $(2,0)$ states do not couple directly to two SM particles and thus will not contribute in the co-annihilation processes. In the table 7.5 we give the branching ration of the $(2,0)$ states into SM particles.

For the resonant particles mentioned above the corresponding co-annihilation processes are

$$
\left.\begin{array}{r} t^{(1)}_{D/S} + A^{(1)}/Z^{(1)} \\ b^{(1)} + W^{(1)} \end{array}\right\} \to \quad t^{(2)}_{S/D} \quad \to \text{SM}
$$

$$
\left.\begin{array}{r} A^{(1)} + W^{(1)} \\ l^{(1)}_{L} + \nu^{(1)} \end{array}\right\} \to \quad W^{(2)} \quad \to \text{SM}
$$

$$
l^{(1)}_{L/R} + \bar{l}^{(1)}_{L/R} \to \quad Z^{(2)} \quad \to \text{SM}
$$

$$
\left.\begin{array}{r} G^{(1)} + G^{(1)} \\ q^{(1)}_{S/D} + \bar{q}^{(1)}_{S/D} \end{array}\right\} \to \quad G^{(2)} \quad \to \text{SM}
$$

$$
\left.\begin{array}{r} V^{(1)} + V^{(1)} \\ t^{(1)}_{S/D} + \bar{t}^{(1)}_{S/D} \end{array}\right\} \to \quad H^{(2)} \quad \to \text{SM}
$$

Note however that the processes can be suppressed by several factors:

1. If the initial particles are heavy, then the process will be Boltzmann suppressed. This condition will be relevant for the initial $G^{(1)}$, $W^{(1)}$, $Z^{(1)}$, $q^{(1)}_{S/D}$ which receive the largest loop corrections to masses.
2. The BR of the $(2,0)$ to the SM is small. This condition will reduce the resonant contributions but is much less important than the Boltzmann suppression factors.
3. As the velocities of the particles near the freeze out temperature are non-relativistic, if one is far below the resonance condition, that is the inequality $(m_1 + m_2)^2 \ll m_3^2$ holds, then and the process will be Boltzmann suppressed as well due to large momenta of the incoming particles required to produce the resonance.

We define m_{KKres} the KK mass at which the resonant condition

$$
(m_1 + m_2)^2 = m_3^2 \tag{7.25}
$$

is verified. Here m_1 and m_2 are the incoming particle masses and m_3 is the mass of the state exchanged in the s-channel. Among many of kinematically allowed resonances listed above, the contributions of some of them will be highly reduced by the factors listed above:

1. $t^{(2)}_{S/D}$ have low branching ratios into the SM particles and the initial states producing this resonance are heavy, thus the processes will be both Boltzmann suppressed and loop suppressed.
2. $Z^{(2)}$ and $W^{(2)}$ resonances have comparable BR to the SM particles. The initial states $l^{(1,0)}$ however are quite light and the process will be Boltzmann suppressed as we are far below the resonance condition.
3. The strong couplings of $G^{(2)}$ result in the very large BR into SM states. However the modes producing the resonance, (1) quarks and gluons, are particles with the largest mass splittings in the model, therefore the processes will be strongly suppressed by Boltzmann factors.
4. $H^{(2)}$ particles, in spite of very weak BR are produced by all the $(1,0)$ coannihilating states including $A^{(1)}$ Therefore the effective cross section will be enhanced mainly due to the process $A^{(1)} + A^{(1)} \to H^{(2)} \to \text{SM}$.

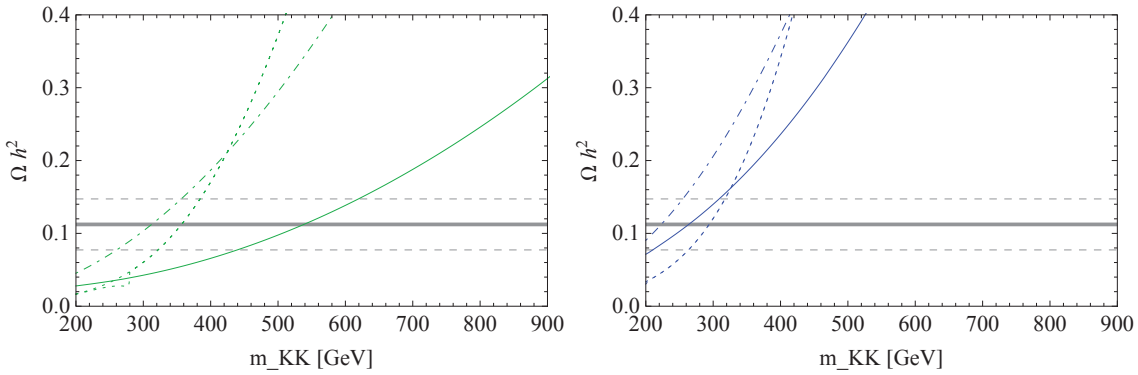

Figure 7.14: Relic abundance in function of m_{KK}. In all the plots we set the convention : dotted - annihilations and annihilations + loops. dot-dashed - co-annihilations, plain line - co-annihilations + loops. For colors conventions: In green - $R_4 \gg R_5$ **(left)**, in blue L1 $R_4 = R_5$ **(right)**

From the plot 7.14 we can easily see the influence of loop induced couplings and inclusion of $(2, 0)$ modes in the final state in the calculation of the relic abundance of dark matter.

When we include only annihilations of $A^{(1)}$ then the unique (20) resonance comes from the second level higgs $H^{(2)}$ exchange additionally to the SM higgs in the process $A^{(1)}A^{(1)} \to H/H^{(2)} \to t\bar{t}$. The resonant condition $4m_{KK}^2 = m_{H^2}^2$ is reached from below. For $m_{KK} \leq m_{KKres}$ we can observe only a small dip created at $m_{KKres} = 267$ GeV which correspond to $H^{(2)}$ resonant exchange in the s-channel of the reaction $A^{(1)}A^{(1)} \to t\bar{t}$. At the same time when m_{KK} exceeds the resonant value, the influence of the s-channel higgs is stopped and we observe a sharp end in the plot of Ωh^2, for $m_{KK} > m_{KKres}$ the Ωh^2 values are the same as in the case without $H^{(2)}$ resonance. The relative contribution of processes contribution to Ωh^2 are plotted in the figure 7.15. The main contribution comes from $A^{(1)}A^{(1)} \to W^+W^-$ when the resonances are turned on the $A^{(1)}A^{(1)} \to t\bar{t}$ contribution, which normally is at 1% level, is enhanced and gives a relative contribution of about 30% into the total effective annihilation cross section.

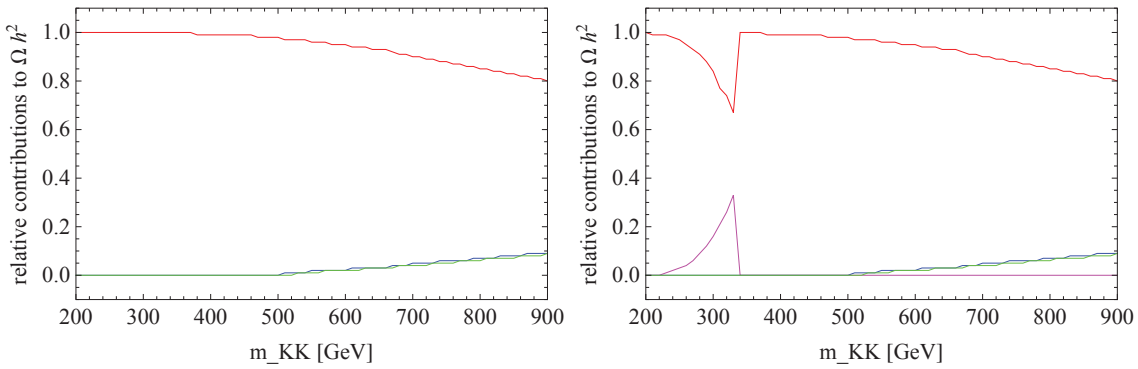

Figure 7.15: Relative contributions of the partial annihilation cross sections to the relic abundance in L1 and L2 scenarios (when we take only annihilations into account these two scenarios give the same result). **On the left panel** we see the dominant contribution of $A^{(1)}A^{(1)} \to W^+W^-$ annihilation in red, and the subleading annihilations into ZZ (blue) and HH (green). **On the right panel** the same colors are applied for the contributions when we include the loop couplings. We clearly see the resonant contribution of $A^{(1)}A^{(1)} \to t\bar{t}$ in magenta which is enhanced by the $H^{(2)}$ exchange.

When we include all the co-annihilations, all the resonant particles mentioned above con-

tribute. The condition eq. 7.25 can be met for processes:

$$\begin{aligned} &t^{(1)}_{D/S} + A^{(1)}/Z^{(1)} \to t^{(2)}_{D/S} && \text{at } m_{KKres} \approx 385/680 \text{ GeV}, \\ &W^{(1)} + A^{(1)} \to W^{(2)} && \text{at } m_{KKres} = 277 \text{ GeV}, \\ &t^{(1)}_{S/D} + t^{(1)}_{S/D} \to G^{(2)} && \text{at } m_{KKres} = 740 \text{ GeV}. \end{aligned}$$

For all those processes the resonant condition is achieved from above. Therefore the resonances will be turned on for m_{KK} higher than the threshold values. The result of this is the strong reduction of the relic abundance for high m_{KK} masses. The co-annihilations into $H^{(2)}$ always pass through the resonant condition from below. The minimum corresponding to $A^{(1)}A^{(1)} \to H^{(2)}$ is not visible now because of the average taken on all the co-annihilations processes with resonant contributions which smooth the Ωh^2 result. The main contribution, of about 30% comes from the $W^{(2)}$ gauge boson as its decay width into SM particle is larger than for other $(2,0)$ states. The $(2,0)$ gluons have large decay rates into two SM states but due to the large mass splittings their influence will be strongly suppressed by the Boltzmann factor.

7.2.3 L2 scenario - relic abundance

Now we turn to the L2 scenario. The processes included in this case include SM particles and $(2,0)$ KK modes in the final states. In the figure 7.16 we show schematically the processes that are mediated by s channel particles. The additional processes when the loop level coupling are turned on are presented in the figure 7.17 where we show the loop induced couplings as red vertices. The t and u channel particles of level $(1,0)$ are also present and are all mediated by tree level couplings.

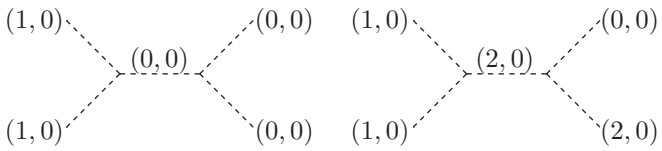

Figure 7.16: L2 scenario - tree level processes. Here we show only schematically the contribution modes, t-channel diagrams also contribute.

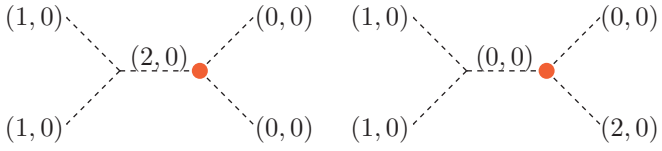

Figure 7.17: L2 scenario - loop level processes. Here we show only schematically the contribution modes, t-channel diagrams also contribute. The loop level vertices are shown in red.

In general the final $(2,0)$ states can decay at tree level into a pair of level $(1,0)$ particles or into SM+$(2,0)$ states. However, the $A^{(2)}$ and $H^{(2)}$ particles are not heavy enough to decay

into $(1,0)$ states and thus will effectively contribute to the relic density (see tab. 7.5 for the branching ratios). Note also that, due to their relatively small masses their production out from the $(1,0)$ states will not be kinematically suppressed at high level. We name the $A^{(2)}$ and $H^{(2)}$ particles as the SM like heavy states.

In the L2 scenario we see that the bounds do not change, compared to L1 case, if we include only annihilations. It is reasonable as the main processes that contribute in both cases are the annihilations $A^{(1)}A^{(1)} \to W^+W^-, ZZ, HH$ that are mediated only by tree level couplings. For kinematical reasons, the SM like heavy states cannot be produced from two $A^{(1)}A^{(1)}$ at non-relativistic energies.

Including co-annihilations we have many new final states including $A^{(2)}$ and $H^{(2)}$ as compared to the L1 scenario. Therefore, as it can be seen form the figure 7.18, the relic abundance bounds on m_{KK} will be pushed up to $m_{KK} \approx 850$ GeV. The main contributions are shown in the figure 7.19. Notice that in the L2 scenario we do not have the problem of crossing lines for annihilations and coannihilations as it was the case for L1 model. This could be explained by the face that now the new contributions from (1,0) final states are so important that Ωh^2 in almost insensitive on the particular mass splitting of incoming particles.

7.2.4 Comparison of the m_{KK} bounds in L1 and L2 scenarios

In the table 7.6 we summarize the bounds on the m_{KK} mass scale deduced from the full (including all the co-annihilation channels) relic abundance calculation in the two scenarios L1 and L2 using MicrOMEGAs. The results for both scenarios including all the co-annihilations and loop couplings are shown in the figure 7.20 for both geometries: $R_4 \gg R_5$ and $R_4 = R_5$. We observe that the loop induced couplings do not influence the relic abundance bounds when we open only annihilation channels. The only resonant particle in this case is the heavy higgs $H^{(2)}$ which produces a resonant minimum but for the m_{KK} far below the expected range compatible with the WMAP data. This behavior is evident in both scenarios L1 and L2, moreover we have the same bounds for m_{KK} with the expected value set quite low at 360 GeV in the asymmetric

m_{KK} [GeV]	500	1000	1500
$l_R^{(2)}$	0	0	0
$l_L^{(2)}$	0	0	0
$q_S^{(2)}$	0	0	0
$q_D^{(2)}$	0	0	0
$t_S^{(2)}$	0.04	0.00	0.00
$t_D^{(2)}$	0.04	0.040	0.01
$Z^{(2)}$	0.43	0.45	0.43
$W^{(2)}$	0.43	0.45	0.43
$G^{(2)}$	0.15	0.14	0.14
$H^{(2)}$	1.00	1.00	1.00
$A^{(2)}$	1.00	1.00	1.00

Table 7.5: Branching ratios of the $(2,0)$ KK modes into SM particles.

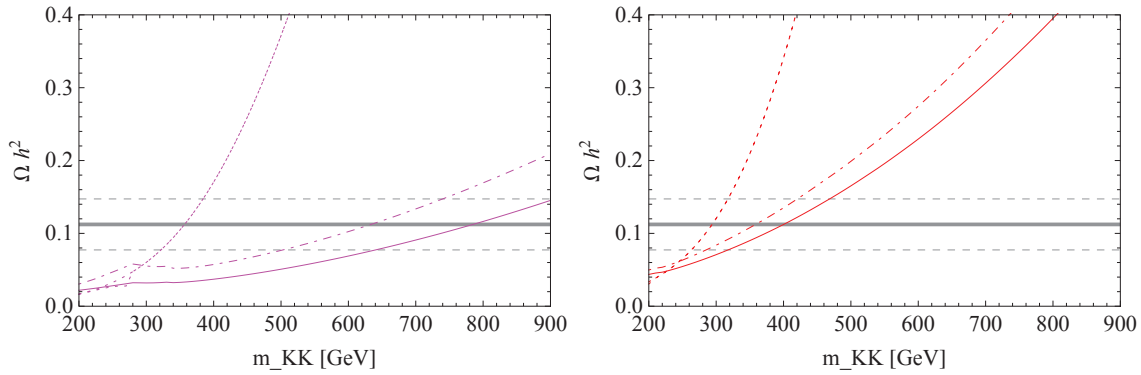

Figure 7.18: Relic abundance in function of m_{KK}. In all the plots we set the convention : dotted - annihilations and annihilations + loops. dot-dashed - co-annihilations, plain line - co-annihilations + loops. For colors conventions: In magenta - L2 $R_4 \gg R_5$, in red L2 $R_4 = R_5$ (right)

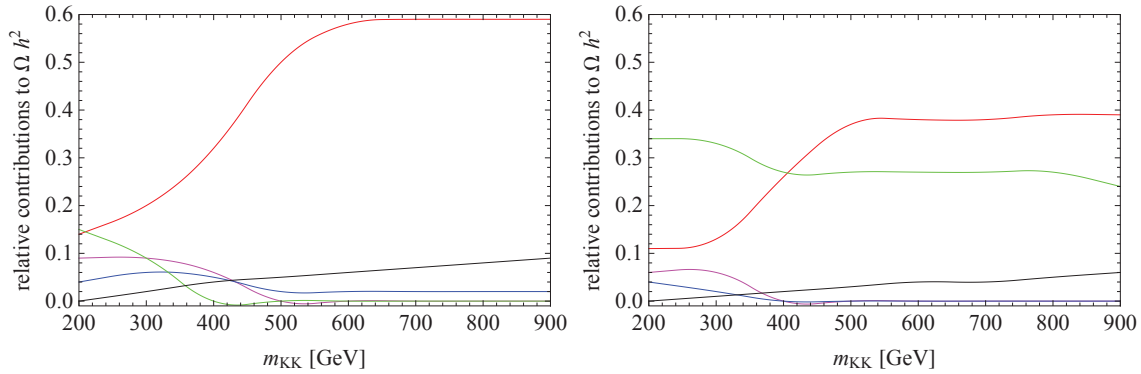

Figure 7.19: Relic abundance in function of m_{KK}. In all the plots we set the convention : dotted - annihilations and annihilations + loops. dot-dashed - co-annihilations, plain line - co-annihilations + loops. For colors conventions: In magenta - L2 $R_4 \gg R_5$, in red L2 $R_4 = R_5$ (right)

scenario $R_4 \gg R_5$ and at 290 GeV in the symmetric case $R_4 = R_5$. In the L1 scenario when we include all the co-annihilation channels but not loop induced couplings the relic abundance is reduced of about 20 (14)% in the $R_4 \gg R_5$ ($R_4 = R_5$) case and when we add the loop couplings the resonant contributions lower the Ωh^2 value of 52% and the expected mass scale is pushed up to $m_{KK} = 540$ (260) GeV. In the L2 scenario, where the (2,0) states are allowed in the final states the impact co-annihilations is more important, lowering the relic abundance value of 55 (26)% for $R_4 \gg R_5$ ($R_4 = R_5$) which traduces into mass scale of about $m_{KK} = 640$ (360) GeV in then adding loop couplings the Ωh^2 value decrease further of about 36 (15)% with respect to the co-annihilations only setting the mass range at 790 (400) GeV. The relative impact of opening the (2,0) final states is always to decrease the relic abundance value and in our study we observe a reduction of about 50 (45)% between the L1 and L2 scenarios when all the co-annihilation channels and the loop induced couplings are taken into account. Notice that the numerically obtained bounds are in prefect agreement with the analytical results summarized in 7.2 for the annihilations.

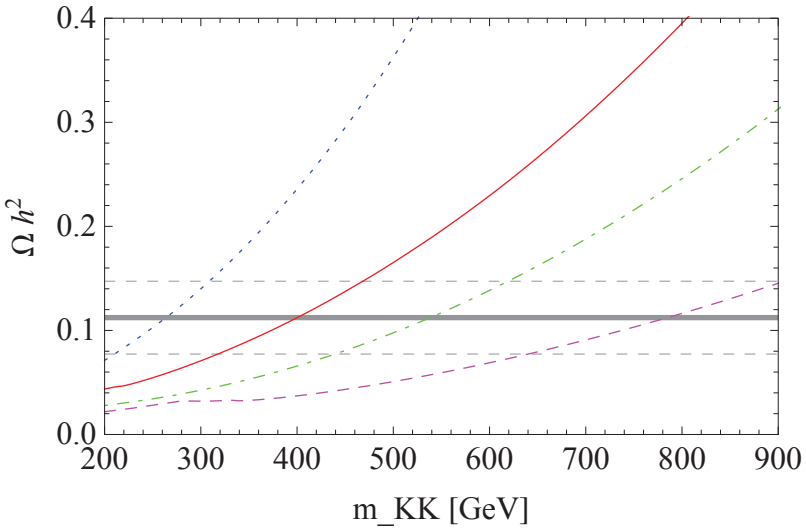

Figure 7.20: Relic abundance for the four scenarios taking into account all the co-annihilations and loop couplings. Form top to bottom we have: blue dashed - L1 $R_4 = R_5$, red plain - L2 $R_4 = R_5$, green dot-dashed - L1 $R_4 \gg R_5$, magenta dashed - L2 $R_4 \gg R_5$.

model	m_{KK}[GeV]	m_{KK}[GeV]	model
L1 A	320 - 385	320 - 385	L2 A
L1 C	260 - 355	630 - 890	L2 C
L1 CL	440 - 620	700 - 990	L2 CL

Table 7.6: Bounds on the m_{KK} form the relic abundance calculation in the models L1 and L2.

7.3 Cut-off dependence of the relic abundance

Electroweak precision observables presented in chapter 2 are very important bounds on the compactification scale in extra-dimensional models. In the paper (29) authors derive bounds from the electroweak data on the size of extra dimensions accessible to all the standard model fields focusing particularly on the 5- and 6-dimensional case.

It is shown that in the case of one extra dimension one can reliably ignore the effects of KK modes heavier than the cut-off Λ. With two extra dimensions the KK modes give corrections to the electroweak observables that depend logarithmically on the cut-off, and in more extra dimensions the dependence is even more sensitive.

They estimate that for a 5-dimensional scenario the bound is rather low of $m_{KK} \sim 300$ GeV. In the case of two universal extra dimensions, the lower bound on the compactification scale depends logarithmically on the ultra-violet cutoff of the higher dimensional theory, but can be estimated to lie between 400 and 800 GeV.

The sensitivity of electroweak parameters S and T on the cut off in our model were studied in (98). It was shown that they in fact depend logarithmically on the cut off scale. This suggests that the UV contributions that can arise from localized kinetic terms or bulk higher order operators can affect in a significant way these parameters. In the (98) the points on the orbifold where these divergences arise were shown. As mentioned, the UV sensitivity of the

precision observables limits the predictive power of these bounds.

Another way to set an upper limit for ΛR is by considering unitarity constraints, which in the higher-dimensional theories typically yield $\Lambda < 20$ (61). We have checked in our model that ΛR cannot exceed much the value of 10 as then the unitarity of the S-matrix is broken.

We will therefore use a typical scale $\Lambda R = 10$ in our model and while performing scans over a range of parameters we will lower ΛR from 10 down to 2 in order not to exceed an already high value $\Lambda R = 10$.

The spectrum of the model as well as the loop induced couplings are cut off dependent. In the table 7.7 we show the mass splittings for $m_{KK} = 500$ and 800 GeV for two different values of the ΛR parameter. How the spectrum vary for a given mass scale m_{KK} as a function of ΛR is plotted in 7.21

m_{KK} [GeV]	ΛR	$l_R^{(1)}$	$l_L^{(1)}$	$q_S^{(1)}$	$q_D^{(1)}$	$t_S^{(1)}$	$t_D^{(1)}$	$V^{(1)}$	$G^{(1)}$
500	10	0.0026	0.0099	0.0458	0.0545	0.1078	0.1165	0.0373	0.0854
500	5	0.0020	0.0073	0.0336	0.0399	0.0952	0.1016	0.0288	0.0602
800	10	0.0039	0.0111	0.0471	0.0558	0.0751	0.0838	0.0298	0.0867
800	50	0.0030	0.0083	0.0346	0.0409	0.0619	0.0682	0.0223	0.0613

Table 7.7: Mass splittings $\Delta_i = \frac{m_i}{m_{KK}} - 1$ for two values of $m_{KK} = 500$, 800 GeV and for two different values of the cutoff $\Lambda R = 10$ and $\Lambda R = 5$. $V^{(1)}$ stands for weak gauge bosons $W^{(1)}$ and $Z^{(1)}$.

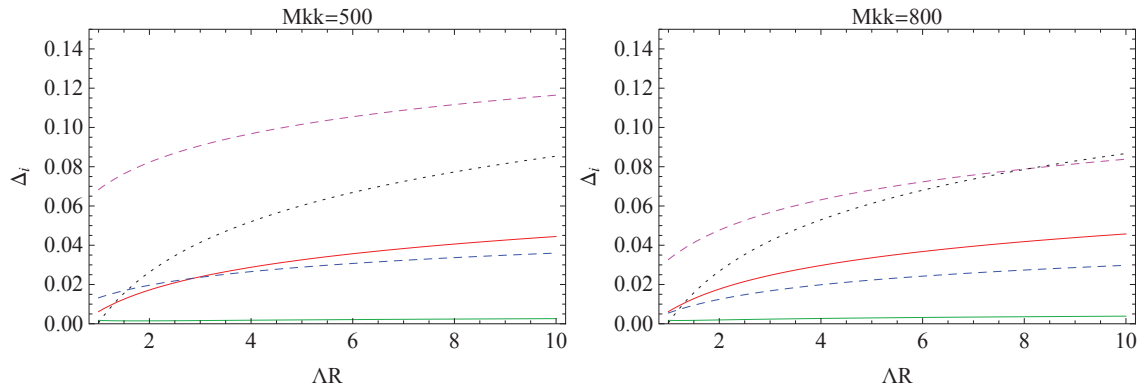

Figure 7.21: First KK level mass splittings as a function of ΛR. **On the left panel:** splittings for $m_{KK} = 500$ GeV, **on the right panel:** splittings for $m_{KK} = 800$ GeV. On both panels we adopt the colors from bottom to the top at $\Lambda R = 10$: leptons (green), electroweak gauge bosons (blue dashed), light quarks (red), tops (magenta dashed), gluons (black dotted).

Due to these variations of the mass spectrum the relic abundance will change with the cutoff as well. In the figures 7.22, for L1 scenario, and 7.23, for L2 scenario, we show how the relic abundance changes with ΛR going form 5 to 10. The qualitative behavior in these two models is the same therefore in the following we will concentrate in the L1 model only. The L2 generalization will be straightforward and the only difference will be quantitative bounds of m_{KK}.

We see that when we include only annihilations the growing cutoff has the effect of increasing the relic abundance. In contrast, when we include all the co-annihilations the situation is inversed

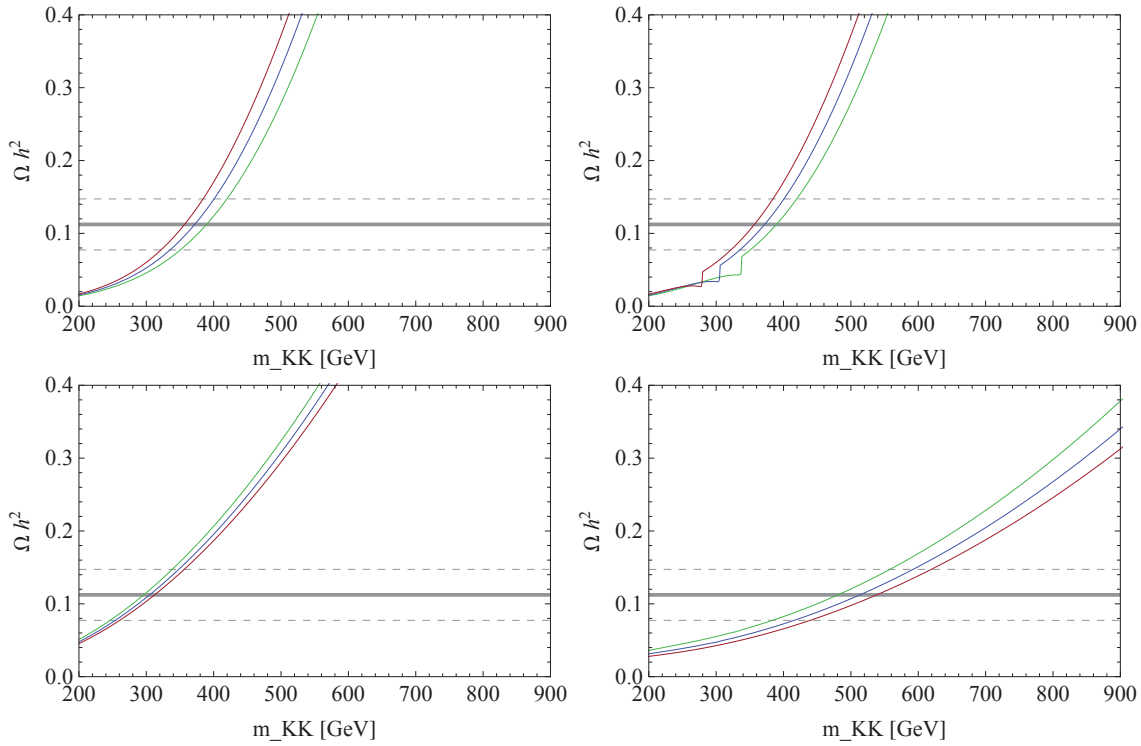

Figure 7.22: Variations of the relic abundance for $R_4 \ll R_5$ in L1 scenario. Annihilations only (top left), annihilations and loop couplings (top right), all co-annihilations (bottom left) and all co-annihilations with loop couplings (bottom right). Magenta $\Lambda R = 10$, blue $\Lambda R = 7$, green $\Lambda R = 5$

- with growing cut off Ωh^2 is getting reduced. To understand these effects we need to know first of all which quantities are most influenced by the cutoff. Of course the principal influence will be on the mass spectrum of the particles which is explicitly cutoff dependent. Then, while we include loop induced processes, the effective couplings violating the KK number are also dependent on the cutoff scale of the theory.

7.3.1 Cut-off dependence of the relic abundance – tree level

Let focus first on the two simple cases L1A (only annihilations) and L1C (all co-annihilations included) which correspond to bottom and top left panels in the figure 7.22. In both cases we do not have any loop induced couplings thus the cut off dependence will enter only in the mass spectrum. With growing cut off for a given m_{KK} the mass splittings are growing as can be seen in the figure 7.21. As the annihilations are mediated by the (1,0) level particles in t-channels mainly (for (1,0) quarks and $A^{(1)}$,$Z^{(1)}$) for larger mass splittings the individual cross sections will be suppressed with growing ΛR. We effectively see this effect while calculating the total cross section for a given value of m_{KK} which we take $m_{KK} = 500$ as the benchmark point but the exhibited behavior will be the same for other values of m_{KK}. We show the variation of the total cross section $A^{(1)}A^{(1)} \to SM$ for two values of $\Lambda R = 10, 5$ (we note then the cross section for the corresponding ΛR values as $\sigma_{\Lambda R}$) in the figure 7.24.

As in the relic abundance it is the mean value of σv that enters the formula we estimate its value by assuming Boltzmann distribution of velocities of DM

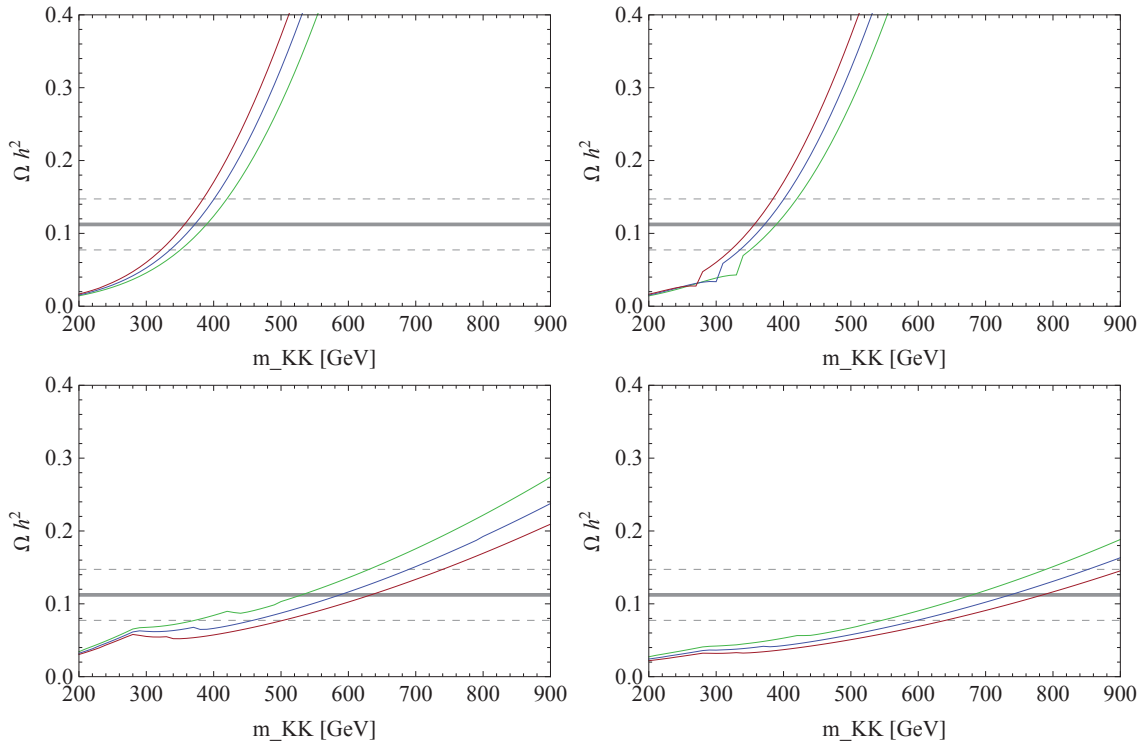

Figure 7.23: Variations of the relic abundance for $R_4 \ll R_5$ in L2 scenario. Annihilations only (top left), annihilations and loop couplings (top right), all co-annihilations (bottom left) and all co-annihilations with loop couplings (bottom right). Magenta $\Lambda R = 10$, blue $\Lambda R = 7$, green $\Lambda R = 5$

$$f(p)dp \sim p^2 \exp\left(\frac{p^2}{2mkT}\right) dp \tag{7.26}$$

where $T = m/x_F$ with $x_F = 25$ (we can safely assume that x is constant. We have checked that during the relic abundance calculation indeed its value varies within the range of 22-26 for all the range of m_{KK} and for all the assumed values of ΛR).

Then we calculate simply the mean value $\langle \sigma v \rangle$ and we obtain 3.76 [pb] for $\Lambda R = 10$ and 3.20 for $\Lambda R = 5$ so effectively the mean value $\langle \sigma v \rangle$ is larger for larger cutoff scale and the relic abundance will be smaller.

Now we turn from the annihilations only to the case where we take into account all the co-annihilations. In this case the decreasing cutoff ΛR implies a decrease in the relic abundance for a given value of m_{KK}. This opposite effect as compared to the annihilations only can be explained by the larger suppression coming from mass splittings. The independent decrease in the cross sections with growing ΛR will be counter-balanced by the growing mass splittings that enter the formula 3.17. The overall effect will be a decrease of the relic abundance value. We observe qualitatively exactly the same behavior in the L2 case, presented in the figure 7.23, with of course different m_{KK} bounds as we have different final states.

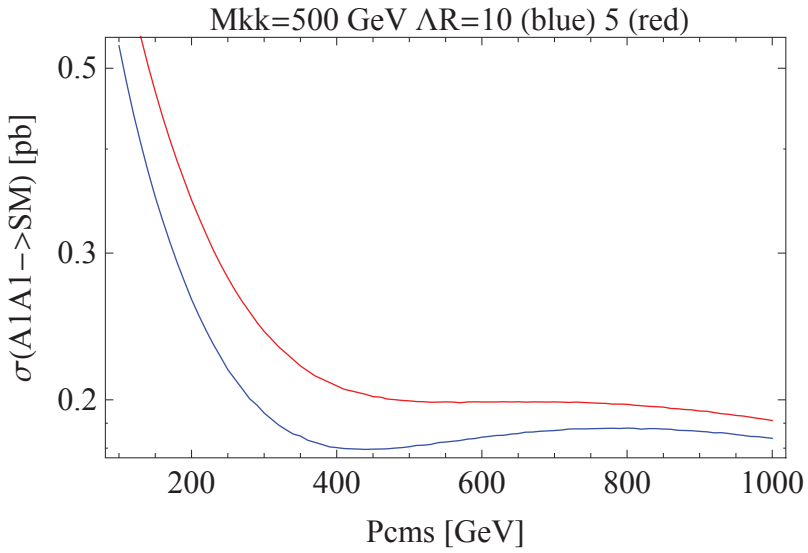

Figure 7.24: Total annihilation cross section $A^{(1)}A^{(1)} \to SM$ as a function of p_{cms} for $M_{KK} = 500$ GeV and $\Lambda R = 5,\ 10$ in red and blue respectively.

7.3.2 Cut-off dependence of the relic abundance – loop level

Results we obtain including loop couplings are plotted on the top and bottom right panels of the figures 7.22 for L1 and 7.23 for L2 scenarios. The qualitative behavior is analogous to the tree level study. Note that the $H^{(2)}$ resonance occurs at larger values of m_{KK} with decreasing ΛR (top left panel in the figure 7.22). This is simply a consequence of the different loop corrections dependence on ΛR for $A^{(1)}$ and $H^{(2)}$ masses and thus the resonance condition will give different values of m_{KKres}.

We summarize the numerical bounds for the different values of the ΛR parameter in the two scenarios L1 and L2 in the tables 7.8 and 7.9. We should focus especially on these values where all the physical processes relevant for the relic abundance calculation, i.e. the co-annihilations and loop induced couplings are taken into account. Note that the allowed mass values vary from about 200 GeV for the symmetric case - a value that is already excluded by the accelerator searches, up to 1 TeV - a region that would be viable as not yet excluded by the LHC data.

ΛR	2	4	6	8	10
L1A	420 - 510	365 - 435	342 - 410	330 - 395	323 - 385
L1AL	427 - 545	370 - 435	342 - 410	330 - 395	323 - 385
L1C	215 - 300	240 - 330	250 - 345	255 - 352	260 - 357
L1CL	235 - 380	360 - 530	405 - 580	425 - 605	440 - 620
L2A	420 - 510	365 - 437	343 - 410	330 - 395	322 - 385
L2AL	427 - 545	370 - 437	343 - 410	330 - 395	322 - 385
L2C	385 - 545	505 - 735	570 - 815	607 - 865	630 - 895
L2CL	500 - 740	570 - 820	640 - 905	675 - 955	700 - 990

Table 7.8: m_{KK} bounds (in GeV) from the relic abundance for different values of ΛR for $R_4 \gg R_5$.

ΛR	2	4	6	8	10
L1 A	332-415	293-358	278-338	269-325	262-318
L1 AL	332-415	293-358	278-338	269-325	268-318
L1 C	excuded	< 235	< 245	< 252	< 255
L1 CL	excuded	< 285	< 300	< 305	< 310
L2 A	330-415	295-360	280-340	270-325	265-318
L2 AL	330-415	295-360	280-340	270-325	265-318
L2 C	225 - 345	275 - 425	305 - 450	320 - 465	325 - 475
L2 CL	240 - 365	295 - 455	330 - 480	340 - 495	350 - 505

Table 7.9: m_{KK} bounds from the relic abundance for different values of ΛR for the symmetric case $R_4 = R_5$.

Decreasing the ΛR parameter from $\Lambda R = 10$ down to $\Lambda R = 2$ we decrease the allowed bounds for m_{KK} of about 30%. The upper limit on ΛR derived from the unitarity constraints can serve as an estimate for the ΛR in more realistic studies. One has to carefully chose the value ΛR in order to estimate the right bounds for the compactification scale. Other question that can be addressed in this case is the influence of UV phenomena on the low-energy effective theory, as varying the cutoff the high-energy completion may play an important role. This study is however far beyond the scope of this thesis.

7.4 H^2 localized mass parameter m_{loc} dependence of the relic abundance

The next step is to vary the m_{loc} parameter which is a free parameter of the model. It corresponds to the mass operator localized on the singular points of the orbifold. Effective theory order of magnitude estimates suggest that reasonable values for the localized term should be $m_{loc} < m_{KK}$. Moreover as it was mentioned in chapter 6 the bounds on the m_{loc} parameter should be applied from the electroweak precision observables as well. This parameter changes the mass of m_{H^2} thus affecting the position of the resonant cross-sections contributing to the relic abundance calculation on one hand. On the other hand higher mass of $H^{(2)}$ will change the possible decay modes of this particle. For $m_{loc} = 0$, the value we have assumed in all the previous analysis, the only possible decays of $H^{(2)}$ are into SM particles. Increasing m_{loc} the decay channels into heavier states from (1,0) tier will open. For example, taking into account the allowed bounds of m_{loc}/m_{KK} from the electroweak constraints, we can put as a benchmark point $m_{KK} = 600$ GeV and then we have the branchings as shown in the table 7.10

Resonance condition

As it was mentioned in section 7.2 main processes including the resonant $H^{(2)}$ are from the annihilations of $A^{(1)}A^{(1)}$ states. The resonance condition 7.25 for $H^{(2)}$, assuming the incoming particles at rest (which is reasonable as the DM at decoupling is highly non-relativistic) can be written as

$$m_{KK} \leq \frac{m_h^2 + m_{loc}^2}{\delta} \qquad \text{with} \qquad \delta = 4\delta_A - \delta_h \tag{7.27}$$

m_{loc}	$t\bar{t}$	$A^{(1)}A^{(1)}$
0	1	0
100	1	0
200	0.92	8

Table 7.10: Branching ratios of $H^{(2)}$ for $m_{loc} = 0$, 100, 200 GeV.

where δ_h and δ_A stands for the loop corrections calculated in chapter 6. In the table 7.11 we give the numerical values for the resonant masses m_{KK} satisfying the equality in eq. 7.27 and the corresponding lower bound from the ρ calculated in chapter 6.

m_{loc}	m^{res}_{KK} [GeV]	m^{ρ}_{KK} [GeV]
0	267	0
100	353	351
200	544	558
300	769	731
400	1005	886
500	1248	1028

Table 7.11: The values of m^{res}_{KK} corresponding to resonances $2m_{A^1} = m_{H^2}$ and the lower bounds for m^{ρ}_{KK} obtained from the electroweak precision constraints for different values of m_{loc}.

In the figure 7.25 we give the electroweak bounds for the m_{loc}/m_{KK} in green and the resonant value of m_{KKres} as a function of m_{loc} in red. We see that the stringent bounds coming from electroweak constraints leave us with only a small possible window for varying m_{loc}/m_{KK}. However it should be remembered that there are other contributions to the electroweak parameters in our model which are not calculable. These extra terms are higher order operators with respect to the contributions we have calculated. Therefore they will be typically suppressed.

Finally we are ready to study the influence of the resonant $H^{(2)}$ diagrams to the relic abundance. In the first step we do not consider the bounds from the electroweak constraints.

First let us focus on the L1 case. We have the model with only annihilations and loop couplings.The resonant $H^{(2)}$ can thus only be exchanged in two processes $A^{(1)}A^{(1)} \to t\bar{t}$, HH. The results of the scans are showed in the figure 7.26 on the two top panels.

We can observe a peculiar behavior of the relic abundance. The enhancement of the effective cross section σ_{eff} begins rather early, far before the resonant value of m_{KK}. The process responsible of this effect, $A^{(1)}A^{(1)} \to t\bar{t}$ is not counter-balanced sufficiently in the region $m_{KK} \leq m^{res}_{KK}$. Thus for $m_{KK} < m^{res}_{KK}$ the process is still below the resonance and effectively enhance the total cross section. Once the resonance condition $m_{KK} = m^{res}_{KK}$ is satisfied, i.e. the incoming particles are above the resonance, the wide minimum is sharply cut. The minima appear very near the resonant value of m_{KK} for the incoming particles at rest, namely $2m_{LKP} = m_{H^2}$. The values of those m^{res}_{KK} masses are listed in the table 7.11. What is worth noticing is that the minimums are getting more deep and wide with increasing m_{loc}. For $m_{loc} \in (100, 250)$ the

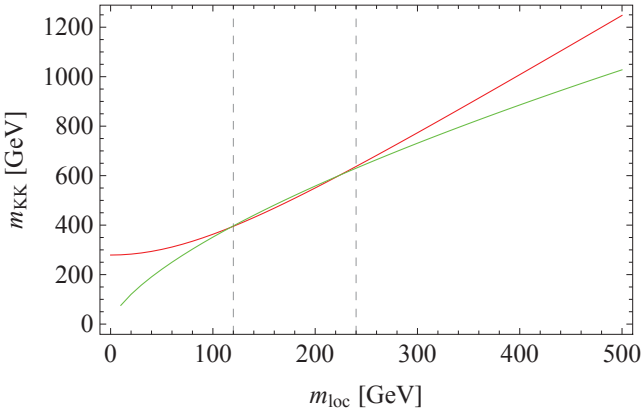

Figure 7.25: Bound on m_{loc} as a function of the m_{KK} mass, obtained imposing that the effect on the ρ parameter is not larger than the allowed measured value within 3σ. The green line shows the lower bounds on m_{loc}/m_{KK}, the region above the line is excluded by electroweak constraints. In red we plot the resonant value of m_{KKres} as a function of m_{loc}. We see that only in the region 110 GeV $< m_{KK} <$ 236 GeV can be relevant physically when we take into account the electroweak constraints. Here we assume the geometry $R_4 \gg R_5$.

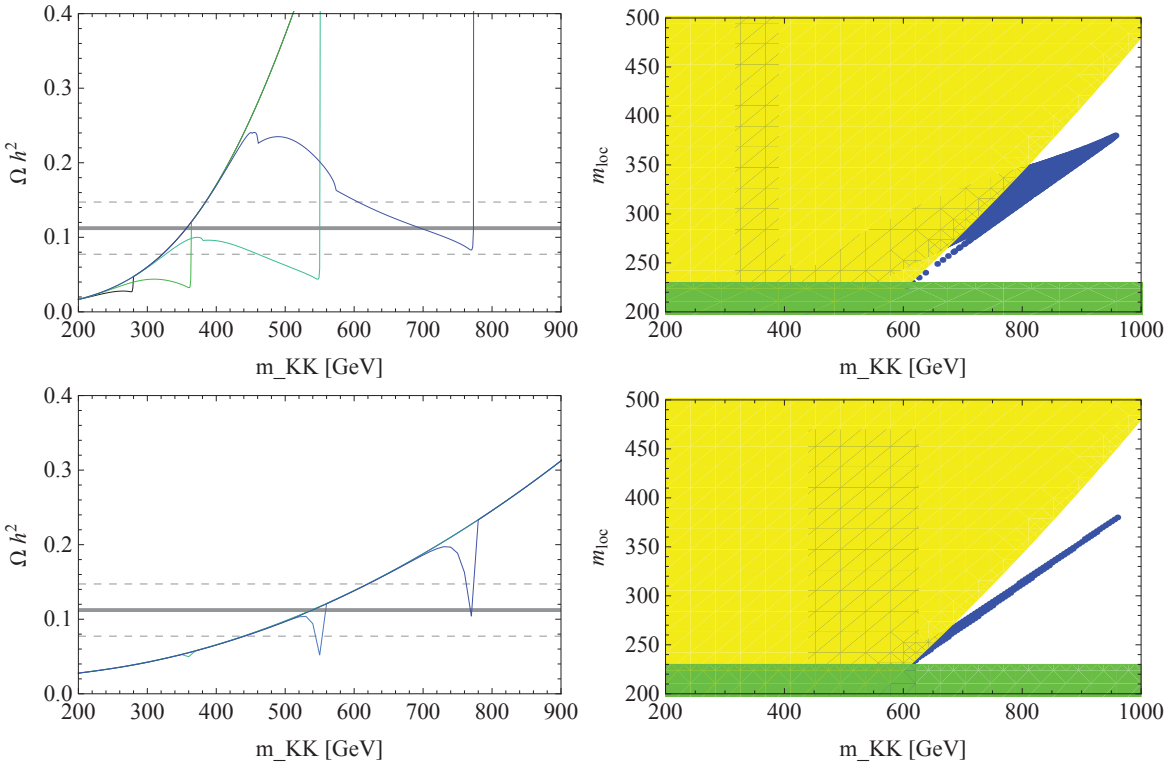

Figure 7.26: **On the left panel:** The shape of the resonances of $H^{(2)}$ in L1 for all the co-annihilations included. $H^{(2)}$ appears in s-channel in reactions $A^{(1)}B^{(1)} \to t\bar{t}$, $f^{(1)}\bar{f}^{(1)} \to t\bar{t}$ where $f^{(1)}$ stands for any fermion of level (1,0) and $A^{(1)}, B^{(1)}$ - any gauge electroweak boson from level (1,0). From the left to the right we see the minima corresponding to $m_{loc} = 0, 100, 200, 300$ GeV. **On the right:** Scan of the allowed m_{KK} masses with varying m_{loc} in the range $0 < m_{loc} < 500$ in the model L1 with all co-annihilations. In yellow we show the range excluded by electroweak precision tests, in green the bound allowed by the condition $m_{KK}^{res} < m_{KK}^{\rho}$.

minimum is deep enough to exclude a region of m_{KK} that was allowed for $m_{loc} = 0$ (i.e. while not including the localized mass operators.) For $m_{loc} > 400$ the minima do not reach the bound of Ωh^2 allowed by WMAP data.

In the figure 7.26 we plot the relic abundance including all co-annihilation channels in the model L1 and we change the value of m_{loc} parameter. We can clearly see the s-channel resonances of $H^{(2)}$ on the left panel. The main contribution to Ωh^2 comes from the reaction $A^{(1)}A^{(1)} \to t\bar{t}$. In this scenario we observe a very clear and narrow minimums appearing in a neighborhood of m_{KK}^{res}. For $m_{loc} = 50, 100$ we can hardly see a small minimum in the relic abundance which do not change the allowed values of m_{KK}. Then for higher values of $200 < m_{loc} < 400$ we see that the m_{KK} values that were forbidden in the absence of resonance are now allowed. Moreover the minimum at $m_{loc} = 150$ is deep enough to exclude a small region of m_{KK} where the relic abundance is below the WMAP limit $\Omega h^2 < 0.0773$. As in the previous case, for $m_{loc} > 400$ the corresponding resonant masses $m_{KK}^{res} > 1000$ GeV and the minima are not deep enough to reach the region of Ωh^2 allowed by WMAP data.

In the right panel of the figure 7.26 we show the full region of allowed m_{KK} for m_{loc} varying between 0 and 500 GeV. In yellow we show the region excluded by the electroweak precision tests. This leaves us with a restricted region for m_{loc} but still we can consider the enhancement of the effective cross section for large m_{loc} and the corresponding window of m_{KK} masses can be open up to ≈ 900 GeV. However, if we add the condition that the m_{KKres} value should not exceed the bound given from the same electroweak tests for a given m_{loc} then the only allowed bound is highlighted in green. This bound is very stringent and leaves only a small window for m_{KK} which is the same as we would obtain for $m_{loc} = 0$.

Now we give the bounds obtained in the L2 scenario. As it was noticed before in the section 7.2 the bounds do not change between the two possible model L1 and L2 when we include only annihilations. Thus we include all the co-annihilation processes and read the allowed ranges of m_{KK} which are plotted in the figure 7.27. Note that the minima are much less deep that in the L1 model thus the allowed regions for m_{KK} will be much more restricted.

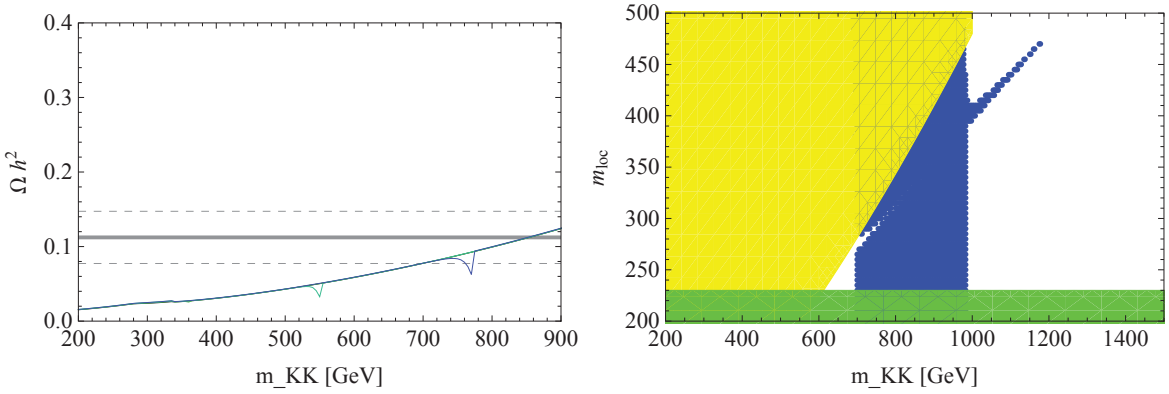

Figure 7.27: **On the left panel:** The shape of the resonances of $H^{(2)}$ in L2 for $m_{loc} = 0, 100, 200, 300$ GeV. Included processes - all co-annihilations. **On the right panel:** Scan of the allowed m_{KK} masses with varying m_{loc} in the range $0 < m_{loc} < 500$ in the model L2. In yellow we show the range excluded by electroweak precision tests, in green the bound allowed by the condition $m_{KK}^{res} < m_{KK}^{\rho}$.

The bounds imposed in green should be however studied in more details. In fact we exclude all the region where the resonant mass m_{KKres} for the $H^{(2)}$ exchange is lower than the bounds imposed by the electroweak tests. One should although remember that there are other co-annihilation processes in which the s-channel resonances are different particles from the $(2, 0)$

level, such as mentioned before weak gauge bosons $W^{(2)}$ and $Z^{(2)}$. The masses of those particles will be affected by m_{loc} parameter as well - the dependence that we should add in our numerical implementation of the model. The new bounds coming from these resonances should be then studied together with the electroweak constraints.

7.5 Direct detection bounds

As mentioned in chapter 3 a number of experiments are currently searching for a cold dark matter. Their sensitivity is being continuously improved and the upper limits are upgraded regularly. The best upper limit for the WIMP-proton spin independent cross section has been recently obtained by Xenon, $\sigma^{SI}_{p\chi} < 3.4 \times 10^{-8}[pb]$ for a 55 GeV WIMP and CDMS $\sigma^{SI}_{p\chi} < 3.8 \times 10^{-8}[pb]$ for a 70 GeV WIMP. For limits from other experiments see 3.1. The spin-dependent cross section is much less restrictive.

In the extra-dimensional models the potential dark matter candidate is usually a KK gauge boson, but it is also possible that a KK scalar, a KK graviton or a KK neutrino is the lightest KK particle. In the minimal UED model the dark matter candidate is the $U(1)_Y$ gauge boson $B^{(1)}$ [2] In our six-dimensional model the dark matter candidate is the first level photon $A^{(1)}$ which is a scalar particle. Thus its interaction properties will be different from the mUED model where the first level photon is a vector particle. It is worth mentioning here that one can find other model in the literature where the dark matter candidate is scalar particle - the inert doublet model (IDM) (99)

The main difference is that there is no spin-dependent interaction. Therefore the direct detection will be mediated only by spin-independent processes. The case where the direct detection signal is mediated only by the SI interaction is much less discriminating (it is more difficult to discriminate the model which is being detected). The only information that can be used is the total cross section and the mass of the DM particle.

We compute the direct detection signal using MicrOMEGAs2.4. The input model is as defined in previous section. The direct detection signal is mediated by the processes showed in the figure 7.28.

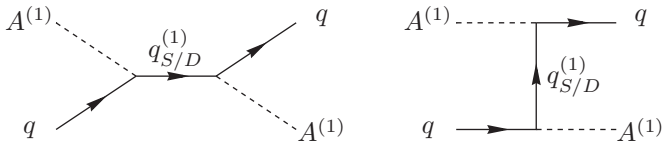

Figure 7.28: Feynman diagrams for direct detection $A^{(1)}q \to A^{(1)}q$ via $q^2_{S/D}$ in s/t channel.

The interactions of $A^{(1)}$ with all the SM quark are mediated by the level one quarks $q^{(1)}_{D/S}$ in s and t channels. Interactions with heavy quarks b, t are mediated also by the higgs boson in t-channel. The Yukawa couplings with light quarks can be safely neglected as they are proportional to the mass of the quark . There are also present the loop induced coupling of second level higgs H^2 with the top quark.

2. More precisely the dark matter candidate is the level 1 photon $A^{(1)}$ -a linear superposition of $B^{(1)}$ and $W^{(1)}_3$ but the mixing angle can be safely neglected.

Given all the model implemented in MicrOMEGAs the parameters we can vary is first of all the cut off of the theory ΛR and the mass of the H^5 via m_{loc} as it was the case in the relic abundance studies. Note however that the $H^{(2)}$ exchange in this case is in t-channel. Thus there will be no resonant effects enhancing cross section $A^{(1)}q \to A^{(1)}q$. Moreover, as the interaction mediated by $H^{(2)}$ exchange have a loop induced coupling, its effect will be negligibly small. We have checked the impact of adding this channel into the total cross section and we have seen that the higgs contribution do not affect in any way the direct detection signal. Thus in our scans we keep $m_{loc} = 0$.

We vary ΛR parameter in the range $2 < \Lambda R < 10$. As with growing cut-off the masses grow the effect of varying ΛR from $\Lambda R = 2$ up to $\Lambda R = 10$ will be the decrease of the SI cross section which is suppressed by the level one quark messes m_{q^1}. The result we find is shown in the figure 7.29 where we show the variation of the spin-independent cross section with m_{KK} for three choices of $\Lambda R = 3,\ 5,\ 10$ as well as various experimental bounds and the numerical values for three example points $\Lambda R = 3,\ 5,\ 10$ are given in the table 7.12. We obain the same results for both geometries of the orbifold $R_4 \gg R_5$ and $R_4 = R_5$ as the $(2, 0)$ particles do not interact in the direct detection processes.

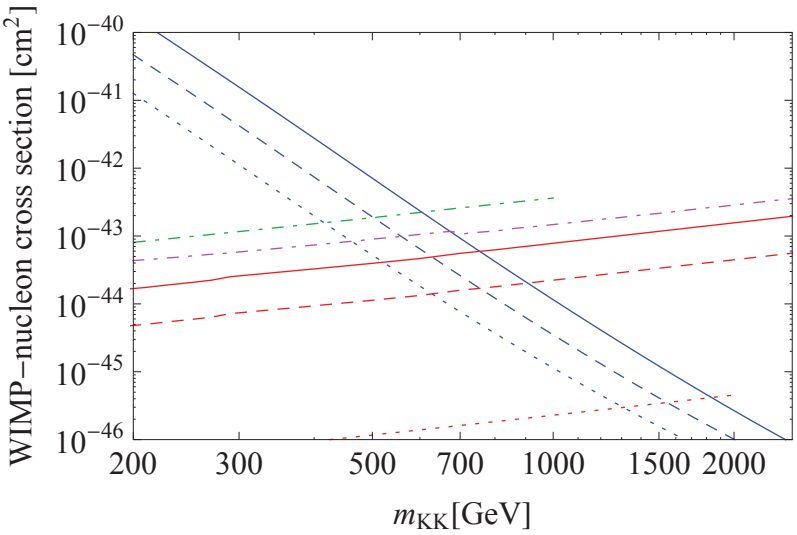

Figure 7.29: Direct detection bounds on m_{KK} masses for the $\mathbb{R}P^2$ for $\Lambda R = 3, 5, 10$ in blue, blue dashed and blue dotted respectively. In blue WIMP - proton cross section in cm^2. In red we give the Xenon limits, plain - 2011, dashed - 2012, dotted - 2017, dot-dashed magenta/green - Zepelin/CDMS+EDELWIESS.

For the "natural" set of parameters $\Lambda R = 10,\ m_{loc} = 0$ we note that the direct detection bounds predict the masses of CDM in the range of $m_{KK} > 410$ GeV for the less constraining ZEPELINIII data and this value is pushed up to 630 GeV for the most constraining Xenon2012 limits. These values are compatible with relic abundance bounds L1 CL and L2 C/CL for the masses lower than 620 GeV while the last obtained bound from Xenon2012 $m_{KK} > 630$GeV is compatible with L2 C/CL predictions.

The lower m_{KK} bound from estimates of Xenon2017 pushes the value of m_{KK} up to more than 1TeV which will be difficult to reconcile with the relic abundance limits.

For lower cut-off the bounds for m_{KK} are pushed up and for example for $\Lambda R = 3$ we get $m_{KK} > 600$ GeV or $m_{KK} > 900$ GeV for the less constraining ZEPLINIII and most constraining XENON2012 bounds respectively. As lowering the cut off have the opposite effect for the relic

Experiment	Zepelin	Edelweiss+CDMS	Xenon2011	Xenon2012	Xenon2017	ΛR
$10^{-44}\sigma[\text{cm}]^2$	23.478	11.045	5.697	2.115	0.041	3
m_{KK}[GeV]	600	675	760	900	1840	
$10^{-44}\sigma[\text{cm}]^2$	19.154	9.721	4.861	1.762	0.036	5
m_{KK}[GeV]	500	560	630	750	1540	
$10^{-44}\sigma[\text{cm}]^2$	14.718	7.615	4.165	1.38922	0.028	10
m_{KK}[GeV]	415	465	520	630	1315	

Table 7.12: Lower bounds for the m_{KK} mass from different direct detection experiments.

abundance calculation, i.e. with growing cut-off the allowed mass range is pushed up the overall parameter space will be much smaller. For the $\Lambda R = 3$ we find indeed that the relic abundance bounds restrict m_{KK} to be lower than 675 GeV and the strongest direct detection bounds $m_{KK} > 900$ will exclude this candidate.

Chapter 8

LHC phenomenology

Some aspects of the phenomenology of the model on the real projective plane have been discussed in refs. (51) and (52). In particular all the loop level decay widths of the $(2,0)$ states were calculated in ref. (52). A detailed study of 4-top events in the scope of the LHC signals was presented in ref. (50). Here we will focus on the even tiers $(2,0)$ and $(0,2)$ phenomenology. These states are important because they lead to events without missing energy, and therefore they can give signatures very different from supersymmetric models.

Notice that the phenomenology of the model will change depending on the relation between the radii $R_4 = \xi R_5$. Here we show the results for two simple cases as we have done for the dark matter phenomenology: $R_4 \gg R_5$ and $R_4 = R_5$. Loop corrections to KK masses of the $(2,0)$ modes are different in both cases, and typically are twice bigger in the degenerate case $R_4 = R_5$. We will observe the influence of this geometrical effect on the phenomenological signals of the model in what follows.

8.1 Decays of the (2,0) KK modes - influence of the geometry of the orbifold.

8.1.1 (2,0) gauge bosons

Gauge bosons can be pair or single produced via loop couplings in the LHC. First we calculate widths and direct branching ratios of all the $(2,0)$ particles to see what are the main decay modes at loop level. In the plots 8.1 we show the total decay widths for the KK gauge bosons. Notice that in general they grow with increasing m_{KK} and that for the asymmetric orbifold $R_4 \gg R_5$ the widths are about one order of magnitude lower than in the symmetric case.

In the tables 8.1 and 8.2 we summarize direct decay branching ratios of $(2,0)$ gauge bosons for $m_{KK} = 600$ GeV for the degenerate and non-degenerate case. Note that the masses of the $(2,0)$ modes as well as total widths change considerably depending on the geometry. In general the decays into heavy KK states $(2,0)$ or a pair (1,0) + (1,0) grows as $R_4 \to R_5$. Two exceptions are the lightest states from the (2,0) tier - the KK photon $A^{(2)}$ and the higgs $H^{(2)}$ which will decay uniquely into SM states independently on the underlying geometry. Also the branching ratio of the KK gluon $G^{(2)}$ into (2,0) quarks will decrease rather than increase due the crossing in masses between $G^{(2)}$ and $q^{(2)}$. Typically, mass corrections to the top quarks $t^{(2)}$ will make the quarks heavier than the $G^{(2)}$ gluon for $m_{KK} \lessapprox 1$ TeV in the asymmetric geometry while gluon is already heavier than top quarks $t^{(2)}$ for $m_{KK} \gtrapprox 500$ GeV in the symmetric case. KK excitations of the higgs boson $H^{(2)}$ will decay into pairs of Standard Model tops but both, the production of higgs excitations and then their decays, are strongly suppressed as compared to other KK bosons

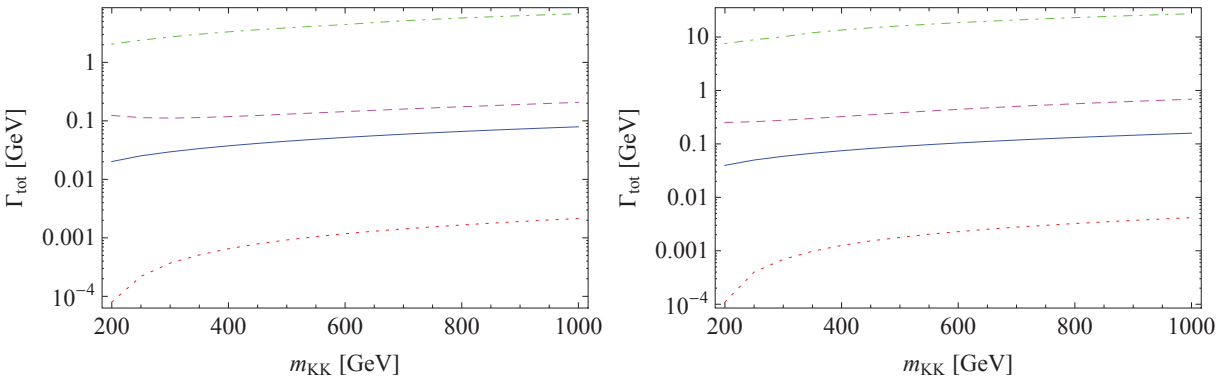

Figure 8.1: Total widths of the $(2,0)$ gauge bosons as a function of m_{KK}. From top to bottom: green dot-dashed - $\Gamma_{G^{(2)}}$, magenta, dashed - $\Gamma_{W^{(2)}} \approx \Gamma_{Z^{(2)}}$, blue - $\Gamma_{A^{(2)}}$, red dotted - $\Gamma_{H^{(2)}}$. **Left panel** $R_4 \gg R_5$ and **right panel** $R_4 = R_5$.

therefore we will neglect the KK higgs in the following study. Other reason for this ignorance is our poor understanding of the higgs sector in the extra-dimensional models. From the tables 8.3 and 8.4 we clearly see that the direct production of phenomenologically interesting SM final states will be suppressed when the geometry of our orbifold become symmetric. In what follows we show the plots of branching ratios only for the non degenerate case $R_4 \gg R_5$. In the limit $R_4 = R_5$ the behavior of the BRs is qualitatively the same with only a quantitative difference shown in the tables where we summarize the BRs for the two different geometries.

particle	mass [GeV]	Γ_{tot} [GeV]	decay mode	BR [%]
$H^{(2)}$	1180.3	0.001	$t\bar{t}$	100
$A^{(2)}$	1200.1	0.05	SM	100
$Z^{(2)}$	1231.5	0.14	SM $l^{(1)}\bar{l}^{(1)} + \nu^{(1)}\bar{\nu}^{(1)}$ $l^{(2)}\bar{l} + \nu\bar{\nu}^{(5)}$	45 18+16 10+10
$W^{(2)}$	1231.5	0.14	SM $l^{(1)}\bar{\nu}^{(1)} + \nu^{(1)}\bar{l}^{(1)}$ $l\bar{\nu}^{(2)} + \nu\bar{l}^{(2)}$	45 35 10+10
$G^{(2)}$	1318.3	4.42	SM $q^{(1)}\bar{q}^{(1)}$ $q\bar{q}^{(2)}$	23 42 21

Table 8.1: Main decay channels and their branching ratios in % of $(2,0)$ gauge bosons at $m_{KK} = 600$ GeV. $R_4 \gg R_5$

KK photon $A^{(2)}$

KK excitation $A^{(2)}$ due to its very small loop corrections can decay uniquely into SM particles via loop couplings. Tree level decays into two particles of (1,0) level or into a pair (2,0) + (0,0) are kinematically forbidden for this particle. Direct branching ratios of $A^{(2)}$ into different SM states are listed in 8.3 and 8.4 for $R_4 \gg R_5$ and $R_4 = R_5$ respectively. The main decay is into a pair of quarks which is at 73% level and the SM top quarks are produced very efficiently in

particle	mass [GeV]	Γ_{tot} [GeV]	decay mode	BR [%]
$H^{(2)}$	1153.5	0.002	$t\bar{t}$	100
$A^{(2)}$	1200.0	0.01	SM	100
$Z^{(2)}$	1259.5	0.4	SM $l^{(1)}\bar{l}^{(1)} + \nu^{(1)}\bar{\nu}^{(1)}$ $l^{(2)}\bar{l} + \nu\bar{\nu}^{(2)}$	29 22+23 10+11
$W^{(2)}$	1259.5	0.4	SM $l^{(1)}\bar{\nu}^{(1)}$ $\nu^{(1)}\bar{l}^{(1)}$ $l\bar{\nu}^{(2)} + \nu\bar{l}^{(2)}$	30 46 11+10
$G^{(2)}$	1426.2	18.6	SM $q^{(1)}\bar{q}^{(1)}$ $q\bar{q}^{(2)}$	7 54 38

Table 8.2: Main decay channels and their branching ratios in % of $(2,0)$ gauge bosons at $m_{KK} = 600$ GeV. $R_4 = R_5$

final state	$A^{(2)}$	$Z^{(2)}$	$G^{(2)}$	final state	$W^{(2)}$
$q\bar{q}$	73.03	34.60	12.66		
$t\bar{t}$	25.30	6.23	2.48	$u\bar{d}$	25.40
$l\bar{l}$	0.85	1.48	-	$t\bar{b}$	11.80
$\nu\bar{\nu}$	0.78	1.37	-	$l\bar{\nu}$	2.32
ZH	0.11	0.28	-	ZW	0.26
W^+W^-	0.06	0.31	-	HW	0.23

Table 8.3: Branching ratios in % of the loop induced decays of the $(2,0)$ gauge bosons into SM states at $m_{KK} = 600$ GeV for $R_4 \gg R_5$.

final state	$A^{(2)}$	$Z^{(2)}$	$G^{(2)}$	final state	$W^{(2)}$
$q\bar{q}$	73.27	22.55	6.49		
$t\bar{t}$	24.78	4.23	0.01	$u\bar{d}$	18.22
$l\bar{l}$	0.91	0.97	-	$t\bar{b}$	8.85
$\nu\bar{\nu}$	0.71	0.93	-	$l\bar{\nu}$	1.89
ZH	0.09	0.18	-	ZW	0.19
W^+W^-	0.07	0.20	-	HW	0.18

Table 8.4: Branching ratios in % of the loop induced decays of the $(2,0)$ gauge bosons into SM states at $m_{KK} = 600$ GeV for $R_4 = R_5$.

$A^{(2)}$ decays. This di-jet signal is very challenging to observe in the LHC and potentially can lead to interesting LHC signatures and to multi-top events. A study of four-top production was presented in (50). Leptonic final states are produced at very small level but can be easily detected in hadronic colliders.

KK electroweak gauge boson $Z^{(2)}$.

KK excitations of the electroweak gauge gauge boson Z receive important loop corrections therefore the tree level decays into heavy KK leptons from the $(1,0)$ and $(2,0)$ tiers will be

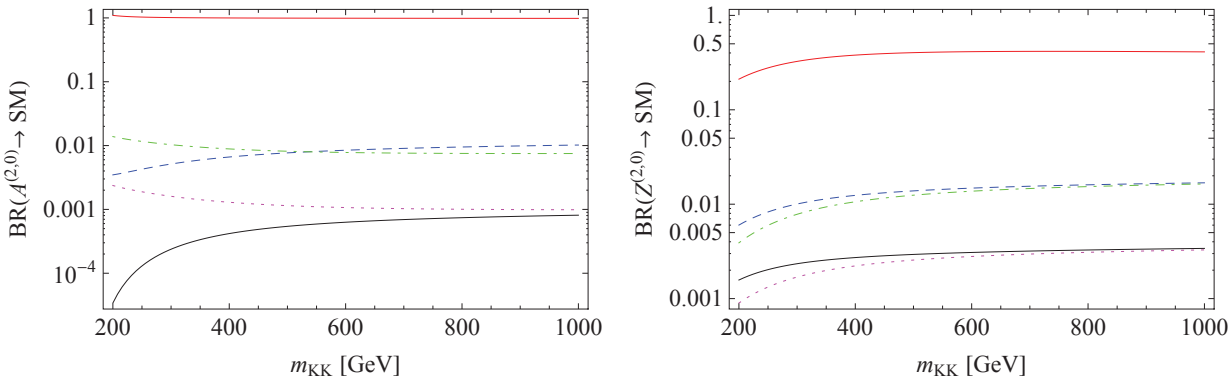

Figure 8.2: BR of $A^{(2)}$ **left panel** and $Z^{(2)}$ **right panel**. Color conventions for final states: red jj, blue dashed - $l\bar{l}$, green dot-dashed - $\nu\bar{\nu}$, magenta dotted - ZH, black WW. $R_4 \gg R_5$

kinematically accessible. Decays into a pair of $(1,0)$ leptons are at 35% level while decays into $(1,0)$ quarks are still, as for $A^{(2)}$, kinematically inaccessible.

Within the resonant production of the SM states, with BR=45% at $m_{KK} = 600$ GeV, the main decays will be in the SM quarks followed by the leptonic decays which typically have lower BRs for all the KK gauge bosons. SM leptons however will be produced more abundantly from the $Z^{(2)}$ decays than from the $A^{(2)}$ photon. The SM decay products of $Z^{(2)}$ are the same as those of $A^{(2)}$ but with different BRs as can be seen in the tables 8.3 and 8.4 for $R_4 \gg R_5$ and $R_4 = R_5$ respectively.

Other 20% of decays will be into pairs $(2,0) + (0,0)$. In the tree level mediated processes most of final states will be invisible matter, namely neutrinos and only a small fraction of $Z^{(2)}$ will decay into easily detectable charged leptons. The branching ratios for the $Z^{(2)}$ decays as a function of m_{KK} in the asymmetric geometry of the orbifold are summarized on the plots 8.3 for the tree level processes and 8.2 for the loop induced couplings.

At tree level there are also possible decays into a pair of gauge scalars from the first KK level or a pair of gauge bosons $(0,0)$ + (2,0) but they are at at most 5% level.

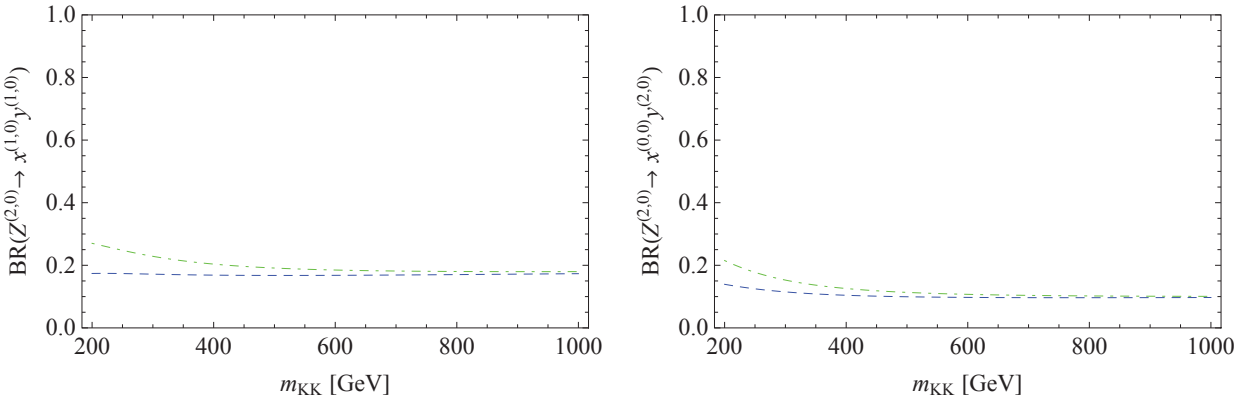

Figure 8.3: BR of $Z^{(2)} \to (1,0) + (1,0)$ **left panel** and $Z^{(2)} \to (0,0) + (2,0)$ **right panel**. Color conventions for final states: blue dashed - $l\bar{l}$, green dot-dashed - $\nu\bar{\nu}$. $R_4 \gg R_5$.

KK electroweak gauge boson $W^{(2)}$.

$W^{(2)}$ KK boson decays at 35% into pairs $l^{(1)}\nu^{(1)}$ and at 25% into $(2,0)+(0,0)$ states. At loop level it decays mostly into light quark pairs as can be seen in the plots 8.4 where we show the evolution of the BRs with m_{KK} for the non-degenerate radii $R_4 \gg R_5$. We can expect that the cascade decays of $(1,0)$ leptons produced with a significant ratio in the $W^{(2)}$ decays will provide quite a clear signal with charged SM leptons. Also the resonant direct production of the SM charged leptons could be challenging to detect and would provide a clear signature of the model.

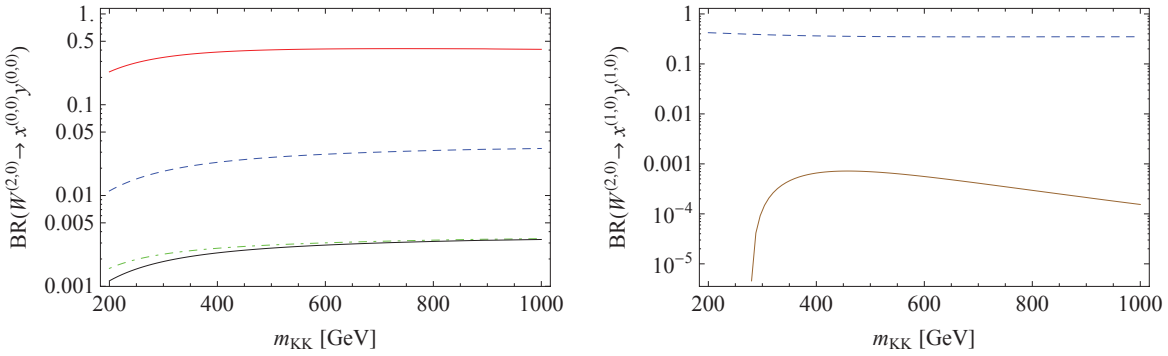

Figure 8.4: BR of $W^{(2)} \to SM$ **(left)** and $W^{(2)} \to (1,0)+(1,0)$ **(right)**. Color conventions for final states: red: $u\bar{d}$, blue dashed: $l\nu$, green dot-dashed: ZW, black:HW, brown: $A^{(1)}W^{(1)}$. $R_4 \gg R_5$.

Branching ratios for the symmetric geometry at the benchmark point $m_{KK} = 600$ GeV can be seen in the tables 8.2 for the (1,0) and (2,0) tiers decay products and in the table 8.4 for direct SM decays.

KK colored gauge boson $G^{(2)}$

Heavy gluon $G^{(2)}$ can decay into $(1,0)$ and $(2,0)$ quarks or into a pair of SM quarks directly. The decay into a pair of gluon scalar partners $G^{(1)}$ is at 1% level. Thus we expect a significant resonant effects from the (2,0) gauge bosons to the LHC signatures. $G^{(2)}$ will decay at ∼50% rate into pairs of (1,0) quarks via tree level couplings. Decays into SM+(2,0) states are subleading (∼ 40%) and finally loop induced decays into SM quarks and gluons are produced at 10% level. Note that the SM final states are quite important in comparison with the tree level processes. This is due to the fact that loop induced mass splittings of the final $(1,0)+(1,0)$ and $(2,0)+(0,0)$ states are large, which makes the processes to be almost on threshold thus they will be kinematically suppressed making them of the same order as the loop induced decays.

Direct branching ratios of the decays into SM particles are listed in the table 8.3 for a benchmark point $m_{KK} = 600$ GeV and plotted in the left panel of the figure 8.5 for a wider range of m_{KK} masses for $R_4 \gg R_5$.

8.1.2 (2,0) leptons

Next we turn to (2,0) leptons. Their total widths are very small compared to gauge bosons and grow when we go from the asymmetric scenario to the symmetric one. We plot the widths for the two geometries of the orbifold in the figure 8.6.

The main decay channels and branchings are summarized in the table 8.5 for $R_4 \gg R_5$ and in tab. 8.6 for $R_4 = R_5$. The $SU(2)_W$ singlet (2,0) leptons will decay into pairs $lA^{(2)}$ and $l^{(1)}A^{(1)}$ (both, charged and neutral). The latter channel is kinematically more suppressed due to larger mass corrections. Also the final states with KK Z excitations are kinematically forbidden.

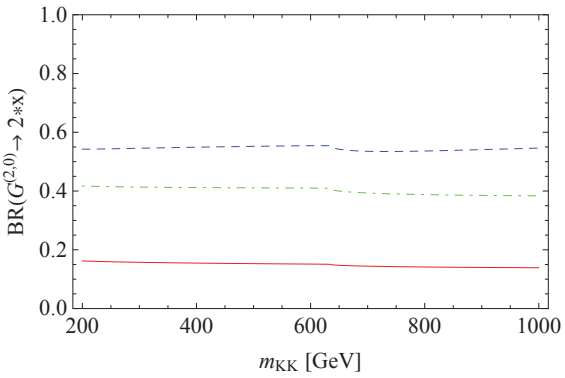

Figure 8.5: BR of $G^{(2)} \to 2 * x$. Color conventions for final states: red: $q\bar{q} + GG$, blue dashed: $q^{(1)}\bar{q}^{(1)}$, green dot-dashed: $q^{(2)}\bar{q}$, black: HW, brown:$A^{(1)}W^{(1)}$.

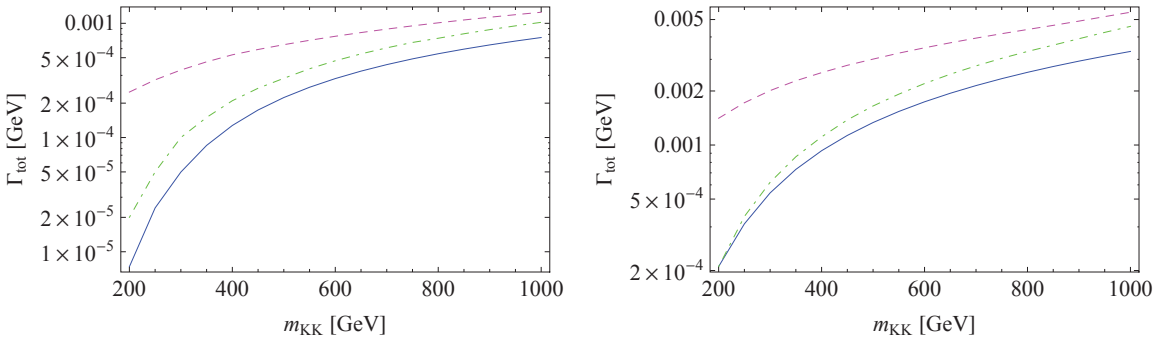

Figure 8.6: Total widths of the $(2,0)$ SU(2) singlet and doublets leptons. From top to bottom: magenta dashed: $\Gamma(l_D^{(2)})$, green dot-dashed: $\Gamma(\nu_D^{(2)})$, blue: $\Gamma(l_S^{(2)})$. **Left panel** $R_4 \gg R_5$ and **right panel** $R_4 = R_5$.

In the figure 8.7 we see a typical behavior of the decay branching ratios into (1,0) or (2,0) states. While for $\mathrm{SU(2)_W}$ doublet leptons the BRs of those two final states, $lA^{(2)}$ and $l^{(1)}A^{(1)}$, are almost constant with m_{KK} scale, for the $\mathrm{SU(2)_W}$ singlet leptons the production of (1,0) pairs will be more efficient with growing m_{KK}. This is a direct consequence of the fact that the $\mathrm{SU(2)_W}$ singlet states are almost degenerate with $A^{(1)}$ photon what will make a direct decay into $A^{(1)}$ very inefficient. With increasing m_{KK} the $A^{(1)}$ mass stays almost untouched while $l_S^{(1)}$ will become heavier. The mass splitting between the $l^{(2)}$ and $A^{(2)}$ is very small thus the produced SM leptons will be soft. The $A^{(2)}$ will in turn decay into a pair of SM particles as we have seen above on the plot 8.2.

Due to larger mass corrections in the symmetric scenario the decays channels into $(1,0)$ pairs will be more accessible kinematically as we can see by comparing the values of branching ratios in the tables 8.5 and 8.6. For the asymmetric case the decays into $A^{(2)}$ boson were at 70% level for both, singlet and doublet charged leptons while for the $R_4 = R_5$ case the decays into $(2,0)$ state and a pair of (1,0) particles are almost at the same level of about 50%. The influence of this geometrical effect should have an impact on the LHC signals as the heavier $A^{(2)}$ states will be produced less efficiently both in the single production and as the decay products thus the resonant contribution to the SM particles production will be somehow suppressed. We should quantify this effect by investigating in details the dependence of LHC signals on the ratio $\frac{R_4}{R_5}$ in the forthcoming work.

particle	mass [GeV]	Γ_{tot} [MeV]	decay mode	BR [%]
$l_S^{(2)}$	1204.5	0.3	$lA^{(2)}$ $l_R^{(1)}A^{(1)}$	74 26
$l_D^{(2)}$	1212.4	0.8	$lA^{(2)}$ $l_D^{(1)}A^{(1)}$	71 29
$\nu_D^{(2)}$	1224.7	0.5	$\nu A^{(2)}$ $\nu^{(1)}A^{(1)}$	84 16

Table 8.5: Main decay channels and their branching ratios in % of $(2,0)$ leptons at $m_{KK} = 600$ GeV for the asymmetric geometry $R_4 \gg R_5$

particle	mass [GeV]	Γ_{tot} [MeV]	decay mode	BR [%]
$l_S^{(2)}$	1209.0	1.7	$lA^{(2)}$ $l_R^{(1)}A^{(1)}$	59 41
$l_D^{(2)}$	1224.7	3.4	$lA^{(2)}$ $l_D^{(1)}A^{(1)}$	60 40
$\nu_D^{(2)}$	1224.7	2.4	$\nu A^{(2)}$ $\nu^{(1)}A^{(1)}$	78 22

Table 8.6: Main decay channels and their branching ratios in % of $(2,0)$ leptons at $m_{KK} = 600$ GeV for the symmetric case $R_4 = R_5$.

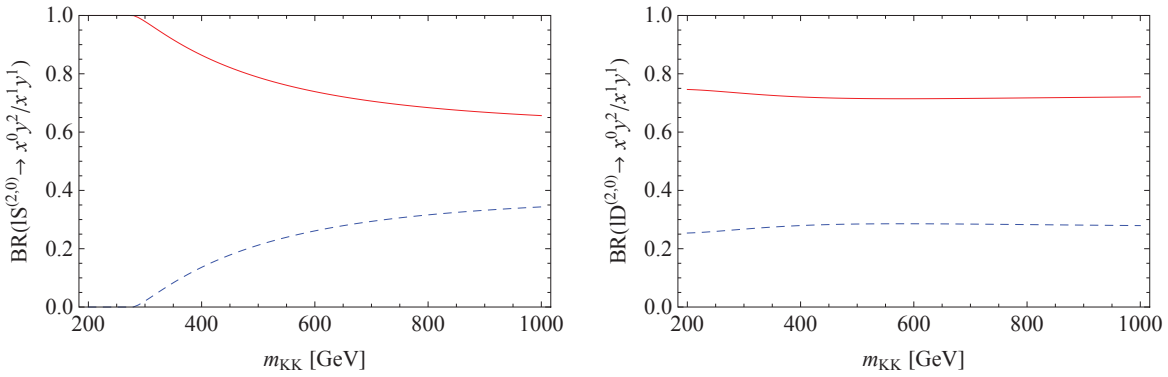

Figure 8.7: Branching ratios of $(2,0)$ $SU(2)_W$ singlet **(left)** and doublet **(right)** leptons. In red: $l_{S/D}^{(2,0)} \to lA^{(2,0)}$ blue: $l_{S/D}^{(2,0)} \to l_{S/D}^{(1,0)}A^{(1,0)}$ for $R_4 \gg R_5$. This typical behavior will not change when we impose $R_4 = R_5$ scenario.

8.1.3 (2,0) quarks

Tree level decays

At tree level the singlet quarks from the $(2,0)$ tier can decay into a quark of the same flavor and a neutral gauge bosons: $q_S^{(2)} \to q^{(1)}A^{(2)}/Z^{(1)}$, $q_S^{(2)} \to qA^{(2)}/Z^{(2)}$. Gluon KK excitations $G^{(1)/(2)}$ are too heavy to appear in the final state. Top quarks, as we have included the mixing between the S and D states will decay also into a b quark and a W boson as $t_S^{(1)} \to b_D^{(1)}W^{(1)}$,

$t_S^{(1)} \to bW^{(2)}$.

Dominant decays of $q_S^{(2)}$ are into KK photon while the BR into KK excitations of the Z boson is three orders of magnitude smaller and opens, for the light singlet quarks at $m_{KK} \approx 450$ GeV for $R_4 \gg R_5$ (for $R_4 = R_5$ the channel is already opened at $m_{KK} = 200$ GeV).

Note that at $m_{KK} = 600$ GeV the channel $t_S^{(1)} \to t_D^{(1)} Z^{(1)}$ is still closed. It opens at $m_{KK} \approx 750$ GeV with BR$\sim 10^{-8}$%.

The SU(2)$_{\rm W}$ doublet quarks $q_D^{(2)}$ will decay more likely into their doublet SM quark partner and the W KK boson or into the same flavor quarks and a Z boson KK states. Decays into $(1,0)$-level pairs $q^{(1)}W^{(1)}$ are at 5% level while the decays into the same flavor quark have the branching ratio of about 3%. Similar thing happens for decays into $qW^{(2)}$ and $qA/Z^{(2)}$ pairs. Note that, the $b_D^{(2)}$ decay channel into $tW^{(2)}$ is closed up to $m_{KK} \approx$750 GeV, therefore the dominant decay mode within the $(2,0)$ tier will be $bZ^{(2)}$. Decays $b_D^{(2)} \to t_D^{(1)} W^{(1)}$ are also closed up to the m_{KK} mass of order of 800 GeV. The heavy gauge bosons produced abundantly from the $q_D^{(1)}$ will then chain decay into the SM jets or into lepton pairs.

Loop induced decays

It was shown in ref. (52) that at loop level the $(2,0)$ quarks cannot couple to a massless gauge boson and a massless quark due to the structure of the gauge coupling. Therefore the possible loop induced decays will include only massive SM bosons and an SM quark $t_S^{(2)} \to t, Z/H$, $t_S^{(2)} \to bW$ and $b_S^{(2)} \to tW$. We neglect the decays of the light quarks into two SM particles as they are highly suppressed by the Yukawa couplings.

Decays into a SM quark plus a (2,0) gauge boson is suppressed by the mass of the gauge boson. Heavy quarks will mainly decay into a SM fermion plus an electroweak gauge boson in the same tier (the gluon is too heavy) or into a pair of fermion and electroweak gauge scalar in the level (1,0). Noticeably, there is no phase space for decays into another fermion in tier (2,0) because such decay would also contain a massive gauge boson. The total widths for the up- and down-type light quarks and for the tops are shown in the figure 8.8. In tables 8.7 and 8.8 we give the typical values of branching ratios for singlet up- and down-type quarks for $R_4 \gg R_5$ and $R_4 = R_5$ geometries.

We see from the tables 8.7 and 8.8 that the influence of the geometry of the underlying orbifold is very important for the quark decays. This is a direct effect of the different mass ratio m_{q^2}/m_{G^2} which in the case $R_4 = R_5$ is smaller than one resulting in a strong enhancement of the decay rate into a pair of quark and gluon in the (1,0) + (1,0) or SM + (2,0) tiers.

From the results shown above we can see that most of events will contain a chain decay within level (2, 0) to the lightest state $A^{(2)}$ or a decay into states of tier (1, 0) that will chain decay to the stable dark matter candidate $A^{(1)}$. In both cases SM particles emitted in the chain will have very little energy due to the small splitting between the masses within each tier. Moreover, states in level (1, 0) will give rise to missing energy. We expect however the particle in level (2, 0) that initiate the chain to have very little transverse momentum. The consequence is that the states in tier (1, 0) at the end of the decay chain will also have little transverse momentum, and therefore the event will not contain significant missing energy after all. This simple picture is affected by the fact that some events will have sufficient transverse momentum at production and that initial state radiation may boost the whole event. To study this effect, a detailed Monte Carlo simulation would be needed.

Heavy gauge bosons, on the other hand, can decay directly into a pair of energetic SM fermions at any stage in the decay chain. Even though the branching ratios are rather small,

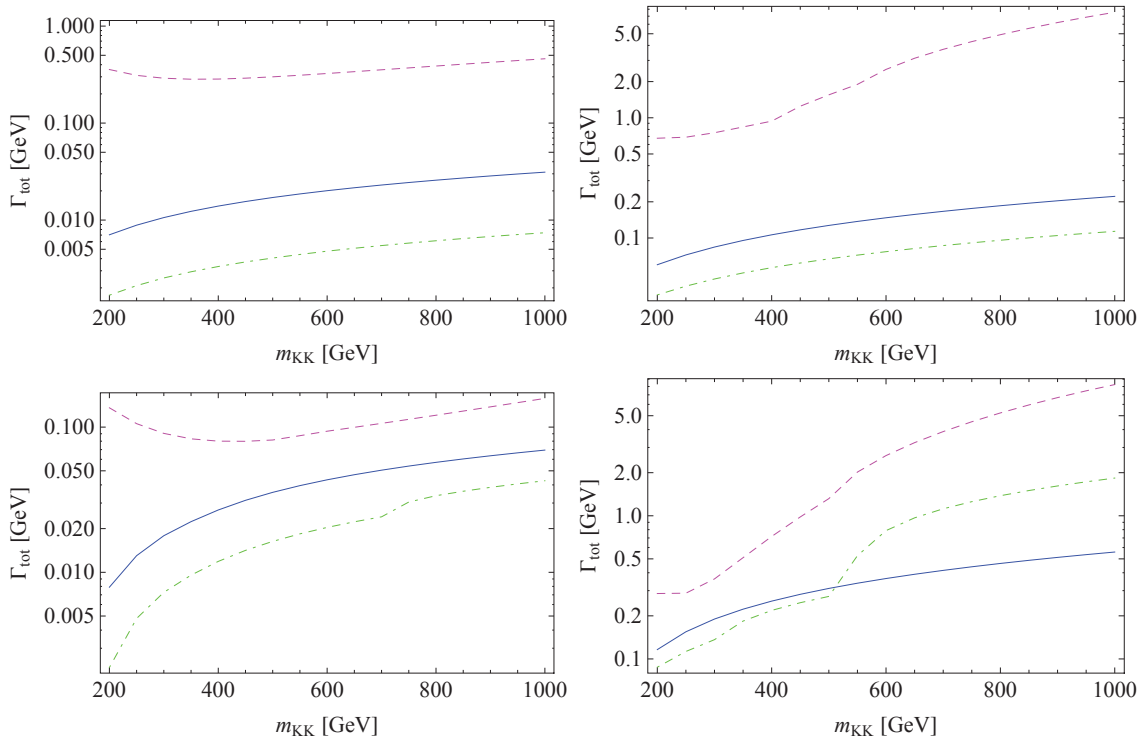

Figure 8.8: Total widths of the $(2,0)$ SU(2) singlet **(top panels)** and doublets **(bottom panels)** quarks as a function of m_{KK}. Assymmetric geometry $R_4 \gg R_5$ is assumed on the **left** and symmetric on the **right**. From bottom to the top: magenta, dashed - $\Gamma_{t^{(2)}}$, blue - $\Gamma_{u^{(2)}}$, green dot-dashed - $\Gamma_{d^{(2)}}$.

the signal can be very clean and easy to be detected by the experiments. The main mode will be into light jets and will be affected by a large QCD background, the cleanest signatures will therefore be given by energetic leptons and tops.

particle	mass [GeV]	Γ_{tot} [MeV]	decay mode	BR [%]
$u_S^{(2)}$	1257.4	20.1	$uA^{(2)}$	86
			$u_S^{(1)}A^{(1)}$	13
$u_D^{(2)}$	1266.8	43.4	$dW^{(2)}$	56
			$uZ^{(2)}$	27
			$uA^{(2)}$	5
			$d_D^{(1)}W^{(1)}$	6
			$u_D^{(1)}Z^{(1)}$	2
			$u_D^{(1)}A^{(1)}$	1
$d_S^{(2)}$	1243.6	4.8	$dA^{(2)}$	86
			$d_S^{(1)}A^{(1)}$	13
$d_D^{(2)}$	1266.8	41.4	$uW^{(2)}$	59
			$dZ^{(2)}$	30
			$dA^{(2)}$	2
			$u_D^{(1)}W^{(1)}$	6
			$d_D^{(1)}Z^{(1)}$	3
$t_S^{(2)}$	1274.1	324.9	$bW^{(2)}$	86
			$b_D^{(1)}W^{(1)}$	12
$t_D^{(2)}$	1283.5	93.7	$bW^{(2)}$	70
			$b_D^{(1)}W^{(1)}$	9
			$t_S^{(1)}A^{(1)}$	8

Table 8.7: Main decay channels and their branching rations in % of $(2,0)$ quarks at $m_{KK} = 600$GeV. $R_4 \gg R_5$.

8.2 Heavy states production in the LHC

At the LHC the most important states to be produced are quarks and gluons, because they have strong interactions and also because the proton is made of quarks. Larger cross sections are obtained in general for the partners of the light quarks. All other cross sections are subdominant. Channels with heavy quarks are larger due to the dominant contribution coming from the production of heavy up quarks which are enhanced due to the presence of a valence up quark in the initial state. Nevertheless, all the other channels involving down and second generation quarks also contribute significantly and cannot be neglected.

The heavy gluon $G^{(2)}$ can be pair-produced or in association with a heavy quark $q_{S/D}^{(2)}$. Pair production is mediated by the bulk interactions and can proceed via a gluon in the s- and t-channel and or a t-channel quark exchange. The associated production is mediated by a quark in s- or t-channel. Another possible production mechanism is via loop induced interactions by annihilation of two SM quarks directly into $G^{(2)}$ and gives comparable results as the associated production mechanism.

The main production cross sections as a function of the KK mass are plotted in the figure 8.9 where the inclusive production cross sections for a pair of (2,0) quarks (and antiquarks), a single heavy quark in association with an heavy gluon and a pair of heavy gluons are shown for two different geometries of the orbifold. From the table 8.9 where we give numerical values

particle	mass [GeV]	Γ_{tot} [MeV]	decay mode	BR [%]
$u_S^{(2)}$	1314.2	147	$uA^{(2)}$	44.53
			$u_S^{(1)}G^{(1)}$	44.91
			$u_S^{(1)}A^{(1)}$	10.41
$u_D^{(2)}$	1332.9	116.21	$dW^{(2)}$	24.19
			$uZ^{(2)}$	10.38
			$uA^{(2)}$	6.42
			$d_D^{(1)}W^{(1)}$	7.31
			$u_D^{(1)}G^{(1)}$	46.13
			$u_D^{(1)}A^{(1)}$	3.74
			$u_D^{(1)}Z^{(1)}$	1.81
$d_S^{(2)}$	1311.2	76.9	$d_S^{(1)}G^{(1)}$	74.69
			$dA^{(2)}$	20.25
			$d_S^{(1)}A^{(1)}$	4.86
$d_D^{(2)}$	1332.9	361.44	$uW^{(2)}$	27.86
			$dZ^{(2)}$	14.03
			$dA^{(2)}$	1.14
			$u_D^{(1)}W^{(1)}$	14.49
			$d_D^{(1)}G^{(1)}$	35.04
			$d_D^{(1)}Z^{(1)}$	7.42
$t_S^{(2)}$	1334.7	2525.83	$bW^{(2)}$	1.12
			SM (tZ+bW+tH)	0.1
			$bS^{(2)}$	26.78
			$tH^{(2)}$	2.56
			$b_D^{(1)}W^{(1)}$	19.51
			$t_{D+S}^{(1)}G^{(1)}$	33.84
			$t_{D+S}^{(1)}Z^{(1)}$	7.91
			$t_{D+S}^{(1)}A^{(1)}$	0.6
$t_D^{(2)}$	1353.4	2633.50	$bW^{(2)}$	4.48
			$bS^{(2)}$	11.16
			$tH^{(2)}$	19.87
			$b_D^{(1)}W^{(1)}$	19.42
			$t_{S+D}^{(1)}G^{(1)}$	54.52
			$t_{S+D}^{(1)}Z^{(1)}$	1.5
			$t_{S+D}^{(1)}A^{(1)}$	4.62
			SM(tZ+bW+tH)	0.02

Table 8.8: Main decay channels and their branching rations in % of $(2,0)$ quarks at $m_{KK} = 600$ GeV. $R_4 = R_5$.

for a benchmark point $m_{KK} = 600$ GeV we notice that the production cross section in the asymmetric case is smaller than in the symmetric scenario of about 12%. In the figure 8.10 we show the single production cross sections of the heavy (2,0) gauge bosons where we take into

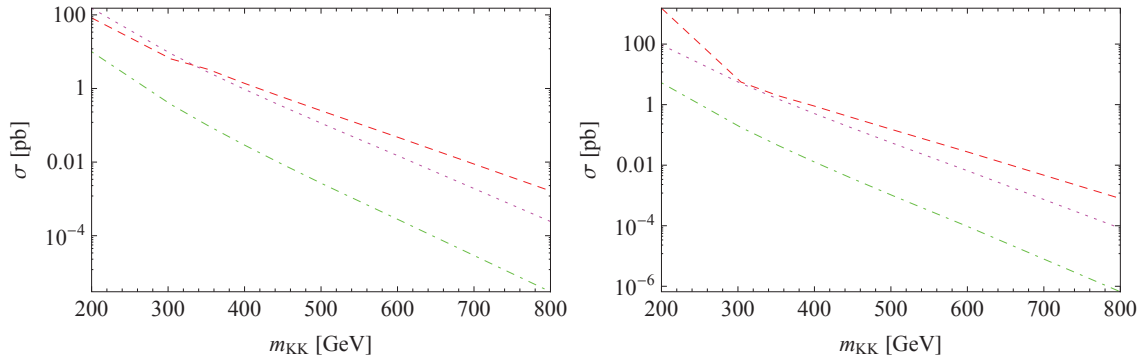

Figure 8.9: Cross sections at the LHC at 7 TeV for the pair productions of heavy states: the red dashed line represents the channel with a pair of heavy quarks, in magenta dotted an heavy gluon in association with an heavy quark, in green dot-dashed a pair of heavy gluons. **On the left panel:** $R_4 \gg R_5$. **On the right panel:** $R_4 = R_5$.

final state	$R_4 \gg R_5$ σ [fb]	$R_4 = R_5$ σ [pb]
$u^{(2)}u^{(2)}$	7.38	27.26
$U^{(2)}U^{(2)}$	0.27	0.26
$q^{(2)}G^{(2)}$	15.03	6.57
$G^{(2)}G^{(2)}$	0.28	0.09
total	22.96	34.18

Table 8.9: Cross sections at the LHC at 7 TeV for the pair productions of heavy states at $m_{KK} = 600$ GeV. $u^{(2)}$ stand for the sum of the light (2,0) quarks (u,c,d,s), $U^{(2)}$ for the heavy quarks $b^{(2)}$ and $t^{(2)}$, $q^{(2)}$ for the sum over all the quarks in the (2,0) state.

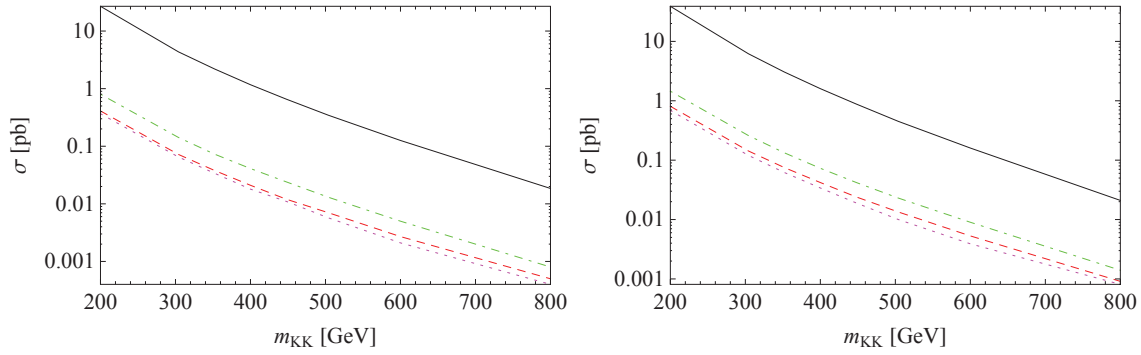

Figure 8.10: Single production cross section of (2,0) gauge boson in the LHC 7 TeV : the red dashed line represents the channel $A^{(2)}$ production, in magenta dotted $Z^{(2)}$, in green dot-dashed $W^{(2)}$ and in black the single $G^{(2)}$ production. **On the left panel:** $R_4 \gg R_5$. **On the right panel:** $R_4 = R_5$.

account only the s-channel cross-section into SM final states for the electroweak gauge bosons and a $q^{(2)} + q_{SM}$ final state for heavy gluon.

We note that the cross sections are quite promising. The production cross sections of colored states are of order of 10 pb at the benchmark point $m_{KK} = 600$ GeV. The single production cross sections are smaller, of order of 1 pb, but still we have a very clean signatures in di-leptons

or di-tops final states therefore we can expect to have a good potential to be discovered in the LHC.

8.3 LHC signatures

Charged and neutral massive gauge bosons, usually named W' and Z' are proposed in many theoretical extensions of the Standard Model. Searches of those new vector particles are performed in the colliders (Tevatron CDF, D0, LHC) and the analyzed data are interpreted in the context of several models proposed in the literature, such as "left-right symmetric" gauge group $\mathrm{SU}(2)_L\times \mathrm{SU}(2)_R\times \mathrm{U}(1)_{B-L}$, (113), model with the Standard Model fermions that couple to the W boson transforming as doublets under $\mathrm{SU}(2)_L$, and the other ones transforming as doublets under $\mathrm{SU}(2)_R$.

W' at hadron colliders can be detected through resonant production of fermions or electroweak gauge bosons. Assuming $\Gamma_{W'} \ll m_{W'}$ one can approximate that

$$\sigma(pp \to f\bar{f}'X) \approx \sigma(pp \to W'X)BR(W' \to f\bar{f}') \tag{8.1}$$

where $f, \bar{f}'$ are SM fermions with difference of charges $|q_f - g_{f'}| = 1$ and X is any final state. The most studied decay channels are $W' \to e\nu_e$ and $W' \to \mu\nu_\mu$. The corresponding branching ratios can in principle be very different and thus those two channels can in principle be studied separately.

Other interesting decay channel is $W' \to t\bar{b}$ which typically will give a signature of two b jets and a leptonically decaying W gauge boson. If $m_{W'} > m_t$ then hadronic decays of W are also possible and can modify the SM s-channel single top production. Finally collider searches concentrate also on decays $W' \to WZ$.

In our model W' corresponds to the KK (2,0) excitation of the W gauge boson. Its decay modes were presented in the previous section. As we have seen, it can decay directly into SM states or chain decay through (2,0) and (1,0) particles down to $A^{(2)}$ and $A^{(1)}$ which will decay only into SM final states at loop level due to their very small mass corrections.

Z' collider searches are based on the decays in two charged SM leptons $Z' \to l^+l^-$ or into two top quarks $Z' \to t\bar{t}$. In our model a generic Z' will correspond to $Z^{(2)}$ and $A^{(2)}$ KK excitations.

We will thus concentrate on the interesting LHC signatures that can arise from the (2,0) resonant particles decaying into SM states via loop couplings. As it was seen above in our model the only resonant decays can arise from the (2,0) gauge bosons. They can be pair or single produced via localized counterterms. We are interested in final states with a resonant pair of SM particles from the decay of heavy gauge bosons. Those in turn can be pair produced via bulk interactions or single produced via localized counterterms. The single production mechanisms are:

1. QCD production of heavy gluons which will decay into quarks

$$pp \to G^{(2)} \to q^{(2)}_{D/S}j$$

2. Drell-Yan production of heavy gauge bosons decaying then into wanted final states

$$\begin{gathered} pp \to A^{(2)}, Z^{(2)} \to l^+l^- \\ pp \to W^{(2)\pm} \to l^\pm\nu \\ pp \to W^{(2)\pm} \to W^\pm Z \\ pp \to A^{(2)}, Z^{(2)}, G^{(2)} \to t\bar{t} \ \text{ or } \ jj \\ pp \to W^{(2)\pm} \to tb \end{gathered} \tag{8.2}$$

(8.3)

These channels are very clean because the lepton and top pairs resonate with the mass of the tier, while the 4 top channel has negligible background from the SM. Due to the way they were calculated in ref. (52) only the production of on-shell (2,0) states is correctly taken into account. Authors of ref. (52) used the effective counter terms to calculate the coefficients of the loop couplings between a (2,0) and two (0,0) states in the "magic" gauge $\xi = 3$. The full implementation would require the inclusion of gauge-dependent loop corrections to all vertices, including bulk ones, and is beyond the scope of this work. In order to impose the resonant states on-shell we can impose a cut on the invariant mass of the final states to be around the mass of the decaying particle.

We have prepared the detailed analysis of the LHC searches using MadGraph implementation of the model connected with BRIDGE[1]. All the decay chains down to SM particles are taken into account and the final state is always accompanied by softer SM states from the decay chains. Here we will shortly summarize the results and the philosophy of the experimental searches . For more details we invite the reader to look for the paper which is under preparation when I am writing this text.

8.3.1 $W' \to l^{\pm}\nu_l$ searches

The searches of decays $W' \to l^{\pm}\nu_l$ are based on events with high p_T lepton and missing energy coming from the neutrino. The studied variable is

$$m_T = \sqrt{2p_T^l E_{Tmiss}^{\nu}(1 - \cos\Delta\phi_{l\nu})} \tag{8.4}$$

where $\Delta\phi_{l\nu}$ is the azimuthal opening angle between the charged lepton's transverse momentump_T^l and the direction of the observed missing energy signal E_{Tmiss}^{ν} direction. It is assumed that all the missing energy is due to neutrino. In our model this signal can come from the decay $W^{2\pm} \to l^{\pm}\nu_l$. The $W^{2\pm}$ is produced as decay product of colored states. It is important to notice also that in pair production of heavy gauge bosons the invisible decays of the second particle can give an extra MET as in the decays of $Z^{(2)} \to \nu\bar{\nu}$ or from decays into two $(1,0)$ states. In the analysis we have done the veto is imposed on the production of heavy states in the first tier and hard leptons from other decays.

The CMS search (59) is based on the 5 fb^{-1} dataset from 2011 collected in pp collisions at a center of mass energy of 7 TeV. Events were selected using the criterion of at least one high-transverse-momentum p_T lepton. The trigger thresholds were raised with the increasing luminosity of the LHC and the highest reached values were $p_T > 80$ for electrons and $p_T > 40$ for muons.

ATLAS analyzed data from 2011 (9) were taken in the 7 TeV (center of mass) pp collisions with a total integrated luminosity of 1.04 fb^{-1}. To select events the cuts on electron transverse energy $E_T > 25$ GeV and on muon transverse momentum $p_T > 25$ GeV were imposed.

In the figure 8.11 we show the limits on the m_{KK} from $W' \to l^{\pm}\nu_l$ for the two possible geometries of the orbifold. We sum over the two possible final states $e\nu_e$ and $\mu\nu_\mu$ and approximate the resonant mass to be $m_{W^2} \approx 2m_{KK}$. The total effective cross section is plotted in black.

The experimental limits are extracted from (59) for CMS (yellow) and (9) for ATLAS (green). We can see that the for the symmetric scenario we don't have any limit on the mass m_{KK}. The asymmetric case gives a bound $m_{KK} \gtrapprox 380$ GeV.

1. Thanks to L. Panizzi for the script and to G.Cacciapaglia for doing the overall scans!!

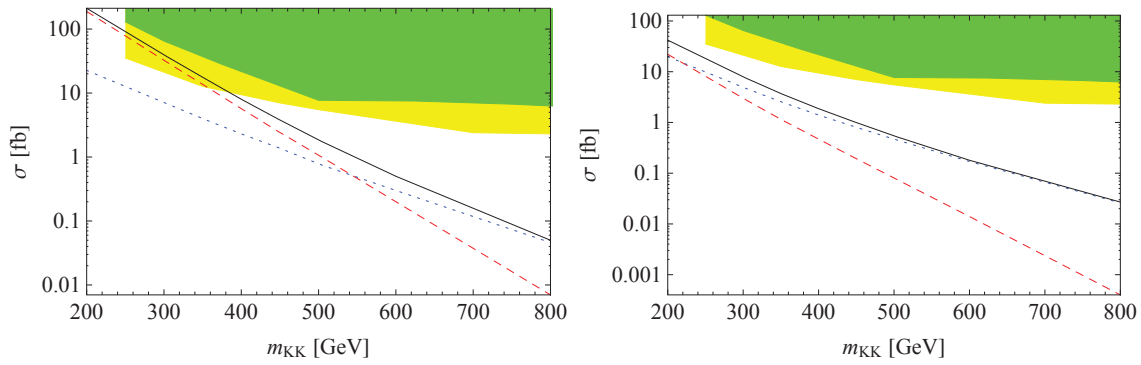

Figure 8.11: Bounds from the study of $W \to l\nu$. Total effective cross section (black), cross section from pair production (blue), cross section from single production (red). Experimental bounds are indicated in yellow (CMS) (59) in green (ATLAS) (9). **On the left**: non degenerate geometry is assumed $R_4 \gg R_5$ and **On the right:** degenerate radii $R_4 = R_5$. Thanks to G. Cacciapaglia.

8.3.2 $W' \to WZ$ searches

Here the searches look for resonances of heavy states decaying into WZ gauge bosons. The two main strategies consist on looking for fully leptonic decays of both Z and W final states as $Z \to ll$ and $W \to l\nu$ with $l = e, \mu$ or for a leptonic decay of Z and hadronic decay of W.

Experimental bounds we use are taken from the CMS last data (58). The CMS search is performed in pp collisions at $\sqrt{s} = 7$ TeV for exotic particles decaying via WZ to final states with electrons and muons. The integrated luminosity if the considered dataset is approximately 5 fb^{-1}. To identify the considered decay mode a double-electron or double-muon signal was required and a p_T thresholds of 17 GeV and 8 GeV were imposed for the highest-p_T and second-highest-p_T leptons respectively.

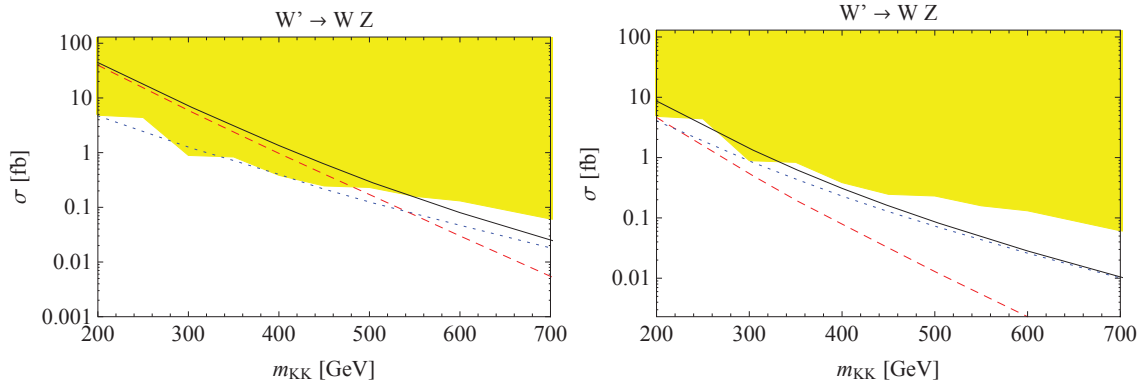

Figure 8.12: Bounds from study of $W' \to WZ$ resonances. Total effective cross section (black), cross section from pair production (blue), cross section from single production (red). CMS bounds (58) are indicated in yellow. **On the left**: non degenerate geometry is assumed $R_4 \gg R_5$ and **On the right:** degenerate radii $R_4 \gg R_5$. Thanks to G. Cacciapaglia.

The results are shown in the figure 8.12. The bounds we obtain here are quite stringent and numerically we estimate $m_{KK} \gtrapprox 560$ GeV for the non symmetric scenario $R_4 \gg R_5$ and $m_{KK} \gtrapprox 340$ GeV for $R_4 = R_5$ case.

8.3.3 $Z' \to l^+l^-$ searches

In this searches the experiments look for a pair of charged leptons with high transverse momentum p_T. We use ATLAS experimental bounds (6) with the dataset taken at 7 TeV pp collisions with total integrated luminosity of 4.9 fb^{-1}. In the di-electron channel the two electron candidates are required to have minimal transverse energy of $E_T > 25$ GeV. In the di-muon channel, two muon candidates must satisfy the condition $p_T > 25$ GeV.

In our model the di-lepton events can arise from the $A^{(2)}$ and $Z^{(2)}$ decays. Note these two particles are quite narrow and their masses can differ of about 30 (60) GeV at $m_{KK} = 600$ GeV for non-degenerate (degenerate) radii respectively. Thus whether the two states would be seen as different or not depends on the experimental sensitivity. In the bounds we give here we have summed for simplicity the contributions coming from the two resonances. We have checked that the main contributions will come from $A^{(2)}$ decays. We can thus safely use the approximation $m_{Z'} \approx 2m_{KK}$ but a more detailed study should be done.

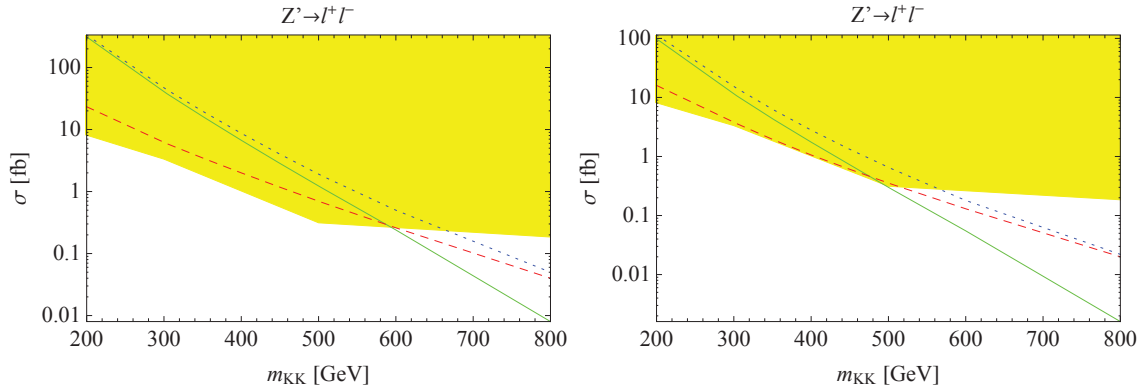

Figure 8.13: Bounds from the study of $Z' \to l^+l^-$. Total effective cross section (black), cross section from pair production (blue), cross section from single production (red). ATLAS bounds (6) are indicated in yellow. **On the left**: non degenerate geometry is assumed $R_4 \gg R_5$ and **On the right:** degenerate radii $R_4 \gg R_5$. Thanks to G. Cacciapaglia.

From the di-lepton decays we have the strongest bounds on the Z' mass. For the a-symmetric scenario $R_4 \gg R_5$ we obtain a lower bound $m_{KK} \gtrapprox 680$ GeV and $m_{KK} \gtrapprox 580$ GeV for the symmetric orbifold $R_4 = R_5$.

8.3.4 Di-jet resonances

At hadron colliders, the search for new phenomena in fully hadronic final states without missing transverse energy or leptons is experimentally challenging because of the large multi-jet background. In our model the multi-jet signal can come from every heavy gauge boson decays $A^{(2)}$, $Z^{(2)}$,$W^{(2)}$ and $G^{(2)}$. Notice that the masses of those KK excitations are very different 6.3 from $A^{(2)}$ with mass of 1200.1 GeV up to $G^{(2)}$ with mass 1318.3 GeV at $m_{KK} = 600$ GeV in the asymmetric case. In our analysis we assume that the experimental uncertainties in the jet reconstruction is such that the four resonances (in fact three as the electroweak gauge bosons $Z^{(2)}$ and $W^{(2)}$ have almost the same masses and will always be seen as one heavy state) cannot be disentangled and we sum the contributions coming from them. As the invariant mass of the heavy states we assume with a good approximation $2m_{KK}$. We have checked that the main contribution to the expected signal comes from the $A^{(2)}A^{(2)}$ desintegrations thus our approximation in the invariant mass can be in fact considered as good.

To have some estimate on the m_{KK} scale we compare our results with the CMS dataset of 2.2 fb^{-1} from pp collisions collected at $\sqrt{s} = 7$ TeV (7). The signal selection is based on a requirement of pairs of dijets with equal mas. To suppress QCD multi-jet backgrounds the requirement that events have at least four jets with a minimum transverse momentum of 150 GeV. is imposed. The efficiency of the detector varies from 3% up to 13% for resonant masses of 300 GeV up to 1000 GeV respectively.

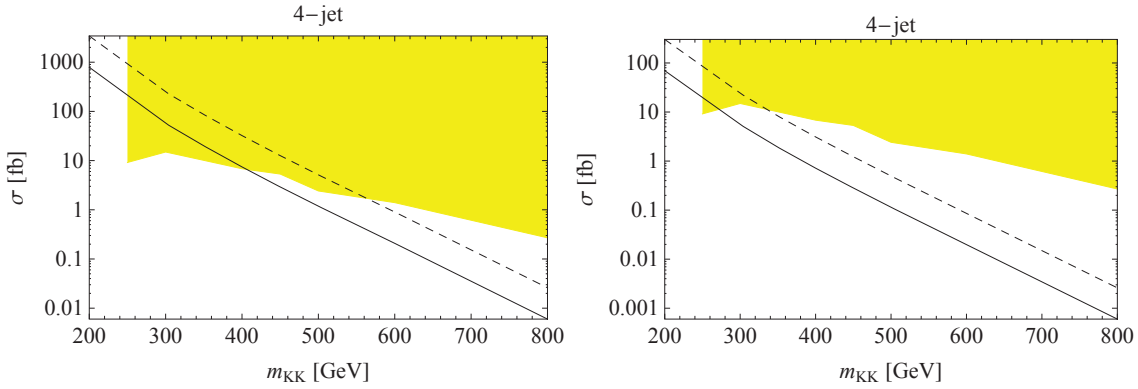

Figure 8.14: Bounds from study of di-jet resonances. We plot the total effective cross section of 4-jet events assuming the efficiency of 3% efficiency (black) and 13% (black dashed). CMS bounds (7) are indicated in yellow. **On the left**: non degenerate geometry is assumed $R_4 \gg R_5$ and **On the right:** degenerate radii $R_4 \gg R_5$. Thanks to G. Cacciapaglia.

From this study we can see that the bounds are $m_{KK} \gtrapprox 410(590)$ GeV assuming the efficiency of 3(13)% in the asymmetric case $R_4 \gg R_5$. In the symmetric case we obtain $m_{KK} \gtrapprox 300(340)$ GeV lower bounds. Other signals, listed in 8.2 don't give any bound on the KK mass m_{KK}.

As conclusion we can say that our model have a clear signatures that can be easily observed at the LHC and put the bounds on the compactification scale R. We summarize the collider bounds in the table 8.10. Limits we obtain from the LHC searches are not incompatible with the relic abundance bounds 7.8 and 7.9. Direct searches of dark matter candidate put also the strongest bounds in the same region as the LHC signals at about $m_{KK} \gtrapprox 600$ GeV 7.12. The bounds we give here are extracted for two simple scenarios of our model: in the decoupling limit $R_4 \gg R_5$ where one of the tiers at each level is completely decoupled or the symmetric scenario $R_4 = R_5$ where at each level we have two states degenerate in mass. We have seen that the limits on the compactification scale are different on both cases but both predict a dark matter candidate at about 1 TeV. As the LHC will collect more data the bounds will become stronger and potentially will exclude the $m_{KK} < 1$ TeV which corresponds to the limiting case of the WMAP privileged region in the non degenerate scenario.

8.4 Summary of all the bounds on the m_{KK}

In the two previous chapters we have studied the experimental bounds on the compactification scale R or equivalently on the characteristic mass scale $m_{KK} \sim R^{-1}$. We have included all the (1,0) and (2,0) KK states together with radiative correction to their masses in order to study in details the phenomenology of the model at one loop order. The mass degeneracy within each KK tier, perfect at tree level while neglecting SM masses, was therefore removed by the loop corrections but a characteristic very small mass splittings remains providing a specific signatures

signal	$R_4 \gg R_5$ m_{KK} [GeV]	$R_4 = R_5$ m_{KK} [GeV]
$W' \to l\nu$	380	none
$W' \to WZ$	560	340
$Z' \to l^+l^-$	680	580
di-jet	410	300

Table 8.10: LHC bounds on the mass scale m_{KK}.

of the model. Here we summarize the bounds on the m_{KK} mass that we have found from the relic abundance calculation, direct detection searches and LHC signatures. We give the results for a natural set of parameters of our model: $\Lambda R = 10$ and $m_{loc} = 0$. The SM higgs mass was always kept at 125 GeV in accordance with the latest discoveries at the LHC. The two simplest geometries of the orbifold were considered: the decoupling limit $R_4 \gg R_5$ and symmetric limit $R_4 = R_5$. We summarize our results in the table 8.11.

For the privileged bound of m_{KK} from the relic abundance calculation we assume that the most complete scenario should be taken into account - that is the L2 model where we allow

Experimental bounds	m_{KK} [GeV] $R_4 \gg R_5$	m_{KK} [GeV] $R_4 = R_5$
Ωh^2 L1CL	440 - 620	< 310
Ωh^2 L2CL	700 - 990	350 - 505
Direct Detection lower bounds		
Zepelin	415	415
Edelweiss + CDMS	465	465
Xenon 2011	520	520
Xenon 2012	630	630
Xenon 2017 (previsional)	1315	1315
LHC lower bounds		
$W' \to l\nu$	380	none
$W' \to WZ$	560	340
$Z' \to l^+l^-$	680	580
di-jet	410	300

Table 8.11: Summary of all the experimental bounds on the Kaluza-Klein mass scale m_{KK} for the asymmetric geometry $R4 \gg R_5$ in the middle column and for the symmetric orbifold $R_4 = R_5$ in the right column.

for the (2,0) KK states to appear as the final states of the dark matter candidate annihilation processes. The bounds are then in higher region of m_{KK} and for the asymmetric scenario we get the maximal allowed value of $m_{KK} = 990$ GeV which is quite high in comparison with other models where the dark matter candidates are typically at 500 GeV scale or lower. The model $R4 \gg R_5$ is not yet excluded as the direct detection and LHC bounds exclude masses up to 630 and 670 GeV respectively which leaves us with a possible window $680 < m_{KK} < 990$ GeV that will be examined while more data will be accessible from the collider searches and with growing sensibility of direct detection devices. As we can see , the previsional bounds for Xenon 2017 would exclude our dark matter candidate with masses lower than 1315 GeV which would be completely incompatible with relic abundance bounds.

The relic abundance bounds for the symmetric scenario are very low, $350 < m_{KK} < 505$ GeV and the experimental bounds from both direct detection and LHC signal set the bounds in a much higher regime.

Changing values of parameters in the model, such as ΛR or m_{loc} would change slightly the allowed bounds on the m_{KK}. But, on one hand we have a strong electroweak constraints on the values of m_{loc} and the final effect of changing its value in the allowed regime will not impact at all the WMAP bounds in the m_{KK}. On the other hand, the cosmologically privileged window is slowly going toward smaller m_{KK} masses with decreasing cut-off ΛR (from $700 - 990$ GeV at $\Lambda R = 10$ down to $500 - 740$ GeV at $\Lambda R = 2$ in the L2 scenario) which can only worse the situation as the direct detection bounds are stronger with decreasing ΛR ($m_{KK} < 630$ (900) GeV for $\Lambda R = 10$ (3) from the strongest bounds set by Xenon 2012).

Conclusion & perspectives

We have extensively studied the structure and phenomenology of an extension of Standard Model with two extra dimensions compactified on a real projective plane.

This scenario can be classified within a group of models called Universal Extra Dimensions where all the Standard Model fields are free to propagate in the extra space. The choice of geometry is crucial. The number of extra dimensions, the symmetry group used to define compactification and the metric influence significantly the particle spectrum of the model, the nature of dark matter candidate (its mass and spin) and therefore have a huge impact on the resulting phenomenology.

Real projective plane is a unique two dimensional orbifold without fixed points where chiral fermions can be defined. The importance of chiral fermions is obvious as the objective is to reconstruct the Standard Model content at the fundamental level of Kaluza-Klein expansion.

The absence of fixed points is required as they can lead to the breaking of the KK symmetry, a remnant of Lorentz invariance extended to extra dimensions, exact when the extra space is infinite and then partially broken by the compactification. Broken KK symmetry means that the operators localized on the fixed points can introduce interactions that do not respect the KK number in vertices and thus there are no stable particle in the Kaluza-Klein expansion.

We have therefore defined the Standard Model on the real projective plane and the first excitation mode of the SM photon is naturally stable and, being a weakly interacting neutral particle, can be considered as a perfect candidate for dark matter.

The first point of this thesis was to calculate one loop spectrum of the (2,0) KK level. Particles in this tier are very important as their masses, at tree level proportional to $2R^{-1}$, are twice the (1,0) level particle masses $\sim R^{-1}$. Therefore the resonant effects of (2,0) modes can be expected to influence the collider and dark matter phenomenology processes.

In order to have an idea of the influence of the geometry of the orbifold on the spectrum we have considered two possible geometries of the orbifold. The first one where the two radii of compactified dimensions are equal $R_4 = R_5$ another one where one of the radii is much larger $R_4 \gg R_5$ resulting in the decoupling of one of the tiers. We have shown that in the non-symmetric case $R_4 \gg R_5$ there is only one dark matter particle, and there are no possible mixings between two tiers $(n, 0)$ and $(0, n)$ with n even. In the symmetric scenario, mixings of the even levels $(n, 0)$ and $(0, n)$ are possible. These mixings will generate additional divergent contributions to the mass corrections. The (2,0) particles in this scenario will be then typically heavier than in the non-symmetric case. General and important feature of the spectrum are very small mass splittings within a given tier which is important in the dark matter studies and provides interesting LHC signatures.

The second step was to investigate the influence of the (2,0) level modes to the phenomeno-

logical observables. First bounds on the Kaluza-Klein mass scale m_{KK} were derived from relic abundance calculation. As the mass splittings in our model are very small the co-annihilation effects become important. In the analytical calculation we have shown the importance of the co-annihilations including KK leptons. We have demonstrated also that the loop corrections to the KK masses as well as the SM masses should not be neglected as they can shift the relic abundance result of about 15%. In order to have an exact bound on the compactification scale we have implemented the model in MicrOMEGAs and numerically derived the bounds in both geometries including co-annihilations with all the (1,0) particles. Using this program we have examined several factors that can change the relic abundance predictions: the inclusion of (2,0) modes, the cut off scale and the localized mass parameter. We have seen that we can obtain a range of masses as high as 1 TeV for the dark matter candidate suggesting that direct searches of other heavy particles at LHC and direct dark matter detection experiments can allow in near future to strongly bound the model or find evidence for it.

Finally, we have studied in details the LHC phenomenology in our model. Typically the heavy KK states produced in the proton-proton collisions will chain decay down the the stable (1,0) photon. But, including loop induced couplings, the (2,0) modes can couple directly to two SM states and thus enhance the resonant cross section. We have chosen clear signals that are studied in the LHC, into di-leptons and into jets and performed a detailed calculation of the expected signal. The 7 TeV data from LHC already put limits on the model and some region of m_{KK} masses privileged by WMAP bounds is ruled out.

This work provides a step to understand extra-dimensional models. The influence of higher Kaluza-Klein modes on the low energy phenomenology was shown to be important. We have shown also that the geometry of the underlying orbifold is crucial to find out the particle spectrum. Within this particular model the explicit dependence of the spectrum and thus of the low-energy signatures on the ratio of the two radii R_4/R_5 should be examined more in details in order to put some bounds on the ratio and to understand how the behavior of the model changes in this case. Another possible modification would be to change the metric introducing a warp factor. All these geometrical modifications should enlighten a lot the general features of extra-dimensional models. One however should not stop here. We have shown that it is possible to find orbifolds without fixed points and define on them an extension of the Standard Model. This effective theory is an insight in the beyond Standard Model physics that is calculable in a finite interval of time [2]. However existence of more extra dimensions is not excluded, higher dimensional orbifolds without fixed points should exist and if LHC data exclude the already defined models we should think to go further. We have choice between mathematical complexity or maybe a redefinition of some concepts that we have introduced with the extra-dimensional theories.

2. The mathematical complexity when one introduces more extra dimensions grows in "exponentially". It can be seen already when one want to classify possible orbifolds: only 2 possibilities in 1D, 17 possible orbifolds in 2D and 230 in 3D!!! What about loop calculation...

Appendix A

Notations

In this text adopt the following notations:
- $\mathcal{M}^4$ - 4-dimensional Minkowski space with the metric noted $\eta^{\mu\nu} = diag(1, -1, -1, -1)$

- RPP or RP^2 - space group defining the real projective plane orbifold with flat metric $diag(-1, -1)$
- $\mathcal{M}^4 \times RP^2$ - the six-dimensional space with flat metric $g^{MN} = diag(1, -1, -1, -1, -1, -1)$
- The letters the middle of the Greek alphabet label the x^μ coordinates of four-dimensional space $\mathcal{M}^4$ and take values $\mu, \nu, \cdots \in \{0, 1, 2, 3\}$.
- The letters from the beginning of the Greek alphabet label y^α - coordinates on the $d-4$-dimensional orbifold with $\alpha, \beta \cdots \in \{4, 5, \ldots d\}$. We adopt also a vector notation $\vec{y} = (y_4, y_5, \ldots, y_d)$ when needed.
- The major letters of the Latin alphabet run over all the coordinates of the six-dimensional space $\mathcal{M}^4 \times RP^2$ with $M, N, \cdots \in \{0, 1, 2, 3, 4, 5\}$.
- Lower case letters form the beginning of the Latin alphabet $a, b, \ldots$ label the gauge fields and gauge group generators of a corresponding group

Appendix B

Annihilation Cross Sections

We give expressions for the co-annihilations of (1,0) level particles assuming degenerate m_{KK} noted as m and neglecting the SM masses $m_{SM} = 0$ in terms of coefficients defined in B.1.

$$\beta = \sqrt{1 - \frac{4m^2}{s}} \tag{B.1}$$

$$L = \ln\left(\frac{1-\beta}{1+\beta}\right) = -2\tanh^{-1}\beta \tag{B.2}$$

B.1 Co-annihilations $A^{(1)}$ with leptons $l^{(1)}_{S/D}$ and $\nu^{(1)}$

The topology of co-annihilations $A^{(1)}$ with leptons $l^{(1)}_{S/D}$ into neutral gauge bosons is shown in the figure B.1.

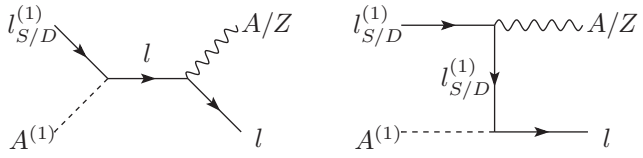

Figure B.1: Co-annihilations $A^{(1)}l^{(1)}_{S/D}$ into neutral gauge bosons. Same topology for the $\nu^{(1)}_l$ co-annihilating with $A^{(1)}$ into Z holds.

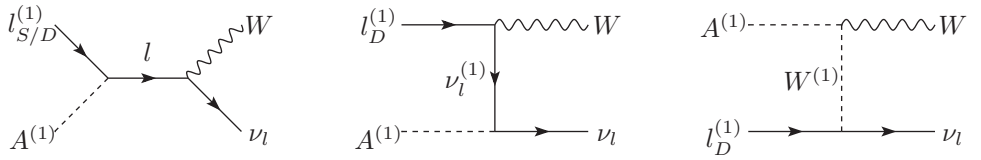

Figure B.2: Co-annihilations $A^{(1)}l^{(1)}_{S/D}$ into W gauge bosons. Same topology for the $\nu^{(1)}_l$ co-annihilating with $A^{(1)}$ holds.

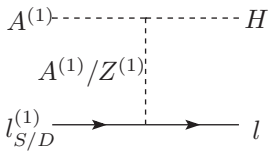

Figure B.3: Co-annihilations $A^{(1)}l^{(1)}_{S/D}$ into Higgs boson H gauge bosons. Same topology for the $\nu^{(1)}_l$ co-annihilating with $A^{(1)}$ holds.

$$\sigma(A^{(1)}l^{(1)}_S \to Al) = \frac{g_2^4 s_w^4 c_{w1}^2}{c_w^2}\ \frac{-3\beta+4L}{32\pi s\beta^2} \tag{B.3}$$

$$\sigma(A^{(1)}l^{(1)}_D \to Al) = \frac{g_2^4 c_w^2 (c_w s_{w1}+c_{w1}s_w)^2}{4c_w^2}\ \frac{-3\beta+4L}{32\pi s\beta^2} \tag{B.4}$$

$$\sigma(A^{(1)}l^{(1)}_S \to Zl) = \frac{g_2^4 s_w^6 c_{w1}^2}{c_w^4}\frac{-3\beta+4L}{32\pi s\beta^2} \tag{B.5}$$

$$\sigma(A^{(1)}l^{(1)}_D \to Zl) = \frac{g_2^4 (c_w s_{w1}+c_{w1}s_w)^2}{4c_w^2}\frac{s_w^2(2-3s_w^2)s\beta+(1-2s_w^2)(4m^2+(1-2s_w^2)s)L}{32\pi s^2\beta^2} \tag{B.6}$$

$$\sigma(A^{(1)}\nu^{(1)} \to Z\nu) = \frac{g_2^4 (c_w s_{w1}-c_{w1}s_w)^2}{4c_w^2}\frac{(2m^2+s)L}{32\pi s^2\beta^2} \tag{B.7}$$

$$\sigma(A^{(1)}l^{(1)}_S \to Wl) = \frac{g_2^4 s_w^2}{2}\frac{1}{32\pi s\beta} \tag{B.8}$$

$$\sigma(A^{(1)}l^{(1)}_D \to Wl) = \frac{g_2^4 (c_w s_{w1}+c_{w1}s_w)^2}{8c_w^2}\frac{1}{32\pi s\beta} \tag{B.9}$$

$$\sigma(A^{(1)}\nu^{(1)} \to W\nu) = \frac{g_2^4 (c_w s_{w1}-c_{w1}s_w)^2}{8c_w^2}\frac{1}{32\pi s\beta} \tag{B.10}$$

$$\sigma(A^{(1)}l^{(1)}_D \to W\nu) = \sigma(A^{(1)}\nu^{(1)} \to Wl) = \frac{As\beta+(Bm^2+Cs)L}{16\pi s^2\beta^2} \tag{B.11}$$

(B.12)

The last cross section must be multiplied for $l^{(1)}_D$ incoming

$$\begin{aligned} A &= \frac{g_w^4 s_{w1}\left(\left(4+\sqrt{2}\right)c_w s_{w1}-\sqrt{2}c_{w1}s_w\right)}{8c_w} \\ B &= -\frac{1}{4}g_w^4\left(\frac{3(c_{w1}s_w-c_w s_{w1})^2}{c_w^2}+8s_{w1}^2\right) \\ C &= -\frac{g_w^4(c_{w1}s_w-c_w s_{w1})^2}{8c_w^2} \end{aligned}$$

and for $\nu^{(1)}$ incoming by

$$\begin{aligned} A &= \frac{g_w^4 s_{w1}\left(\left(4-\sqrt{2}\right)c_w s_{w1}-\sqrt{2}c_{w1}s_w\right)}{8c_w} \\ B &= -\frac{1}{4}g_w^4\left(\frac{3(c_{w1}s_w+c_w s_{w1})^2}{c_w^2}+8s_{w1}^2\right) \\ C &= -\frac{g_w^4(c_{w1}s_w+c_w s_{w1})^2}{8c_w^2} \end{aligned}$$

(B.13)

$$\sigma(A^{(1)}l^{(1)_S}\to Hl) = \frac{g_w^6 s_w^2 s_{w1}^2 v^2 (c_{w1}s_w-c_w s_{w1})^2 (c_w(c_{w1}+s_{w1})+s_w(s_{w1}-c_{w1}))^2}{4c_w^6}\frac{L}{16\pi s^2\beta^2}$$

$$\sigma(A^{(1)}l^{(1)_D}\to Hl) = \frac{g_w^6 v^2\left(c_{w1}^2-s_{w1}^2\right)^2(c_{w1}s_w-c_w s_{w1})^2}{16c_w^6}\frac{L}{16\pi s^2\beta^2} \quad \text{(B.14)}$$

$$\sigma(A^{(1)}\nu^{(1)}\to H\nu) = \frac{g_w^6 v^2(c_{w1}s_w-c_w s_{w1})^2}{16c_w^6}\frac{L}{16\pi s^2\beta^2} \quad \text{(B.15)}$$

(B.16)

B.2 Co-annihilations of leptons $l^{(1)}_{S/D}$

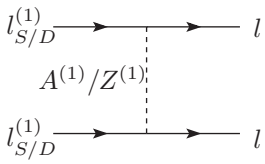

Figure B.4: Co-annihilations $l^{(1)}_{S/D}l^{(1)}_{S/D}$ into ll]. To simplify we show only the t-channel. If the particles are of the same flavor then, also u-channel diagrams contribute. Same topology for the $\nu^{(1)}$ holds.

$$\sigma(l^{(1)}_{Sa}l^{(1)}_{Sa}\to ll) = \sigma(l^{(1)}_{Da}l^{(1)}_{Da}\to ll) = \sigma(l^{(1)}_{Da}l^{(1)}_{Sa}\to ll) = \quad \text{(B.17)}$$

$$\sigma(\nu^{(1)}_a\nu^{(1)}_a\to ll) = \frac{2m^2-s+4m^2\beta L}{128\pi m^2 s\beta}$$

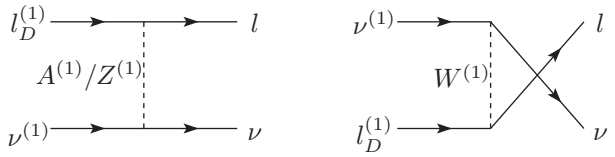

Figure B.5: Co-annihilations $l_D^{(1)}\nu^{(1)}$ into $l\nu$. If different flavor, then only t-channel diagrams contribute.

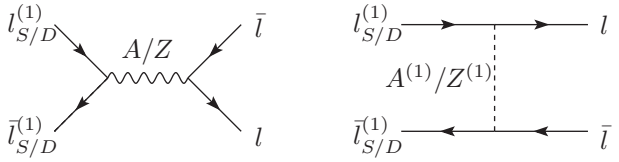

Figure B.6: Co-annihilations $l_{S/D}^{(1)}\bar{l}_{S/D}^{(1)}$ into $l\bar{l}$]. Same topology for the $\nu^{(1)}$ holds. To simplify we show only the t-channel.

The cross sections B.17, respectively to incoming particles must be multiplied by the coefficients :

$$\begin{aligned} A_{l_S l_S} &= \frac{g_2^4 s_w^4}{c_w^4} \\ A_{l_D l_D} &= A_{\nu\nu} = \frac{g_2^4}{16 c_w^4} \\ A_{l_S l_D} &= \frac{g_w^4 s_w^2 \left(2 c_w c_{w1} s_{w1} + s_w (c_{w1}^2 s_{w1}^2)\right)^2}{4 c_w^4} \end{aligned}$$

$$\begin{aligned} \sigma(l_{Sa}^{(1)} l_{Sb}^{(1)} \to l_a l_b) &= \sigma(l_{Da}^{(1)} l_{Db}^{(1)} \to l_a l_b) = \sigma(l_{Sa}^{(1)} l_{Db}^{(1)} \to l_a l_b) = \\ \sigma(l_S^{(1)} \nu^{(1)} \to l\nu) &= \sigma(l_{Da}^{(1)} \nu_b^{(1)} \to l_a \nu_b) = \sigma(\nu_a^{(1)} \nu_b^{(1)} \to \nu_a \nu_b) = \frac{1}{64\pi s\beta} \end{aligned} \tag{B.18}$$

The cross sections B.18, respectively to incoming particles must be multiplied by the coefficients :

$$A_{l_S l_S} = \frac{g_2^2 s_w^2}{c_w^2} \tag{B.19}$$

$$A_{l_D l_D} = A_{\nu\nu} = \frac{g_2^2}{4c_w^2} \tag{B.20}$$

$$A_{l_S l_D} = \frac{g_2^2 s_w (sw(c_{w1}^2 - s_{w1}^2) + 2c_w c_{w1} s_{w1})}{c_w^2} \tag{B.21}$$

$$A_{l_S \nu} = \frac{g_2^2 s_w^2}{2c_w^2} \tag{B.22}$$

$$A_{l_D \nu} = \frac{g_2^2 (c_{w1}^2 - s_{w1}^2)}{4c_w^2} \tag{B.23}$$

B.3 Co-annihilations of lepton - antilepton $l^{(1)}_{S/D}\bar{l}^{(1)}_{S/D}$

(check)

$$\sigma(l_S^{(1)}\bar{l}_S^{(1)} \to l\bar{l}) = \frac{5g_2^4 s_w^4}{96c_w^4}\frac{2m^2+s}{\pi s^2\beta} \tag{B.24}$$

$$\sigma(l_D^{(1)}\bar{l}_D^{(1)} \to l\bar{l}) = \frac{g_2^4}{192\pi s^2\beta}\left(16m^2+11s\right) \tag{B.25}$$

$$\sigma(l_D^{(1)}\bar{l'}_D^{(1)} \to l\bar{l'}) = \frac{g_2^4}{24\pi s^2\beta}\left(16m^2+2s\right) \tag{B.26}$$

$$\sigma(\nu^{(1)}\bar{\nu}^{(1)} \to \nu\bar{\nu}) = \frac{g_2^4}{24\pi s^2\beta}\left(16m^2+2s\right) \tag{B.27}$$

$$\sigma(\nu^{(1)}\bar{\nu'}^{(1)} \to \nu\bar{\nu'}) = \frac{g_2^4}{24\pi s^2\beta}\left(16m^2+2s\right) \tag{B.28}$$

$$\sigma(l_S^{(1)}\bar{l}_S^{(1)} \to AA) = g_w^4 s_w^4 \frac{\beta}{4\pi s} \tag{B.29}$$

$$\sigma(l_S^{(1)}\bar{l}_S^{(1)} \to ZZ) = \frac{g_w^4 s_w^8}{cw^4}\frac{\beta}{4\pi s} \tag{B.30}$$

$$\sigma(l_S^{(1)}\bar{l}_S^{(1)} \to ZZ) = \frac{g_w^4 s_w^6}{cw^2}\frac{\beta}{4\pi s} \tag{B.31}$$

$$\sigma(l_S^{(1)}\bar{l}_S^{(1)} \to WW) = g_w^4 s_w^4 \frac{19(s+2m^2)}{96\pi s^2\beta} \tag{B.32}$$

(B.33)

References

[1] *Proceedings of the National Academy of Sciences*, volume 42, 1956. 49

[2] Combined standard model higgs boson searches with up to 2.3 fb-1 of pp collisions at sqrts=7 tev at the lhc. Technical Report ATLAS-CONF-2011-157, CERN, Geneva, Nov 2011. 64, 65

[3] Search for add extra-dimensions in monophotons. 2011. 64

[4] Update of the combination of higgs boson searches in pp collisions at sqrt(s) = 7 tev with the atlas experiment at the lhc. Technical Report ATLAS-CONF-2011-135, CERN, Geneva, Sep 2011. 20

[5] Observation of an excess of events in the search for the standard model higgs boson with the atlas detector at the lhc. Technical Report ATLAS-CONF-2012-093, CERN, Geneva, Jul 2012. 18

[6] Search for high-mass dilepton resonances with 5 fb-1 pf pp collisions at sqrt(s) = 7 tev with the atlas experiment. Technical Report ATLAS-CONF-2012-007, CERN, Geneva, Mar 2012. 163

[7] Search for new physics in the paired dijet mass spectrum. 2012. 164

[8] Precision electroweak measurements on the Z resonance. *Phys.Rept.*, 427:257–454, 2006. 17

[9] Georges Aad et al. Search for a heavy gauge boson decaying to a charged lepton and a neutrino in 1 fb-1 of pp collisions at sqrt(s) = 7 TeV using the ATLAS detector. *Phys.Lett.*, B705:28–46, 2011. 161, 162

[10] Kevork Abazajian, George M. Fuller, and Mitesh Patel. Sterile neutrino hot, warm, and cold dark matter. *Phys.Rev.*, D64:023501, 2001. 35

[11] Kevork N. Abazajian et al. The Seventh Data Release of the Sloan Digital Sky Survey. *Astrophys.J.Suppl.*, 182:543–558, 2009. 32

[12] Victor Mukhamedovich Abazov et al. Search for diphoton events with large missing transverse energy in 6.3 fb^{-1} of $\mathbf{p\bar{p}}$ collisions at $\sqrt{s} = \mathbf{1.96}$ TeV. *Phys.Rev.Lett.*, 105:221802, 2010.

[13] J. Abdallah et al. Search for one large extra dimension with the DELPHI detector at LEP. *Eur.Phys.J.*, C60:17–23, 2009. 64

[14] M. Ackermann et al. Limits to the muon flux from neutralino annihilations in the sun with the amanda detector. *Astropart.Phys.*, 24:459–466, 2006. 40

[15] E.G. Adelberger, Blayne R. Heckel, and A.E. Nelson. Tests of the gravitational inverse square law. *Ann.Rev.Nucl.Part.Sci.*, 53:77–121, 2003. 47

[16] Oscar Adriani et al. An anomalous positron abundance in cosmic rays with energies 1.5-100 GeV. *Nature*, 458:607–609, 2009. 40

[17] Kaustubh Agashe. Extra dimensions. pages 1–48, 2006. 57, 58

[18] Kaustubh Agashe, Antonio Delgado, Michael J. May, and Raman Sundrum. RS1, custodial isospin and precision tests. *JHEP*, 0308:050, 2003. 65

[19] Kaustubh Agashe and Geraldine Servant. Warped unification, proton stability and dark matter. *Phys.Rev.Lett.*, 93:231805, 2004. 34

[20] Z. Ahmed et al. Dark Matter Search Results from the CDMS II Experiment. *Science*, 327:1619–1621, 2010. 37, 38

[21] Z. Ahmed et al. Combined Limits on WIMPs from the CDMS and EDELWEISS Experiments. *Phys.Rev.*, D84:011102, 2011. 38

[22] D.S. Akerib et al. New results from the cryogenic dark matter search experiment. *Phys.Rev.*, D68:082002, 2003. 39

[23] D. Yu. Akimov, H.M. Araujo, E.J. Barnes, V.A. Belov, A. Bewick, et al. WIMP-nucleon cross-section results from the second science run of ZEPLIN-III. *Phys.Lett.*, B709:14–20, 2012. 38

[24] Natxo Alonso Alberca, Eric Bergshoeff, Ulf Gran, Roman Linares, Tomas Ortin, et al. Domain walls of D = 8 gauged supergravities and their D = 11 origin. *JHEP*, 0306:038, 2003. 47

[25] J. Angle et al. First Results from the XENON10 Dark Matter Experiment at the Gran Sasso National Laboratory. *Phys.Rev.Lett.*, 100:021303, 2008. 37, 38

[26] I. Antoniadis. A possible new dimension at a few TeV. *Phys. Lett. B*, 246:377, 1990. 48

[27] Ignatios Antoniadis, Nima Arkani-Hamed, Savas Dimopoulos, and G.R. Dvali. New dimensions at a millimeter to a Fermi and superstrings at a TeV. *Phys.Lett.*, B436:257–263, 1998. 63

[28] Ignatios Antoniadis and M. Quiros. Large radii and string unification. *Phys.Lett.*, B392:61–66, 1997. 48

[29] Thomas Appelquist, Hsin-Chia Cheng, and Bogdan A. Dobrescu. Bounds on universal extra dimensions. *Phys.Rev.*, D64:035002, 2001. 134

[30] E. Aprile et al. First Dark Matter Results from the XENON100 Experiment. *Phys.Rev.Lett.*, 105:131302, 2010. 38

[31] Nima Arkani-Hamed, Andrew G. Cohen, and Howard Georgi. Electroweak symmetry breaking from dimensional deconstruction. *Phys.Lett.*, B513:232–240, 2001. 23

[32] E. Armengaud et al. Final results of the EDELWEISS-II WIMP search using a 4-kg array of cryogenic germanium detectors with interleaved electrodes. *Phys.Lett.*, B702:329–335, 2011. 37, 38

[33] Howard Baer and Csaba Balazs. Chi**2 analysis of the minimal supergravity model including WMAP, g(mu)-2 and b —gt; s gamma constraints. *JCAP*, 0305:006, 2003. 29

[34] J.J. Beatty, A. Bhattacharyya, C. Bower, S. Coutu, M.A. DuVernois, et al. New measurement of the cosmic-ray positron fraction from 5 to 15-GeV. *Phys.Rev.Lett.*, 93:241102, 2004. 40

[35] K.G. Begeman, A.H. Broeils, and R.H. Sanders. Extended rotation curves of spiral galaxies: Dark haloes and modified dynamics. *Mon.Not.Roy.Astron.Soc.*, 249:523, 1991. 28

[36] G. Belanger, F. Boudjema, P. Brun, A. Pukhov, S. Rosier-Lees, et al. Indirect search for dark matter with micrOMEGAs2.4. *Comput.Phys.Commun.*, 182:842–856, 2011. 121, 126

[37] G. Belanger, F. Boudjema, A. Pukhov, and A. Semenov. MicrOMEGAs: A Program for calculating the relic density in the MSSM. *Comput.Phys.Commun.*, 149:103–120, 2002.

127

[38] G. Belanger, F. Boudjema, A. Pukhov, and A. Semenov. micrOMEGAs: Version 1.3. *Comput.Phys.Commun.*, 174:577–604, 2006. 127

[39] G. Belanger, M. Kakizaki, and A. Pukhov. Dark matter in UED: The Role of the second KK level. *JCAP*, 1102:009, 2011. 128

[40] G. Belanger, E. Nezri, and A. Pukhov. Discriminating dark matter candidates using direct detection. *Phys.Rev.*, D79:015008, 2009. 34

[41] Doug Benjamin. Combined CDF and D0 upper limits on $gg \to H \to W^+W^-$ and constraints on the Higgs boson mass in fourth-generation fermion models with up to 8.2 fb^{-1} of data. 2011. 20

[42] A. Benoit, L. Berge, A. Broniatowski, L. Chabert, B. Chambon, et al. Improved exclusion limits from the edelweiss wimp search. *Phys.Lett.*, B545:43–49, 2002. 39

[43] L. Bergstrom, J. Edsjo, Michael Gustafsson, and P. Salati. Is the dark matter interpretation of the egret gamma excess compatible with antiproton measurements? *JCAP*, 0605:006, 2006. 39

[44] R. Bernabei, P. Belli, R. Cerulli, F. Montecchia, M. Amato, G. Ignesti, A. Incicchitti, D. Prosperi, C.J. Dai, H.L. He, H.H. Kuang, and J.M. Ma. Search for wimp annual modulation signature: results from dama/nai-3 and dama/nai-4 and the global combined analysis. *Physics Letters B*, 480(1–2):23 – 31, 2000. 39

[45] J. R. Bond, G. Efstathiou, and J. Silk. Massive neutrinos and the large-scale structure of the universe. *Phys. Rev. Lett.*, 45:1980–1984, Dec 1980. 34

[46] Marusa Bradac, Steven W. Allen, Tommaso Treu, Harald Ebeling, Richard Massey, et al. Revealing the properties of dark matter in the merging cluster MACSJ0025.4-1222. 2008. 29

[47] Gustavo Burdman, Bogdan A. Dobrescu, and Eduardo Ponton. Six-dimensional gauge theory on the chiral square. *JHEP*, 0602:033, 2006. 72

[48] Fiona Burnell and Graham D. Kribs. The Abundance of Kaluza-Klein dark matter with coannihilation. *Phys.Rev.*, D73:015001, 2006. 125

[49] D. Burstein and V. C. Rubin. The distribution of mass in spiral galaxies. ApJ, 297:423–435, October 1985. 27

[50] Giacomo Cacciapaglia, Roberto Chierici, Aldo Deandrea, Luca Panizzi, Stephane Perries, et al. Four tops on the real projective plane at LHC. *JHEP*, 1110:042, 2011. 87, 147, 149

[51] Giacomo Cacciapaglia, Aldo Deandrea, and Jeremie Llodra-Perez. A Dark Matter candidate from Lorentz Invariance in 6D. *JHEP*, 1003:083, 2010. 69, 71, 73, 74, 76, 79, 81, 83, 85, 88, 147

[52] Giacomo Cacciapaglia, Aldo Deandrea, and Jeremie Llodra-Perez. The Universal Real Projective Plane: LHC phenomenology at one Loop. *JHEP*, 1110:146, 2011. * Temporary entry *. 75, 77, 88, 91, 128, 147, 154, 161

[53] P. Candelas, Gary T. Horowitz, Andrew Strominger, and Edward Witten. SUPERSTRING PHENOMENOLOGY. 1985. 48

[54] Marcela S. Carena, Timothy M.P. Tait, and C.E.M. Wagner. Branes and orbifolds are opaque. *Acta Phys.Polon.*, B33:2355, 2002. 65

[55] David G. Charlton. LEP, SLC and the standard model. *eConf*, C020805:TW05, 2002. 17

[56] Serguei Chatrchyan et al. Search for Large Extra Dimensions in the Diphoton Final State at the Large Hadron Collider. *JHEP*, 1105:085, 2011. 64

[57] Serguei Chatrchyan et al. Search for Resonances in the Dilepton Mass Distribution in pp Collisions at $\sqrt(s) = 7$ TeV. *JHEP*, 1105:093, 2011. 65

[58] Serguei Chatrchyan et al. Search for exotic particles decaying to WZ in pp collisions at sqrt(s)=7 TeV. 2012. 162

[59] Serguei Chatrchyan et al. Search for leptonic decays of W' bosons in pp collisions at sqrt(s)=7 TeV. 2012. 161, 162

[60] Hsin-Chia Cheng, Konstantin T. Matchev, and Martin Schmaltz. Radiative corrections to Kaluza-Klein masses. *Phys.Rev.*, D66:036005, 2002. 59

[61] R. Sekhar Chivukula, Duane A. Dicus, Hong-Jian He, and Satyanarayan Nandi. Unitarity of the higher dimensional standard model. *Phys.Lett.*, B562:109–117, 2003. 135

[62] Sidney Coleman and Jeffrey Mandula. All possible symmetries of the s matrix. *Phys. Rev.*, 159:1251–1256, Jul 1967. 22

[63] Craig J. Copi and Lawrence M. Krauss. Comparing WIMP interaction rate detectors with annual modulation detectors. *Phys.Rev.*, D67:103507, 2003.

[64] Richard H. Cyburt. Primordial nucleosynthesis for the new cosmology: Determining uncertainties and examining concordance. *Phys.Rev.*, D70:023505, 2004. 32

[65] Leandro Da Rold. Radiative corrections in 5-D and 6-D expanding in winding modes. *Phys.Rev.*, D69:105015, 2004. 59, 88, 91

[66] D.D. Dixon, D.H. Hartmann, E.D. Kolaczyk, J. Samimi, R. Diehl, et al. Evidence for a galactic gamma-ray halo. *New Astron.*, 3:539, 1998. 39

[67] Scott Dodelson and Lawrence M. Widrow. Sterile-neutrinos as dark matter. *Phys.Rev.Lett.*, 72:17–20, 1994. 35

[68] Hideto Dohi and Kin-ya Oda. Universal Extra Dimensions on Real Projective Plane. *Phys.Lett.*, B692:114–120, 2010. 69

[69] A.K. Drukier, Katherine Freese, and Joshua A. Frieman. BOLOMETRIC DETECTION OF COLD DARK MATTER CANDIDATES: SOME MATERIAL CONSIDERATIONS. *J. Appl. Phys.*, 1988. 39

[70] M.J. Duff. Kaluza-Klein theory in perspective. 1994. 47

[71] John R. Ellis, R.A. Flores, and J.D. Lewin. RATES FOR INELASTIC NUCLEAR EXCITATION BY DARK MATTER PARTICLES. *Phys.Lett.*, B212:375, 1988. 36

[72] Beringer et al. Particle Data Group. *Phys.Rev.*, D86:023501, 2012. 19, 20, 21, 64, 65

[73] M. C. Smith et al. *Mon. Not. Roy. Astron. Soc.*, 379:755 – 772, 2007. 36

[74] Toby Falk, Keith A. Olive, and Mark Srednicki. Heavy sneutrinos as dark matter. *Phys.Lett.*, B339:248–251, 1994. 34

[75] W.L. Freedman et al. Final results from the Hubble Space Telescope key project to measure the Hubble constant. *Astrophys.J.*, 553:47–72, 2001. 32

[76] Katherine Garrett and Gintaras Duda. Dark Matter: A Primer. *Adv.Astron.*, 2011:968283, 2011. 36, 41

[77] Tony Gherghetta. TASI Lectures on a Holographic View of Beyond the Standard Model Physics. 2010. 65

[78] The Tevatron Electroweak Working Group. Combination of CDF and D0 Results on the Mass of the Top Quark Using Up to 5.6 fb^{-1} of Data. 2010. 18

[79] Rudolf Haag, Jan T. Łopuszański, and Martin Sohnius. All possible generators of supersymmetries of the s-matrix. *Nuclear Physics B*, 88(2):257 – 274, 1975. 22

[80] Jiyeon Han. The Angular Coefficients and A_{fb} of Drell-Yan e^+e^- Pairs in the Z Mass Region from $p\bar{p}$ Collision at $\sqrt{s} = 1.96$ TeV. 2011. 18

[81] S.W. Hawking. On the Rotation of the universe. *Mon.Not.Roy.Astron.Soc.*, 142:129–141, 1969. 47

[82] Henk Hoekstra, Howard Yee, and Mike Gladders. Current status of weak gravitational lensing. *New Astron.Rev.*, 46:767–781, 2002. 29

[83] N. Jarosik, C.L. Bennett, J. Dunkley, B. Gold, M.R. Greason, et al. Seven-Year Wilkinson Microwave Anisotropy Probe (WMAP) Observations: Sky Maps, Systematic Errors, and Basic Results. *Astrophys.J.Suppl.*, 192:14, 2011. 31

[84] A. Gould J.N. Bahcall, C. Flynn. . *ApJ*, 389:234, 1992. 28

[85] Gerard Jungman, Marc Kamionkowski, and Kim Griest. Supersymmetric dark matter. *Phys.Rept.*, 267:195–373, 1996. 36

[86] Mitsuru Kakizaki, Shigeki Matsumoto, Yoshio Sato, and Masato Senami. Relic abundance of LKP dark matter in UED model including effects of second KK resonances. *Nucl.Phys.*, B735:84–95, 2006. 128

[87] Mitsuru Kakizaki, Shigeki Matsumoto, and Masato Senami. Relic abundance of dark matter in the minimal universal extra dimension model. *Phys.Rev.*, D74:023504, 2006. 128

[88] J. Kiryluk. The latest results from the IceCube experiment. *AIP Conf.Proc.*, 1441:454–457, 2012. 40

[89] Ian I. Kogan and Graham G. Ross. Brane universe and multigravity: Modification of gravity at large and small distances. *Phys.Lett.*, B485:255–262, 2000. 65

[90] Edward W. Kolb, Daniel J.H. Chung, and Antonio Riotto. WIMPzillas! pages 91–105, 1998. 35

[91] Kyoungchul Kong and Konstantin T. Matchev. Precise calculation of the relic density of Kaluza-Klein dark matter in universal extra dimensions. *JHEP*, 0601:038, 2006. 124, 125, 126

[92] M. Kowalski et al. Improved Cosmological Constraints from New, Old and Combined Supernova Datasets. *Astrophys.J.*, 686:749–778, 2008. 33

[93] Andrzej Krasinski, Christoph G. Behr, Engelbert Schucking, Frank B. Estabrook, Hugo D. Wahlquist, et al. The Bianchi classification in the Schucking-Behr approach. *Gen.Rel.Grav.*, 35:475–489, 2003. 47

[94] A.B. Lahanas, Dimitri V. Nanopoulos, and V.C. Spanos. Neutralino relic density in a universe with nonvanishing cosmological constant. *Phys.Rev.*, D62:023515, 2000. 44

[95] Kenneth Lane. Two lectures on technicolor. 2002. 23

[96] David J. Lange. Study of CP violation in B mesons using the BABAR detector. *eConf*, C020805:TW01, 2002. 18

[97] Julien Lesgourgues. An Overview of cosmology. 2004. 9, 25

[98] Jérémie Llodra-Perez. Modèles effectifs de nouvelle physique au Large Hadron Collider. 134

[99] Laura Lopez Honorez, Emmanuel Nezri, Josep F. Oliver, and Michel H.G. Tytgat. The Inert Doublet Model: An Archetype for Dark Matter. *JCAP*, 0702:028, 2007. 143

[100] Joseph D. Lykken. Weak scale superstrings. *Phys. Rev. D*, 54:R3693–R3697, Sep 1996. 48

[101] R. Benton Metcalf, Leonidas A. Moustakas, Andrew J. Bunker, and Ian R. Parry. Spectroscopic gravitational lensing and limits on the dark matter substructure in Q2237+0305. *Astrophys.J.*, 607:43–59, 2004. 28

[102] R.N. Mohapatra, S. Nussinov, and V.L. Teplitz. Mirror matter as selfinteracting dark matter. *Phys.Rev.*, D66:063002, 2002. 29

[103] Leonidas A. Moustakas and R. Benton Metcalf. Detecting dark matter substructure spectroscopically in strong gravitational lenses. *Mon.Not.Roy.Astron.Soc.*, 339:607, 2003. 28

[104] Lars Nilse. Classification of 1-D and 2-D orbifolds. *AIP Conf.Proc.*, 903:411–414, 2007. 49, 73

[105] J. H. Oort. The force exerted by the stellar system in the direction perpendicular to the galactic plane and some related problems. Bull. Astron. Inst. Netherlands, 6:249, August 1932. 27

[106] Lochlain O'Raifeartaigh and Norbert Straumann. Early history of gauge theories and Kaluza-Klein theories. 1998. 47

[107] A. A. Penzias and R. W. Wilson. A Measurement of Excess Antenna Temperature at 4080 Mc/s. ApJ, 142:419–421, July 1965. 30

[108] Josep M. Pons. Dimensional reduction, truncations, constraints and the issue of consistency. *J.Phys.Conf.Ser.*, 68:012030, 2007. 48

[109] Eduardo Ponton and Lin Wang. Radiative effects on the chiral square. *JHEP*, 0611:018, 2006. 88

[110] Martin Puchwein and Zoltan Kunszt. Radiative corrections with 5-D mixed position / momentum space propagators. *Annals Phys.*, 311:288–313, 2004. 59, 61, 89, 91

[111] Lisa Randall and Raman Sundrum. A Large mass hierarchy from a small extra dimension. *Phys.Rev.Lett.*, 83:3370–3373, 1999. 64

[112] Finn Ravndal. Scalar gravitation and extra dimensions. 2004. 47

[113] Riazuddin and Fayyazuddin. A model for electroweak interactions based on the left-right symmetric gauge group. *Physics Letters B*, 90(4):401 – 404, 1980. 160

[114] Leslie J Rosenberg and Karl A. van Bibber. Searches for invisible axions. *Physics Reports*, 325(1):1 – 39, 2000. 35

[115] Subir Sarkar. Cosmic ray signatures of massive relic particles. 1999. 35

[116] Ichiro Satake. The Gauss-Bonnet Theorem for V-manifolds. *J. Math. Cos. Japan*, 9(4):464–492, 1957. 49

[117] Doris Schattschneider. The plane symmetry groups: Their Recognition and Notation. *American Mathematical Monthly*, 85(6):439–450, 1978. 49

[118] Joel Scherk and John H. Schwarz. Dual Field Theory of Quarks and Gluons. *Phys.Lett.*, B57:463–466, 1975. 48

[119] Joel Scherk and John H. Schwarz. How to Get Masses from Extra Dimensions. *Nucl.Phys.*, B153:61–88, 1979. 47

[120] Geraldine Servant and Timothy M.P. Tait. Is the lightest Kaluza-Klein particle a viable dark matter candidate? *Nucl.Phys.*, B650:391–419, 2003. 42, 124

[121] G. F. Smoot, C. L. Bennett, A. Kogut, E. L. Wright, J. Aymon, N. W. Boggess, E. S. Cheng, G. de Amici, S. Gulkis, M. G. Hauser, G. Hinshaw, P. D. Jackson, M. Janssen, E. Kaita, T. Kelsall, P. Keegstra, C. Lineweaver, K. Loewenstein, P. Lubin, J. Mather, S. S. Meyer, S. H. Moseley, T. Murdock, L. Rokke, R. F. Silverberg, L. Tenorio, R. Weiss, and D. T. Wilkinson. Structure in the COBE differential microwave radiometer first-year maps. ApJ, 396:L1–L5, September 1992. 31

[122] G.D. Starkman and D.N. Spergel. Proposed new technique for detecting supersymmetric dark matter. *Phys.Rev.Lett.*, 74:2623–2625, 1995. 36

[123] William Thurston. *The Geometry and Topology of Three-Manifolds*. Princeton University Press, 2002. 49

[124] J. Anthony Tyson, Greg P. Kochanski, and Ian P. Dell'Antonio. Detailed mass map of cl 0024+1654 from strong lensing. *The Astrophysical Journal Letters*, 498(2):L107, 1998. 30

[125] R. A. Remillard W. H. Tucker, H. Tananbaum. . *ApJ*, 444, 1995. 29

[126] Christian Weinheimer. The Neutrino mass direct measurements. pages 335–344, 2003. 34

[127] James D. Wells. Annihilation cross-sections for relic densities in the low velocity limit. 1994. 44

[128] R. Jeffrey Wilkes. Recent results from Super-Kamiokande. 2011. 40

[129] Masashi Yokoyama. Observation of large CP violation in the neutral B meson system using B0 —gt; J/psi K(L) decay. 2001. 18

[130] Naoki Yoshida, Aaron Sokasian, Lars Hernquist, and Volker Springel. Early structure formation and reionization in a warm dark matter cosmology. *Astrophys.J.*, 591:L1–L4, 2003. 35

[131] Houri Ziaeepour. Searching the footprint of WIMPZILLAs. *Astropart.Phys.*, 16:101–120, 2001. 35